Application of Surface Enhanced Raman Spectroscopy to Biological Systems

vorgelegt von
Diplom-Chemiker
Hoang Khoa Ly
aus Hanoi

von der Fakultät II – Mathematik und Naturwissenschaften
der Technischen Universität Berlin
zur Erlangung des akademischen Grades

Doktor der Naturwissenschaften
– Dr. rer. nat. –

genehmigte Dissertation

Promotionsausschuss:

Vorsitzender:	Prof. Dr. Reinhard Schomäcker
Gutachter:	Prof. Dr. Peter Hildebrandt
Gutachter:	Prof. Dr. Ulla Wollenberger

Tag der wissenschaftlichen Aussprache: 05. Oktober 2012

Berlin 2013
D 83

Mama und Papa

...đời đời không tàn với khúc nhạc lòng tôi

Abstract

In this thesis resonance Raman (RR) and surface enhanced resonance Raman (SERR) spectroscopy were applied to investigate biological systems, particularly heme containing proteins. The electronic transition of the heme group can be exploited so that, with a properly tuned light excitation, highly intense Raman signals solely of the cofactor were obtained. If the proteins are adsorbed on a rough silver surface, then the resonance effect can be combined with the surface enhancement effect to yield a highly sensitive technique, which allows probing of molecules even at sub-monolayer coverage. Additionally, if the surface is constituted by an electrode, surface redox reactions and kinetics of adsorbed molecules can be investigated.

Such a setup was used to study the electron transfer (ET) properties of cytochrome *c* (cyt*c*), a small soluble redox protein which acts as an electron shuttle in the respiratory chain. Cyt*c* was immobilized on a rough silver electrode coated with a biomimetic monolayer of ω-carboxylated alkanethiols and investigated by stationary and time resolved SERR spectroscopy. Specifically, the ET kinetics of the protein at short distances to the electrode was monitored. The results provide new insights into the heterogeneous protein ET and indicate a central role of the interfacial electric field that has influence on the protein orientational dynamics as well as on the electronic coupling and the rearrangement of hydrogen bond networks at the protein-monolayer interface.

Beside its function in bioenergetics, cyt*c* also plays a key role as a signal transducer in the apoptosis, the programmed cell death. To exert this function, it has to be detached from the inner mitochondrial membrane, where it is bound to under normal conditions and released to the cytosol. The factors that control the transfer of cyt*c* are still under debate. In this respect a possible influence of posttranslational Tyr nitration to switch cyt*c*'s function from ET to peroxidation, which is considered to be the first step in initiating apoptosis, is discussed. Therefore, mono-tyrosine and nitrated mono-tyrosine mutants were investigated using RR spectroscopy in order to evaluate the impact of tyrosine nitration on the integrity of the heme pocket. It could be shown that the destabilization caused by nitration is not directly correlated with the respective peroxidase activity of the mutant. Moreover, experiments in which the mutants were immobilized on a monolayer coated electrode showed that the destabilization, promoted by the interfacial electric field, did not depend on the nitration.

Furthermore, the applicability of time resolved SERR spectroscopy for kinetic investigations of biofilms of the bacterium *Geobacter Sulfurreducens*, grown on rough silver electrodes, was demonstrated. The bacterium possesses a large number of multi-heme proteins, so-called outer membrane cytochromes (Omcs), which facilitate the extracellular ET. These cytochromes are accumulated at the biofilm-electrode interface and therefore can be probed using SERR spectroscopy. By applying stationary and time resolved SERR spectroscopy, it could be shown that these cytochromes function as electron 'gates' between the biofilm and the electrode, and an average heterogeneous ET rate constant could be determined. Finally, results obtained from kinetic simulations indicate that the interfacial ET is the bottleneck of the biofilm-electrode ET process.

The last part of the thesis is dedicated to methodological developments to expand the applicability of surface enhanced Raman (SER) spectroscopy to non-coinage metals. Here, a Pt-Ag device was fabricated, using a nanostructured Ag support which was coated by a dielectric layer and subsequently covered by a Pt island film. The idea is that the isolated underlying Ag support should provide the necessary surface enhancement, while the top metal layer promotes the interfacial reactions to be studied. The fabricated hybrid device was tested in terms of stability and SER performance.

Zusammenfassung

In dieser Arbeit wurden die Resonanz-Raman-Spektroskopie (RR-Spektroskopie) sowie die oberflächenverstärkte Resonanz-Raman-Spektroskopie (SERR-Spektroskopie) verwendet, um biologische Systeme, insbesondere Hämproteine, zu untersuchen. Der elektronische Übergang der Hämgruppe kann ausgenutzt werden, um über gezielte Lichtanregung ausschließlich stark verstärkte Raman-Streusignale des Kofaktors zu erhalten. Adsorbiert an aufgerauten Silberelektroden kommt der Oberflächenverstärkungseffekt zum Tragen, der es ermöglicht, Proteine selbst bei Submonolagen-Beschichtung zu untersuchen. Darüber hinaus ermöglicht die Elektrode die Ansteuerung von Oberflächenredoxreaktionen, was ausgenutzt werden kann, um Informationen über die Redox-Eigenschaften und Dynamik von Hämproteinen zu erhalten.
Dieser experimentelle Ansatz wurde verwendet, um die Elektronentransferkinetik des Proteins Cytochrom *c* - ein kleines, redox-aktives Hämprotein in der mitochondrialen Atmungskette - zu untersuchen. Cytochrom *c* wurde dafür auf einer rauen Silberelektrode, beschichtet mit einer biomimetischen Monoschicht aus carboxyl-terminierten Alkanthiolen, immobilisiert und mit stationärer und zeitaufgelöster SERR-Spektroskopie untersucht. Besonderes Augenmerk wurde auf die Elektronentransfereigenschaften des Proteins bei kleinen Abständen zur Elektrode gelegt. Die Ergebnisse der Untersuchungen geben neue Aufschlüsse über den heterogenen Elektronentransfer und deuten dabei auf eine besondere Rolle des elektrischen Feldes an Grenzflächen hin. Dieses beeinflusst die Oberflächenorientierungsdynamik, die Elektronentunnel-Wahrscheinlichkeit und die Umstrukturierung der Wasserstoffbrückennetzwerke des Protein und an der Grenzfläche.
Neben der Rolle als Elektronenüberträger in der Atmungskette fungiert Cytochrom *c* ebenso als Signalprotein in der Apoptose, dem programmierten Zelltod. Dafür muss es die mitochondriale Membran, an die es normalerweise gebunden ist, verlassen und ins Zellplasma übergehen. Die Ursache für diese Migration ist noch weitestgehend ungeklärt. Als ein Faktor, der den damit verbundenen Verlust an Redox- und die Zunahme an Peroxidase-Aktivität erklärt, wird die post-translationale Nitrierung von Tyrosinresten des Proteins diskutiert. Folglich wurde mittels RR-Spektroskopie der Einfluss von post-translationaler Tyrosin-Nitrierung auf die Integrität der Hämtasche untersucht. Es zeigte sich, dass die Destabilisierungen, hervorgerufen durch die Nitrierung verschiedener Tyrosinreste, nicht mit der jeweiligen gesteigerten Peroxidase-Aktivität korrelieren. Experimente, bei denen die verschiedenen Tyrosin-Mutanten auf eine Elektrode adsorbiert wurden, zeigten außerdem, dass die Grenzflächen bedingte Destabilisierung der Hämtasche unabhängig von der Nitrierung wirkt.
Des Weiteren wurde die Anwendbarkeit der zeitaufgelösten SERR-Spektroskopie zur kinetischen Untersuchung von Biofilmen des Bakteriums *Geobacter Sulfurreducens* demonstriert. Dies ist möglich, da das Bakterium eine Reihe von Multihämproteinen, sogenannten "outer membrane cytochromes" (Omcs), besitzt, die für den extrazellulären Elektronentransfer verantwortlich sind. Besonders stark sind diese Cytochrome an der Grenzfläche zwischen Biofilm und Elektrode akkumuliert. Durch Anwendung von stationärer und zeitaufgelöster SERR-Spektroskopie konnte die besondere Rolle der Omcs als "Elektronenschleuse" zwischen Biofilm und Elektrode nachgewiesen und eine gemittelte heterogene Elektronentransferratenkonstante bestimmt werden. Weiter deuten die Experimente zusammen mit kinetischen Simulationen darauf hin, dass der heterogene Elektronentransfer der geschwindigkeitsbestimmende Schritt beim Elektronenaustausch Biofilm-Elektrode ist.
Der letzte Teil der Arbeit ist der methodischen Entwicklung der oberflächenverstärkten Raman-Spektroskopie zur Ausdehnung auf Nicht-Münzmetalle gewidmet. Dazu wurde eine Pt-Ag-Hybrid-

Elektrode konstruiert, die aus einem nanoskopisch rauen Silberuntergrund, welcher zuerst mit einem dielektrischen Material beschichtet und anschließend mit einem Platinfilm überzogen wurde. Während der abgeschottete Silberuntergrund für die notwendige Oberflächenverstärkung sorgt, laufen an der Pt-Oberfläche die zu untersuchenden Grenzflächenreaktionen ab. Die Hybrid-Elektrode wurde in Bezug auf ihre Stabilität und ihre Signalverstärkungseigenschaften bei verschiedenen Wellenlängen untersucht. Die Resultate zeigen, dass starke Raman-Signale von Probenmolekülen, adsorbiert auf der äußeren Pt-Schicht, erhalten werden können. Die Signale sind nur geringfügig schwächer im Vergleich zu einer direkten Adsorption auf Ag.

Publications

Parts of this work are published in the following articles:

1. Ly, H. K.; Marti, M. A.; Martin, D. F.; Alvarez-Paggi, D.; Meister, W.; Kranich, A.; Weidinger, I. M.; Hildebrandt, P.; Murgida, D. M. Thermal Fluctuations Determine the Electron-Transfer Rates of Cytochrome c in Electrostatic and Covalent Complexes. *ChemPhysChem* **2010**, 11(6), 1225–1235.
2. Ly, H. K.; Wisitruangsakul, N.; Sezer, M.; Feng, J. J.; Kranich, A.; Weidinger, I. M.; Zebger, I.; Murgida, D. M.; Hildebrandt, P. Electric Field Effects on the Interfacial Electron Transfer and Protein Dynamics of Cytochrome c. *J. Electroanal. Chem.* **2011**, 660, 367–376.
3. Ly, H. K.; Sezer, M.; Wisitruangsakul, N.; Feng, J. J.; Kranich, A.; Millo, D.; Weidinger, I. M.; Zebger, I.; Murgida, D. M.; Hildebrandt, P. Surface Enhanced Vibrational Spectroscopy for Probing Transient Interactions of Proteins with Biomimetic Interfaces: Electric Field Effects on Structure, Dynamics and Function of Cytochrome c. *FEBS Review* **2011**, 278, 1382–1390.
4. Ly, H. K.; Köhler, C.; Fischer, A.; Kabuß, J.; Schlosser, F.; Schoth, M.; Knorr, A.; Weidinger, I. M. Induced Surface Enhancement in Coral Pt Island Films Attached to Nanostructured Ag Electrodes. *Langmuir* **2012**, 28, 5819–5825.
5. Ly, H. K.; Utesch, T.; Díaz-Moreno, I.; Garía-Heredia, J. M.; Rósa, M. A. d. l.; Hildebrandt, P. Pertubation of the Redox Site Structure of Cytochrome c upon Tyrosine Nitration. *J. Phys. Chem. C* **2012**, 116, 5694–5702.
6. Ly, H. K.; Harnisch, F.; Hong, S.-F.; Schröder, U.; Hildebrandt, P; Millo, D. Unraveling the Interfacial Electron Transfer Dynamics of Electroactive Microbial Biofilms using Surface-Enhanced Raman Spectroscopy. *ChemSusChem* **2012**; DOI: 10.1002/cssc.201200626.

Other publications in peer-reviewed journals:

1. Ledesma, G. A.; Murgida D. H.; Ly, H. K.; Wackerbarth, H.; Ulstrup, J.; Costa-Filho, A. J.; Vila, A. J. The Met Axial Ligand Determines the Redox Potential in CuA Sites. *J. Amer. Chem. Soc. Comm.* **2007**, 129(39), 11884–11885.
2. Wisitruangsakul, N.; Zebger, I; Ly, H. K.; Murgida, D. H.; Ekgasit, S.; Hildebrandt, P. Redox-linked Protein Dynamics of Cytochrome c Probed by Time-Resolved Surface Enhanced Infrared Absorption Spectroscopy. *Phys. Chem. Chem. Phys* **2008**, 10, 5267–5268.
3. Kranich, A.; Ly, H. K.; Hildebrandt, P.; Murgida, D. M. Direct Observation of the Gating Step in Protein Electron Transfer: Electric-Field-Controlled Protein Dynamics. *J. Am. Chem. Soc.* **2008**, 130, 9844–9848.
4. Millo, D.; Ranieri, A.; Gross, P.; Ly, H. K.; Borsari, M.; Hildebrandt, P.; Wuite, G. J. L.; Gooijer, C.; Zwan, G. v. d. Electrochemical Response of Cytochrome c Immobilized on Smooth and Roughened Silver and Gold Surfaces Chemically Modified with 11-Mercaptounodecanoic Acid. *J. Phys. Chem. C* **2009**, 113(7), 2861-2866.
5. Sezer, M.; Feng, J. J.; Ly, H. K.; Shen, Y; Nakanishi, T.; Kuhlmann, U.; Hildebrandt, P.; Möhwald, H.; Weidinger, I. M. Multi-layer Electron Transfer Across Nanostructured Ag-SAM-Au-SAM Junctions Probed by Surface Enhanced Raman Spectroscopy. *Phys. Chem. Chem. Phys* **2010**, 12, 9822–9829.
6. Hildebrandt, P.; Feng, J. J.; Kranich, A.; Ly, H. K.; Martin, D. F.; Martin, M.; Murgida, D. H.; Alvarez-Paggi, D.; Wisitruangsakul, N.; Sezer, M.; Weidinger, I. M.; Zebger, I. Electron Transfer of Proteins at Membrane Models. In *Surface Enhanced Raman Spectroscopy: Analytical, Biophysical and Life Science Applications*; Schlücker, S., Ed.; Wiley-VCH, 2010; 219–241.
7. Millo, D.; Harnisch, F.; Patil, S. A.; Ly, H. K.; Schröder, U.; Hildebrandt, P. In situ Spectroelectrochemcial Investigation of Electrocatalytic Microbial Biofilms by Surface-Enhanced Resonance Raman Spectroscopy. *Angew. Chem. Int. Ed.* **2011**, 123(11), 2673-2675.
8. Sivanesan, A.; Ly, H. K.; Kozuch, J.; Sezer, M.; Kuhlmann, U.; Fischer, A.; Weidinger, I. M. Functionalized Ag Nanoparticles with Tunable Optical Properties for Selective Protein Analysis. *Chem. Commun.* **2011**, 47, 3553–3555.
9. Sivanesan, A.; Kozuch, J.; Ly, H. K.; Kalaivani, G.; Fischer, A.; Weidinger, I. M. Tailored Silica Coated Ag Nanoparticles for Non-Invasive Surface Enhanced Raman Spectroscopy of Biomolecular Targets. *RSC Adv* **2012**, 2, 805–808.

Talks:

1. *Electron transfer kinetics of electrostatically and covalently immobilized horse heart Cytochrome c on OH/COOH terminated SAMs*, Invited Lecture at: *Workshop on Structure, dynamics, and function of proteins*. 2008 Sept. 23 - 25; ITQB Oeiras, Portugal - Technical University of Berlin/ UNICAT - Unifying Concepts in Catalysis..

Poster contributions:

1. Sezer, M.; Ly, H. K.; Feng, J.-J.; Kranich, A.; Utesch, T.; Mroginski, M. A.; Kuhlmann, U.; Murgida, D. H.; Hildebrandt, P.; Weidinger. I. M. *Electron Transfer Properties of Cytochrome c on Ag Electrodes Measured with Surface Enhanced Resonance Raman Spectroscopy*. Poster at: *Tagung der Deutschen Gesellschaft für Biophysik*; 2008 Sept. 28 - Oct 01.; Freie Universität Berlin, Germany.
2. Ly, H. K.; Fischer, A.; Hildebrandt, P.; Weidinger, I. M.; Induced SER Activity in Ag-Pt Hybrid Devices. Poster at: *International Conference on Raman Spectroscopy*; 2010 Oct. 08 - 15, Boston, MA, USA.
3. Ly, H. K.; Harnisch, F.; Hong, S-F; Schröder, U.; Hildebrandt, P.; Millo, D. *Kinetics of the Heterogeneous Electron Transfer of Outer Membrane Cytochromes in Electrocatalytic Biofilms Studied by Time Resolved Surface Enhanced Resonance Raman Spectroscopy*. Poster at: *International Microbial Fuelcells Conference*, 2011 June 06 - 08; Leeuwarden, The Netherlands.
4. Ly, H. K.; Fischer, A.; Köhler, C.; Kabuß, J.; Schlosser, F.; Knorr, A.; Hildebrandt, P.; Weidinger, I. M. *SER active Pt-Ag Hybrid Device for Probing Pt-Catalyzed Reactions*. Poster at: *International Symposium on Relations between Homogeneous and Heterogeneous Catalysis*. 2011 Sept 11 - 16; Freie Universität Berlin, Germany.

Contents

Abstract III

Zusammenfassung V

Publications VII

Contents XI

1 Introduction and Motivation 1

2 Materials and Methods 5
- 2.0.1 Raman Effect . . . 5
- 2.0.2 Quantum Mechanical Treatment of the Raman Effect . . . 6
- 2.0.3 Resonance Raman Effect . . . 7
- 2.0.4 Surface Enhanced Raman . . . 9
- 2.0.5 Surface Enhanced Resonance Raman . . . 12

2.1 Properties of Electrochemical Interfaces . . . 13
- 2.1.1 Self Assembled Monolayer - SAM . . . 14

2.2 Heme proteins . . . 15
- 2.2.1 Cytochromes . . . 16
- 2.2.2 Resonance Raman Spectroscopy of Cytochromes . . . 18

2.3 Electron Transfer Theory . . . 20
- 2.3.1 Homogeneous ET and Classical Marcus Theory . . . 20
- 2.3.2 Heterogeneous ET . . . 23

3 Experimental Details and Instrumentation 25

3.1 Confocal Raman Spectrometer . . . 25

3.2 Electrochemical Measurements . . . 25

3.3 Resonance Raman and Surface Enhanced Resonance Raman Measurements . . . 26

4 Results 29

4.1 Electron Transfer Properties of Cytochrome *c* at Electrochemical Interfaces . . . 29

4.2 Tyrosine Nitrated Cytochrome *c* - Role in Apoptosis . . . 33

4.3 Interfacial ET of Outer Membrane Cytochromes Embedded in Biofilms of *Geobacter* 35

4.4 Surface Enhanced Raman Active materials - Pt Coated Ag Electrodes . . . 41

5 Conclusions and Outlook 43

Bibliography 47

6 Thermal Fluctuations Determine the Electron-Transfer Rates of Cytochrome *c* in Electrostatic and Covalent Complexes 63

7 Electric Field Effects on the Interfacial Electron Transfer and Protein Dynamics of Cytochrome *c* 77

8 Perturbation of the Redox Site Structure of Cytochrome *c* upon Tyrosine Nitration 91

9 Unraveling the Interfacial Electron Transfer Dynamics of Electroactive Microbial Biofilms Using Surface-Enhanced Raman Spectroscopy 103

10 Induced Surface Enhancement in Coral Pt Island Films Attached to Nanostructured Ag Electrodes 113

Abbreviations

5c	five coordinated
5cHS	five coordinated high spin
6c	six coordinated
6cHS	six coordinated high spin
6cLS	six coordinated low spin
BES	bioelectrochemical systems
CCD	charged coupled device
CE	couter electrode
CV	cyclic voltammetry
Cytc	Cytochrom c
DOS	density of states
EC	electrochemistry
ET	electron transfer
FC	Franck-Condon
FCWD	Franck-Condon weighted density of states
HS	high spin
LS	low spin
MFC	microbial fuel cells
MO	molecular orbital
MUA	11-mercaptoundecanoic acid
NHE	normal hydrogen electrode
Omc	outer membrane cytochrome
RE	reference electrode
RR	resonance Raman
RT	room temperature
SAM	self assembled monolayer
SEIRA	surface enhanced infrared absorption
SER	surface enhanced Raman
SERR	surface enhanced resonance Raman
UV/Vis	ultraviolet / visible
WE	working electrode

1 Introduction and Motivation

Resonance Raman (RR) and surface enhanced Raman (SER) are vibrational spectroscopic methods of high sensitivity. While resonance Raman spectroscopy is suitable to probe molecules that exhibit an electronic transition matching the excitation laser line, surface enhanced Raman spectroscopy focusses on molecules in vicinity of metal surfaces that allow the optical excitations of surface plasmons. In both cases, the obtained signal intensities are very high and can exceed those of ordinary Raman spectroscopy by several orders of magnitude.

In the 1970th, Spiro *et al* successfully employed resonance Raman spectroscopy for the investigation of chromophore containing proteins. These were specifically heme containing proteins such as the cytochromes, the cytochrome c oxidase and the cytochrome P450 but also the oxygen transporting proteins myo- and hemoglobin. The advantage of resonance Raman spectroscopy is that, if the excitation laser line is tuned to match an electronic transition of the chromophore, then only vibrational bands originating from the cofactor will be obtained. Hence, signal interferences from the protein backbone as in IR absorption experiments are negligible. Thus, this method represents a versatile technique for detailed investigation of constitution and functioning of a cofactor.

The best investigated protein in this context so far is the small soluble heme protein cytochrome *c*. This protein is found in aerobic organisms where it is located at the inner mitochondrial membrane and plays a central role in the respiratory chain. It acts as an electron carrier protein and shuttles electrons between the integral membrane enzymes cytochrome *c* reductase and cytochrome *c* oxdiase (complex III and complex IV, respectively). Moreover, recent studies also point to a crucial role of cytochrome *c* in the mitochondrial mediated apoptosis, revitalizing the discussion about this protein. In many studies using also various other spectroscopic and electrochemical methods, cytochrome *c* was used as a model compound to gain general insights into biological electron transfer (ET) processes. A common experimental setup to probe electron transfer kinetics of cytochrome *c* consists of a solid metal electrode coated with self-assembled monolayers to promote an adsorption of the protein in its native state. Redox reactions are triggered by changing the applied potential either stepwise or in a potential-jump mode. The employment of solid electrodes inheres numerous advantages compared to studies in solution. The electrode-SAM system can be adapted to mimic biological membranes where most electron transfer reactions occur. For cytochrome *c*, a monolayer consisting of negatively charged ω-carboxylated alkanethiols has turned out to be most suitable.

However, the adsorption of cytochrome *c* on such monolayers yields coverages in the order of picomol per cm^2, which is even below a monolayer coverage. Under these conditions even resonance Raman spectroscopy reaches its limits. Therefore, to boost the signal intensity dramatically, a combination of resonance Raman and surface enhanced Raman is required, *i.e.* surface enhanced resonance Raman (SERR) spectroscopy. This technique utilizes a rough metal support that can produce surface plasmon resonances upon light excitation. These plasmons are quantized vibrations of conducting electrons within the metal, which, in turn, generate strongly oscillating electric fields in the near-field of the surface. These enhanced electric fields are commonly believed to be responsible for a drastically increase in Raman scattering cross section of molecules in close vicinity to such a metal surface. To combine resonance Raman and surface enhanced Raman spectroscopy, an excitation line has to be selected that is in resonance with both the electronic transition of the chromophore of the adsorbed molecule and the plasmons of the underlying metal support. The required wavelength in the latter case varies strongly with the kind of metal due to the different electronic properties. For cytochromes exhibiting a strong electronic absorption in the near UV region at ca. 400 nm (Soret

band), nanoscopically rough Ag surfaces match both conditions. Upon using such nanostructured Ag electrodes coated with an appropriate SAM, high intensity signals of cytochrome *c* are obtained. The vibrational band pattern of heme proteins is well known and undergoes only slight changes upon adsorption. Therefore, it is possible to draw conclusion about the spin, ligation and oxidation state of the adsorbed proteins by analyzing the spectra. Such an approach was successfully applied by Hildebrandt *et al* to study the redox and conformational kinetics and equilibria of adsorbed cytochrome *c* and other redox enzymes.
In addition to biological applications of SE(R)R spectroscopy, there is an enormous potential of non-resonant surface enhanced Raman (SER) and SERR spectroscopy in surface an interfacial science in general, such as in heterogeneous catalysis or photovoltaic. To optimize such processes, a profound knowledge about the underlying molecular mechanisms is required. In principle, this can be provided by SER spectroscopy. The only drawback is related to the metal support. Unfortunately, most technically relevant reactions require metals or materials (e.g. Pt, Rh or MgO and TiO_2) that provide only low or no intrinsic surface enhancements. Consequently, those metals that exhibit high surface enhancements (Ag and Au) are of lower technological interests. A possible solution for this problem are hybrid metal composites, consisting of a supporting metal with high field enhancements covered by a layer of metal of choice for a certain technical application. Although this principle is known for a long time, the exploitation of this synergetic effect, provided by metals with different electronic properties, is about to be investigated more systematically. Real applications to relevant technical processes are yet still missing.

In the first part of this thesis, surface enhanced resonance Raman spectroscopy with Soret band excitation was applied to investigate the electron transfer kinetics of horse heart cytochrome *c* adsorbed on an Ag electrode coated with a carboxyl-terminated alkanethiol SAM. Additionally, Q band excitation methods, which allow probing of the orientational dynamics and kinetics of the protein, were employed. In combination with findings obtained by other methods such as theoretical calculations, cyclic voltammetry and surface enhanced infrared absorption spectroscopy, the results provide novel insights into the electric field dependence of the various steps of the interfacial redox process.
In the second part, RR and SERR spectroscopy was used to study the effects of tyrosine nitration on the heme site structure of human heart cytochrome *c*. Tyrosine nitration and other posttranslational protein modifications are believed to play a key role in altering the function of cytochrome *c* from an electron shuttle protein to a crucial signal transducer in the apoptotic reaction cascades. Information on the effects of different tyrosine nitrations was obtained by using mono-tyrosine and nitrated mono-tyrosine mutants. Immobilizing the protein variants on electrodes coated with biomimetic membrane models allows studying the combined effects of Tyr nitration and local electric fields on the structural and functional properties of the protein.
In the third part of this work, the application of time resolved SERR spectroscopy for determining ET kinetics of outer membrane cytochromes (Omcs) embedded in electro-catalytically active biofilms of *Geobacter sulfurreducens* grown on rough Ag electrodes is demonstrated. These microbes are metal-reducing bacteria that can consume small organic compounds such as lactate or acetate to generate electrons, which - if present - can be delivered to a solid terminal electron acceptor. Omcs are either integral membrane or peripherally bound proteins including several heme cofactors to provide ET routes from the cell to an external acceptor, in this case the electrode. After demonstrating the applicability of SERR spectroscopy to probe redox processes of the Omcs, time resolved SERR studies were carried out to monitor the ET dynamics of the Omcs directly. The results were discussed in terms of an overall ET mechanism.
In the last part of this thesis, a Pt-Ag hybrid electrode was manufactured and systematically investigated in terms of SER signal enhancements. Following a procedure proposed by Feng *et al*, a rough silver electrode was covered with different dielectric spacers, and subsequently a platinum island film

was placed on top via reductive metallation. The signal performance was tested using cytochrome *c* and 2-mercaptopyridine as probe molecules for 413 nm and 514 nm excitation, respectively.

2 Materials and Methods

In this chapter, the materials and the fundamentals of the applied methods are briefly introduced. This includes a short description of Raman, resonance Raman and surface enhanced Raman spectroscopy. Furthermore, an overview of the properties of electrochemical interfaces and a short introduction to heme proteins, particularly cytochromes, are provided. Finally, a brief summary of electron transfer theory is presented.

2.0.1 Raman Effect

The discussion on light scattering effects can be traced back to the times of Leonardo Da Vinci who ascribed the blue color of the sky to light scattering on suspended macroparticles in the atmosphere such as dusk, water droplets and ice crystals [1]. It took a long time until in 1873 Maxwell came to the conclusion that it might be the molecule itself who acts as scattering center and thus, information on the molecule's properties are inherent in the scattered radiation. Although the first experimental evidences for that were already stated by Lallemand in 1869, it was Lord Rayleigh who provided a profound survey on that issue in 1899 [2]. The first indication for the existence of frequency modified scattered radiation was stated by Smekal in 1923 [3]. In his theoretical work, he found that upon photon induced transition of a molecule from one quantum state to another, the scattered light contains frequencies that are smaller and larger than the frequency of the incident light by the energy difference between the states. This observation could be experimentally proven by C. V. Raman in 1928 and independently by Landsberg and Mandelstam [4, 6]. Raman was awarded the Nobel prize for his discovery. The frequency shift of a scattered radiation with respect to the incident radiation due to energy transfer with molecules is referred to as Raman effect [5].

A classical approach to the theoretical fundamentals of Raman scattering is based on first order induced electric dipoles. These are generated upon interaction between the oscillating electric field vector E of the incoming light and the electron cloud of the scattering center. The magnitude and direction of the induced dipole moment vectors p depend on the polarizability of the molecule. This correlation is expressed as

$$p = \alpha \cdot E. \tag{2.1}$$

α denotes the 3x3 polarizability tensor and depends on the positions of the nuclei with respect to the electron cloud and thus, is also sensitive to changes of the molecule's internal coordinates. Each non-linear molecule with N atoms possesses 3N-6 normal modes Q_k which describes the oscillations of each atom with the frequency ω_k. The time dependence of Q_k is given by

$$Q_k(t) = Q_{k_0} \cos(\omega_k t + \delta_k). \tag{2.2}$$

Q_{k_0} and δ_k denote the amplitude and the phase factor of the vibration, respectively. The change of the tensor components of α with the molecular vibration along Q_k can be estimated using a Taylor series

$$\alpha_{\rho\sigma} = (\alpha_{\rho\sigma})_0 + \sum_k \left(\frac{\partial \alpha_{\rho\sigma}}{\partial Q_k} \right)_0 Q_k + \dots. \tag{2.3}$$

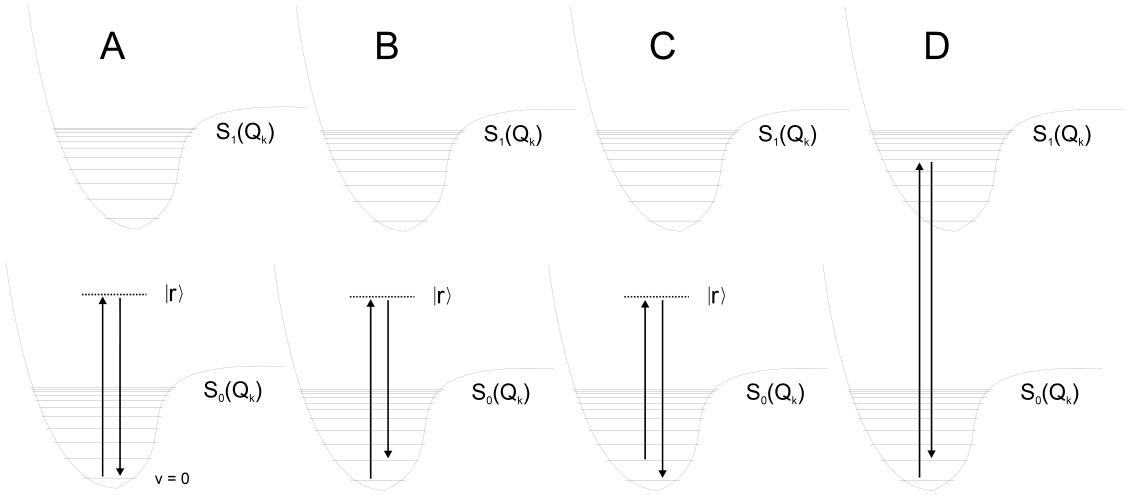

Figure 2.1: Jablonski diagram of different vibrational transitions induced by photon scattering. $S_0(Q_k)$ and $S_1(Q_k)$ denote the electronic ground and the first excited singlet state, respectively. v = 0 indicates the vibrational ground state. $|r\rangle$ is the virtual state. *A* Rayleigh scattering. *B* Stokes Raman scattering. *C* Anti-Stokes Raman scattering. *D* Resonance Stokes Raman scattering.

ρ and σ denote the molecules fixed internal coordinates and replace the Cartesian variables x, y and z. The time dependence of α is then given by the combination of 2.2 and 2.3,

$$\alpha_k = \alpha_0 + \left(\frac{\partial \alpha_{\rho\sigma}}{\partial Q_k}\right)_0 Q_{k_0} \cos(\omega_k t + \delta_k). \tag{2.4}$$

For a plane electromagnetic wave represented by $E = E_0 \cos(\omega_1 t)$, the induced dipole moment vector is given by

$$p = \alpha_0 E_0 \cos(\omega_1 t) + \frac{1}{2}\left(\frac{\partial \alpha_{\rho\sigma}}{\partial Q_k}\right)_0 E_0 Q_{k_0} \cos(\omega_1 \pm \omega_k \pm \delta_k). \tag{2.5}$$

The first term in equation 2.5 represents the Rayleigh scattering, which depends on the polarizability of the molecule at nuclei equilibrium positions. The two last terms refer to the Raman scattering. Accordingly, the scattered radiation is frequency shifted by ω_k - the frequency of the kth normal mode. Furthermore, the equation states that to obtain Raman scattered radiation the polarizability tensor α has to change with Q_k, *i.e.* at least one component of the tensor $\left(\frac{\partial \alpha_{\rho\sigma}}{\partial Q_k}\right)_0$ has to be non-zero. In general, the classical theory is able to describe the frequencies of scattered radiation but fails with respect to the intensity of the scattered light. Moreover, it allows no conclusion on the molecule's properties. This information is only accessible by means of quantum theory.

2.0.2 Quantum Mechanical Treatment of the Raman Effect

The general quantum mechanical treatment of the two photon involving Raman scattering process is based on second order perturbation theory and was first derived by Placzek on the basis of Kramers and Heisenberg's dispersion theory [9–11]. In this way, the molecule is described by quantum mechanics while the radiation is treated classically. As a result, the Raman scattering originates

from a transition of the molecule from a vibrational quantum state $|i\rangle$ to another vibrational quantum state $|f\rangle$ with the energies E_i and E_f, respectively. The transition is not direct but involves a virtual state $|r\rangle$ with the energy E_r. Figure 2.1 depicts different possible transitions with different positions of E_i, E_f and E_r relative to each other. The intensity of Raman bands which originate from such a transition is proportional to following quantities

$$I_{fi} \approx I_1 \exp\left(-\frac{E_i}{k_b T}\right)(\omega_1 \pm \omega_{fi})^4 \sum_{\rho\sigma} \left|\alpha_{\rho\sigma}\right|^2_{fi}. \tag{2.6}$$

I_1 and ω_1 are the intensity and the frequency of the incident radiation, respectively. ω_{fi} denotes the frequency of the energy difference of $|f\rangle$ and $|i\rangle$. The exponential term represents the Boltzmann distribution and determines the number of possible scattering centers in state $|i\rangle$ as a function of temperature. $\alpha_{\rho\sigma\,fi}$ denotes the respective $\rho\sigma$ element of the transition polarizability tensor. This tensor is obtained from the solution of $p_{fi} = \left\langle \psi_f^1 \middle| \hat{p} \middle| \psi_i^0 \right\rangle + \left\langle \psi_f^0 \middle| \hat{p} \middle| \psi_i^1 \right\rangle$ by comparison with the classical case described in equation 2.1 and together with the transition dipole moment replace the oscillating electric dipole and the polarizability from the classical treatment. In general, the elements of the transition polarizability tensor after Placzek can be calculated after

$$\left(\alpha_{\rho\sigma}\right)_{if} = \frac{1}{\hbar} \sum_{r \neq i,f} \left\{ \frac{\langle f|\hat{p}_\rho|r\rangle\langle r|\hat{p}_\sigma|i\rangle}{\omega_{ri} - \omega_1 - i\Gamma_r} + \frac{\langle f|\hat{p}_\sigma|r\rangle\langle r|\hat{p}_\rho|i\rangle}{\omega_{rf} + \omega_1 + i\Gamma_r} \right\}. \tag{2.7}$$

$\hat{p}_{\rho,\sigma}$ denote the dipole operator in σ and ρ direction, respectively. $\hbar\omega_{ri}$, $\hbar\omega_{rf}$ and $\hbar\omega_1$ represent the energy necessary for the transition from $|r\rangle$ to $|i\rangle$, from $|r\rangle$ to $|f\rangle$ and the energy of the incident light, respectively. The energy of the scattered radiation is $\hbar(\omega_1 - \omega_{fi}) = \hbar\omega_s$. $i\Gamma_r$ accounts for the life time of the state $|r\rangle$. The sum is made over all possible intermediate states $|r\rangle$. In principle, no restrictions on the energy E_r of these states are made and they can lay either below E_i or above E_f. For normal Raman scattering where $\omega_1 << \omega_{ri}$, the value of $\left(\alpha_{\rho\sigma}\right)_{fi}$ is therefore determined by the weighted sum over the states $|r\rangle$ of the product $\langle f|\hat{p}_\rho|r\rangle\langle r|\hat{p}_\sigma|i\rangle$, each state weighted by $\omega_{ri} - \omega_1 - i\Gamma_r$. Thus, normal Raman scattering can be regarded as a transition from $|i\rangle$ to $|r\rangle$ and $|r\rangle$ to $|f\rangle$, involving all possible states $|r\rangle$, where the transition dipole moment between the states $|r\rangle$ to both $|i\rangle$ as well as $|f\rangle$ is non-zero.

2.0.3 Resonance Raman Effect

In case of resonant Raman scattering, the frequency of the exciting light ω_1 approaches an electronic transition with the frequency ω_{ri} (*i.e.* $|r\rangle = |e\rangle$ where $|e\rangle$ denotes an excited electronic state), see figure 2.1 D. Then, the transition polarizability tensor $\left(\alpha_{\rho\sigma}\right)_{fi}$ is mainly dominated by one term of the sum where $\omega_{ri} - \omega_1 - i\Gamma_r \approx -i\Gamma_r$ is very small and additionally, $\langle f|\hat{p}_\rho|r\rangle\langle r|\hat{p}_\sigma|i\rangle$ becomes very large. This strongly increasing term is the resonant term. Accordingly, $\left(\alpha_{\rho\sigma}\right)_{fi}$ is reduced to

$$\left(\alpha_{\rho\sigma}\right)_{fi} = \frac{1}{\hbar} \sum_{r=f} \left\{ \frac{\langle f|\hat{p}_\rho|r\rangle\langle r|\hat{p}_\sigma|i\rangle}{\omega_{ri} - \omega_1 - i\Gamma_r} \right\}. \tag{2.8}$$

Since an electronic transition is involved, it is convenient to employ the Born-Oppenheimer approximation, which allows to separate the nuclear wave functions from those of the electrons, yielding $|i\rangle = |v_i\rangle|g\rangle$, $|f\rangle = |v_f\rangle|g\rangle$ and $|r\rangle = |n\rangle|e\rangle$. $|g\rangle$ and $|e\rangle$ denote the electronic ground and the first excited state while $|v_i\rangle$, $|v_f\rangle$ and $|n\rangle$ represent the initial, final and virtual vibrational states, respectively. Under this simplification, each integral can be separated into two parts according to $\langle v_i n\rangle\, p_{ge,\rho}$ and $\langle n v_f\rangle\, p_{ge,\sigma}$, and the transition polarizability is further simplified to

$$\left(\alpha_{\rho\sigma}\right)_{fi} = \frac{1}{\hbar}\sum_{r}\left\{\frac{\langle v_i n\rangle\, p_{ge,\rho}\,\langle n v_f\rangle\, p_{ge,\sigma}}{\omega_{ri}-\omega_1-i\Gamma_e}\right\}, \tag{2.9}$$

where $p_{ge,\rho}$ and $p_{ge,\sigma}$ denote the electronic transition dipole moments in ρ and σ direction, respectively. To account for the dependence of $p_{\rho,\sigma}$ on the nuclear vibrations Q_k, the transition dipole moments are expanded in a Taylor series around the displacement from the equilibrium position Q^0, yielding

$$p_{ge,\rho}(Q_k) = p^0_{ge,\rho}\left(Q^0_k\right) + \sum\left(\frac{\partial p_{ge,\rho}}{\partial Q_k}\right)_k Q_k + \ldots \tag{2.10}$$

$$p_{ge,\sigma}(Q_k) = p^0_{ge,\sigma}\left(Q^0_k\right) + \sum\left(\frac{\partial p_{ge,\sigma}}{\partial Q_k}\right)_k Q_k + \ldots. \tag{2.11}$$

$p^0_{ge,\rho}\left(Q^0_k\right)$ denotes the transition dipole moment at nuclei equilibrium positions. Upon combination of equation 2.9 and 2.11, the transition polarizability can be divided in different terms that represent different contribution mechanisms to resonance Raman scattering.

$$\left(\alpha_{\rho\sigma}\right)_{fi} = A_{\rho\sigma} + B_{\rho\sigma} + C_{\rho\sigma} \tag{2.12}$$

with

$$A_{\rho\sigma} = \frac{1}{\hbar}p^0_{ge,\rho}p^0_{ge,\sigma}\sum\frac{\langle v_i n\rangle\langle n v_f\rangle}{\omega_{ri}-\omega_1-i\Gamma_{e\,r}} \tag{2.13}$$

$$B_{\rho\sigma} = \frac{1}{\hbar}\left(p^{'}_{ge,\rho}p_{ge,\sigma}\sum\frac{\langle v_i|\,Q_k\,|n\rangle\langle n v_f\rangle}{\omega_{ri}-\omega_1-i\Gamma_{e\;r}}\right) \tag{2.14}$$

$$\ldots \quad + p^{'}_{ge,\sigma}p_{ge,\rho}\sum\frac{\langle v_i n\rangle\langle n|\,Q_k\,|v_f\rangle}{\omega_{ri}-\omega_1-i\Gamma_{e\;r}} \tag{2.15}$$

$$C_{\rho\sigma} = \ldots. \tag{2.16}$$

The $A_{\rho\sigma}$ term contains two Franck-Condon (FC) integrals. Accordingly, the contribution of this term to resonance enhancement is stronger with decreasing orthogonality character of the wave functions in the ground and the exited state. This is particular the case for total symmetric vibrational modes that are coupled to strong electronic transitions such as $\sigma-\sigma^*$ or $\pi-\pi^*$. Those modes gain most of their intensity via the $A_{\rho\sigma}$ term.

The $B_{\rho\sigma}$ term arises from the Herzberg-Teller vibronic coupling, which is expressed by $p^{'}_{\rho,\sigma}$ for small displacements of Q_k. There, two or more electronic states are coupled as a consequence of mixing of the respective Hamiltonians (*i.e.* perturbation of the respective Hamiltonian due to vibration). It can be shown that the resulting transition dipole moment of a transition of from $|g\rangle$ to $|e\rangle$ may contain (borrow) also contributions from transitions originating from $|g\rangle$ to another nearby excited electronic state $|h\rangle$. For the kth vibration, the amount of the 'borrowed' transition dipole moment is proportional to the appropriate coupling integral and the displacement Q_k. Furthermore, the coupling is higher, the smaller the energy difference of the coupled exited states is. The $B_{\rho\sigma}$ term scattering can account for the RR activity of total symmetric and non-total symmetric modes. However, due to parity selection rules, the $B_{\rho\sigma}$ term enhancement of total symmetric modes require the coupling of electronic excited states with same symmetry. This condition is usually not matched. Furthermore, $B_{\rho\sigma}$ term scattering becomes most pronounced when the ω_1 matches a weak electronic transition that is in turn

vibronically coupled with a nearby strong one. The $C_{\rho\sigma}$ terms considers overtones, which are usually not well pronounced.

2.0.4 Surface Enhanced Raman

Surface enhanced Raman (SER) scattering denotes the significant Raman signal enhancement of probe molecules close to rough metal surfaces. Depending on the setup of the experiment, the enhancement can exceed ordinary Raman signal intensities by a factor of 10^6 and more [17–19]. Thus, after the first observation by Fleischmann *et al*, in 1974, the potential of this effect was soon recognized [15, 16]. Since then, SER spectroscopy has been continuously refined and has become a powerful tool to probe structures and dynamics even at a nanomolar concentration level. Inspired by the work of Nie *et al* as well as Kneipp *et al* who showed that under proper chosen conditions, surface enhancement can be strong enough to detect even Raman signals of single molecules, the field of SER spectroscopy has gained a lot of scientific ascent lately [20, 21]. Finally, SER spectroscopy has also put a lot of momentum to other fields of science such as nanotechnology, nanodesign, near-field optics and last but not least gave birth to the field of plasmonics [22, 23].

The surface enhancement (SE) effect can be largely understood on the basis of classical electromagnetic theory, as proposed by Moskovitz and Kerker *et al* [24–26]. The general idea is the generation of dipolar surface plasmon resonances upon light irradiation on a metal (particle) surface. Surface plasmons are collective plasmonic vibrations of free electrons with respect to the nuclei, parallel to the metal surface. For a particle, which size is small with respect to the wavelength of the incident light with a frequency ω_1, the local (or near-) field is given by

$$E_{loc}(\omega_1) = E_{inc}(\omega_1) + E_{dipole}(\omega_p). \tag{2.17}$$

$E_{inc}(\omega_1)$ and $E_{dipole}(\omega_1)$ denote the electric field vector of the incident light and the field vector due to induced dipole moments, respectively. The total induced dipole moment p_p in a particle is according to classical theory $p_p = \alpha_p E_{loc}$. The polarizability α_p depends mainly on the kind of metal and is connected to its characteristic dielectric function $\varepsilon(\omega)$ by

$$\alpha_p = R^3 \frac{\varepsilon - 1}{\varepsilon + 2}. \tag{2.18}$$

R denotes the radius of the metal particle. The dielectric function is frequency dependent and is, considering interband transitions, given by

$$\varepsilon = \varepsilon_b + 1 - \frac{\omega_p^2}{\omega^2 + i\omega\gamma}, \tag{2.19}$$

where ε_b denotes the frequency dependent contribution of interband transitions to the dielectric function and ω_p and γ are the metal's plasmon resonance frequency and the electronic scattering rate (or the inverse electron mean-free-path), respectively. α_p can be expressed upon combining equation 2.18 and equation 2.19 as

$$\alpha_p = \frac{R^3\left(\varepsilon_b\omega^2 - \omega_p^2\right) + i\omega\gamma\varepsilon_b}{\left((\varepsilon_b + 3)\,\omega^2 - \omega_p^2\right) + i\omega\gamma(\varepsilon_b + 3)}. \tag{2.20}$$

Equation 2.20 will reach a maximum for

$$\omega = \omega_r = \frac{\omega_p}{\sqrt{\varepsilon_b + 3}} \tag{2.21}$$

with a half width given by

$$\gamma(\varepsilon_b + 3)\,. \tag{2.22}$$

From that crude model few properties of surface enhancement can be derived. First, γ is the electronic scattering rate, which is a competing process to resonance absorption. If γ is high, then the scattering on the electrons will dominate and thus SE is reduced. Moreover, since γ is inversely proportional to the DC conductivity, metals with high internal resistance will therefore exhibit reduced surface enhancement compared to metal with high conduction properties. For the contribution of interband transitions to the dielectric properties, it is found that if ε_b is high, then ε is also high, which will decrease α and therefore the SE. Additionally, a high contribution of interband transitions will according to equation 2.21 shift the resonance frequency to higher wavelengths.
The effect of particle size on the SE is given by two main factors. The smallest dimension of a particle has to be at least in the order of the size of a molecule. For too small metallic objects, that is when they are much smaller than the electron free-mean-path, conductivity will drop and hence SE will decrease as well. Moreover, if the particle consists of only few atoms, then classical description as given above may no longer be valid and quantum theory has to be applied to evaluate its electronic properties. On the other hand, the upper size limit is given by the excitation wavelength. If the object is much larger than 100 nm, then the incident radiation will excite multipoles instead of dipoles exclusively. Since multipoles are non-radiative, they cannot contribute to the surface enhancement. Therefore, the optimal size for a metal particle (or other structures) to show surface enhancement ranges for coinage metals from 10 nm to 100 nm [20, 29, 30].
In summary, the magnitude of enhancement depends largely on the morphology and the electronic properties of the metal. The metals that are expected to display the strongest enhancements are (sorted in decreasing order of provided SE) silver, the alkali metals followed by gold, copper and the good conductors aluminum, indium, platinum and finally the less good conductors and other transition metals.

A SER spectrum of a probe molecule on a SE active support differs in many aspects from a normal Raman spectrum of the very same probe in solution as shown for mercaptobenzene in figure 2.2. Usually, the overall SER signal intensity I_{SERS} is, given a proper choice of excitation wavelength and respective support, much stronger than respective Raman signal intensity I_{Raman}. To evaluate now the intensity gain through surface enhancement, it is necessary to define a few values. Assuming that E_{tot} denotes the averaged total field strength induced by plasmon excitation, then g will be the enhancement factor given by $E_{tot} = g\,E_0$, where E_0 is the field strength of the incoming light. The Raman scattered light will then have the field strength $E_{sca}(\omega_s) \propto \alpha\,E_{tot} \propto \alpha_{SER}\,g\,E_0(\omega_1)$, where α_{SER} denotes the polarizability tensor of the surface attached molecule. Also, the scattered light is - given that its frequency $\omega_s = \omega_1 - \omega_{fi}$ can excite surface plasmons - enhanced by the factor g' . The field strength of a SER scattered radiation is therefore given by

$$E_{SERS} \propto \alpha_{SER}\,g\,g'\,E_0. \tag{2.23}$$

As shown above, the intensity of a Raman signal is proportional to the square of the induced dipole moments and hence to the square of the electric field inducing the dipoles and thus equation 2.23 can be transformed to

$$I_{SERS} \propto (\alpha_{SER})^2 \left(gg'\right)^2 I_0. \tag{2.24}$$

For $\omega_s \approx \omega_1$ and $g \approx g'$, the electric field will be enhanced by the power of four. The total enhancement G, provided by the metal particle, can then be expressed as

$$G = \left|\frac{\alpha_{SER}}{\alpha}\right| \left|gg'\right|^2. \tag{2.25}$$

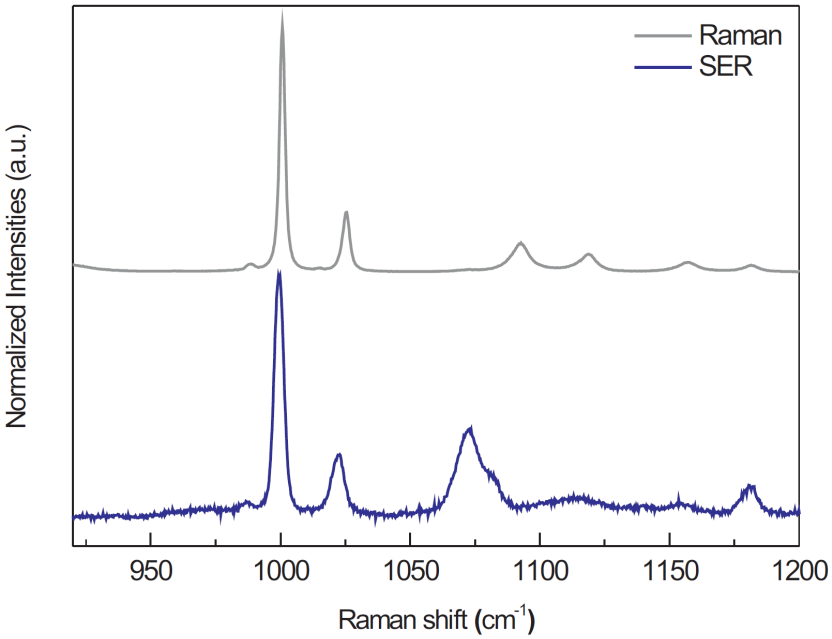

Figure 2.2: Normalized Raman (top) and surface enhanced Raman (bottom) spectra of mercaptobenzene obtained with 413 nm excitation. The SE active support was constituted by a rough Ag surface.

Usually, α_{SER} is equal or similar to α and hence the ratio will be one. However, for molecules with certain chemical properties, a significant change of the polarizability tensor, leading to high scattering yields, was observed upon adsorption. Raman signals of these molecules are strongly enhanced, even though there might be no plasmonic enhancement involved. This effect is called chemical enhancement effect and is ascribed to interactions between the probe molecule and the metal surface which in turn change the electronic properties of both [31].

In principle, SER is not only restricted to adsorbed molecules. According to the electromagnetic theory, the strength (magnitude) of the local electric field decreases with the $1/d^3$, where d is the distance to the metal surface [34, 35]. Because the signal enhancement varies with g^4, the distance dependence is accordingly scaled with $1/d^{12}$ [35]. For a particle with a diameter of a_0, the distance dependence is described by

$$G_{SER}(d) = G_{SER}(0) \cdot \left(\frac{a_0}{a_0 + d} \right)^{12}. \tag{2.26}$$

$G_{SER}(0)$ denotes the maximum enhancement at the surface. For an a_0 in the order of a few tenth of nanometer, the electric field enhancement is drastically reduced at a distance several nanometers away from the surface.

Surface enhancement cannot only be observed for particle ensembles, but also for bulk materials that exhibit a nanostructural geometry on the surface. These nanostructures can function as center for surface enhancement due to the very same mechanism as described for particles, given a proper size of these structures. In that case, the total field enhancement is a mean value over the complete surface. The magnitude of maximum and minimum enhancement for a certain nanostructural surface

geometry can vary strongly as a function of space [20]. Thus, it might be the case that for a metal structure that exhibits a high mean field enhancement, SER signals of adsorbed molecules may only arise from a fraction of molecules that sit at so called 'hot spots'. These spots are areas on the surface showing the strongest field enhancements, which can be several orders of magnitude higher than that of other areas. In single molecule SER(R)S (*vide infra*), it is believed that only molecules sitting at these hot spots will give rise to a spectrum [19]. The determination of the location of these spots is purely a task of computational methods since no experimental technique exists that can probe the field enhancement of nanostructures spatially resolved. Since the surface enhancement effects can be described satisfyingly by classical electromagnetic theory, field enhancement arising from different nanostructures can be calculated by modeling these structures and solving the related Maxwell equations [20]. Due to computational restriction, there exists a variety of methods which can simplify the calculations, allowing reasonable numerical solutions of the Maxwell equations. The most prominent method is the finite difference time domain approach (FDTD) [36, 37]. This method is along with other approaches grid-based in which the structure is modeled by finite elements. In this way, nanostructures with dimensions of several hundreds of nanometers can be treated theoretically without facing computational limitations. These kind of calculations are of high potential since they can either be used to predict which geometry exhibits the highest surface enhancements or may help to rationalize experimental results [118, 233]. Also, they can be applied to investigate complicated composites including metal/metal combinations and structural geometries which are not yet accessible by synthesis and thus are not pliable for experiments.

2.0.5 Surface Enhanced Resonance Raman

The surface enhancement can boost the Raman signal intensity drastically, making this method very sensitive and thus particularly interesting for probing adsorbed molecules. The sensitivity can be further improved by combining the surface enhancement with the molecular resonance Raman effect, in case the probe molecule, e.g. a dye, exhibits an electronic transition close to the wavelength required for exciting plasmon resonances of an underlying metal support. The resulting technique is called surface enhanced resonance Raman (SERR) spectroscopy and is suitable to probe simple dye molecules as well as to monitor large molecules such as enzymes that contain one or more chromophores (*vide infra*).
The choice of the substrate is crucial when employing SERR spectroscopy. Since most of dyes and absorbing molecules exhibit strong electronic transitions that lie in the visible region, it is also necessary to have a metal support that can be excited using the very same wavelength. Most of the metals are therefore not suitable for this purpose, since they either show low intrinsic surface enhancement or the necessary excitation wavelength is shifted to the UV or infrared region. In this respect, Ag and Au are often employed since they can be excited using visible light [45], while the exact position of the plasmon resonance frequencies depend on the structure and the geometry of the Ag/Au support (*vide supra*). Therefore, Ag or Au in form of nanoparticles are often employed in SERR experiments, either for detecting molecules in solution or coated with good Raman scatterers to be used as markers in spatial resolved confocal Raman measurements [46–48]. One of the advantages of nanoparticles is that the exact plasmon absorption wavelength can be tuned by changing shape, radius or dielectric properties such as coating with an additional metal layer [48–50]. Thus, the plasmon resonance frequency can be adjusted to match the electronic absorption frequency of the sample molecule, which in turn provides high sensitivity and selectivity. Also, solid electrodes made of Ag or Au are used as SERR supports [35]. To obtain the field enhancement, the surface of these electrodes has to exhibit a roughness on the nanometer scale. Since the roughness is based on irregular shaped metal structure geometries, the plasmon resonance frequency of these electrodes is not well-defined as in the case of monodisperse nanoparticles but is distributed over a region, such that these supports can be used at different excitation wavelengths. Additionally, these electrodes can be employed in

electrochemical experiments, enabling the coupling of spectroscopy and electrochemistry to vibrational spectro-electrochemistry [35]. This is particularly interesting for probing redox enzymes and electro-catalytic reactions [38, 51–54]. Most enzymes carry a chromophore unit that constitutes also the active site of the catalyzed reaction. If the plasmon excitation wavelength is tuned to match the respective electronic transition of the chromophore, vibrational bands originating from the chromophore unit will be selectively enhanced. Hence, SERR spectroscopy provides also a powerful tool to investigate structure and mechanism of enzymes without interfering contributions from the protein matrix [35, 38, 39, 79]. Vibrational bands of the protein backbone can be obtained by performing IR absorption spectroscopy or surface enhanced infrared absorption (SEIRA) spectroscopy [35, 40].

2.1 Properties of Electrochemical Interfaces

The insertion of a bare metal electrode into an aqueous solution leads to adsorption of ions on the electrode surface and thus to the formation of an electrical double layer at the solid/water interface as shown in figure 2.3. The distrubtion of the potential Φ at such an interface can be described using the Gouy-Chapmann-Stern theory. According to this, the first layer of adsorbed ions is called the Stern layer and its properties depend on the kind of metal and the type of electrolyte. The electrode together with the layer of adsorbed ions is treated as a molecular capacitor, and thus the potential drops linearly from the electrode surface to d_c, which denotes the thickness of the Stern layer. Beyond the Stern layer, the distribution of ions is diffuse, and thus the potential drops exponentially with increasing distance from the metal surface.
The charge densities at the interface can be quantified using the approach of Smith and White [55]. Accordingly, the charge density on the metal is given by

$$\sigma_M = \frac{\varepsilon_0 \varepsilon_C}{d_C} \left(\Phi_M - \Phi_C\right), \tag{2.27}$$

where ε_0 is the permittivity and d_C and ε_C represent the thickness and dielectric constant of the Stern layer, respectively. Φ_M and Φ_C denote the potential of the metal and the potential measured after the Stern layer as shown in figure 2.3, respectively. The charge density in the solution can be derived from the Gouy-Chapman distribution in which an exponential decrease of the potential with increasing distance from the Stern layer is assumed. The decrease is scaled with the potential difference between Φ_C and Φ_S, the solution's potential. Accordingly, the charge density can be expressed as

$$\sigma_S = -\varepsilon_0 \varepsilon_S \kappa \frac{2kT}{e} \sinh\left(\frac{e}{2kT}\left(\Phi_C - \Phi_S\right)\right). \tag{2.28}$$

Here, κ denotes the inverse Debye length while k and T have the usual meaning. The charge densities vary upon applying an electrode potential, *i.e.* changing the value of Φ_M. Two special cases can be distinguished. If Φ_M is equal to Φ_S, then σ_M will become zero. This value for Φ_M is called the potential of zero charge E_{pzc} and is roughly - 0.7 V and + 0.2 V vs SHE for the metals Ag and Au, respectively. If Φ_M is very high with respect to Φ_C (or Φ_S), then the consequence will be a sharp potential drop along the Stern layer. This fast potential drop causes an high electric field E_F that is determined by

$$E_F = \frac{\phi_M - \phi_C}{d_C} = \frac{\sigma_M}{\varepsilon_0 \varepsilon_C}. \tag{2.29}$$

The field strength depends also on the kind of bound anions since these ions determine the properties of the Stern layer. For sulfate as binding ion, the electric field can reach magnitudes up to 10^9 V m^{-1} at an applied electrode potential of + 0.2 V [35].

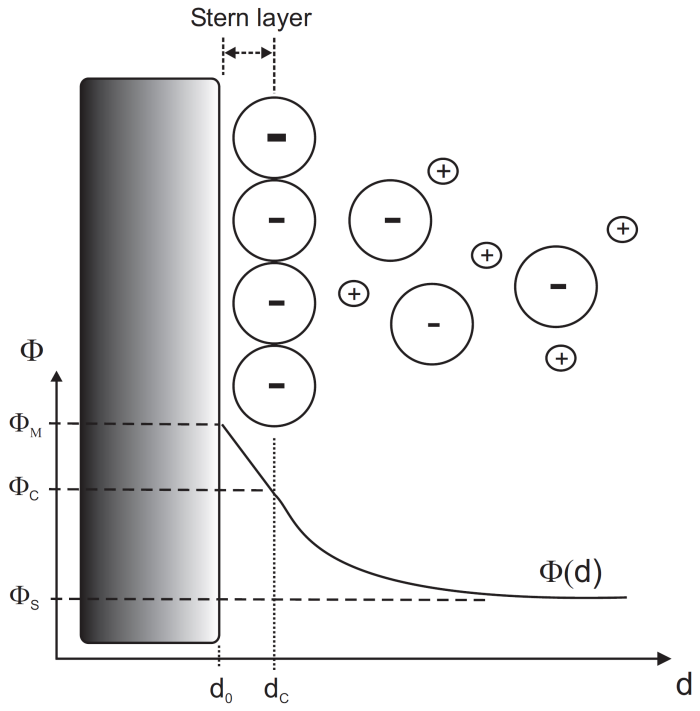

Figure 2.3: Schematic representation of an electrical double layer and the potential distribution at the solid/water interface. The first layer of adsorbed ions is called the Stern layer, which has a thickness of $d_c - d_0$. The potential Φ drops linearly with increasing distance from d_0 to d_c. Beyond the Stern layer, the distrubtion of ions is diffuse. Accordingly, the potential $\Phi(d)$ more far away from the electrode can be approximated using an exponential decay.

2.1.1 Self Assembled Monolayer - SAM

Adsorption of biomolecules on bare metal surfaces may cause denaturation due to the high electric fields present at the electrode/water interface [56]. To avoid such effects, the metal surface is usually covered by bio-compatible coatings [57–59, 67]. The most versatile coating type is based on the self-assembly of amphiphilic alkanethiols of the type R-$(CH)_n$-SH, where n denotes the length of the alkyl chain. The sulfur group can bind strongly to a variety of metals, forming a monolayer via self-assembly (self assembled monolayer, SAM) [60, 61]. The properties, such as density of package, degree of order or metal-S-chain angle, of the resulting monolayer depend on the type of the employed SAM, *i.e.* on the number of n and the nature of R, which represents a functional head group. Depending on the properties of the protein, R can be varied to ensure an efficient adsorption.

For example, the heme protein cytochrome *c* can be effectively adsorbed using negatively charged SAMs (R is for example a carboxylic acid group) via electrostatic forces. Figure 2.4 illustrates the different mechanisms for protein adsorption using different kind of head groups. The most complex immobilization strategy refers to the cases B and D where adsorption of the protein is achieved via formation of covalent bonds between the SAM and the molecule [38, 157].

The choice of R also affects the charge density at the interface. In case of R = CH_3, the smallest charge densities were reported while for phosphate, sulfate and polyanions the highest charge densities and therefore the highest electric fields were measured [35]. Also, the charge on the electrode affects the chemical properties of the head groups. For example, adsorption of carboxyl terminated SAMs on an Ag electrode will increase the pK_a of the carboxylate group and thus in turn increase the electric field strength. This can be further manipulated by adjusting length, *i.e.* the effective

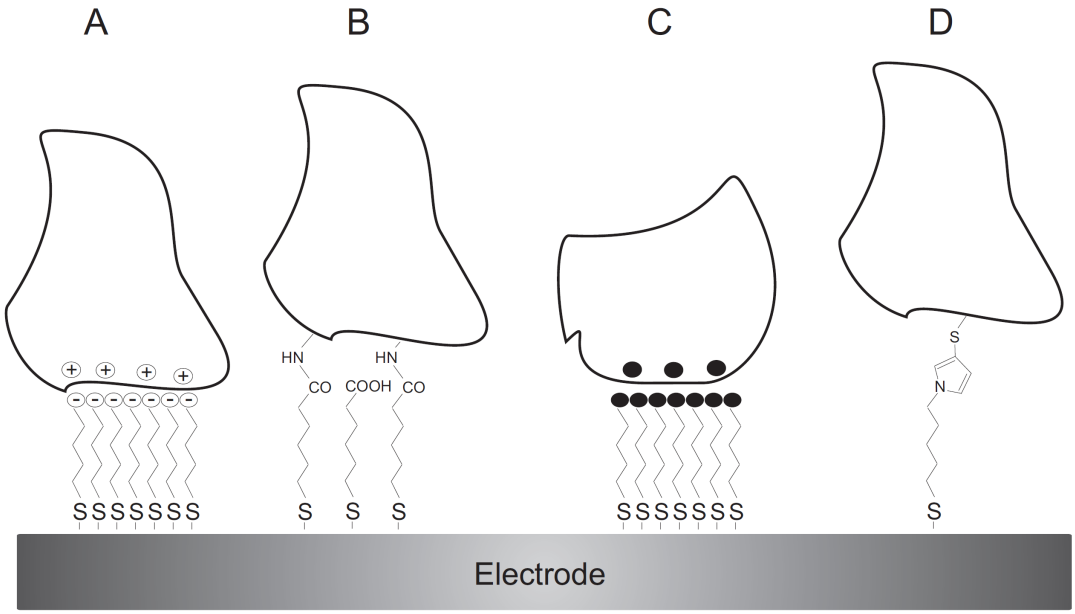

Figure 2.4: Different modes of protein (black polygon) immobilization. The stabilizing interaction can be mediated via electrostatic forces (*A*), covalent bonds (*B*) or hydrophobic forces (*C*). Additionally, the protein can also be immobilized via typical protein tags as used for HPLC (*D*).

separation between the headgroup and the electrode surface, whereas small n lead to high electric fields and *vice versa*. For $n = 11$, the electric field strength was measured to be around of 10^9 V/m [62–64]. This is in the order of values expected for phospholipid membranes [65]. A more profound introduction to SAMs can be found in the cited literature [66, 67].

2.2 Heme proteins

Heme proteins carry an iron porphyrin cofactor. These proteins play a key role in many reactions in biological systems and can act as electron and oxygen carriers, signal transducers and function as metabolizing enzymes. The heme groups can be distinguished by the chemical constitution of the porphyrin macrocyle and the ligation, spin and oxidation state of the heme iron center atom. The chemical formula for *a*-, *b*- and *c*-type hemes are shown in figure 2.5. Type-*b* hemes carry two vinyl substituents whereas type-*a* hemes exhibit a vinyl and a formyl functional group. Additionally, type-*a* hemes possess an aliphatic substituent whose length can differ from organism to organism. Both heme types are linked to the rest of the protein by non-covalent interactions. For example, the binding to the protein matrix can be achieved by the coordinating axial ligand of the iron atom. In contrast, type-*c* hemes exhibit two vinyl groups that are used to link the cofactor covalently to the protein matrix by forming thioether bridges with cysteine residues. Furthermore, within one heme type, the coordination pattern of the heme iron can differ depending on the exogenous or endogenous axial ligands. Either both axial positions are occupied or one position remains vacant, according to a sixfold (6c) or fivefold (5c) coordination pattern, respectively. 5c and 6c coordination with low field ligands lead to a formation of a complex where the iron atom is in a high spin state (HS), in analogy

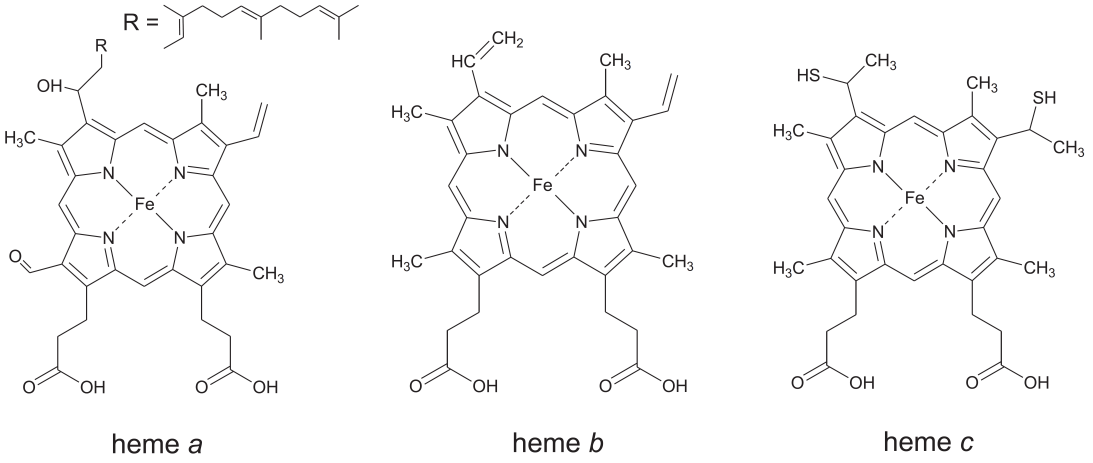

Figure 2.5: Chemical constitution of the different natural appearing heme types *a*, *b* and *c*. All hemes consist of a conjugated tetrapyrrol macrocyle coordinating a metal atom. The peripheral substituents attached to this macrocyle differ depending on the type of heme.

to octaedrical complexes where the five d-orbitals of the iron atom split up into three degenerate e_g and two lower energetic degenerate t_{2g} orbital. High field ligands, in contrast, favor the formation of a low spin iron state (LS). Beside this, the iron atom can vary between a ferric and a ferrous oxidation state in which the formal charge on the iron atom is 3^+ and 2^+, respectively. The transition between the various spin, coordination (or conformational) and oxidation states depends on many factors and can be probed with different spectroscopic, electrochemical and spectro-electrochemical techniques.

2.2.1 Cytochromes

Cytochromes are heme proteins, which function as electron carriers (e.g. cytochrome *c*) or enzymes (e.g. cytochrome P450) [68]. They are widely spread throughout animal and plant life and appear in the different types *a*, *b*, *c* and *d* depending on the chemical constitution of the heme group (*vida infra*) [69].
Cytochrome *b* is an integral membrane protein with a molecular mass of about 40 kDa. Similar to the other cytochromes, there exists a variety of modifications of that protein type depending on the organism the enzyme was isolated from. The archetype is the cytochrome *b* from the cytochrome *bc1* complex, *i.e.* the cytochrome *c* reductase (complex III of the mitochondrial respiratory chain of eukaryotes). This cytochrome contains two low spin heme groups, which can be distinguished by their electronic absorption and their redox potentials. Both iron atoms are ligated by two highly conserved histidine axial ligands. The major protagonist of *a*-type cytochromes is the cytochrome complex aa_3. This membrane bound complex is a subunit of the cytochrome *c* oxidase enzyme (complex IV of the eukaryotic respiratory chain), which supplies the electrons for the reduction of oxygen to water, to generate a proton gradient for ATP synthesis. Cytochrome aa_3 contains two *a*-type heme groups, one in the low spin (*a*) the other one in the high spin configuration (a_3) [70, 71]. It has, additionally, two copper atoms and catalyzes the oxidation of mitochondrial cytochrome *c*, a small soluble enzyme with 103 to 112 amino acid residues and a molecular mass of approximately 12 kDa.

Under normal conditions, cytochrome *c* is attached to the inner mitochondrial membrane where it functions as an electron carrier and transports electrons from complex III to complex IV, promoting the oxidative phosphorylation. As shown in figure 2.6, it accommodates one low spin heme group that

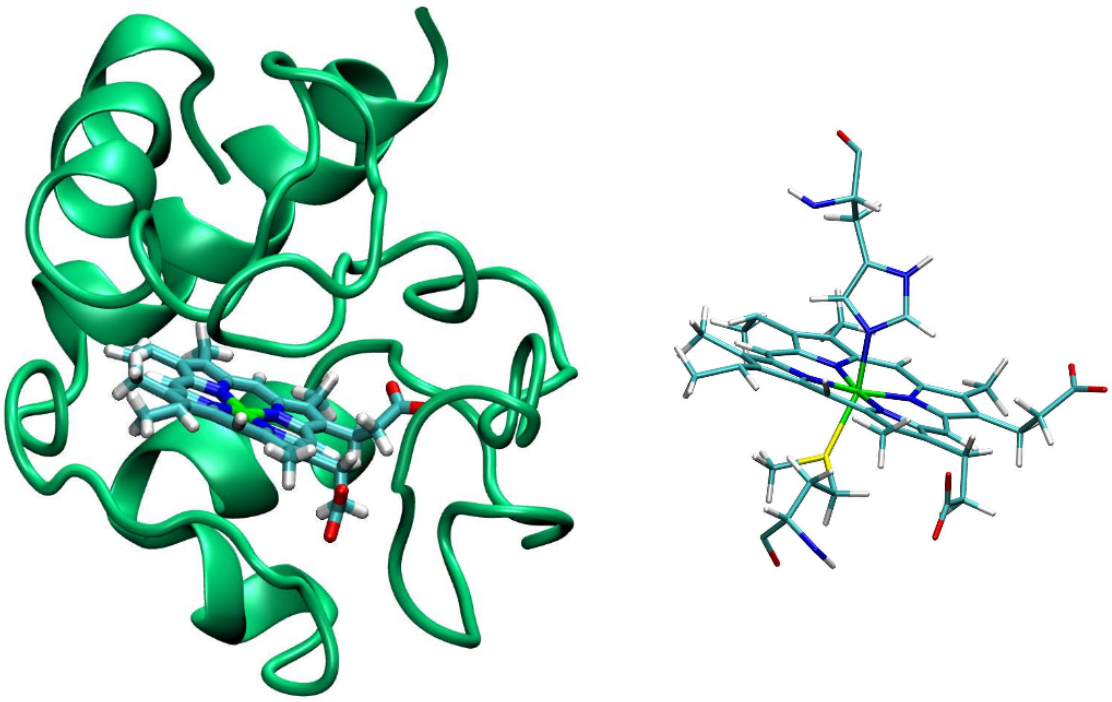

Figure 2.6: *Left.* 3D structure of cytochrome *c*. The covalently attached *c*-type heme is highlighted. *Right*. 3D structure of the heme group with the axial ligands histidine (top) and methionine (bottom).

is axially coordinated by a methionine and a histidine ligand. The redox potential of the Fe^{2+}/Fe^{3+} transition is comparably high with around 270 mV vs. SHE. Furthermore, it possesses a relatively high dipole moment of roughly 300 Debye, which alters only slightly upon reduction [128, 129]. Additionally, cytochrome *c* exhibits a partially positively charged area that can be used for electrostatically mediated immobilization. Conformational transitions are reported upon high pHs (alkaline transition), under oxidative stress and at high electric fields and is related to an axial re-ligation [38, 93, 98, 99]. The loss of the axial ligand methionine, forming a 5cHS species, is accompanied by a lowering of the redox potential by several hundreds of mV [38]. The coordination site can be occupied by other ligands such as a lysine or transiently by another histidine, both yielding a 6cLS heme species. Also, the site can remain vacant which is reported to lead to an increase of peroxidase activity of cytochrome *c* [170]. Furthermore, the transition to a 5cHS iron is believed to be of particular importance for altering the function of cytochrome *c* as an electron carrier to a signal transducer in the apoptotic reaction cascade [161].
Finally, cytochrome *d* are proteins which contain a heme, where the iron atom is chelated by a tetrapyrrol marcocyle in which the degree of conjugation of double bonds is lower than in a normal porphyrin. Specifically, this is the case for dihydroporphyrin (chlorin, reduced by one double bond), tetrahydroporphyrin (reduced by two double bonds) and siroheme. Heme *d* is formerly denoted as heme a_2.

2.2.2 Resonance Raman Spectroscopy of Cytochromes

Heme proteins have been intensively studied over the last decades using various spectroscopic techniques. The heme group constitutes a chromophore unit that gives rise to an intensive UV/Vis

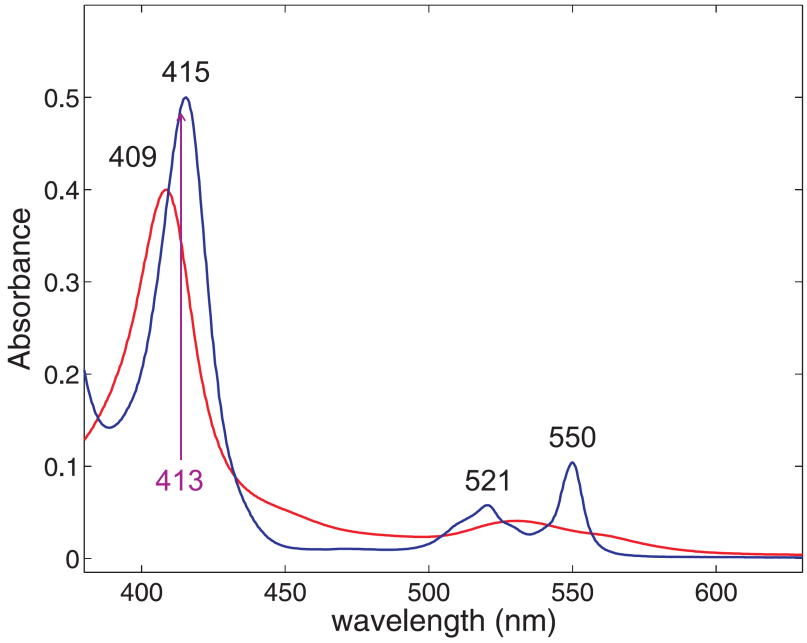

Figure 2.7: UV/Vis optical spectrum of oxidized (red) and reduced (blue) cytochrome *c*. In RR experiments, a laser excitation line at 413 nm (purple) is used to obtain strong resonantly scattered signals. Figure taken from [76].

absorption spectrum. This spectrum exhibits typical features that can be rationalized using molecular orbital (MO) theory, as proposed by Goutermann *et al* [72]. In this model, a D_{4h} symmetry is assumed for the porphyrin ring, which is treated as a two dimensional system of conjugated π bonds. Accordingly, the highest occupied MOs have a_{1u} and a_{2u} symmetry and are similar in energy [73, 74]. The transitions occur into the lowest unoccupied MO, which has e_g symmetry and is double degenerated. The transition from the a_{2u} give rise to a very intense band (γ or Soret Band) at roughly 400 nm while the transition originating from a_{1u} leads to the lower energy bands in the region around 540 nm (Q or α and β band), which is split due to a $(0,0)$ and a $(0,1)$ vibrational transition, respectively. Both electronic transitions are of E_u symmetry and thus are strongly mixed by configuration interaction such that the transition dipole moments of both transitions combine additively and substractively with the γ or Soret band gaining most of the intensity. A typical UV/Vis spectrum of cytochrome *c* is depicted in figure 2.8.

Therefore, in order to obtain high quality resonance Raman spectra of heme proteins, the exciting laser line has to be chosen to match either the γ or the α or β electronic transition. Assuming a D_{4h} symmetry for the porphyrin marcocycle, the transition dipole moment vector lies for both transitions in the *x*,*y* plane, *i.e.* in the porphyrin plane, hence resonance enhancements are only expected for the in-plane modes with A_{1g}, B_{1g}, A_{2g} and B_{2g} symmetry. Upon Soret excitation, the RR spectrum is dominated by the total symmetric A_{1g} modes according to the *A* term resonance enhancement. The high intensities of these modes are mainly due to the large oscillator strength of the electronic transition. *B* term enhancement plays only a minor role for these modes due to small excited state displacements. In contrast, the non-total symmetric B_{1g}, A_{2g} and B_{2g} modes are enhanced strongly by the vibronic coupling (*B* term) and gain intensity under Q band excitation. Under these conditions B_{1g} modes are mainly enhanced. Also, modes with A_{2g} symmetry are observed, which are Raman inactive under non-resonant excitation conditions. However, the symmetry of natural porphyrin macrocycles is lower than D_{4h} since the individual side chains lead to an asymmetric substitution

pattern. This has some consequences for the resonance Raman activity of the different vibrational modes [77–79]. For example, the vinyl and formyl substituents present in *a* and *b* type hemes can couple with the conjugated π-electron system of the macrocycle and thus the internal modes of these side chains are also enhanced. For *c* type hemes the vibrational modes of the thioether bridges are coupled to the porphyrin ring, leading to a prominent resonance enhanced band with high C-S stretching contributions at around 700 cm^{-1} [80]. Additionally, also out-of-plane modes can gain resonance enhancement due to coupling of in-plane and out-of-plane modes and thus 'borrowing' intensity via respective *A* or *B* term enhancement (*vide infra*).

In figure 2.8, Soret and Q band excitation spectra of ferrous and ferric cytochrome *c* are shown. Due to a large number of experimental data available, the vibrational bands are well assigned [81–86]. The region between 1200 cm^{-1} and 1700 cm^{-1} is the so-called marker band region. The band pattern there reflects the oxidation, spin and ligation state of the heme iron atom. Under Soret excitation, the most prominent band in the ferric spectrum is the ν_4 (A_{1g}) mode at around 1371 cm^{-1} which corresponds to an almost pure C-N stretching mode. Other important modes are the ν_3 (A_{1g}) and the ν_{10} (B_{1g}) mode. Latter one dominates the spectrum upon Q band excitation. Upon reduction, all these bands shift to lower wavenumbers. The ν_4 mode displays the largest shift by roughly 10 cm^{-1} to ca. 1361 cm^{-1}. This can be rationalized by taken into account the electronic interplay between the iron and the porphyrin. The additional charge on the iron atom increases the back-bonding properties and thus increases the electron density in the π^* orbitals of the macrocycle. This in turn weakens the C-N bond strength which finally leads to the downshift. Coordination with other electron-rich axial ligands such as thiolate can even cause shifts up to 25 - 30 cm^{-1}, as found for cytochrome P450 [79, 87, 88].

The spectral region below 1000 cm^{-1} displays bands associated mainly with protein-heme interactions due to the covalent attachment of the heme group to the protein backbone. The low frequency region between 300 and 450 cm^{-1} is the so-called fingerprint region and contains spectral signatures of modes arising from bending and out-of-plane modes of substituents and the porphyrin macrocycle. This region is unique for cytochrome *c*. The band intensities and frequencies are indicative of transformation processes associated with the heme group. Cytochrome *c* exhibits a variety of conformational states which were addressed by many electrochemical and spectroscopic studies [89–94]. Most of these conformational transitions are restricted to oxidized cytochrome *c* exclusively due to a weak Fe-S(Met80) bond in this redox state. As aforementioned, this bond can be easily broken and the vacant axial position can be occupied by another amino acid residue. This re-ligation is, however, also associated with movements of protein peptide segments. All these changes are nicely reflected in the marker band and the fingerprint region of a resonance Raman spectrum. For example, upon lowering the pH a bis-histidine (His-33 or His-26/His-18) ligated 6cLS heme species can be formed [95]. The attachment of this high-field ligand leads to an increase of the iron-porphyrin bond strength accompanied by a smaller core size and hence an upshift of the marker bands, in particular of the ν_4 (to ca. 1374-1375 cm^{-1}), ν_3 (to ca. 1505-1507 cm^{-1}) and ν_{10} (to ca. 1639-1644 cm^{-1}). This ligation pattern can be distinguished from the likewise 6cLS conformation that is formed upon alkaline pH, known as the alkaline transition of cytochrome *c* [96, 97]. There, a Lys(72,73 or 79)/His(18) ligation configuration is present [98, 99]. The different ligation requires a different tilting of involved peptide segments, which has impact, in particular, on the low frequency region of the RR spectra. Based on that, a spectroscopic distinguishing between both states is possible [93]. Beside the 6cLS configuration, one may also find two HS states in which the iron atom is either five- or six-coordinated. In the 5c and 6c states the former axial position of Met80 remains vacant and is occupied by a water molecule, respectively. This leads to a significant down shift of the ν_3 band to either 1488-92 cm^{-1} or 1475-80 cm^{-1}, respectively. It is known that all these states are involved during the folding processes of cytochrome *c*, but are also formed upon interaction between cytochrome *c* and highly charged surfaces such as metal electrodes, phospholipid vesicles or SDS micelles [90, 91].

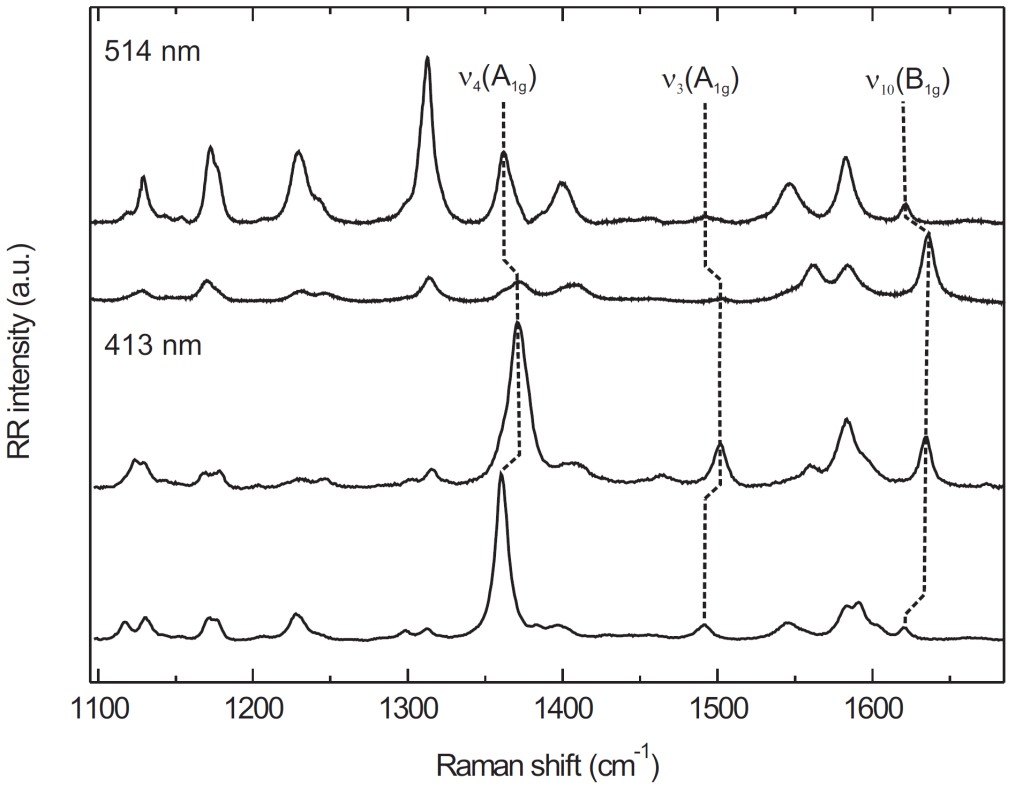

Figure 2.8: Resonance Raman spectra of reduced (top, bottom) and oxidized (middle) cytochrome *c* obtained with 413 nm and 514 nm excitation, respectively. The significant marker bands ν_4, ν_3 and ν_{10} are highlighted to track their frequency and intensity changes upon redox transition.

2.3 Electron Transfer Theory

Electron transfer (ET) reactions play a fundamental role in chemical and biochemical processes. To understand these processes, it is crucial to have profound knowledge about the properties that control these transfer reactions. The first generally accepted theoretical description of electron transfer was provided by R. A. Marcus [100–104].

2.3.1 Homogeneous ET and Classical Marcus Theory

The Marcus theory is usually used for outer-sphere ET reactions between a donor *(D)* and an acceptor *(A)* molecule. The process of ET can be divided in three steps. First, the diffusion of D and A to form a complex takes place. The second step is the actual ET process: $\left(D/A \underset{k_{-ET}}{\overset{k_{ET}}{\rightleftharpoons}} D^+/A^- \right)$. In the third step, D and A finally seperate by diffusion. The Gibbs energy of such an ET reaction is given by

$$\Delta G^0 = e(E_D^0 - E_A^0 + w^P - w^R), \tag{2.30}$$

where E_D^0 and E_A^0 are the redox potentials of the redox couple D/D^+ and A/A^-, respectively. w^P and w^R denote the required energy to form D/A (reactant) and to induce the separation of D^+/A^- (product), respectively. The potential energy of these states, *i.e.* of the reactant and the product, is a

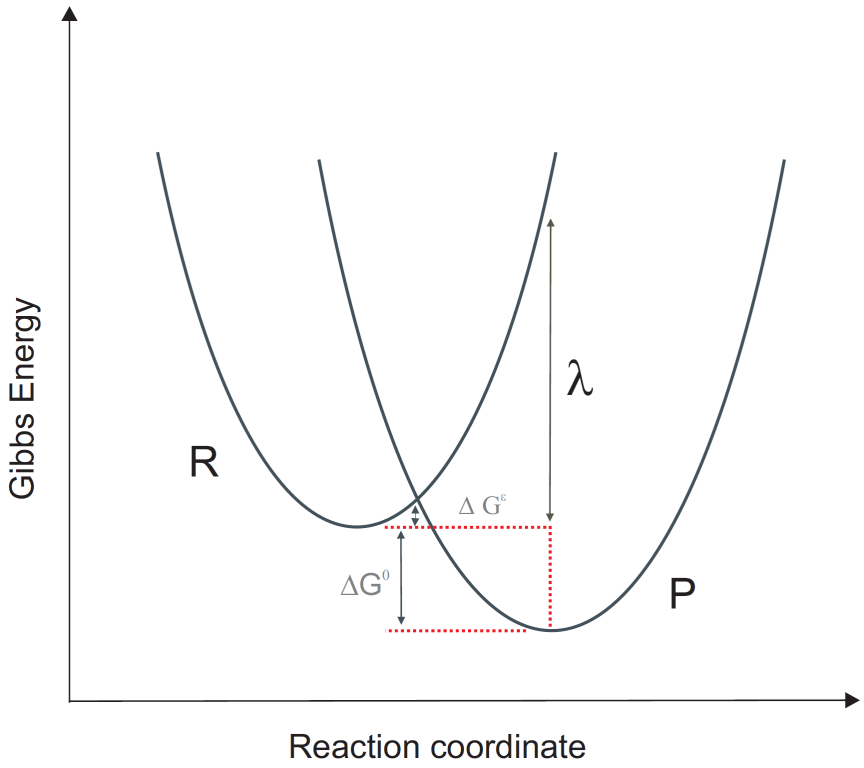

Figure 2.9: Gibbs energy curves as a function of the reaction coordinate for the reactant (R) and product (P) state. ΔG is defined as the Gibbs energy difference between the parabola minimum of R and P. ΔG^{ε} denotes the necessary activation Gibbs energy and is defined as the difference of the Gibbs energy minimum of R and the Gibbs energy at the intersection between both parabola. The reorganization energy λ is the energy necessary to distort the geometry of the reactant state to match with the geometry of the product state at minimum energy.

complicated multi-dimensional energy surface including also the potential energy of the surrounding solvent sphere. For simplification and in analogy to transition state theory, a reaction coordinate is introduced to reduce the problem to one dimension. Additionally, it is more convenient to plot free Gibbs energies instead of potential energies, since they can be approximated using simple parabola.

Such an exemplary plot is shown in figure 2.9. The reacant (R) and the product (P) are represented by the same parabola but with different vertices. This is justified for small changes (both in energies and internal coordinates) of the complexes upon ET reaction. To induce an electron transfer, the reactant system has to reach the intersection of both parabola. This can be achieved classically for example by thermal activation. According to classical transition state theory, the first-order rate constant of such an ET process is given by

$$k_{ET} = \kappa_{el} \nu_n \exp\left(\frac{-\Delta G^{\varepsilon}}{k_B T}\right). \tag{2.31}$$

κ_{el} and ν_n denote the electronic transmission coefficient and the frequency of the system reaching the transition state ($\approx 10^{13} s^{-1}$), respectively. ΔG^{ε} represents the Gibbs energy of the activation as shown in figure 2.9. Since ΔG^{ε} is not accessible by experiment, it is more convenient to express the equation 2.31 as a function of ΔG^0 and λ, which represent the standard Gibbs energy of the reaction at a certain donor/acceptor distance r_{DA} and the reorganization energy, respectively. Using analytical geometry, ΔG^{ε} can be expressed as

$$\Delta G^{\varepsilon} = \frac{\left(\lambda + \Delta G^{0}\right)^{2}}{4\lambda}. \tag{2.32}$$

The reorganization energy λ is also shown in figure 2.9 and is defined by the energy required to bring the reactants to the same nuclei configuration where the products exhibit minimum energy without transferring an electron. λ consists of two additive terms: λ_{in} and λ_{out}. The first term represents the solvent-independent inner term which arises from structural differences between the equilibrium configurations of the reactants and products. The second term contains the solvent reorganization energies and accounts for differences in orientation and polarization of the surrounding solvent molecules of the reactant and product complex. Both contributions to the reorganization energy can be calculated theoretically if a proper model of the transition state is available. Upon combining these substitutions, one yields the classical Marcus equation

$$k_{ET} = \kappa_{el}\nu_{n}\exp\left(\frac{-\left(\lambda + \Delta G^{0}\right)^{2}}{4\lambda k_{B}T}\right). \tag{2.33}$$

As can be derived from equation 2.33, k_{ET} increases for decreasing ΔG^{0} and reaches its maximum at $-\Delta G^{0} = \lambda$ ($\Delta G^{\varepsilon} = 0$). A further decrease of ΔG^{0} does not increase the reaction rate, but it leads to a decrease of k_{ET} for these kind of highly exergonic reactions due to a re-increase of ΔG^{ε}. The region where $\left|\Delta G^{0}\right| > \lambda$ is called the Marcus *inverted region* and was confirmed by experiments [105, 106]. Its prediction is one of the advantages of the Marcus theory in comparison to other ET models [107].

The classical Marcus theory can predict very well rate constants of *adiabatic* (κ_{el} 1) ET reactions but fails with respect to *non-adiabatic* ($\kappa_{el} << 1$) processes. In these reactions, tunneling of electrons from D to A and nuclei from reactant to product states play a major role and thus a quantum mechanical approach has to be chosen [108–111]. The first major difference is the introduction of the electronic coupling element $\hat{H}_{el}$, defined as the overlap of the electronic wavefunction of the donor and acceptor ψ_{D} and ψ_{A}, respectively.

$$H_{DA} = \left\langle \psi_{R}^{0} \left| \hat{H}_{el} \right| \psi_{P}^{0} \right\rangle \tag{2.34}$$

$\hat{H}_{el}$ denotes the electronic Hamilton operator in the Born-Oppenheimer approximation. The magnitude of the coupling decays exponentially with separation of donor and acceptor r according to

$$|H_{DA}(r)|^{2} = |H_{0}|^{2}\exp(-\beta(r - r_{0})). \tag{2.35}$$

H_{0} denotes the Hamilton operator at the Van-der-Waals distance r_{0}. β represents the tunneling parameter and depends on the separating medium. The quantum mechanical approach treats the reactants and product as complete system of states represented by nuclear and electronic wave functions. To estimate the transition probability from one state to the other, time dependent perturbation theory has to be applied. In analogy to Fermi's golden rule, one obtains for the transition probability ω_{j} from the reactant (R) to a product state (P)

$$\omega_{j} = \frac{2\pi}{\hbar}H_{RP}^{2}\sum_{i,j}\left\langle \chi_{Pi}^{0}|\chi_{Rj}^{0}\right\rangle^{2}\delta_{ij}\left(\varepsilon_{Pi} - \varepsilon_{Rj}\right). \tag{2.36}$$

$\left\langle \chi_{Pi}^{0}|\chi_{Rj}^{0}\right\rangle$ denotes the Franck-Condon (FC) integral containing χ_{Pi}^{0} and χ_{Rj}^{0}, the nuclear wave function of the product and reactant in the state j and i with the respective energy ε_{Rj} and ε_{Pi}, respectively. The transition probability is summed over all possible states i. δ denotes the Dirac delta-function which ensures energy conservation (transition from state i can only lead to product

state j which has the same energy). Accordingly, the first-order rate constant of an ET process can be derived by multiplying the probability with the number of possible states and is expressed as

$$k_{ET} = \frac{2\pi}{\hbar} |H_{DA}|^2 FCWD. \tag{2.37}$$

$FCWD$ denotes thereby the Franck-Condon-weighted-density-of-states term in which the FC integrals are weighted according to the probability of occupation $P(\varepsilon_{Rj})$ of respective states using the Boltzmann distribution statistic. $FCWD$ has the form

$$FCWD = \sum_{i,j} \left\langle \chi^0_{Pi} | \chi^0_{Rj} \right\rangle^2 P(\varepsilon_{Rj}) \delta(\varepsilon_{Pi} - \varepsilon_{Rj}). \tag{2.38}$$

In a fully quantum mechanical description, the sum in equation 2.37 is taken over all vibrational modes including those of the surrounding solvent molecules. However, since these modes have lower frequencies than the internal molecule vibrations, the solvent molecules are often treated classically. The refined resulting equation is called the *semi-classical* Marcus equation and has the form

$$\begin{aligned} k_{\mathrm{ET}} &= \frac{2\pi}{\hbar} |H_{\mathrm{DA}}|^2 \frac{1}{\sqrt{4\pi\lambda_o k_{\mathrm{B}} T}} \times \\ &\sum_{i,j} \left\langle \chi^0_{Pi} | \chi^0_{Rj} \right\rangle^2 P(\varepsilon_{Rj}) \exp\left[-\frac{\left(\Delta G^0 + \varepsilon_{Pi} - \varepsilon_{Rj} + \lambda_o\right)^2}{4\lambda_o k_{\mathrm{B}} T} \right]. \end{aligned} \tag{2.39}$$

In the high-temperature approximation, the equation further reduces to

$$k_{ET} = \frac{2\pi}{\hbar} |H_{DA}|^2 \frac{1}{\sqrt{4\pi\lambda_0 k_B T}} \exp\left[-\frac{(\lambda + \delta G^0)^2}{4\lambda k_b T} \right] \tag{2.40}$$

2.3.2 Heterogeneous ET

In heterogeneous ET reactions, one of the reaction partners is replaced by an electrode. The driving force of these heterogeneous reactions is given by the applied overpotential η.

$$\eta = E - E^0 \tag{2.41}$$

E denotes the applied electrode potential and E^0 represents the redox potential of the surface ET reaction defined by the Nernst equation

$$E = E^0 - \frac{k_B T}{ne} \ln\left(\frac{c_{red}}{c_{ox}}\right). \tag{2.42}$$

c_{red} and c_{ox} denote the respective concentrations of the electrochemically active species while n represents the number of transferred electrons per reaction formula.
In analogy to homogeneous reactions, one finally obtains the expression for non-adiabatic ET reactions (Marcus-*DOS*, *density of states*) [112]

$$k_{ET} = \frac{2\pi}{\hbar} \frac{1}{\sqrt{4\pi\lambda_0 k_B T}} \int d\varepsilon f(\varepsilon) \rho(\varepsilon) |H_{DA}(\varepsilon)|^2 P(\varepsilon_{R_j}) \exp\left[-\frac{(\lambda + \delta G^0(\varepsilon, \eta)^2}{4\lambda k_b T} \right]. \tag{2.43}$$

Here, the acceptor or donor is replaced by the metal electrode. The sum is accordingly made over all possible energy states ε of the metal and therefore replaced by the integral and extended with the

state density function $\rho(\varepsilon)$. Furthermore, $\rho(\varepsilon)|H_{DA}(\varepsilon)|^2 = |V(\varepsilon)|^2$ yields the electronic coupling strength between the electrochemical species and the electrode. The expression contains, in analogy to the Boltzmann distribution, the Fermi distribution function $f(\varepsilon)$, which accounts for the different occupation probability of different energy states ε of the metal.
The equation can be further simplified by introducing few assumptions [113–115]. For the oxidation one yields

$$k_{ox} = A\frac{\sqrt{\pi\lambda k_b T}}{e}\left(1 + erf\frac{e\eta - \lambda}{2\sqrt{\lambda k_B T}}\right) \tag{2.44}$$

and accordingly for the reduction

$$k_{ox} = A\frac{\sqrt{\pi\lambda k_b T}}{e}\left(1 - erf\frac{e\eta + \lambda}{2\sqrt{\lambda k_B T}}\right). \tag{2.45}$$

The error function erf is defined as

$$erf(x) = \frac{2}{\sqrt{\pi}}\int_0^x \exp(-t^2)dt \tag{2.46}$$

A denotes a parameter that depends on $|H_{DA}(\varepsilon)|^2$ and r. Furthermore, the Fermi-Dirac distribution function was replaced by a ladder function accounting for the difference in energies. Also, contributions from energy levels far away from the Fermi level are not considered.

3 Experimental Details and Instrumentation

This chapter contains details on the methods and equipment of the experiments presented in the attached publications.

3.1 Confocal Raman Spectrometer

SE(R)R and RR spectra were collected using a LabRam HR-800 (Dylor-Jobin Yvon-Spex) confocal Raman microscope (Olympus Bx 40) equipped with a nitrogen cooled CCD detector. The 413 nm and the 514 nm line of a Krypton (cw Coherent Innova 330c) and an Argon ion (cw Coherent Innova 70c) laser were used as excitation lines. The laser light was focused onto the sample using a Nikon 20*x* objective with a numerical aperture N.A. of 0.35 and a working distance of 20.5 mm. The Raman signals were collected in 180° back scattering geometry. A schematic representation of the experimental Raman setup is shown in figure 3.1.

After leaving the laser tube, the light passes two electro-optical laser intensity modulators (Pockel cells, Linos M 0202). With these modulators, laser pulses in the ms-time scale are created, enabling time resolved measurements (*vide infra*). Behind the spectrometer entrance, an interference filter (IF) is placed to remove laser plasma lines. The laser light is then focused through a pinhole onto a notch filter (NF) that reflects the beam into the microscope exit. The laser light is focused onto the sample using a microscope objective. The scattered laser light is collected through the same objective in back-scattering mode. The scattered beam passes the notch filter again, which is now transparent for the frequency shifted light. Behind the notch filter, the light beam is reflected by a mirror on the confocal hole (1000 μm) and is subsequently focused on the slit entrance (100 μm) of the monochromator unit. The monochromator is setup in the *Czerny-Turner* mode and can be operated with two different gratings, 2400 mm^{-1} and 514 mm^{-1}, respectively. The dispersed light is finally focused on a nitrogen cooled CCD chip. This chip consists of 2048×512 single pixels which can be used for light detection. In most of the experiments, a binning factor of two was used. This yields a resolution of 1 cm^{-1} with an increment per data point of 0.28 cm^{-1} and 0.15 cm^{-1} upon using the 413 nm and the 514 nm excitation line, respectively. The spectrometer is controlled using the company supplied software *LabSpec* v4.07 (Jobin Yvon, 2007). For calibration, the intense mercury line at 435.8238 nm and at 546.074 nm was used, respectively. The accuracy of the band positions was $\pm$ 0.5 cm^{-1}.

3.2 Electrochemical Measurements

Electrochemical measurements and electrode roughening were carried out with a computer controlled multistat (CH Instruments 660b, Austin, TX, USA). The control interface was supplied by the company software CHI660c v6.13, which allowed also data evaluation (baseline cut, determination of peak positions and widths and peak integration). The electrochemical cell was a homemade three electrodes containing electrochemical cell with a volume of ca. 5 ml. As counter electrode, a thick platinum metal sheet was used. An Ag/AgCl 3 M KCl (DriRef, World Precision Instruments) served as reference electrode. Ag ring electrodes were fabricated from Ag rods (99.9 %, Good Fellow

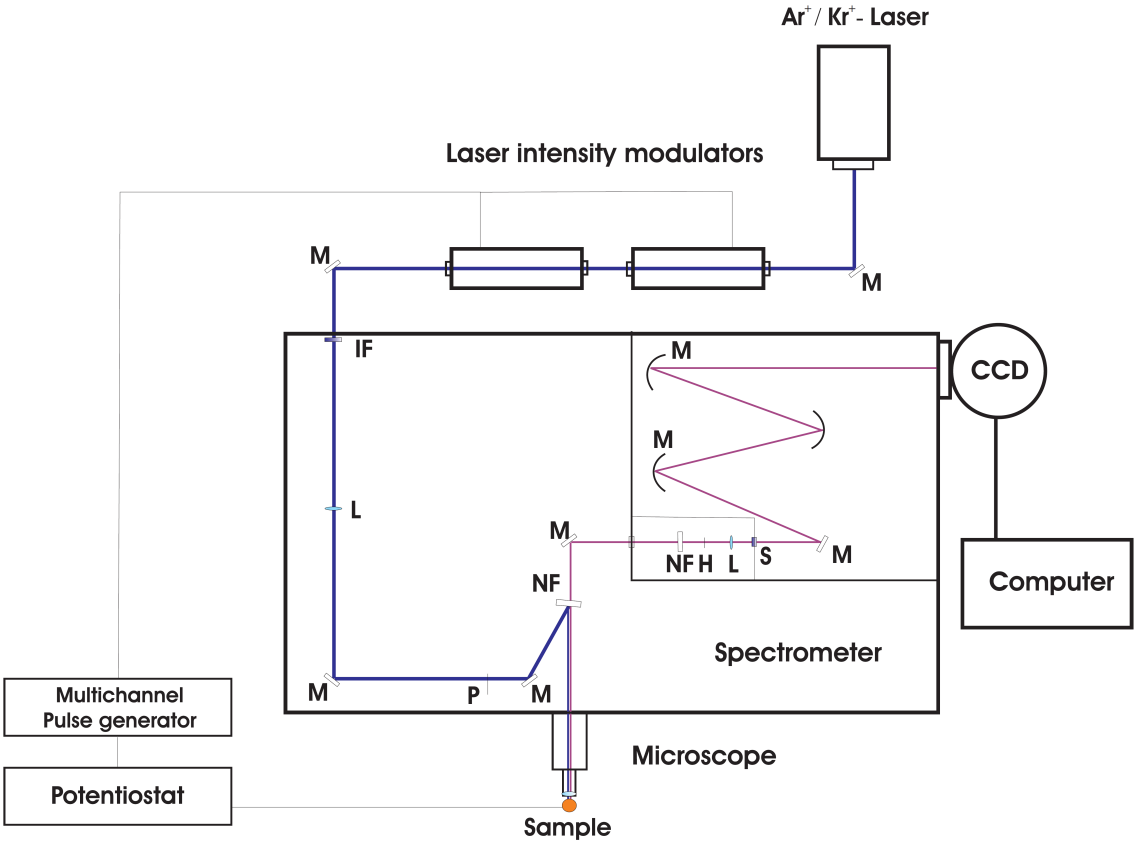

Figure 3.1: Schematic representation of the Raman setup. Details are given in the text. CCD charged coupled display; H hole; L lens; M mirror; NF notch filter; P pinhole; S slit.

GmbH) and exhibited an averaged geometrical area of around 1 cm^2.

3.3 Resonance Raman and Surface Enhanced Resonance Raman Measurements

Resonance Raman measurements were carried out in a cylindrical quartz cuvette (Hellma). Sample volumes ranged from 50 to 500 μl. During the measurement, the cuvette was rotated using a home-made motor device. The applied laser power was 1 to 5 mW. Spectral acquisition times varied from 5s to 60s depending on the desired spectrum quality.
SE(R)R measurements were carried out using a cylindrical Ag bulk ring electrode as SE active material. For that purpose, the Ag ring electrode was polished with different sand papers with increasing order of grain size. In total, the polishing procedure consisted of five steps (grain sizes 1000, 20, 9, 5, 0.3 mic). After each step, the Ag electrode was sonicated for five minutes in water and in ethanol. To obtain roughnesses on the nanometer scale, the blank polished electrode was finally roughened electrochemically. Therefore, the polished Ag ring was mounted into a three electrode containing electrochemical cell filled with 0.1 M KCl electrolyte solution. Potentials jumps from 0.5 to - 0.5 V were applied, and the Ag electrode oxidized and reduced, respectively. Details can be found in a protocol published elsewhere [116, 117]. Due to the occurring nucleation reactions associated with

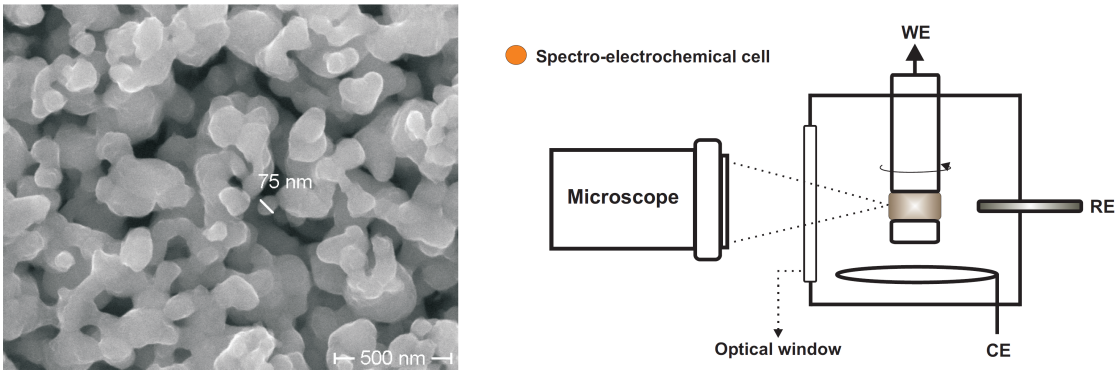

Figure 3.2: *Left.* SEM picture of an electrochemically roughened Ag electrode surface. *Right.* Schematic representation of the electrochemical cell for SERR measurements. The roughened Ag electrode is mounted on a rotating holder and functions as working electrode (WE). CE counter electrode. RE reference electrode. Details are given in the text.

the re-reduction, a nanometer scale coral like surface structure of the Ag electrode was obtained. Figure 3.2 shows a SEM picture of an Ag electrode surface after electrochemical roughening. This kind of electrodes functioned as the basis for all the SE(R)R measurements.

To generate hybrid devices, the electrode was subsequently coated with silica layers of different types and subsequently charged positively by attaching a silica compound which exhibited an amino-terminated headgroup. This positively charged surface can be used for immobilization of $\left[Me^{M+}Cl_n\right]^{M-n}$ (Me = metal) ions for subsequent metallation by reduction. The so fabricated hybrid electrode will be introduced in the *Results* section [118].
For protein studies, the electrode was coated with a proper SAM for protein immobilization. In most cases, carboxyl-terminated alkanethiol compounds of variable chain length were used (see section *Self Assembled Monolayer*). The formation of a monolayer was achieved by incubating the freshly roughened electrode into a 1 mM ethanolic solution of alkanethiols over night. The quality of the formed SAM was checked by performing cyclic voltammetry [119].
The SE active Ag electrodes were mounted on a homemade electrode holder system, which exhibited a sliding contact between electrode and holder. By connection to an external motor, it was possible to constantly rotate the Ag rings during measurements. This was necessary to avoid laser induced sample degradations when working with biological samples. Moreover, the rotation ensured an accumulation of signals arising from many different surface features. To complete the spectro-electrochemical device, an adapter cell made of plastic (Delrin) was finally attached to the holder, compassing the working electrode. The adapter cell contained ca. 10 mL of an oxygen-free buffer solution and a platinum wire that acted as counter electrode. An Ag/AgCl 3 M KCl (DriRef, World Precision Instruments) was placed into the cell via a special entrance and functioned as reference electrode. Furthermore, the cell exhibited an optical window of ca. 40 mm in diameter for entrance and exit of laser and scattered light, respectively. A schematic representation of the spectro-electrochemical cell is shown in figure 3.2. In all SE(R)R experiments, potentials were adjusted using a potentiostat (potentiostat/galvanostat model 263 A, EG&G Princeton Applied Research). Potential dependent (stationary) measurements were carried out by applying potentials to the working electrode. The system was led to equilibrate for 30 s to 1 min before a spectrum was acquired.

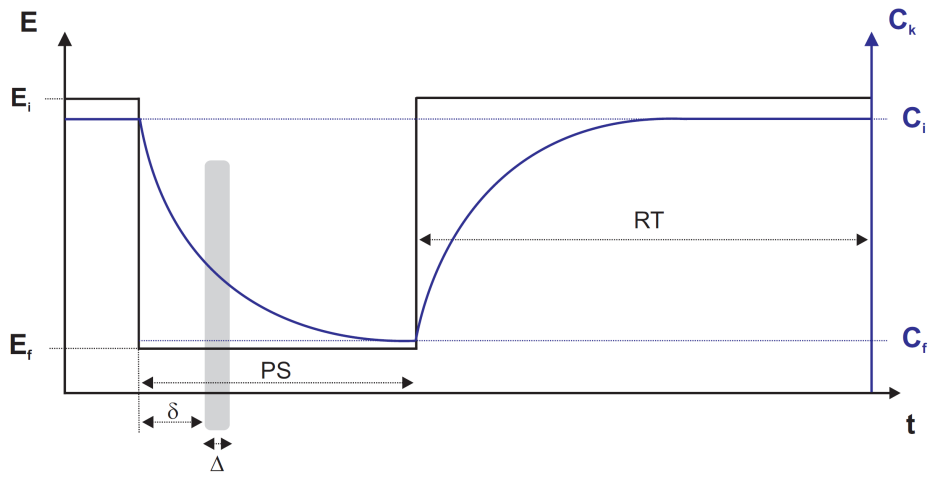

Figure 3.3: Schematic representation of the time resolved SERR measurement for one delay time δ. C_i and C_f denote the concentration C of the surface adsorbed molecules (in blue) at the initial potential E_i and at the final potential E_f (in black), respectively. *PS* denotes the pulse time, *i.e.* the time E_f is applied to the working electrode. *RT* denotes the recovery time, *i.e.* the time E_i is applied after the potential jump in order to recover initial conditions. A description of the sequence of measurement is given in the text.

Time resolved experiments were carried out by coupling potential jumps with short measure intervals [38]. For that purpose, a multi-channel delay generator was used to connect the potentiostat and the laser intensity modulators, which allowed defined spectra acquisition after different reaction times. The measurements itself followed a scheme as summarized in figure 3.3. First, a potential jump from an initial potential E_i to a final potential E_f was triggered at the working electrode. After a defined delay time δ, the measurement started by setting the modulator on transmisson for a certain period of time (measure interval) Δ. Then, the potential was set back to E_i to let the system recover to initial conditions for another period of time RT. Since Δ is usually very short, this procedure had to be repeated for one δ many times until the resulting sum spectrum was of acceptable quality. By varying δ, the complete relaxation process, triggered by the applied potential jump, could be probed SERR spectroscopically. The precise values for δ, Δ and RT depended on the investigated reaction. Normally, δ and Δ is substituted by δ', which is calculated via $\delta' = \frac{\delta+\Delta}{2}$.

4 Results

This chapter summarizes the results obtained in the particular projects of this thesis. Each topic is introduced through a short description of the broader context. The publications are attached in the bibliography.

4.1 Electron Transfer Properties of Cytochrome *c* at Electrochemical Interfaces

Cytochrome *c*, a small soluble heme protein with a molecular mass of ca. 12 kDa, is present in all organisms [89]. Its molecular structure is highly conserved and varies in different eukaryotes by only few amino acids, indicating a preservation of its function throughout the evolutionary process [120]. In aerobic organisms, cytochrome *c* is *inter alia* attached to the inner mitochondrial membrane, where it acts as an electron shuttle in the respiratory chain by transferring an electron from cytochrome *c* reductase (complex III) to cytochrome *c* oxidase (complex IV). Therefore, it can change reversibly between the ferric and ferrous oxidation state by donating and accepting an electron, respectively (see section *Cytochromes*). Due to its important role in bioenergetics and its high stability in solution, cytochrome *c* has been intensively studied by various spectroscopic techniques [121–125]. Aim of many studies was the investigation of fundamental biological electron transfer processes and the parameters that control these reactions, using cytochrome *c* as a model protein [127]. To probe the properties of biological ET under controlled conditions, the protein is attached to a metal electrode which is able to trigger the redox transitions by applying potentials. To mimic the natural environment and to prevent protein denaturation, the electrodes are coated with self assembled monolayers. The chemical composition of the SAMs can vary depending of the goal of study (see section *Self Assembled Monolayers*). In this respect, a widely used system is an electrode covered with ω-carboxylated alkanethiols which possesses a negatively charged surface. The interaction of the protein and the coated electrode is of electrostatic nature. As a result of a symmetric charge distribution, cytochrome *c* exhibits a relatively high molecular dipole moment of several hundreds of Debye [128, 129]. Around the solvent expose heme edge, seven lysine residues are located which are positively charged at physiological pH and thus form a positively charged patch. The adsorption of cytochrome *c* to the coated electrode is also assumed to resemble native biological reaction conditions as most of the redox processes take place at charged interfaces. For cytochrome *c*, this is particularly true for example upon complex formation with cytochrome *c* oxidase [130, 131].
The first studies aiming at the heterogeneous electron transfer kinetics of cytochrome *c* were carried out using electrochemical methods [132, 133]. Electron transfer rate constants were determined according to a method proposed by Laviron [134]. Due to the relatively high distance between cytochrome *c* and the electrode, a non-adiabatic slow electron transfer process was expected. Accordingly, by employing different SAMs with decreasing chain length, the heterogeneous electron transfer rate should increase as a function of the distance, as is expected for long-range electron transfer due to the increase of electronic coupling strength according to

$$k_{ET} \propto \exp(-\beta r), \tag{4.1}$$

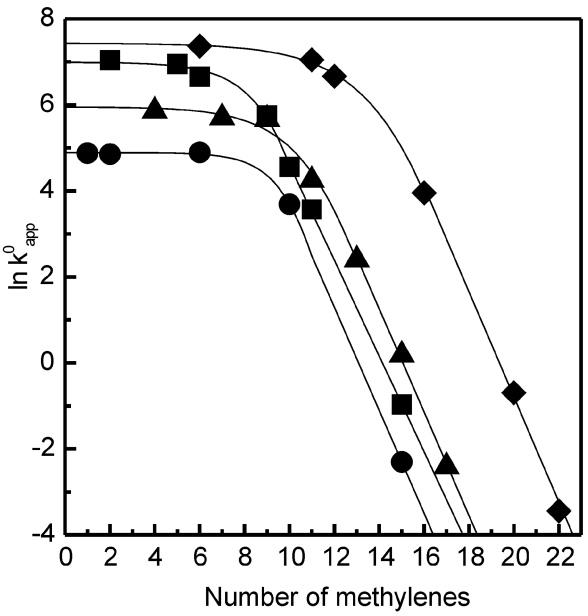

Figure 4.1: The ET rate constants of cytochrome *c* and azurin as a function of the thickness of the SAM layer (distance from the electrode). Circles, cytochrome *c* on Ag. Squares, cytochrome *c* on Au. Diamonds, cytochrome *c* on Ag coated with a pyridine terminated SAM. Triangles, azurin on Au coated with a hydrophobic SAM. Reprinted with kind permission from [38]. Copyright 2013 Royal Society of Chemistry.

where β is the tunneling parameter and r the effective distance to the electrode. A value of 1.1 per SAM methylene (carboxyl-terminated alkanethiols) unit was determined for β. Interestingly, this value was found to be essentially the same for different immobilized redox proteins [135–140].
In general, the distance dependence of the heterogeneous electron transfer kinetics of cytochrome *c* can be divided in two regimes. For far distances, *i.e.* for SAMs with 10 or more methylene groups, it is commonly accepted that the kinetics are dominated by electron tunneling. Accordingly, the ET rates increase from 0.07 s^{-1} to roughly 50 s^1 when switching from a C15 to a C10 monolayer (alkyl chain consisting of 15 and 10 methylene groups, respectively) [141, 142]. A reorganization energy of 0.22 eV was determined by overpotential dependent SERR measurements performed on cytochrome *c* adsorbed on C15 SAMs and subsequently fitting of equation 2.45 to the data [38]. However, when further approaching the electrode, no continuous increase of the ET kinetics can be observed. In fact, the values of the rate constants determined using a C1, C2 and C5 monolayer level off at around 130 s^{-1}, *i.e.* the ET kinetics become distance independent for SAMs with six or less methylene groups as shown in figure 4.1. This region is the so-called *plateau region*. Due to the unexpected behavior, this region was object in numerous studies aiming to clarify the origin of the plateau. The fact that this behavior was also observed for a number of other heme and non-heme proteins suggested, moreover, that the plateau region might be of general relevance in biological ET processes [143–145, 147, 155].

Although a large body of experimental data was collected, there existed for a long time no consensus about the origin of the distance independence of the ET rates. It was commonly accepted that a change in mechanism is existent and thus electron tunneling is no longer rate limiting for short protein-electrode separations [148–150]. In this respect, two different interpretations were postulated. Avila and coworkers proposed a gated electron transfer mechanism [132]. According to this, the protein binds to the SAM surface in an orientation which is indeed thermodynamically stable but does not facilitate the electron tunneling due to a weak electronic coupling. To undergo the redox reaction, the protein has to re-orientate to a position that favors the electron transfer. This

re-orientation is assigned to a rate constant that is the same for all distances to the electrode. While the electron tunneling rate increases significantly with smaller distances, the re-orientation rate is constant and therefore becomes rate limiting for a sufficiently small protein-electrode interspace. Furthermore, this interpretation explains why the rate constants decrease with increasing buffer viscosity and pH [151, 152]. Both factors have a direct negative influence on the re-orientation rate. High pHs are equivalent to high surface charge densities due to an increase of the deprotonation degree of the COOH SAM headgroups. The resulting increased electric field strength slows down the re-orientation rate, according to $k_{re} \propto \exp(-\Delta\mu \cdot E_f)$, where $\Delta\mu$ is the difference in the effective dipole moment of the protein at the initial and the final orientation and E_f is the electric field strength, respectively. The other model describes the plateau region as a result of a transition from a non-adiabatic to an adiabatic electron transfer process [153]. Although the electron tunneling probability is very high, the relaxation of the surrounding medium is comparably slow and thus dominates the observable ET kinetics. This transition from non-adiabatic to adiabatic ET takes place at small electrode distances where the electronic coupling strength is sufficiently high [153, 154, 156]. Conducted experiments, where the heme group is directly wired to the electrode by coordination of a pyrdine group to the iron central atom, revealed evidences for the validity of this model [157].

However, all the experimental data supported one or the other model only in an indirect manner. Finally, using Q band excited SERR spectroscopy, it was possible to give the first tentative answers to the longstanding question about the origin of the plateau region, by probing the protein re-orientation directly [158]. The approach is based on an exploitation of SE Raman selection rules. The re-orientation becomes noticeable through changes in the relative intensity of bands of different symmetry. The reason for this intensity change is the different relative orientation of the heme group with respect to the surface normal, *i.e.* the direction of the enhanced electric field vector. Vibrational modes of the heme group with different symmetry gain surface enhancement due to different entries of the polarizability tensor α.

$$\alpha_{por} = \begin{pmatrix} \alpha_{xx} & \alpha_{xy} & \alpha_{xz} \\ \alpha_{yx} & \alpha_{yy} & \alpha_{yz} \\ \alpha_{zx} & \alpha_{zy} & \alpha_{zz} \end{pmatrix} \tag{4.2}$$

In an adsorption geometry as indicated in figure 4.2 in which the green plane represents the heme group attached on a (much bigger) roughened Ag surface, all entries of the tensor with x character gain surface enhancement since they are positioned in parallel direction to the enhanced electric field vector [32, 159] (T direction). In a D_{4h} approximation of the heme group, vibrational modes with A_{1g} and B_{1g} symmetry gain enhancement due to the matrix elements α_{xx},$+\alpha_{yy}$,αzz and α_{xx},$-\alpha_{yy}$, respectively [74]. If we now assume a starting geometry as shown in figure 4.2 and expect a slow re-orientation to a configuration where the heme plane is oriented in a parallel way to the surface, *i.e.* x,y plane perpendicular to T, then, as a result, the intensity of the B_{1g} modes will consequently decrease stronger than the intensity of A_{1g} modes.

The reason is the extra α_{zz} entry of the latter symmetry. For increasingly parallel orientations, the z axis (in heme coordinates) becomes more and more T like and thus will gain increasing enhancement. As a result, the intensity ratio of B_{1g} to A_{1g} modes will be higher if the heme plane is oriented perpendicular to the surface and will become smaller if the angle between heme plane and surface normal (in T direction) increases. These considerations hold strictly for non-resonant conditions. This symmetry-based approach was successfully applied using Q band spectra of cytochrome c, where the rigorous resonance Raman selection rules are weakened [158]. As a result, it is concluded that orientational dynamics control the overall electron transfer properties. The local electric field strength determines the mean orientation and the mobility of the protein at the interface. The measured ET kinetics are concluded to be a convolution of both, the dynamic re-reorientational process

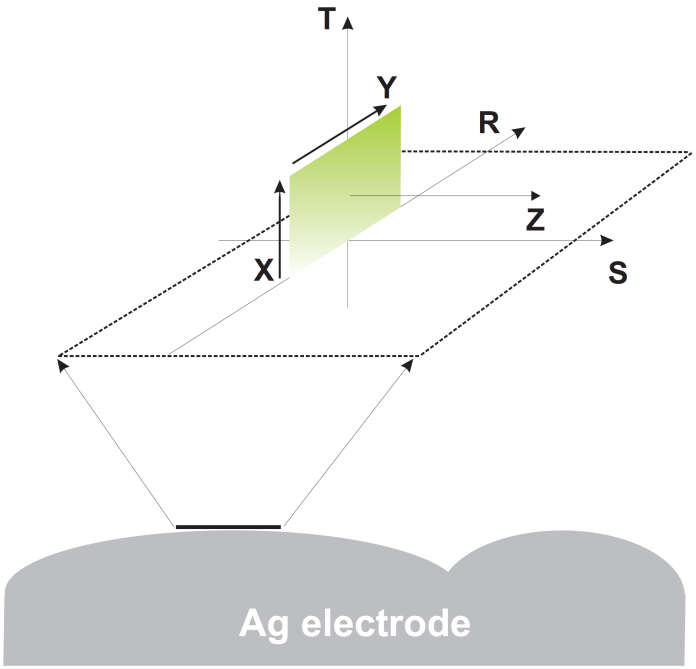

Figure 4.2: Model for determining the relative orientation of the heme with respect to the electrode surface normal (T). *x*, *y* and *z* denote the heme (green plane) coordinates while T, R, and S represent the electrode coordinates. The enhanced electric field vector is parallel to T.

and the tunneling probability inherent in each protein orientation.

Although the direct detection of the orientational dynamics constitutes a big step towards understanding the biological interfacial ET, substantial questions still remain. In the first project, the properties of protein surface dynamics were investigated. For that issue, cytochrome *c* was attached covalently to a SAM surface by forming amide bonds between the COOH headgroups of the SAM and the NH_2 groups of the lysine residues. The effect of a covalent immobilization on the electron transfer kinetics was studied using the approach proposed by Kranich *et al*, and the measurements were supported by calculations.
In a second work, kinetic studies of cytochrome *c* immobilized on short SAMs were performed and the results were combined with results obtained from SEIRA measurements, which probes the relaxation of the protein backbone. As a crucial parameter, the interfacial electric field could be identified. It was found that electric field effects modulate strongly the overall ET kinetics by influencing protein motion, electron tunneling probability and also hydrogen bond re-arrangements.
The obtained results afford a qualitatively consistent description of the interfacial ET process of cytochrome *c*.

4.2 Tyrosine Nitrated Cytochrome *c* - Role in Apoptosis

In contrast to necrosis, the traumatic cell death due to external forces such as injury, apoptosis denotes the programmed cell death self-initiated by the cell system. The wanted dieback of body cells may be irritating at the first glance but is of high importance for many biological processes and a crucial component of life. Apoptosis is mainly employed by multicellular organisms to remove malfunctioning or dispensable cells and plays a role during the embryonic growth, e.g. for differentiation of extremities and brain development [160, 161]. As a result of apoptosis, the affected cells suffered shrinkage, plasma membrane blebbing, chromatin condensation and nuclear membrane breakdown. These cells are subsequently detected and engulfed by phagocytes to avoid an affection to neighboring healthy cells by the released chemical compounds. A disregulation of the apoptotic function will finally lead to disease or death of the organism. Cancer, the uncontrolled growth of body cells, is often mentioned in this respect.
On a molecular level, there are different forms of apoptosis. The most well-known form is the caspase-dependent (caspase are Cys proteases) apoptosis that may occur via two different pathways: the extrinsic and the intrinsic pathway [162]. In the extrinsic pathway, the apoptotic stimuli are recognized extracellularly by a transmembrane protein which acts as death receptor and finally induces the death-inducing-signalling complex (DISC). The intrinsic pathway, also known as mitochondrial pathway, is activated by apoptotic inducing factors within the cell leading to permeability of the outer mitochondrial membrane and a subsequent release of mitochondrial proteins to the cytosol. Cytochrome *c* is one of these proteins [163, 164]. Under normal circumstances, cytochrome *c* is attached to the inner mitochondrial membrane in the double membrane interspace, where it acts as an electron carrier to shuttle electrons from complex III to complex IV in the respiratory chain (compare section *Cytochromes*). The first experiments pointing at the double role of cytochrome *c* in life and death of cells were conducted around 1996 [165, 166]. Further studies revealed that once cytochrome *c* is released to the cytosol, it binds to the oligomer Apaf-1, forming a complex that, in turn, activates the procaspase-9 (apoptosome) to start the apoptotic caspase-dependent reaction cascade [164, 166]. A more detailed description is given in the references [160, 161].
Before cytochrome *c* can be released, a prior detachment from the inner mitochondrial membrane is necessary. Under normal conditions, it was found that a high fraction of the protein is strongly bound to the anionic phospholipid cardiolipin via electrostatic interactions [167, 168]. The mechanism of detaching of cytochrome *c* from cardiolipin is still under debate.

One possibility is the oxidation of cardiolipin to reduce its negative charge and therefore the binding affinity to cytochrome *c* [169–171]. This oxidation process can be accomplished either by reactive oxygen species (ROS) present due to the ongoing respiratory process or by the cytochrome *c*-cardiolipin complex itself. The binding promotes a change in the conformation of the protein allowing oxygen to access to the otherwise closed heme site [172]. Also possible is an effect of the electric field present at the membrane interface and promoted by the high negative charge of the cardiolipin that induces a configuration change of the oxidized cytochrome *c* from a native 6cLS Met/His ligation to a 5cHS /His ligation, where the sixth coordination place remains vacant for oxygen binding and subsequent peroxidation reactions [173–175]. Other cytochrome *c* modifications are adducts formed upon reaction with reactive nitric oxides (RNS). Cytochrome *c* has been shown to be nitrosylated at the heme iron atom during the apoptosis [176]. Beside this, nitrated tyrosines are also possible reaction products. Tyrosine nitration is proposed to be one of the initial steps of the transformation of cytochrome *c*'s function from an electron carrier to a signal transducer [177–180]. Human cytochrome *c* exhibits five different tyrosines, the heme near buried tyrosine Y48 and Y67 and the solvent exposed Y46, Y74 and Y97.

In the study conducted in this thesis, the effects of different tyrosine nitrations on the heme site of cytochrome *c* were investigated. Single tyrosine mutants for each five tyrosines were prepared by

specific Tyr to Phe substitution of four tyrosine groups. The remaining tyrosine residue was subsequently nitrated. The thus treated mutants were first investigated by means of resonance Raman to estimate the effects of tyrosine nitration on the heme structure. To probe the effects of electric fields on the stability and the conformational equilibria, the nitrated mutants were immobilized on a SAM coated electrode and studied by means of surface enhanced resonance Raman spectroscopy. The results indicate that the heme pocket destabilizations caused by nitration and by electric fields occur via different driving forces and mechanisms. Moreover, it is concluded that the higher accessibility of the heme site, caused by nitration, facilitates the peroxidase activity of the protein.

4.3 Interfacial ET of Outer Membrane Cytochromes Embedded in Biofilms of *Geobacter*

The first metal reducing bacteria strain was discovered in 1987 where it was isolated from sediments of the Potomoc river, USA [181]. These bacteria, named therefore with the suffix *metallireducens*, were found to be capable of oxidizing small organic compounds to carbon dioxide using iron oxides as electron acceptors [182]. The application potential of these bacteria was soon realized. In the following years, many other strains were discovered exhibiting similar abilities [183].
Among all of them, two species have been studied most extensively. These are the strains *Geobacter sulfurreducens* and *Geobacter metallireducens*. Beside academic research interests, a lot of efforts have also been made to employ these bacteria in technical applications [184, 185]. Two major aspects of the bacteria's properties are in this respect important. One concerns the potential substrates. *Geobacter* species have been shown to be able to metabolize (oxidize) many different kinds of organic compounds [186, 187]. Accordingly, they can be used in environmental restoration processes, for example for decomposing harmful organic pollutants such as petroleum or aromatic compounds, both exposing a high threat to the qualtity of groundwater [188, 189]. Also metal ions can be used as electron donors. This includes especially Fe(II) and U(IV) [191–193]. *Geobacter* can oxidize these metals to the higher oxiditation states, *i.e.* Fe(III), U(VI) and U(V), which is accompanied by a significantly lowering of the solubility of the compounds. In the case of U(IV), this is of special interest in terms of binding this highly toxic element for subsequent removal from water or in general environmental systems [191]. The other aspect concerns the potential electron acceptor. It has been found that these bacteria can not only grow on iron oxides but also accept a variety of other oxides and elements as client (*i.e.* extracelluar electron acceptors). To mention the most important, these are bulk carbons, tin oxide, silver and gold.
Given a stable food and an insoluble electron acceptor source, *Geobacter* can even form biofilms of up to 50 μm thickness above these materials, exhibiting a relatively high substrate consumption rate, see figure 4.3 [194]. Therefore, a major interest has been focused on the use of Geobacter for producing electricity by growing the bacteria on solid electrodes and using their metabolism as electron generating source [184, 196]. This approach finally led to establishing the field of microbial fuel cells (MFC)(in bioelectrochemical systems, BES) in analogy to ordinary H_2/O_2 fuel cells [184]. In these MFCs, the bacteria are grown on a solid anode material to yield stable biofilms and subsequently exploiting their substrate metabolism for electricity generation. On the prime time of MFC development, even the American aerospace organisation *NASA* considered to install MFCs in shuttles to gain electricity out of the inevitably accumulating waste water during space missions. There have also been efforts to upscale these MFCs to be used industrially [197]. However, a kind of disenchantment seems to be slowly manifestating in the MFC community lately. It seems that the performance in terms of electricity generation of MFCs are far too low to be used for "real world" applications [197]. To reach a higher current output, two approaches are in principle possible. On the one hand the anode material can be optimized to enhance the bacteria/electrode interactions and thus allowing possibly higher current density outputs. On the other hand genetic manipulations can be applied to increase the overall bacterial turnover activity [194].
However, both approaches require a deep understanding of the processes ongoing in the bacteria. In this respect, particularly the electron transfer mechanism through the bactaria colony, *i.e.* the biofilm, and finally to the electrode (insoluble acceptor) is an important factor. Accordingly, there have been many studies carried out addressing especially this issue. A lot of interesting information has been gathered but still an overall clear picture is missing.

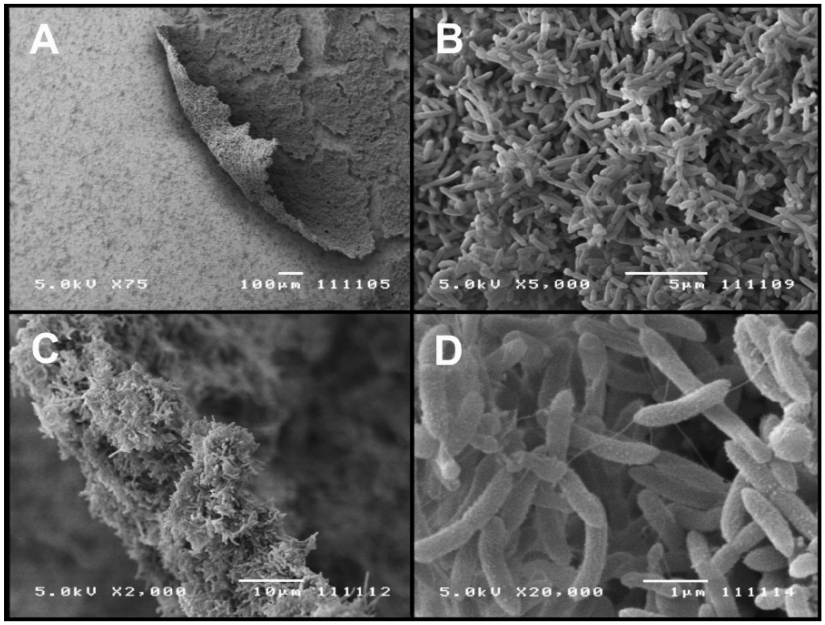

Figure 4.3: SEM images of *G. sulfurreducens* growing on a gold electrode. Magnification: 75-20 000 x. *A*. Biofilm attached to the surface, partially peeling off. *B*. Closeup of Figure 3A where the biofilm was attached to the electrode surface. *C* and *D*. Closeups of *A* at the edge of the biofilm. Reprinted with kind permission from [195]. Copyright 2013 American Chemical Society.

Electron Transfer Properties

Most of the studies on the electron transfer properties referred to the strain *Geobacter sulfurreducens*. Although there are a lot of unknown parameters, it could be concluded that an efficient electron transfer of *Geobacter* requires a number of certain proteins. For extracellular electron transfer, it seems that *Geobacter* possesses a variety of redox active outer membrane cytochromes (Omcs) which are located either in or on the circumferum of the cell's outer membrane [198]. These Omcs are multi *c*-type heme proteins whereby the exact number of heme groups within a protein can differ from type to type. The most important Omcs discovered so far are the OmcB, OmcS and OmcZ [194]. Each protein is associated with another function. For example, OmcB contains twelve heme groups and is mainly embedded in the outer membrane with a small part exposed [199]. It is assumed that this protein plays a role in the direct electron transfer between the bacterium and an acceptor. In contrast, OmcS can be found on the outer membrane of bacteria cells [202]. The exact role of this six heme groups containing protein is not known yet. OmcZ is also located on the outer membrane and will be accumulated heavily at the bacterium/solid interface if the electron acceptor constitutes an insoluble solid anode. In that case, *Geobacter* tend to form thick biofilms. It was found that OmcZ is crucial for the electron transfer through the biofilm (high current densities for biofilm/anode systems) but not for reducing small soluble electron acceptors [203]. The general determination of respective roles of certain Omcs is very difficult as one has to rely of gene deletions methods. The bacteria, however, can replace easily the removed Omc type by expressing another one instead, complicating the assignment severely. Overall, the accumulated knowledge about the Omcs is still very limited [194].

In case of *Geobacter* biofilms, it is important to distinguish between major electron transport steps. One step is the heterogeneous electron transfer reaction at the interface of bacterial film and solid

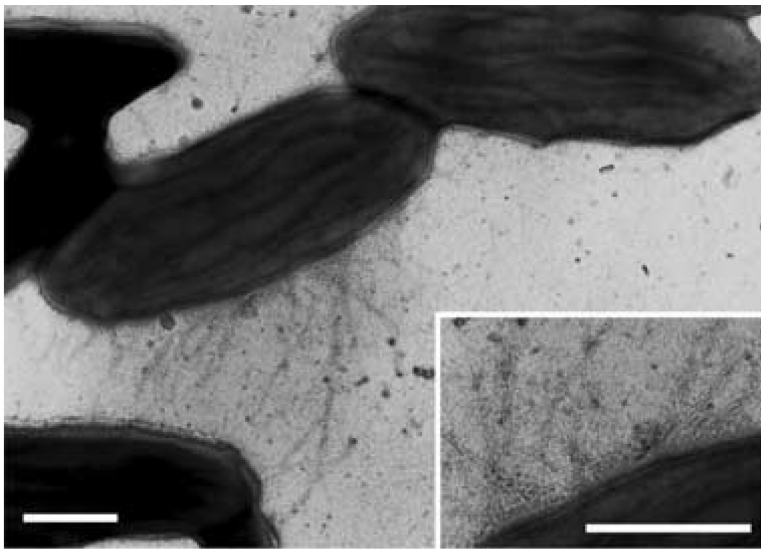

Figure 4.4: Transmission electron microscopy picture of *G. Sulfurreducens* cells. The filament strucutres constitute the pili protein network produced by the bacterium. Scale bar, 0.2 μm. Reprinted with permission from Macmillan Publishers Ltd: Nature. Figure from [201].

support. It is commonly accepted that *Geobacter* can transfer directly electrons to the acceptor, in contrast to other species which employ a variety of electron shuttles and mediators for this purpose. For that, it is likely to assume that a very close (tunneling) contact between bacterium and acceptor is needed in order to enable heterogeneous ET. In previous studies, a number of Omcs are proposed to play a role in this process, e.g. the aforementioned OmcZ [203].
The other electron transfer step concerns the shuttling of electrons through the biofilm, which includes also the transfer of electrons from out of the inner cell of distant bacteria, where chemical conversion takes place, and subsequently transporting through the biofilm matrix and finally to the electrode. Since a biofilm can have a thickness up to 50 μm, there are bacteria cells that are not in contact with the electrode surface. However, it was observed that the current production increases with increasing biomass present in the biofilm, suggesting that a) cells more remote from the electrode are in electronic contact and can transfer electrons and b) hence the biofilm has to exhibit a certain electron conductivity [204].
In this respect, two major approaches are proposed to explain the intrabiofilm electron flow. The more traditional approach involves the electron transport through (matrix-)cytochromes, abundantly present in the biofilm as it shines red as a result of the electronic absorption properties of the heme groups. The electron transport mechanism was proposed to be similar to that in hydro-gels or other biological systems (e.g. cytochrome *c* oxidase, PSI&II) involving electron hopping mechanism between distant redox centers, *i.e.* cytochromes [205, 206]. In contrast to this, the other approach states that pili constructs, inherent in biofilms, play a major role in the electron transport cascade [204]. The pili structures constitute a major discovery and are found to be produced in particular by *Geobacter Sulfurreducens* when grown in biofilms. In SEM pictures of *Geobacter* biofilms, see figure 4.4, these filament-like pili constructs, mainly consisting of the structure protein pilA, can be easily identified as they are abundantly produced and form network-like structures to connect distant bacterial cells with each other [207]. Although previous studies suggested that these pili are mainly insulators, recent studies carried out indicate a high conductance along the pili. In fact, the conductivity was found to increase exponentially with decreasing temperature similar to metal systems [208]. Therefore, it was concluded that these pili may play also a role in the electron transport chain through the biofilm matrix. Moreover, associated with the pili are the OmcS and OmcZ which both seem to

be necessary in order to obtain high current densities in anode/biofilm systems [202]. Consequently, it was propsed by Lovley *et al.* that these pili act as electron channels. The electrons are transported possibly via π-π stack interactions, as no cytochromes are present along the pili.
However, to prove or disprove the validity of one or the other model, way more experimental studies have to be carried out. The current art of knowledge on that topic is far from being complete.

Spectro-electrochemistry of electro-active Biofilms of *Geobacter Sulfurreducens*

The simplest method for characterizing the electro-activity of biofilms is cyclic voltammetry (CV). Here, the electrode potential is linearly swept and the resulting currents measured and plotted as a function of cell potential. The CV experiment can be performed for biofilms (grown on the working electrode) in two modes, in the presence or absence of substrate. Each condition delivers different information about the system. In the presence of substrate, the voltammogram shows the typical turnover signal, a quasi-sigmoidal current trace [209, 210]. It could be shown that the turnover activity, *i.e.* the total produced current density, depends on the electrode potential and is higher the more positive the applied electrode potential is [211]. Under non-turnover conditions, *i.e.* in the absence of substrate, the voltammogram obtained for very low scan rates (1 mV/s) shows a variety of unique peaks. These peaks result from electrode nearby redox centers whose reactions were triggered by the changing electrode potential. It is likely to assume that the nature of these redox centers might include Omcs that are expressed by the bacteria in order to allow electron exchange with the bulk metal (*vide supra*). Unfortunately, CV cannot provide information about the chemical constitution of the reaction partners involved. To investigate further the compounds involved in the electron transport cascade, CV and in general electrochemical techniques need to be coupled with spectroscopic methods. The yielded combination, spectro-electrochemistry, has proven to be a powerful method, particularly for investigating surface-confined redox active biological systems [38, 40, 212, 213].
For biofilms that contain a lot of heme proteins such as plasmic cytochromes and Omcs, SERR spectroscopy turned out to be the ideal spectroscopic tool [210]. In a first study by Millo *et al.*, SERR spectroscopy was successfully applied for investigations of surface-confined Omcs in biofilms of *Geobacter Sulfurreducens*. The biofilm was therefore grown on a roughened Ag electrode that constitutes the SER active support. Interestingly, the bacteria could grow also in the presence of silver cations, which normally have a disinfectant effect. In fact, the bacterial turnover activity resulted in high current densities up to 600 $\mu A/cm^2$. SERR spectra collected from that system, using a 413 nm excitation which is in resonance with both the heme group and the support, clearly showed a spectral signature of a *c*-type heme with two His residues functioning as axial ligands (bis-His 6cLS). Upon changing the electrode potential, the relative amount of oxidized and reduced hemes changed indicating that the heme groups are involved in the electron transport reaction / surface redox reaction. As a result of the electrochemical titration experiments, it could be shown that, consistent with CV experimental predictions, two kinds of heme containing redox species are involved in the heterogeneous electron transfer process. These heme groups belong most likely to two different Omcs of bacterial cells in close contact with the electrode surface. Along with findings obtained with other spectroscopic techniques such as UV/Vis or SEIRA, it could be conclusively shown that, as predicted by microbiological methods, cytochromes are involved in the interfacial electron transport of biofilms [214–218].

As a part of this thesis, the well-established time resolved SERR spectroscopic approach was applied to investigate the heterogeneous electron transfer properties of the Omcs in close vicinity to the electrode surface [38]. Similar to the previous study of Millo *et al*, bacterial biofilms of *Geobacter Sulfurreducens* were grown on roughened silver electrodes. Then, potential jumps were applied to trigger the redox reaction at the working electrode and SERR spectra were recorded as a function of different delay times following the potential jumps. The interfacial redox process could be resolved

as a function of time and the applied (over-)potential. As a result, we were able to determine different rate constants for the surface relaxation process. The experiments were furthermore combined with electrochemical measurements, *i.e.* CV and chrono-amperometry, and kinetic simulations to support the Raman results. The overall obtained picture indicates that the heterogeneous electron transfer seems to be the rate limiting step of the biofilm/electrode ET process, while the intra-biofilm electron shuttling (at least at a distance close to the electrode) is much faster. Moreover, we obtained evidences that Omcs may act as electron gates and therefore functioning as electronic link between the biofilm(-matrix) and the solid anode.

4.4 Surface Enhanced Raman Active materials - Pt Coated Ag Electrodes

SER spectroscopy has been constantly further developed over the last decades. Although nowadays this technique is already employed in various kinds of scientific studies, the limits of its potential are still not reached. The largest progress in this field has been made since the middle of the 1990s with the beginning of controlled design of SE active support materials. These supports are crucial for the sensitivity of the method, since their electronic properties determine the surface enhancement and therefore the signal intensity increase. The efforts made in searching for different nanostructures and geometries producing the highest field enhancements had finally led to an own field of research named plasmonics [219].
Most of the studies focus on the coinage metals silver, gold and copper. All these three belong to the free-electron (Drude) metals, which can be excited resonantly using visible light to generate intense surface plasmon resonances [220]. Accordingly, their field enhancements are very high, so that they constitute suitable materials for SER studies. Other metals such as the transitions elements Pt, Ti and Ru, however, show only weak surface enhancements with plasmon resonance frequencies expected to lie in the UV region [221, 222]. Their Fermi energy levels are in the region of the *d* bands that are subject to strong mixing with *s* orbitals, and thus interband transitions become very likely. As a result, surface enhancement is almost depleted completely [223–225].
This constitutes a major drawback and is a clear restriction of SER spectroscopy. Specifically, the metals like Rh, Ru and Pt are more widely used in technical applications such as heterogeneous catalysis, semiconductors and energy conversion systems. Elucidation of the underlying processes would benefit greatly from an application of SER spectroscopy to non-coinage metals.
There have been efforts made to expand the applicability of SER spectroscopy in this respect. Among those, three different approaches can be distinguished. In the first approach, the surface roughness of these metals is increased by a factor of up to 200 via electrochemical roughening procedures as also applied in this work for silver electrodes [220]. The massively increased surface area allows binding of a significantly higher number of molecules and thus enables probing them under off-resonance conditions [226–230]. Admittedly, this approach represents no kind of SER spectroscopy since no surface enhancement is involved, but corresponds to surface Raman spectroscopy. Another approach exploits the weak surface enhancement effect of these metals, manifesting upon irradiation with soft to hard UV light [231, 232]. Tian *et al.* managed to obtain moderate signals by performing UV-SER spectroscopy in solution [220]. Possible drawback of this method is the high energetic light source, which may introduce side reactions and decomposition of probe molecules. In the third approach, a non-SER active material is deposited on a SER active support. The plasmons excited in the lower layer can induce SER activity in the outer layer, given that certain requirements are fulfilled. With this method, considerable SE can be gained [233].
There are different ways of generating such a bilayer composite of two materials with different electronic properties. Usually, the lower support is a highly SER active material such as silver or gold. The top layer can be deposited through various techniques. Vapor deposition and electrochemical deposition methods can be used, if the second layer should be another metal like Pt, Pd, Rh, Fe etc. In case the second layer is a composite like TiO_2 or SiO_2, standard nucleation techniques are applicable. The obtained signal intensities are different depending on the applied technique. For example, bimetallic devices generated via direct electrochemical deposition exhibit only moderate signal intensities of probes attached at the outer layer, while rough Ag coated with a thin TiO_2 by evaporation induced self-assembly (EISA) yielded comparably high signals also for thicker oxide layers.
Recently, Feng *et al* reported a method to fabricate bimetallic Au-Ag hybrid devices that exhibit only low intensity loss measured at the outer metal [233]. Here, a solid silver electrode is first roughened

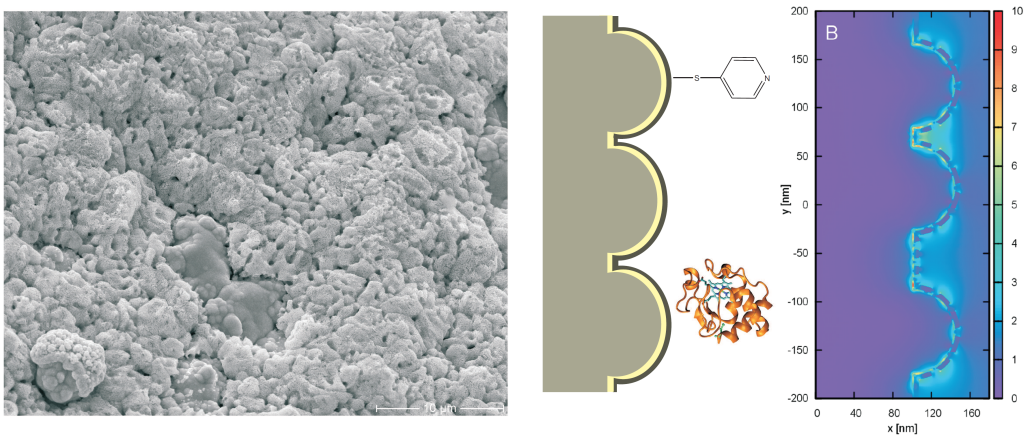

Figure 4.5: *Left*. SEM picture of a Pt island film on a rough Ag electrode. *Center*. Schematic representation of the hybrid device. The rough Ag electrode is depicted in grey. The yellow layer represents the dielectric spacer. The dark grey layer on top represents the deposited Pt film (here closed film). The probe molecules are mercaptopyridine and the protein cytochrome *c*. *Right*. Modeled Pt-Ag hybrid device (Pt island film with defects) in field calculations. The color code on the right displays the intensity of the near-field. Reprinted with kind permission from [118]. Copyright 2013 American Chemical Society.

to yield a SER active surface. Before depositing the top metal via metallation by electrochemical reduction from metal salts in solution, a dielectric spacer is coated on the lower layer. With this procedure, relatively high signal intensities of probe molecules on the outer metal layer can be obtained. Additionally, it could be shown that the outer metal kept its original electrochemical and chemical properties, which is crucial since the outer metal represents the platform for the surface-confined processes to be studied.
Inspired by these results, a similar method was employed to generate Pt-Ag hybrid devices (Figure 4.5). Pt was chosen due to its high relevance, especially in heterogeneous catalysis like CO conversion and hydrogen formation. The overall goal was to fabricate a solid support to probe adsorbed molecules on the Pt surface at different stages of a catalytic reaction. The device should provide high SER signal intensities and should be easy to handle and stable even at relatively high temperatures up to 500 °C.

In the final part of this thesis, the first results on the Pt-Ag hybrid device are reported. Here, the main focus lied on the overall signal performance, *i.e.* the relative enhancement factors obtained by using spacers of different kind and length. The experiments were supported by calculation. As a crucial point, it could be shown that films with defects facilitate high SER signal intensities while closed films tend to deplete SER activity. Intense SE(R)R signals of probe molecules, attached at the outer Pt layer, were obtained. The signals were only slightly weaker compared to signals of molecules directly adsorbed on the Ag. Although not included in the publication, first tentative experiments indicated that also good quality signals of CO and H_2, adsorbed on Pt, can be obtained.

5 Conclusions and Outlook

In this thesis, RR and SERR spectroscopy was successfully applied to investigate heme containing proteins. Aim of the studies was to obtain insights into the function and mechanism of these biomolecules. In particular, the heterogeneous electron transfer properties of horse heart cytochrome *c* and the electron transfer of outer membrane cytochromes embedded in biofilms of *Geobacter Sulfurreducens* were investigated using SERR and TR-SERR spectroscopy. Furthermore, RR spectroscopy was used to study the effects of nitration of tyrosines in human heart cytochrome *c* on the integrity of the heme site structure in order to estimate the effects of this posttranslational amino acid modification on the properties of the protein with respect to its role in the apoptosis. The results obtained in the individual subprojects provide novel insights into the biophysics of these proteins. In summary, it could be demonstrated that the different types of Raman spectroscopy constitute valuable techniques for investigating biological systems. The last part of the thesis was dedicated to the development of the SER methodology, aiming at expanding the technique to study processes on metal surfaces other than Ag or Au.

Electron Transfer Properties of Cytochrome *c* at Electrochemical Interfaces

The studies allowed disentangling the complex redox process of cytochrome *c* at electrochemical interfaces. It was shown that the heterogeneous ET of cytochrome *c* is a convolution of at least four different fundamental steps. These steps are electron tunneling coupled with the protein reorganization, protein surface dynamics and rearrangement of hydrogen bond networks at the interface and possibly also inside the protein. Moreover, it was found that the interfacial electric field is a crucial parameter that controls the overall ET process by affecting each single step. On the basis of that, it was possible to provide a qualitatively consistent picture of the interfacial ET process that explains present and previous findings. It is also concluded that electric fields may be of general relevance for interfacial processes in biology, beyond the ET of cytochrome *c*.
Although the findings represent a significant gain of knowledge about the interfacial ET, a detailed picture of this issue is far from being complete. In this respect, also a quantitative description of the ET process would be needed, which constitutes a challenging task and would require new experimental approaches and strategies. Finally, it would be interesting to move on from model systems, *i.e.* the adsorption on a SAM coated electrode, to natural reaction complexes and to study for example the ET transfer within the CcO/cytc complex, using the knowledge accumulated so far as a basis for the interpretation.

Tyrosine Nitrated Cytochrome *c*

It was shown that the Tyr to Phe substitution had less impact on the heme pocket but led to significant shifts of the redox potential of the $Fe^{2+/3+}$ transition, depending on the substituted tyrosine residue. These shifts were additive, indicating that there might be long-range electrostatic perturbation effects on the redox potential. The nitration of the remaining Tyr caused severe changes in the ligation pattern and led to formation of heme states in which the Fe-S(Met80) bond is broken. It was found that

a 5cHS and also a 6cLS species, where the Met80 is replaced by a Lys, are formed. Furthermore, no correlation between increased peroxidase activity and relative HS content could be identified, indicating that the increased H_2O_2 accessibility may be more important for the peroxidase activity than the vacant coordination sphere. Upon electrostatic immobilization on a SAM coated electrode, significant destabilizations of the heme pocket were noted for both the mono-Tyr and the nitrated proteins. In contrast to the situation in solution, a His-His 6cLS heme species was found. These findings indicate that the destabilizing effects caused by the interfacial electric field and by nitration of Tyr have different structural consequences, supporting the view that either nitration or binding to cardiolipin and possibly also both in concert are responsible for the alteration of the function of cytochrome *c*.
With regard to further possible Raman investigations of apoptotic cytochromes, cytochromes isolated from the cytosol of dying cells during different stages of apoptosis, should be investigated. These experiments would clarify which type of ligation the cytochromes exhibit after leaving the mitochondrium and if the alteration of the heme site, *i.e.* ligation pattern and electrostatics, is required for the apoptotic function of cytochrome *c* in the cytosol. Further possible investigations may also focus on other posttranslational tyrosine or protein modifications such as phosphated tyrosines or oxidized methonines.

Interfacial ET of Outer Membrane Cytochromes Embedded in Biofilms of *Geobacter*

The study reveals a first picture about the heterogeneous electron transfer of the surface confined heme proteins. Here, the Omcs located at the biofilm/electrode interface act as electron 'gates' and provide the electric connection between the biofilm and the electrode. The heterogeneous ET of these surface confined Omcs is relatively slow (0.03 s^{-1}) compared to the intramolecular ET with the first layer of redox partners located in the bulk biofilm (ca. 40 times faster), and therefore can be considered as the bottleneck process of the overall ET cascade. Furthermore, pure electron tunneling is most likely not the mechanism of electron transfer at the interface.
This study demonstrates the applicability of SERR and TR-SERR spectroscopy for investigating biofilms and other MFC systems. This constitutes a major progress since usual investigations of the biofilm activity and kinetics rely mainly on electrochemical methods, which are inherently insensitive to the nature of the probes. Future experiments using SERR spectroscopy may address particularly the interface reactions, aiming to identify the exact mechanism of the heterogeneous ET process, e.g. hopping or coupled ET. Also the SERR/TR-SERR spectroscopic approach could be applied to other bacteria strains, for example the metal reducing bacteria strains of *Shewanella*.

Surface Enhanced Raman Active materials - Pt Coated Ag Electrodes

The fabricated Pt-Ag hybrid device shows good SE(R)R performance for the probe molecules mercaptopyridine and cytochrome *c*. The coating with dielectric spacers effectively isolates the Ag support, blocking the direct adsorption of probe molecules on the Ag. Furthermore, it was found that the SER signal intensity did not depend on the nature of the outer metal and only weakly on the thickness of the dielectric layer. The crucial parameters are the enhancement of the Ag support and the kind of metal film at the outer layer. From electromagnetic field calculations it could be concluded that Pt island films that exhibit defects and holes, provide a significantly stronger induced surface enhancement at the outer layer and thus higher SER signal intensities. The first tests of the hybrid device for probing adsorbed CO and H_2 were promising, and good signals of the CO stretching and of the Pt-H stretching modes were observed.
Future studies may focus on the performance of the Pt-Ag hybrid device at high temperatures up to

800 K. Additionally, it would be desirable to replace the electro-deposition of Pt by another method, e.g. vapor deposition onto a patterned rough Ag surface, which would allow for more controlled design of the Pt surface structures.

Bibliography

[1] Leonardo da Vinci, Trattato della Pittura.

[2] Lord Rayleigh, Strutt, J. W. On the transmission of light through an atmosphere containing small particles in suspension, and on the origin of the blue of the sky. *Phil. Mag.* **1899**, 47, 375-394.

[3] Smekal, A. Zur Quantentheorie der Dispersion. *Die Naturwissenschaften* **1923**, 43, 873-875.

[4] Raman, C. V.; Krishnan, K. S. A. A New Type of Secondary Radiation. *Nature* **1928**, 121, 501-502.

[5] Raman, C. V.; Krishnan, K. S. A. A Change of Wave-Length in Light Scattering. *Nature* **1928**, 121, 619-620.

[6] Landsberg, G.; Mandelstam, L. Eine neue Erscheinung bei der Lichtzerstreuung in Krystallen. *Naturwissenschaften* **1928**, 16(57), p 772.

[7] Long, D. A. *Raman Spectroscopy*; McGraw Hill Higher Education Inc.: New York City, 1977.

[8] Long, D. A. *The Raman Effect*; John Wiley and Sons: New York, 2002.

[9] Placzek, G. *Quantenmechanik der Strahlung*; Akademische Verlagsgesellschaft mbH: Leipzig, 1934.

[10] Kramers, H. A.; Heisenberg, W. Über die Streuung von Strahlung durch Atome. *ZS. f. Phys.* **1925**, 31, 681-708.

[11] Dirac, P. M. A. The Quantum Theory of Absorption and Emission. *Proc. Roy. Soc. London* **1927**, 114, 243-265.

[12] Albrecht, A. C. Vibronic Calculations in Benzene. *J. Chem. Phys* **1960**, 33(1), 156-169.

[13] Albrecht, A. C. On the Theory of Raman Intensities. *J. Chem. Phys* **1961**, 34(5), 1476-1484.

[14] Tang, J.; Albrecht, A. C. Studies in Raman Intensity Theory. *J. Chem. Phys* **1968**, 49(3), 1144-1155.

[15] Fleischmann, M.; Hendra, P. J.; Mcquillan, A. J. Raman Spectra of Pyridine Adsorbed at a Silver Electrode. *Chem. Phys. Lett.* **1974**, 26(2), 163-166.

[16] Jeanmaire, D. L.; Van Duyne, R. P. Surface Raman Spectroelectrochemistry Part I. Heterocyclic, Aromatic, and Aliphatic Amines Adsorbed on the Anodized Silver Electrode. *J. Electroanal. Chem.* **1977**, 84, 1-20.

[17] Moskovits, M. Surface-enhanced spectroscopy. *Review of Modern Physics* **1985**, 57(3), 783-826.

[18] Kneipp, K.; Wang, Y.; Kneipp, H.; Itzkan, I.; Dasari, R. R.; Feld, M. S. Population Pumping of Excited Vibrational States by Spontaneous Surface-Enhanced Raman Scattering. *Phys. Rev. Let.* **1996**, 76, 2444-2447.

[19] Kneipp, K.; Wang, Y.; Kneipp, H.; Perelman, I.; Itzkan, R.; Dasari, R; Feld, M. S. Single Molecule Detection Using Surface-Enhanced Raman Scattering (SERS). *Phys. Rev. Lett.* **1997**, 78, 1667-1670.

[20] Kneipp, K.; Moskovitz, M.; Kneipp, H. *Surface-Enhanced Raman Scattering - Physics and Application*; Springer Verlag: Heidelberg, 2006.

[21] Nie, S.; Emory, S. R. Probing Single Molecules and Single Nanoparticles by Surface-Enhanced. Raman Scattering. *Science* **1997**, 275, 1102-1106.

[22] Paesler, M. A.; Moyer, P. J. *Near-field Optics: Theory, Instrumentation and Applications*; Wiley: New York, 1996.

[23] Jackson, J. B.; Halas, N. J. Surface-Enhanced Raman Scattering on Tunable Plasmonic Nanoparticle Substrates. *Proc. Natl. Acad. Sci. USA* **2004**, 101, 17930-17935.

[24] Moskovits, M. Surface roughness and the Enhanced Intensity of Raman Scattering by Molecules Adsorbed on Metals. *J. Chem. Phys.* **1978**, 69, 4159-4161.

[25] Kerker, M. Resonances in Electromagnetic Scattering by Objects with Negative Absorption. *Appl. Opt.* **1979**, 18, 1180-1189.

[26] Kerker, M.; Wang, S.; Chew, H. Surface Enhanced Raman Scattering (SERS) of Molecules Adsorbed at Spherical Particles. *Appl. Opt.* **1980**, 19, 4159-4174.

[27] Albrecht, M. G.; Creighton, J. A. Anomalously Intense Raman Spectra of Pyridine at a Silver Electrode. *J. Am. Chem. Soc.* **1977**, 99(15), 5215-5217.

[28] Moskovits, M. Surface-Enhanced Raman Spectroscopy: A Brief Retrospective. *J. Raman Spectrosc.* **2005**, 36(4), 241-250.

[29] Campion, A.; Kambhampati, P. Surface-Enhanced Raman Scattering. *Chem. Soc. Rev.* **1998**, 27(4), 241-250.

[30] Daniels, J. K.; Chumanov, G. Nanoparticle-Mirror Sandwich Substrates for Surface-Enhanced Raman Scattering. *J. Phys. Chem. B* **2005**, 109(38), 17936-17942.

[31] Cotton, T. M.; Kim, J.-H.; Holt, R. E. Surface-Enhanced Resonance Raman Scattering (SERRS) Spectroscopy: A Probe of Biomolecular Structure and Bonding at Surfaces. In *Advances in Biophysical Chemistry Vol. 2*; Bush, C. A., Ed.; London: JAI Press, 1992; 115-147.

[32] Creighton, J. A. Surface Raman Electromagnetic Enhancement Factors for Molecules at the Surface of Small Isolated Metal Spheres: The Determination of Adsorbate Orientation from SERS Relative Intensities. *Surf. Sci.* **1983**, 124, 209-219.

[33] Cao, P.; Yao, P. L.; Ren, B.; Gu, R.; Tian, Z. Q. Potential Dependence of the Orientation of Thiocyanate Adsorbed on an Iron Electrode as Probed by Surface-Enhanced Raman Spectroscopy. *J. Phys. Chem. B* **2002**, 106(29), 7283-7285.

[34] Jackson, J. D. *Electromagnetic Theory, 3rd. Ed.*; Wiley: New York, 1998.

[35] Hildebrandt, P.; Siebert, F. *Tutorials in Biophysics: Vibrational Spectroscopy in Life Science*; Wiley-VCH: Berlin, 2007.

[36] Taflove, A.; Hagness, S. C. *The Finite-Difference Time-Domain Method*; Artech House Inc.: Norwood, MA 2005.

[37] Yin, L.; Vlasko-Vlasov, V. K.; Rydh, A.; Pearson, J.; Welp, U.; Chang S.-H.; Gray, S. K.; Schatz, G. C.; Brown, D. E.; Kimball,C. W. Surface Plasmons at Single Nanoholes in Au Films. *Applied Physics Letters* **2004**, 85, 467-469.

[38] Murgida, D. H.; Hildebrandt, P. Redox and Redox Coupled Processes of Heme Proteins and Enzymes at Elektrochemical Interfaces. *Phys. Chem. Chem. Phys.* **2005**, 7(22), 3773-3784.

[39] Spiro, T. G. Resonance Raman Spectroscopy: A New Structure Probe for Biological Chromophores. *Acc. Chem. Rev.* **1974**, 7, 339-344.

[40] Wisitruangsakul, N.; Zebger, I; Ly, H. K.; Murgida, D. H.; Ekgasit, S.; Hildebrandt, P. Redox-linked Protein Dynamics of Cytochrome c Probed by Time-Resolved Surface Enhanced Infrared Absorption Spectroscopy. *Phys. Chem. Chem. Phys* **2008**, 10, 5267-5268.

[41] Hildebrandt, P.; Stockburger, M. Surface Enhanced Raman Spectroscopy of Rhodamine 6G Adsorbed on Collodial Silver. *J. Phys. Chem.* **1984**, 83, 5935-5944.

[42] Austin, J. C.; Zhao, Q.; Jordan, T.; Talalay, P.; Mildvan, A. S.; Spiro, T. G. Ultraviolet Resonance Raman Spectroscopy of Δ 5-3-ketosteroid Isomerase Revisited: Substrate Polarization by Active-Site Residues. *Biochemistry* **1995**, 34(13), 4441-4447.

[43] Vasanthi, J.; Spiro, T. G. Structure of a Third Cooperativity State of Hemoglobin: Ultraviolet Resonance Raman Spectroscopy of Cyanomethemoglobin Ligation Microstates. *Biochemistry* **1995**, 34(14), 4511-4515.

[44] Hildebrandt, P.; Czernuszewicz, R. S.; Grygon, C. A.; Spiro, T. G. Ultraviolet Resonance Raman Enhancement of the Carboxylate and Guanidinium Groups in Amino-Acids. *J. Raman Spec.* **1989**, 20(10), 645-650.

[45] Tian, Z. Q.; Ren, B.; Wu, D. Y. Surface-Enhanced Raman Scattering: From Noble to Transition Metals and from Rough Surfaces to Ordered Nanostructures. *J. Phys. Chem. B* **2002**, 106(37), 9463-9483.

[46] Sivanesan, A.; Kozuch, J.; Ly, H K.; Kalaivani, G.; Fischer, A.; Weidinger, I. M. Tailored Silica Coated Ag Nanoparticles for non-Invasive Surface Enhanced Raman Spectroscopy of Biomolecular Targets. *RSC Adv.* **2012**, 2, 805-808.

[47] Kuestner, B.; Gellner, M.; Schuetz, Schueppler, M. F.; Marx, A.; Stroebel, P; Adam, P.; Schmuck, C.; Schluecker, S. SERS Labels for Red Laser Excitation: Silica-Encapsulated SAMs on Tunable Gold/Silver Nanoshells. *Angw. Chem. Int. Ed.* **2010**, 48, 1950-1953.

[48] Qin, L. D.; Zou, S. L.; Xue, C.; Atkinson, A.; Schatz, G. C.; Mirkin, C. A. Designing, Fabricating, and Imaging Raman Hot Spots. *Proc. Natl. Acad. Sci. U.S.A* **2006**, 103, 13300-13303.

[49] Wei, W.; Li, S. Z.; Qin, L. D.; Xue, C.; Millstone, J. E.; Xu, X. Y.; Schatz, G. C.; Mirkin, C. A. Surface Plasmon-Mediated Energy Transfer in Heterogap Au-Ag Nanowires. *Nano Lett.* **2008**, 8, 3446-3449.

[50] Liz-Marzan, L. M.; Giersig, M.; Mulvaney, P. Synthesis of Nanosized Gold-Silica Core-Shell Particles. *Langmuir* **1996**, 12(18), 4329-4335.

[51] Murgida, D. H.; Hildebrandt, P. Disentangling Interfacial Redox Processes of Proteins by SERR spectroscopy. *Chem. Soc. Rev.* **2008** 37, 937-945.

[52] Albrecht, T. *Dynamik und Mechanismen der heterogenen Elektronentransferprozesse von synthetischen und natürlichen Hämproteinen*, PhD Thesis, TU Berlin, Berlin, 2003.

[53] Murgida, D. H.; Hildebrandt, P. Heterogeneous Electron Transfer of Cytochrome c on Coated Silver Electrodes. Electric Field Effects on Structure and Redox Potential. *J. Phys. Chem. B* **2001**, 105(8), 1578-1586.

[54] Murgida, D. H.; Hildebrandt, P. Active-Side Structure and Dynamics of Cytochrome c Immobilized on Self-Assembled Monolayers - A Time-Resolved Surface Enhanced Resonance Raman Spectroscopic Study. *Angew. Chem. Int. Ed.* **2001**, 40(1), 728-731.

[55] C. P. Smith, H. S. White, Theory of the Interfacial Potential Distribution and Reversible Voltammetric Response of Electrodes Coated with Electroactive Molecular Films. *Analytical Chemistry* **1992**, 64(20), 2398-2405.

[56] Smulevich, G.; Spiro, T. G. Surface Enhanced Raman Spectroscopic Evidence that Adsorption on Silver Particles Can Denature Heme Proteins. *J. Phys. Chem.* **1985**, 89(24), 5168-5173.

[57] Lenaz, G.; Milazzo, G. Bioelectrochemistry: Principles and Practice; Birkhäuser Verlag Basel: Basel, 1997.

[58] Bartlett, P. N. Bioelectrochemistry: Fundamentals, Experimental Techniques and Applications; Wiley: New York, 2008.

[59] Jianga, L.; Glidlea, A.; Griffitha, A.; McNeilb, C. J.; Cooper, J. M. Characterising the Formation of a Bioelectrochemical Interface at a Self-Assembled Monolayer Using X-ray Photoelectron Spectroscopy. *Bioelectroch. Bioener.* **1997**, 42(1), 15-23.

[60] Schreiber, F. Self-Assembled Monolayers: From Simple Model Systems to Biofunctionalized Interfaces. *Journal of Physics: Condensed Matter* **2004**, 16(28), 881-900.

[61] Love, J. C.; Estroff, L. A.; Kriebel, J. K.; Nuzzo, R. G.; Whitesides, G. M. Self-Assembled Monolayers of Thiolates on Metals as a form of Nanotechnology. *Chemical Reviews* **2005**, 105(4), 1103-1169.

[62] Park, E. S.; Boxer, S. G. Origins of the Sensitivity of Molecular Vibrations to Electric Fields: Carbonyl and Nitrosyl Stretches in Model Compounds and Proteins. *J. Phys. Chem. B* **2002**, 106(22), 5800-5806.

[63] Oklejas, V. ; Sjostrom, C.; Harris, J. M. Surface-Enhanced Raman Scattering Based Vibrational Stark Effect as a Spatial Probe of Interfacial Electric Fields in the Diffuse Double Layers. *J. Phys. Chem. B* **2003**, 107(31), 7788-7794.

[64] Oklejas, V. Harris, J. M. In-situ Investigation of Binary-Component Self-Assembled Monolayers: A SERS-based Spectroelectrochemical Study of the Effects of Monolayer Composition on the Interfacial Structure. *Langmuir* **2003**, 19(14), 5794-5801.

[65] Clarke, R. J. The Dipol Potential of Phospholipids Membranes and Methods for its Detection. *Adv. Coll. Int. Sci.* **2001**, 89, 263-281.

[66] Schwartz, D. K. Mechanisms and Kinetics of Self-Assembled Monolayer Formation. *Annu. Rev. Phys. Chem.* **2001**, 52, 107-137.

[67] Samanta, D.; Sarkar, A. Immobilization of Bio-macromolecules on Self-Assembled Aonolayers: Methods and Sensor Applications. *Chem. Soc. Rev.* **2011**, 40, 2567-2592.

[68] Smith, D. W.; Williams, R. J. P. The Spectra of Ferric Haems and Haemoproteins. *Structure and Bonding* **1970**, 4, 1-45.

[69] Messerschmidt, A.; Huber, R.; Wieghardt, K.; Poulos, T. *Handbock of Metalloproteins*; Wiley: New York, 2001.

[70] Ray, G. B.; Copeland, R. A.; Lee, C. P.; Spiro, T. G. Resonance Raman Evidence for Low-Spin Iron(2+) Heme a3 in Energized Cytochrome c Oxidase: Implications for the Inhibition of Oxygen Reduction. *Biochemistry* **1990**, 34(44), 14300-14303.

[71] Spiro, T. G.; Smulevich, G.; Su, C. Probin Protein Structure and Dynamics with Resonance Raman Spectroscopy: Cytochrome c Peroxidase and Hemoglobin. *Biochemistry* **1990**, 29(19), 4497-4508.

[72] Gouterman, M. Spectra of porphyrins. *J. Mol. Spectrosc.* **1961**, 6, 138-163.

[73] Dickerson, R. E.; Takano, T.; Eisenberg, D.; Kallain, O. B.; Samson, L.; Margolaish, E. Ferricytochrome c. I. General Features of the Horse and Bonito Proteins at 2.8 A resolution. *J. Biol. Chem.* **1971**, 246, 1511-1535.

[74] Spiro, T. G.; Strekas, T. C. Resonance Raman Spectra of Hemoglobin and Cytochrome c: Inverse Polarization and Vibronic scattering. *Proc. Natl. Acad. Sci. USA* **1972**, 69, 9, 2622-2626.

[75] Spiro, T. G.; Strekas, T. C. Resonance Raman Spectra of Heme Proteins. Effects of Oxidation and Spin State. *J. Am. Chem. Soc.* **1974**, 96(2), 338-345.

[76] Grochol, J. *Raman Spectroelectrochemical Investigations of Immobilized Redox Proteins*, PhD Thesis, TU Berlin, Berlin, 2007.

[77] Babcok, G. T. Raman Scattering by Cytochrome c Oxidase and by a Heme Model Compound. In *Biological Applications of Raman Spectroscopy*, Vol. III; Spiro, T. G., Ed.; Wiley: New York, 1988.

[78] Kitagawa, T.; Ozaki, Y. Infrared and Raman Spectra of Metalloporphyrins. *Struct. Bonding* **1987**, 64, 72-113.

[79] Spiro, T. G. The Resonance Raman Spectroscopy of Metalloporphyrins and Heme Proteins. In *Iron Porphyrins*, Vol. II; Lever, A. B. P., Gray, H. B., Eds.; Addison-Wesley: Reading, 1983.

[80] Copeland, R. A.; Spiro, T. G. Ultraviolet Resonance Raman Spectra of Cytochrome c Conformational States. *Biochemistry* **1985**, 24(18), 4960-4968.

[81] Abe, M; Kitagawa, T.; Kyogoku, Y. Resonance Raman Spectra of Octaethylporphyrinato-Ni(I) and meso-deuterated and 15N-substituted Derivatives. II. A Normal Coordinate Analysis. *J. Chem. Phys.* **1978**, 69, 4526-4534.

[82] Li, X.-Y.; Czernuszewicz, R. S.; Kincaid, J. R.; Spiro, T. G. Consistent Porphyrin Force Field. 3. Out-of-plane Modes in the Resonance Raman Spectra of Planar and Ruffled Nickel Octaethylporphyrin. *J. Am. Chem. Soc.* **1989**, 111, 7012-7023.

[83] Li, X.-Y.; Czernuszewicz, R. S.; Kincaid, J. R.; Su, Y. O.; Spiro, T. G. Consistent Porphyrin Force Field. 1. Normal Mode Analysis for Nickel Porphine and Nickel Tetraphenylporphine from Resonance Raman and Infrared Spectra and Isotope Shifts. *J. Phys. Chem.* **1990**, 94, 31-47.

[84] Kozlowski, P. M.; Rush III, T. S.; Jarzecki, A. A.; Zgierski, M. Z.; Chase, B.; Piffat, C.; Ye, B.-H.; Li, X.-Y.; Pulay, P.; Spiro, T. G. DFT-SQM Force Field for Ni Porphyrin: Intrinsic Ruffling. *J. Phys. Chem.* **1999**, 103, 1357-1366.

[85] Hu, S.; Morris, I. K.; Singh, J. P.; Smith, K. M.; Spiro, T. G. Complete Assignment of Cytochrome c Resonance Raman spectra via Enzymatic Reconstitution with Isotopically Labeled Enzymes. *J. Am. Chem. Soc.* **1993**, 115, 12446-12458.

[86] Hu, S.; Smith, K. M.; Spiro, T. G. Assignment of Protoheme Resonance Raman Spectrum by Heme Labeling in Myoglobin. *J. Am. Chem. Soc.* **1996**, 118, 12638-12646.

[87] Anzenbach, P.; Evangelista-Kirkup, R.; Schenkman, J.; Spiro, T. G. Influence of Thiolate Ligation on the Heme Electronic Structure in Microsomal Cytochrome P-450 and Model Compounds - Resonance Raman Spectroscopic Evidence. *Inorg. Chem.* **1989**, 50, 613-620.

[88] Hildebrandt, P. Resonance Raman Spectroscopy of Cytochrome P-450. In *Frontiers in Biotransformation*, Vol. VII; Ruckpaul, K., Rein, H., Eds.; Akademie-Verlag / VCH: Berlin / Weinheim 1992, 166-215.

[89] Scott, R. A.; Mauk, S. *Cytochrome c - A Multidisciplinary Approach*; University Science Books: Sausalito, CA, 1995.

[90] Oellerich, S.; Wackerbarth, H.; Hildebrandt, P. Conformational Equilibria and Dynamics of Cytochrome c Induced by Binding of Sodium Dodecyl Sulfate Monomers and Micelles. *Eur. Biophys.* **2003**, 32, 599-613.

[91] Oellerich, S.; Wackerbarth, H.; Hildebrandt, P. Spectroscopic Characterization of Nonnative Conformational States of Cytochrome c. *J. Phys. Chem. B* **2002**, 106, 6566-6580.

[92] Wackerbarth, H.; Murgida, D. H.; Oellerich, S.; Doepner, S.; Rivas, L.; Hildebrandt, P. Dynamics and Mechanism of the Electron Transfer Process of Cytochrome c Probed by Resonance Raman and Surface Enhanced Resonance Raman Spectroscopy. *J. Mol. Struct.* **2001**, 51, 563-564.

[93] Oellerich, S.; Lecomte, S.; Paternostre, M.; Heimburg, T.; Hildebrandt, P. Peripheral and Integral Binding of Cytochrome c to Phospholipids Vesicles. *J. Phys. Chem. B* **2004**, 108, 3871-3878.

[94] Basova, L. V.; Kurnikov, I. V.; Wang, L.; Ritov, V. N.; Belikova, N. A.; Vlasova, I. I.; Pacheco, A. A.; Winnica, D. E.; Peterson, J.; Bayir, H. Cardiolipin Switch in Mitochondria: Shutting off the Reduction of Cytochrome c and Turning on the Peroxidase Activity. *Biochemistry* **2007**, 46(11), 3423-3434.

[95] Yeh, S.-R.; Han, S.; Rousseau, D. L. Cytochrome c Folding and Unfolding: A Biphasic Mechanism. *Acc. Chem. Res.* **1998**, 31, 727-736.

[96] Theorell, H.; Akesson, A. Studies on Cytochrome c. *J. Am. Chem. Soc.* **1941**, 63, 1812-1818.

[97] Wilson, M. T.; Greenwood, C. The Alkaline Transitions in Ferricytochrome c. In *Cytochrome c: A multipdisciplinary Approach*. Scott, R. A., Mauk, A. G., Eds.; Univeristy Science Books: Sausolito, 1996.

[98] Smith, H. T.; Millet, F. Involvement of Lysinse-72 and -79 in the Alkaline Isomerization of Horse Heart Ferricytochrome c. *Biochemistry* **1980**, 19, 1117-1120.

[99] Pollock, W. B.; Rosell, F. I.; Twitchett, M. B., Dumont, M. E., Mauk, A. G. Bacterial Expression of a Mitochondrial Cytochrome c. Trimethylation of Lys72 in Yeast iso-1-Cytorchome c and the Alkaline Conformational Transitions. *Biochemistry* **1998**, 37, 6124-6131.

[100] Marcus, R. A. Theory of Oxidation-Reduction Reactions Involving Electron Transfer 1. *J. Chem. Phys.* **1956**, 24(5), 966-978.

[101] Marcus, R. A. Chemical and Electrochemical Electron-Transfer Theory. *Annu. Rev. Phys. Chem.* **1964**, 15, 155-196.

[102] Marcus, R. A. Electron Transfer in Chemistry - Theory and experiment. *J. Electroanal. Chem.* **1997**, 438(1-2), 251-259.

[103] Marcus, R. A.; Stutin, N. Electron Transfer in Chemistry and Biology., *Biochim. Biophys. Acta* **1985**, 811(3), 265-322.

[104] Newton, M. D.; Sutin, N. Electron Transfer Reactions in Condensed Phases. *Annu. Rev. Phys. Chem.* **1984**, 35, 437-448.

[105] Miller, J. R.; Beitz, J. V.; Huddleston, R. K. Effect of Free Energy on Rates of Electron Transfer Between Molecules. *J. Am. Chem. Soc.* **1984**, 106(18), 5057-5068.

[106] Closs, G. L.; Calacterra, L. T.; Green, N. J.; Penfield, N. W.; Miller, J. R. Distance, Stereoelectronic Effects, and the Marcus Inverted Region in Intramolecular Electron Transfer in Organic Radical Anions. *J. Phys. Chem.* **1986**, 90(16), 3673-3683.

[107] Hush, N. S. Adiabatic Theory of Outer Sphere Electron Transfer Reactions in Solution. *Trans. Faraday Soc.* **1961**, 57, 557-580.

[108] Jortner, J. Temperature Dependent Activation Energy for Electron Transfer between Biological Molecules. *J. Chem. Phys.* **1976**, 64(12), 4860-4867.

[109] Kestner, N. R.; Logan, J.; Jortner, J. Thermal Electron Transfer Reactions in Polar Solvents. *J. Chem. Phys* **1974**, 78(219), 2148-2166.

[110] Ulstrup, J.; Jortner, J. The effect of Intramolecular Quantum Modes on Free Energy Relationships for Electron Transfer Reactions. *J. Chem. Phys* **1975**, 63(10), 4358-4368.

[111] Levich, V. G.; Dogonadze, R. R. Theory of non-Radiative Electron Transitions in Solution from Ion to Ion. *Doklady Akademii Nauk Sssr* **1959**, 129(1), 123-126.

[112] Ulstrup, J.; Kuznetsov, A. M. *Electron Transfer in Chemistry and Biology - An Introduction to the Theory*; Wiley&Sons: New York City, 1998.

[113] C. E. D., Chidsey, Free Energy and Temperature Dependence of Electron Transfer at Metal-Electrolyte Interface. *Science* **1991**, 251, 919-922.

[114] T. M. Nahir, E. F. Bowden, The Distribution of Standard Rate Constants for Electron Transfer between Thiol-Modified Gold Electrodes and Adsorbed Cytochrome c. *J. Electroanal. Chem.* **1996**, 401(1), 9-13.

[115] T. M. Nahir, R. A. Clark, E. F. Bowden, Linear Sweep Voltammetry of Irreversible Electron Transfer in Surface Confined Species Using the Marcus Theory. *Anal. Chem.* **1994**, 66(15), 2595-2598.

[116] Hildebrandt, P.; Macor, K. A.; Czernuszewicz, R. S. Novel Cylindrical Rotating Electrode for Anaerobic Surface-Enhanced Raman Spectroscopy. *J. Raman Spectrosc.* **1988**, 53, 65-69.

[117] Wackerbarth, H.; Klar, U.; Gunther, W.; Hildebrandt, P. Novel Time-Resolved Surface-Enhanced (Resonance) Raman Spectroscopic Technique for Studying the Dynamics of Interfacial Processes: Application to the Electron Transfer Reaction of Cytochrome c at a Silver Electrode. *Appl. Spectrosc.* **1999**, 53, 283-291.

[118] Ly, H. K.; Köhler, C.; Fischer, A.; Kabuss, J.; Schlosser, F.; Schoth, M.; Knorr, A.; Weidinger, I.M. Induced Surface Enhancement in Coral Pt Island Films attached to nanostrucutred Ag electrodes. *Langmuir* **2012**, dx.doi.org/10.1021/la205139g.

[119] Ly, H. K. Spektroelektrochemische Untersuchungen von Redoxproteinen, Diploma Thesis; Technische Universität Berlin, Berlin: 2007.

[120] Fitch, W. M. The Molecular Evolution of Cytochrome c in Eukaryotes. *J. Mol. Evolution* **1976**, 8(1), 13-40.

[121] Moore, G. R.; Pettigrew, G. W. *Cytochrome C: Evolutionary, Structural and Physicochemical Aspects (Springer Series in Molecular Biology)*; Springer-Verlag: Heidelberg, 1991.

[122] Bushnell, G. W.; Louie, G. V.; Brayer, G. D. High-Resolution Three-Dimensional Structure of Horse Heart Cytochrome c. *J. Mol. Biology* **1990**, 213(2), 585-595.

[123] Takano, T.; Dickerson, R. E. Conformation Change of Cytochrome c. II. Ferricytochrome c Refinement at 1.8 A and Comparison with the Ferrocytochrome Structure. *J. Mol. Biol.* **1981**, 153(1), 95-115.

[124] Takano, T.; Dickerson, R. E. Conformation Change of Cytochrome c. I. Ferrocytochrome c Structure Refined at 1.5 A Resolution. *J. Mol. Biology* **1981**, 153(1), 79-94.

[125] Takano, T.; Dickerson, R. E. Redox Conformation Changes in Refined Tuna Cytochrome c. *Proc. Natl. Acad. Sci.* **1980**, 77(11), 6371-6375.

[126] Banci, L.; Bertini, I.; Rosato, A.; Varani, G. Mitochondrial Cytochromes c: A Comparative Analysis *J. Biol. Inorg. Chem.* **1999**, 4(6), 824-837.

[127] Winkler, J.; Gray, H. B. Electron Transfer in Ruthenium-modified Proteins. *Chem. Rev.* **1992**, 92, 369-379.

[128] Koppenol, W. H.; Margoliash, E. The Asymmetric Distribution of Charges on the Surface of Horse Heart Cytochrome c. Functional Implications. *J. Biol. chem.* **1982**, 257(8), 4426-4437.

[129] Feng, J.-J.; Murgida, D. H.; Kuhlmann, U.; Utesch, T.; Mroginski, M. A.; Hildebrandt, P.; Weidinger, I. M. Gated Electron Transfer of Yeast Iso-1 Cytochrome c on Self-Assembled Monolayer Coated Electrodes. *J. Phys. Chem. B* **2008**, 112(47), 15202-15211

[130] Staudenmayer, N.; Ng, S.; Smith, M. B.; Millet, F. Effects of Specific Trifluoroacetylation of Individual Cytochrome c Lysines on the Reaction with Cytochrome c Oxidase. *Biochemistry* **1977**, 16, 600-604.

[131] Witt, H.; Zickermann, V.; Ludwig, B. Site-directed Mmutagenesis of Cytochrome c Oxidase Reveals two Acidic Residues Involved in the Binding of Cytochrome c. *Biochim. Biophys. Acta* **1995**, 1, 74-76.

[132] Avila, A.; Gregory, B. W.; Niki, K.; Cotton, T. M. An Electrochemical Approach to Investigate Gated Electron Transfer using Aphysiological Model System: Cytochrome c Immobilized on Carboxylic Acid-terminated Alkanethiol Self-Assembled Monolayers on Gold Electrodes. *J. Phys. Chem. B* **2000**, 104, 2759-2766.

[133] Azzaroni, Q.; Vela, M. E.; Andreasen, G.; Carro, P.; Varezza, R. C. Electrodesorption Potentials of Self-Assembled Alkanethiolate Monolayers on Ag(111) and Au(111). An Electrochemical Scanning Tunneling Microscopy and Density Functional Theory. *J. Phys. Chem. B* **2002**, 106(47), 12267-12273.

[134] Laviron, E. General Expression of the Linear Potential Sweep Voltammogram in the Case of Diffusionless Electrochemical Systems. *J. Electroanal. Chem.* **1979**, 101, 19-28.

[135] Feng, Z. Q.; Imabayashi, S.; Kakiuchi, T.; Niki, K. Long-range Electron-transfer Reaction-rates to Cytochrome-c Across Long-chain and Short-chain Alkanethiol Self-Assembled Monolayers - Electroreflectance Studies. *J. Chem. Soc., Faraday Trans.* **1997**, 93, 1367-1370.

[136] Becka, A. M.; Miller, C. J. Electrochemistry at ω-hydroxy Thiol Coated Electrodes. Voltage Independence of the Electron Tunneling Barrier and Measurements of Redox Kinetics at Large Overpotentials. *J. Phys. Chem.* **1992**, 96(6), 2657-2668.

[137] Finklea, H. O.; Hanshew, D. D. Electron-Transfer Kinetics in Organized Thiol Monolayers with Attached Pentaammine(pyridine)ruthenium Redox Centers. *J. Am. Chem. Soc.* **1992**, 114, 3173-3181.

[138] Smalley, J. F.; Feldberg, S. W.; Chidsey, C. E.; Limford, M. R.; Newton, M. D.; Liu, Y. P. The Kinetics of Electron Transfer through Ferrocene-terminated Alkanethiol Monolayers on Gold. "*J. Phys. Chem.* **1995**, 99, 13141-13149.

[139] Xu, J.; Li, H. L.; Zhang, Y. J. Relationship between Electronic Tunneling Coefficient and Electrode Potential Investigated by using Self-Assembled Alkanethiol Monolayers on Gold Electrodes. *J. Phys. Chem.* **1993**, 97, 11497-11500.

[140] Finklea, H. O. In *Electroanalytical Chemistry*; Bard, A. J., Rubinstein, I., Eds.; Dekker: New York, 1996, Vol. 19, 110-335.

[141] Murgida, D. H.; Hildebrandt, P. Heterogeneous Electron Transfer of Cytochrome c on Coated Silver Electrodes. Electric Field Effects on Structure and Redox Potential. *J. Phys. Chem. B* **2001**, 105, 1578-1586.

[142] Murgida, D. H.; Hildebrandt, P. Active-site Structure and Dynamics of Cytochrome c Immobilized on Self-Assembled Monolayers - A Time-Resolved Surface Enhanced rResonance Raman Spectroscopic Study *Angew. Chem. Int. Ed.* **2001**, 113(4), 751-754.

[143] Chi, Q. J.; Zhang, J. D.; Andersen, J. E. T.; Ulstrup, J. Ordered Assembly and Controlled Electron Transfer of the Blue Copper Protein Azurin at Gold (111) Single-crystal Substrates. *J. Phys. Chem. B* **2001**, 105(20), 4669-4679.

[144] Fujita, K.; Nakamura, N.; Ohno, H.; Leigh, B. S.; Niki, K.; Gray, H. B.; Richards, J. H. Mimicking Protein-Protein Electron Transfer: Voltammerty of Pseudomonas Aeruginosa Azurin and the Thermus Thermophilus Cu-A Domain at omega-derivated Self-Assembled-Monolayer Gold Electrodes. *J. Am. Chem. Soc.* **2004**, 126(43), 13954-13961.

[145] Kranich, A.; De La Rosa, M.; Murgida, D. H.; Hildebrandt, P. *unpublished work.*

[146] Wei, J. J.; Liu, H. Y.; Dick, A. R.; Yamamoto, H.; He, Y. F.; Waldeck, D. H. Direct Wiring of Cytochrome c's Heme Unit to an Electrode: Electrochemical Studies. *J. Am. Chem. Soc* **2002**, 124(32), 9591-9599.

[147] Lecomte, S.; Hildebrandt, P.; Soulimane, T. Dynamics of the Heterogeneous Electron-transfer Reaction of Cytochrome c(552) from Thermus Thermophilus. A Time-Resolved Surface-Enhanced Resonance Raman Spectroscopic Study. *J. Phys. Chem. B* **1999**, 103(45), 10053-10064.

[148] Kasmi, A. E.; Wallace, J. M.; Bowden, E. F.; Binet, S. M.; Linderman, J. R. Controlling Interfacial Electron-Transfer Kinetics of Cytochrome c with Mixed Self-Assembled Monolayers. *J. Am. Chem. Soc.* **1998**, 120, 225-226.

[149] Wei J. J.; Liu, H.Y.; Khoshtariya, D. E.; Yamamoto, H.; Dick, A.; Waldeck, D. H. Electron-Transfer Dynamics of Cytochrome C: A Change in the Reaction Mechanism with Distance. *Angew. Chem. Int. Ed.* **2002**, 41, 4700-4703.

[150] Murgida, D. H.; Hildebrandt, P. Proton Coupled Electron Transfer of Cytochrome c. *J. Am. Chem. Soc.* **2001**, 123, 4062-4068.

[151] Rivas, L.; Marti, M.; Hildebrandt, P.; Murgida, D. M. *unpublished work*.

[152] Wackerbarth, H.; Hildebrandt, P. Redox and Conformational Equilibria and Dynamics of Cytochrome c at High Electric Fields. *ChemPhysChem* **2003**, 4, 714-724.

[153] Khoshtariya, D. E.; Wei, J. J.; Liu, H. Y.; Yue, H. J.; Waldeck, D. H. Charge-transfer mechanism for cytochrome c adsorbed on nanometer thick films. Disthinguishing frictional control from conformational gating. *J. Am. Chem. Soc.* **2003**, 125(25), 7704-7714.

[154] Wei, J. J.; Liu, H. Y.; Khoshtariya, D. E.; Yue, H. J.; Dick, A. R.; Waldeck, D.H. Electron-Transfer Dynamics of Cytochrome c: A Change in the Reaction Mechanism with Distance. *Angew. Chem., Int. Ed.* **2002**, 41, 4700-4703.

[155] Wei, J. J.; Liu, H.; Dick, A. R.; Yamamoto, H.; He, Y.; Waldeck, D. H. Direct Wiring of Cytochrome c's Heme Unit to an Electrode: Electrochemical Studies. *J. Am. Chem. Soc.* **2002**, 124(32), 9591-9599.

[156] Dolidze, T. D.; Khoshtariya, D. E.; Waldeck, D. H.; Macyk, J.; van Eldik, R. Positive Activation Volume for a Cytochrome C Electrode Process: Evidence for a Protein Friction Mechanism from High-Pressure Studies. *J. Phys. Chem. B* **2003**, 107, 7172-7176.

[157] Yue, H.; Khoshtariya, D.; Waldeck, D. H.; Grochol, J.; Hildebrandt, P.; Murgida, D. H. On the Electron Transfer Mechanism Between Cytochrome c and Metal Electrodes. Evidence for Dynamic Control at Short Distances. *J. Phys. Chem. B* **2006**, 40, 110, 19906-19913.

[158] Kranich, A.; Ly, H. K.; Hildebrandt, P.; Murgida, D. M. Direct Observation of the Gating Step in Protein Electron Transfer: Electric-Field-controlled Protein Dynamics. *J. Am. Chem. Soc.* **2008**, 130, 9844-9848.

[159] Zhou, J.; Zheng, J.; Jiang, S. Molecular Simulation Studies of Orientation and Conformation of Cytochrome c Adsorbed on Self-Assembled Monolayers. *J. Phys. Chem. B* **2004**, 108, 17418-17423.

[160] Jiang, X.; Wang, X. Cytochrome c-mediated apoptosis. *Annu. Rev. Biochem.* **2004**, 73, 87-106.

[161] Ow, Y.-L.; Green, D. R.; Hao, Z.; Mak, T. W. Cytochrome c: Functions beyond Respiration. *Nature Reviews* **2008**, 9, 532-542.

[162] Riedl, S. J. Salvesen, G. S. The Apoptosome: Signalling Platform of Cell Death. *Nature Rev. Mol. Cell Biol.* **2007**, 8, 405-413.

[163] Kluck, R. M.; Bossy-Wetzel, E.; Green, D. R.; Newmeyer, D. D. The Release of Cytochrome c from Mitochondria: A Primary Site for Bcl-2 Regulation of Apoptosis. *Science* **1997**, 275, 1132-1136.

[164] Yang, J. *et al.* Prevention of Apoptosis by Bcl-2: Release of Cytochrome c from Mitochondria Blocked. *Science* **1997**, 275, 1129-1132.

[165] Liu, X. S.; Kim, C. N.; Yang, J.; Jemmerson, R.; Wang, X. Induction of Apoptotic Program in Cell-free Extracts: Requirement for dATP and Cytochrome c. *Cell* **1996**, 86, 147-157.

[166] Zou, H.; Henzel, W. J.; Liu, X. S.; Lutschg, A.; Wang, X. D. Apaf-1, A Human Protein Homologous to C. elegans CED-4, Participates in Cytochrome c-dependent Activation of Caspase-3. *Cell* **1997**, 90, 405-413.

[167] Ott, M.; Zhivotovsky, B; Orrenius, S. Role of Cardiolipin in Cytochrome c Celease from Mitochondria. *Cell Death Differ.* **2007**, 14, 1243-1247.

[168] Gonzalvez, F.; Gottlieb, E. Cardiolipin: Setting the Beat of Apoptosis. *Apoptosis* **2007**, 12, 877-885.

[169] Kagan, V. E.; Tyurin, V. A.; Jiang, J.; Tyurina, Y. Y.; Ritov, V. B.; Amoscato, A. A.; Osipov, A. N.; Belikova, N. A.; Kapralov, A. A.; Kini, V.; Vlasova, I. I.; Zhao, Q.; Zou, M.; Di, P.; Svistunenko, D. A.; Kurnikov, I. V.; Borisenko, G. G. Cytochrome c Acts as a Cardiolipin Oxygenase Required for Release of Proapoptotic Factors. *Nature Chem. Biol.* **2005**, 4, 223-232.

[170] Belikova, N. A.; Vladimorov, Y. A.; Osipov, A. N.; Kapralov, A. A.; Tyurin, V. A.; Potapovich, M. V.; Basova, L. V.; Peterson, J.; Kurnikov, I. V.; Kagan, V. E. Peroxidase Activity and Structural Transitions of Cytochrome c Bound to Cardiolipin-containing Membranes. *Biochemistry* **2006**, 45, 4998-5009.

[171] Kagan, V. E.; Bayir, A.; Bayir, H.; Stoyanovsky, D.; Borisenko, G. G.; Tyurina, Y. Y.; Wipf, P.; Atkinson, J.; Greenberger, J. S.; Chapkin, R. S.; Belikova, N. A. Mitochondria-targeted Disruptors and Inhibitors of Cytochrome c/Cardiolipin Peroxidase Complexes: A New Strategy in anti-Apoptotic Drug Discovery. *Mol. Nutr. Food Res.* **2009**, 53, 104-114.

[172] Balakrishnan, G.; Hu, Y.; Oyerinde, F. O.; Su, J.; Groves, J. T.; Spiro, T. G. A Conformatioanl Switch to β-sheet Structure in Cytochrome *c* Leads to Heme Exposure. Implications for Cardiolipin Peroxdiation and Apoptosis. *J. Am. Chem. Soc.* **2006**, 129, 504-505.

[173] Ly, H. K.; Sezer, M.; Wisitruangsakul, N.; Feng, J. J.; Kranich, A., Millo, D.; Weidinger, I. M.; Zebger, I.; Murgida, D. H.; Hildebrandt, P. Surface-Enhanced Vibrational Spectroscopy for Probing Transient Interactions of Proteins with Biomimetic Interfaces: Electric Field Effects on Structure, Dynamics and Function of Cytochrome c. *FEBS* **2011**, 278, 1382-1390.

[174] Kluck, R. M. *et al.* Cytochrome *c* Activation of CPP32-like Proteolysis Plays a Critical Role in a Xenopus Cell-free Apoptosis System. *EMBO J.* **1997**, 16, 4639-4649.

[175] Borutaite, V.; Brown, G. C. Mitochondrial Regulation of Caspase Activation by Cytochrome Oxidase and Tetramethylphenylenediamine via Cytosolic Cytochrome *c* Redox State. *J. Biol. Chem.* **2007**, 282, 31124-31130.

[176] Schonhoff, C. M.; Gaston, B.; Mannick, J. B. Nitrosylation of Cytochrome *c* During Apoptosis. *J. Biol. Chem.* **2003**, 278, 18265-18270.

[177] Jang, B.; Han, S. Biochemical Properties of Cytochrome c Nitrated by Peroxynitrite. *Biochimie* **2005**, 88, 53-58.

[178] García-Heredia, J. M.; Díaz-Moreno, I.; Díaz-Quintana, A.; Orzáez, M.; Navarro, J.A.; Hervás, M.; De la Rosa, M. A. Specific Nitration of Tyrosines 46 and 48 Makes Cytochrome c Assemble a non-functional Apoptosome. *FEBS Lett.* **2012**, 586, 154-158.

[179] Abriata, L. A.; Cassina, A.; Tórtora, V.; Marín, M.; Souza, J. M.; Castro, L.; Vila, A. J.; Radi, R. Nitration of Solvent-Exposed Tyrosine 74 on Cytochrome c Triggers Heme Iron-methionine 80 Dond Disruption. Nuclear Magnetic Resonance and Optical Spectroscopy Studies. *J. Biol. Chem.* **2009**, 284, 17-26.

[180] Díaz-Moreno, I.; García-Heredia, J. M.; Díaz-Quintana, A.; Teixeira, M.; De la Rosa, M. A. Nitration of Tyrosines 46 and 48 Induces the Specific Degradation of Cytochrome c Upon Change of the Heme Iron State to High-Spin. *Biochim. Biophys. Acta* **2011**, 1807, 1616-1623.

[181] Lovley, D. R. Organic Matter Mineralization with the Reduction of Ferric Iron: A Review. *Geomicrobiol. J.* **1987**, 5, 375-399.

[182] Lovley, D. R. Dissimilatory metal reduction. *Annu. Rev. Microbiol.* **1993**, 47, 263-290.

[183] Lonergan, D. J.; Jenter, H. L.; Coates, J. D.; Phillips, E. J.; Schmidt, T. M.; Lovley, D. R. (1996). Phylogenetic Analysis of Dissimilatory Fe(III)-Reducing Bacteria. *J. Bacteriol.* **1996**, 178, 2402-2408.

[184] Logan, B. E.; Hamelers, B.; Rozendal, R. A.; Schrörder, U.; Keller, J.; Freguia, S.; Aelterman, P.; Verstraete, W.; Rabaey, K. Microbial Fuel Cells: Methodology and Technology. *Environ. Sci. Technol.* **2006**, 40, 5181-5192.

[185] Rozendal, R. A.; Hamelers, H. V. M.; Rabaey, K.; Keller, J.; Buisman, C. J. N. Towards Practical Implementation of Bioelectrochemical Wastewater Treatment. *Trends Biotechnol.* **2008**, 26, 450-459.

[186] Lovley, D. R. and Phillips, E. J. Novel Mode of Microbial Energy Metabolism: Organic Carbon Oxidation Coupled to Dissimilatory Reduction of Iron or Manganese. *Appl. Environ. Microbiol. 1988*, 54, 1472-1480.

[187] Lovley, D. R. and Phillips, E. J. Requirement for a Microbial Consortium to Completely Oxidize Glucose in Fe(III)-Reducing Sediments. *Appl. Environ. Microbiol.* **1989**, 55, 3234-3236.

[188] Lovley, D. R. and Lonergan, D. J. Anaerobic Oxidation of Toluene, Phenol, and p-Cresol by the Dissimilatory Iron-Reducing Organism, GS-15. *Appl. Environ. Microbiol.* **1990**, 56, 1858-1864.

[189] Zhang, T.; Gannon, S. M.; Nevin, K. P.; Franks, A. E.; Lovley, D. R. Stimulating the Anaerobic Degradation of Aromatic Hydrocarbons in Contaminated Sediments by Providing an Electrode as the Electron Acceptor. *Environ. Microbiol.* **2010**, 12, 1011-1020.

[190] Phillips, E. J.; Lovley, D. R.; Roden, E. E. Composition of non-microbially Reducible Fe(III) in Aquatic Sediments. *Appl. Environ. Microbiol.* **1993** 59, 2727-2729.

[191] Lovley, D. R.; Phillips, E. J.; Gorby, Y. A.; Landa, E. R. Microbial Reduction of Uranium. *Nature* **1991** 350, 413-416.

[192] Lovley, D. R. Dissimilatory Fe(III) and Mn(IV) Reduction. *Microbiol. Rev.* **1991** 55, 259-287.

[193] Lovley, D. R.; Holmes, D. E.; Nevin, K. P. Dissimilatory Fe(III) and Mn (IV) Reduction. *Adv. Microb. Physiol.* **2004** 49, 219-286.

[194] Lovley, D. R. Geobacter: The Microbe Electric's Physiology, Ecology, and Practical Applications. In *Advances in Microbial Physiology*; Poole, R. K., Ed.; Elsevier, Academic Press: Amsterdam, The Netherlands, 2011.

[195] Richter, H.; McCarthy, K.; Nevin, K. P.; Johnson, J. P.; Rotello, M. V.; Lovley, D. R. Electricity Generation by Geobacter sulfurreducens Attached to Gold Electrodes. *Langmuir* **2008**, 24 (8), 4376-4379.

[196] Rabaey, K.; Rodriguez, J.; Blackall, L. L.; Keller, J.; Gross , P.; Batstone, D.; Verstraete, W.; Nealson, K. H. Microbial Ecology Meets Electrochemistry: Electricity-Driven and Driving Communities. *Isme J.* **2007**, 1, 9-18.

[197] Schröder, U. Discover the Possibilities: Microbial Bioelectrochemical Systems and the Revival of a 100-year-old Discovery. *J. Solid State Electrochem.* **2011**, 15, 1481-1486.

[198] Gaspard, S.; Vazquez, F.; Holliger, C. Localization and Solubilization of the Iron(III) Reductase of Geobacter Sulfurreducens. *Appl. Environ. Microbiol.* **1998**, 64, 3188-3194.

[199] Leang, C.; Coppi, M. V.; Lovley, D. R. OmcB, a *c*-type Polyheme cytochrome, Involved in Fe(III) Reduction in Geobacter Sulfurreducens. *J. Bacteriol.* **2003**, 185, 2096-2103.

[200] www.geobacter.org/nanowires, Copyright by the *University of Massachusetts Amherst*.

[201] Reguera, G.; McCarthy, K. D.; Mehta, T.; Nicoll, J. S.; Tuominen, M. T.; Lovley, D. R. Extracellular Electron Transfer via Microbial Nanowires. *Nature* **2005**, 435(23), 1098-1101.

[202] Qian, X.; Mester, T.; Morgado, L.; Arakawa, T.; Sharma, M. L.; Inoue, K.; Joseph, C.; Salgueiro, C. A.; Maroney, M. J.; Lovley, D. R. Biochemical Characterization of Purified OmcS, a *c*-type Cytochrome Required for Insoluble Fe(III) Reduction in *Geobacter sulfurreducens*. *Biochim. Biophys. Acta* **2011** 1807, 404-412.

[203] Inoue, K.; Leang, C.; Franks, A. E.; Woodard, T. L.; Nevin, K. P.; Lovley, D. R. Specific Localization of the c-type Cytochrome OmcZ at the Anode Surface in Current-Producing Biofilms of Geobacter Sulfurreducens. *Environ. Microbiol.* **2011** Rep. 3, 211-217.

[204] Reguera, G.; Nevin, K. P.; Nicoll, J. S.; Covalla, S. F.; Woodard, T. L.; Lovley, D. R. Biofilm and Nanowire Production Leads to Increased Current in Geobacter Sulfurreducens Fuel Cells. *Appl. Environ. Microbiol.* **2006** 72, 7345-7348.

[205] Strycharz-Glaven, S. M.; Snider, R. M.; Guiseppi-Elie, A.; Tender, L. M. On Electrical Conductivity of Microbial Nanowires and Biofilms. *Energy Environ. Sci.* **2011**, 4, 4366.

[206] Malvankar, N. S.; Tuominen, M. T.; Lovley, D. R. Comment on "'On Electrical Conductivity of Microbial Nanowires and Biofilms"' by S. M. Strycharz-Glaven, R. M. Snider, A. Guiseppi-Elie and L. M. Tender, Energy Environ. Sci., 2011, 4, 4366. *Energy Environ. Sci.* **2012**, 5, 6247-6249.

[207] Klimes, A.; Franks, A. E.; Glaven, R. H.; Tran, H.; Barrett, C. L.; Qiu, Y.; Zengler, K.; Lovley, D. R. Production of Pilus-like Filaments in Geobacter Sulfurreducens in the Absence of the Type IV Pilin Protein PilA. *FEMS Microbiol. Lett.* **2010**, 310, 62-68.

[208] Malvankar, N. S.; Vargas, M.; Nevin, K. P.; Franks, A. E.; Leang, C.; Kim, B.-C.; Inoue, K.; Mester, T.; Covalla, S. F.; Johnson, J. P.; Rotello, V. M.; Tuominen, M. et al. Tunable Metallic-like Conductivity in Microbial Nanowires Networks. *Nat. Nanotechnol.* **2011** 6, 573-579.

[209] Fricke, K.; Harnisch, F.; Schröder, U. On the use of Cyclic Voltammetry for the Study of Anodic Electron Transfer in Microbial Fuel Cells. *Energy Environ. Sci.* **2008**, 1, 144-147.

[210] Millo, D.; Harnisch, F.; Patil, S. A.; Ly, H. K.; Schröder, U.; Hildebrandt, P. In situ Spectroelectrochemcial Investigation of electrocatalytic microbial biofilms by surface-enhanced resonance raman spectroscopy. *Angew. Chem. Int. Ed.* **2011**, 123(11), 2673-2675.

[211] Strycharz, S. M.; Malanoski, A. P.; Snider, R. M.; Yi, H.; Lovley, D. R.; Tender, L. M. Application of Cyclic Voltammetry to Investigate Enhanced Catalytic Current Generation by Biofilm-modified Anodes of Geobacter Sulfurreducens Strain DL1 vs. Variant Strain KN400. *Energy Environ. Sci.* **2011**, 4, 896-913.

[212] Ledesma, G. A.; Murgida D. H.; Ly, H. K.; Wackerbarth, H.; Ulstrup, J.; Costa-Filho, A. J.; Vila, A. J. The Met Axial Ligand Determines the Redox Potential in CuA Sites. *J. Amer. Chem. Soc. Comm.* **2007**, 129(39), 11884-11885.

[213] Millo, D. Spectroelectrochemical analysis of microbial biofilms. to be published in *Biochemical Society Transactions*, 2012.

[214] van der Sneppen, L.; Gooijer, C.; Ubachs, W.; Ariese, F. Evanescent-wave Cavity Ring-down Detection of Cytochrome c on Surface-modified Prisms. *Sensor Actuat. B-Chem.* **2009**, 139, 505-510.

[215] Nakamura. R.; Ishii, K.; Hashimoto, K. Electronic Absorption Spectra and Redox Properties of c Type Cytochromes in Living Bacteria. *Angew. Chem. Int. Ed.* **2009**, 48, 1606-1608.

[216] Okamoto, A.; Nakamura, R.; Ishii, K.; Hashimoto, K. In vivo Electrochemistry of c-type Cytochromes-mediated Electron Transfer with Chemical Marking. *ChemBioChem* **2009**, 10, 2329-2332.

[217] Jain, A.; Gazzola, G.; Panzera, A.; Zanoni, M.; Marsili, E. Visible Spectroelectrochemical Characterization of Geobacter Sulfurreducens Biofilms on Optically Transparent Indium Tin Oxide Electrode. *Electrochim. Acta* **2011**, 56, 10776-10785.

[218] Shibanuma, T.; Nakamura, R.; Hirakawa, Y.; Hashimoto, K.; Ishii, K. Observation of in vivo Cytochromes-based Electron Transport Dynamics using Time-Resolved Evanescent Wave Electroabsorption Spectroscopy. *Angew. Chem. Int. Ed.* **2011**, 123, 9303-9306.

[219] Bhavya Sharma, Renee R. Frontiera, Anne-Isabelle Henry, Emilie Ringe, and Richard P. Van Duyne. SERS: Materials, Applications, and the Future. *Materials Today* **2012**, 15, 16-26.

[220] Tian, Z. Q.; Yang, Z. L.; Ren, B.; Wu, D. Y. SERS From Transition Metals and Excited by Ultraviolett Light. In *Surface Enhance Raman Scattering, Physics and Application*; Kneipp, K., Moskovitz, M., Kneipp, H., Eds.; Springer: Heidelberg, 2006.

[221] Cline, M. P.; Barber, P. W.; Chang, R. K.; Surface-enhanced Electric Intensities on Transition- and Noble-metal Spheroids *J. Opt. Soc. Am. B* **1986**, 3, 15-21.

[222] Messinger, B. J.; von Raben, K. U.; Chang, R. K.; Barber, P. W. Local Fields at the Surface of Noble-metal Microspheres. *Phys. Rev. B* **1981**, 24, 649-657.

[223] Ebert, H. Magneto-optical Effects in Transition Metal Systems. *Rep. Prog. Phys.* **1996**, 59, 1665-1735.

[224] Weaver, J. H. Optical Properties of Rh, Pd, Ir, and Pt. *Phys. Rev. B* **1975**, 11, 1416-1425.

[225] Ordal, M. A.; Bell, R. J.; Alexander, W.; Long, L. L.; Querry, M. R. Optical Properties of Fourteen Metals in the Infrared and far Infrared: Al, Co, Cu, Au, Fe, Pb, Mo, Ni, Pd, Pt, Ag, Ti, V, and W. *Appl. Opt.* **1985**, 24, 4493-4499.

[226] Tian, Z. Q.; Ren, B. Adsorption and Reaction at Electrochemical Interfaces as Probed by Surface-Enhanced Raman Spectroscopy. *Ann. Rev. Phys. Chem.* **2004**, 55, pp 197-299.

[227] Tian, Z. Q.; Ren, B.; Wu, Y. Surface-Enhanced Raman Scattering: From Noble to Transition Metals and from Rough Surfaces to Ordered Nanostructures. *J. Phys. Chem. B* **2002**, 106, 9463-9483.

[228] Tian, Z. Q.; Gao, J. S.; Li, Q.; Ren, B.; Huang, Q. J. Cai, W. B.; Liu, F. M.; Mao, B. W. Can Surface Raman Spectroscopy be a General Technique for Surface Science and Electrochemistry. *J. Raman Spectrosc.* **1998**, 29, 703-711.

[229] Tian, Z. Q.; Ren, B.; Mao, B. W. Extending Surface Raman Spectroscopy to Transition Metals for Practical Applications I. Vibrational Properties of SCN- and CO Adsorbed on Electrochemical Acitivated Pt Surfaces. *J. Phys. Chem.* **1997**, 101, pp. 1338-1346.

[230] Cai, W. B.; Ren, B.; Li, Q.; She, X.; Liu, F. M.; Cai, X. W.; Tian, Z. Q. Investigation of Surface-Enhanced Raman Sscattering from Platinum Electrodes Using A Confocal Raman Microscope: Dependence of Surface Roughening Pretreatment. *Surf. Sci.* **1998**, 406, 9-22.

[231] Ren, B.; Lin, X. F.; Yang, Z. L.; Aroca, R. F.; Mao, B. W.; Tian, Z. Q. Surface-Enhanced Raman Scattering in the Ultraviolet Spectral Region: UV-SERS on Rhodium and Ruthenium Electrodes. *J. Am. Chem. Soc.* **2003**, 125, 9598-9599.

[232] Lin, X. F.; Ren, B.; Yang, Z. L.; Liu, G. K.; Tian, Z. Q. Surface-Enhanced Raman Spectroscopy with Ultraviolet Excitation. *J. Raman Spectrosc.* **2005**, 36, 606-612.

[233] Feng, J. J.; Gernert, U.; Sezer, M.; Kuhlmann, U.; Murgida, D. H.; David, C.; Richter, M.; Knorr, A.; Hildebrandt, P.; Weidinger, I. M. Novel Au-Ag Hybrid Device for Electrochemical SE(R)R Spectroscopy in a Wide Potential and Spectral Range. *Nano Lett.* **2009**, 9(1), 298-303.

6

Thermal Fluctuations Determine the Electron-Transfer Rates of Cytochrome *c* in Electrostatic and Covalent Complexes

Ly, H. K.; Marti, M. A.; Martin, D. F.; Alvarez-Paggi, D.; Meister, W.; Kranich, A.; Weidinger, I. M.; Hildebrandt, P.; Murgida, D. M. Thermal Fluctuations Determine the Electron-Transfer Rates of Cytochrome c in Electrostatic and Covalent Complexes. *ChemPhysChem* **2010**, 11(6), 1225–1235.

DOI: 10.1002/cphc.200900966

Thermal Fluctuations Determine the Electron-Transfer Rates of Cytochrome c in Electrostatic and Covalent Complexes

Hoang Khoa Ly,[a] Marcelo A. Marti,[b] Diego F. Martin,[b] Damian Alvarez-Paggi,[b] Wiebke Meister,[a] Anja Kranich,[a] Inez M. Weidinger,[a] Peter Hildebrandt,*[a] and Daniel H. Murgida*[b]

The heterogeneous electron-transfer (ET) reaction of cytochrome c (Cyt-c) electrostatically or covalently immobilized on electrodes coated with self-assembled monolayers (SAMs) of ω-functionalized alkanethiols is analyzed by surface-enhanced resonance Raman (SERR) spectroscopy and molecular dynamics (MD) simulations. Electrostatically bound Cyt-c on pure carboxyl-terminated and mixed carboxyl/hydroxyl-terminated SAMs reveals the same distance dependence of the rate constants, that is, electron tunneling at long distances and a regime controlled by the protein orientational distribution and dynamics that leads to a nearly distance-independent rate constant at short distances. Qualitatively, the same behavior is found for covalently bound Cyt-c, although the apparent ET rates in the plateau region are lower since protein mobility is restricted due to formation of amide bonds between the protein and the SAM. The experimental findings are consistent with the results of MD simulations indicating that thermal fluctuations of the protein and interfacial solvent molecules can effectively modulate the electron tunneling probability.

1. Introduction

Direct electrochemistry of redox metalloproteins immobilized on electrodes coated with biocompatible or biomimetic films is an active field of fundamental and applied research. On the one hand, electrochemical and spectroelectrochemical methods can afford a great deal of information on the electron-transfer (ET) mechanisms and dynamics of the anchored protein that can contribute to the understanding of its functioning in vivo.[1–3] For instance, protein dynamics has been recently recognized as a key factor in controlling or limiting inter- and intraprotein ET reactions.[4–15] However, in most cases the complexity of the systems impairs direct observations of conformational gating, configurational fluctuations, or rearrangement of protein complexes under reactive conditions. In this context, the combination of suitable spectroelectrochemical techniques with simplified model systems, such as proteins immobilized on biomimetic electrodes, can greatly contribute to the elucidation of the biophysical fundamentals in better detail. On the other hand, the knowledge gained from these studies is essential for the rational design of protein-based technological devices such as biosensors and biofuel cells.[16–18]

The most widely used electrode coatings are self-assembled monolayers (SAMs) of single or mixed alkanethiols containing ω-functional groups that are chosen according to the protein's surface properties.[2,3] One of the specific advantages of this approach is to facilitate the determination of ET rate constants k_{ET} as a function of distance by simply varying the chain length of the thiols, as first shown by Chidsey.[19] In principle, the heterogeneous ET reaction for such systems is expected to follow a nonadiabatic mechanism, and thus its rate can be described in terms of the high-temperature limit of the semiclassical Marcus expression, integrated to account for all the electronic levels ε of the metal electrode contributing to the process [Eq. (1)]:[20]

$$k_{ET} = \frac{\pi}{\hbar}\frac{|V|^2\rho}{\sqrt{\pi\lambda k_B T}} \int_{-\infty}^{\infty} \exp\left[-\left(\frac{(\lambda + (\varepsilon_F - \varepsilon) + e\eta)^2}{4\lambda k_B T}\right)\right] \frac{1}{1+\exp[(\varepsilon-\varepsilon_F)/k_B T]}\,d\varepsilon \quad (1)$$

where $\rho(\varepsilon)$ is the density of electronic states in the electrode, and ε_F the energy of the Fermi level. The applied overpotential,

[a] H. K. Ly,[+] W. Meister, Dr. A. Kranich, Dr. I. M. Weidinger, Prof. P. Hildebrandt
Technische Universität Berlin, Institut für Chemie
Str. des 17. Juni 135, Sekr. PC14, Berlin (Germany)
Fax: (+49) 30-31421122
E-mail: hildebrandt@chem.tu-berlin.de

[b] Dr. M. A. Marti,[+] D. F. Martin,[+] D. Alvarez-Paggi, Prof. D. H. Murgida
Departamento de Química Inorgánica, Analítica y
Química Física INQUIMAE-CONICET
Facultad de Ciencias Exactas y Naturales
Universidad de Buenos Aires, Ciudad Universitaria
Pab. 2, piso 1, C1428EHA Buenos Aires (Argentina)
Fax: (+54) 11-4576-3341
E-mail: dhmurgida@qi.fcen.uba.ar

[+] These authors made equal contributions to this work and are thus listed in alphabetical order.

Supporting information for this article is available on the WWW under http://dx.doi.org/10.1002/cphc.200900966.

reorganization energy, and magnitude of the electronic coupling are denoted by η, λ, and $|V|$, respectively. The remaining parameters have the usual meaning. Equation (1) can be expressed in a simplified form by approximating the Fermi distribution law as a step function [Eq. (2)]:

$$k_{ET} \approx \frac{\pi}{\hbar}|V|^2 \rho \ \mathrm{erfc}\left(\frac{\lambda + e\eta}{\sqrt{4\lambda k_B T}}\right) \quad (2)$$

where erfc(z) is the complementary error function.

The electronic coupling $|V|$ decays exponentially with increasing separation of the redox center from the electrode, and therefore Equations (1) and (2) predict an exponential distance dependence of k_{ET}, that is, decreasing rate with increasing chain length of the alkanethiols. This prediction has been verified for a variety of redox proteins immobilized on different types of SAM-coated electrodes, including Cu_A centers, azurin, iso-cytochrome c and cytochromes *c*, c_6, and b_{562}, among others.[21–26] The average tunneling decay parameter β obtained for the different proteins is about 1.1 per methylene group of the thiols.

A common feature encountered for all cases studied so far is that the exponential variation of the apparent ET rate constant k_{ET}^{app} is only verified when the proteins are attached to relatively long chain tethers, usually containing nine or more methylene groups. In contrast, for thinner SAMs, k_{ET}^{app} becomes distance-independent, thus suggesting a change of the reaction mechanism. This "unusual" distance dependence has been most extensively studied for mammalian cytochrome c (Cyt-c) by several groups employing different approaches. Most of the work refers to Cyt-c electrostatically adsorbed to electrodes coated with SAMs including ω-carboxyl alkanethiols.[23,27–34] In addition, Waldeck and co-workers have studied the ET kinetics of Cyt-c coordinatively bound to electrodes coated with mixed SAMs in which one of the thiol components contained a tail group able to bind to the heme iron atom by displacing the native axial ligand Met80.[23,35–38] Both modes of immobilization yield a qualitatively similar "unusual" distance dependence of k_{ET}^{app}, although values for coordinative binding are higher due to the artificially improved electron-transfer pathway. Furthermore, in both cases the ET rates in the plateau region of the k_{ET}^{app} versus distance plots depend on the viscosity of the solution, which has been discussed controversially. Niki et al. proposed a gated mechanism based on a two-state model, in which the thermodynamically stable electrostatic complex Cyt-c/SAM represents an unfavorable configuration for ET such that protein reorientation is required to generate the electrochemically active state.[23,32] The model assumes that the rate of reorientation is distance-independent, while electron tunneling rates vary exponentially. Therefore, at sufficiently short chain lengths reorientation becomes rate-limiting and k_{ET}^{app} reaches a plateau. In contrast, based on studies of coordinatively bound Cyt-c, Waldeck et al. proposed a change from the nonadiabatic regime at long distances to the friction-controlled (adiabatic) regime at short distances,[38] which in principle could also apply to electrostatic Cyt-c/SAM complexes. Time-resolved surface-enhanced resonance Raman (TRSERR) spectroeletrochemical experiments showed that coordinative Cyt-c/SAM complexes exhibit a pronounced overpotential dependence of k_{ET}^{app} in the plateau region with a reorganization energy of 0.58 eV, and thus support the friction model.[35] For electrostatic complexes, instead, k_{ET}^{app} is nearly independent of the applied overpotential in the plateau region, and thereby points to a process other than ET that becomes rate-limiting at short distances.[3] By using Q-band excitation TRSERR[27,30] and molecular dynamics (MD) simulations,[27,39] we have provided the first direct evidence that this gating mechanism is related to protein reorientation in search of efficient electron pathways. The resulting model, however, differs from that originally proposed by Niki et al., since reorientation rates have been found to be modulated by the interfacial electric field, which in turn varies with the chain length of the SAMs. Moreover, we have shown, both experimentally[2,3,40] and theoretically,[41] that electric fields of the magnitude estimated for short SAMs as well as for biological interfaces, are able to modulate not only the ET dynamics but also the structure and function of the protein. These findings support the hypothesis that the transmembrane potential in mitochondria may regulate the ET-driven proton-pumping activity of cytochrome *c* oxidase (CcO) through electric field dependent interprotein ET from Cyt-c to CcO. Furthermore, the interfacial electric field may constitute the switch for the transition from the redox to the apoptotic function of Cyt-c.

In a recent electrochemical study, Davis et al. reported that the ET kinetics of Cyt-c cross-linked to mixed SAMs composed of COOH- and OH-terminated alkanethiols exhibits identical distance dependence to electrostatic complexes with the same SAMs, and is qualitatively similar to that of electrostatic complexes with pure ω-carboxyl alkanethiol SAMs.[42] Since covalent attachment is expected to restrict protein mobility, these results cast some doubts on the general validity of the electric field dependent protein-dynamics model proposed previously.[2,30]

The present work is dedicated to elucidating this contradiction. Using TRSERR and MD simulations we have performed a comparative study of the ET properties of Cyt-c in electrostatic and covalent SAM/Cyt-c complexes with single-component and mixed SAMs. The results suggest that in all cases the ET rates are modulated by low-amplitude motions of the protein and thermal fluctuations of interfacial water molecules, which in turn are influenced by the interfacial electric field.

2. Results and Discussion

2.1. Structural and Redox Equilibria of the Immobilized Protein

Nanostructured Ag electrodes were coated with SAMs of different compositions for subsequent immobilization of horse heart Cyt-c. The different films include single-component SAMs of 6-mercaptohexanoic acid (C5-COOH) and of 11-mercaptoundecanoic acid (C10-COOH), as well as mixed SAMs of 1:1 mixtures of C5-COOH/6-mercaptohexan-1-ol (C5-COOH/C6-OH) and of C10-COOH/11-mercaptoundecan-1-ol (C10-COOH/C11-OH). All experiments were carried out at pH 7.0 such that the SAMs ex-

hibited a negatively charged surface due to partial dissociation of the carboxylic acid tail groups, thereby allowing the positively charged Cyt-c to bind electrostatically, as reflected by the strong and characteristic SERR signals. The SERR spectra of ferrous Cyt-c adsorbed on the different SAMs, recorded upon Soret-band excitation, are identical to the corresponding resonance Raman (RR) spectrum in solution, that is, the structure of the heme pocket is preserved upon adsorption. Furthermore, the sensitive response of the spectra to the applied electrode potential indicates that Cyt-c undergoes direct electrochemistry in all of the SAM/Cyt-c electrostatic complexes investigated, in agreement with previous findings.[2,3] Within the potential range from −400 mV to about 50 mV (vs. Ag/AgCl), all SERR spectra can be quantitatively described by a superposition of the RR spectra of the native state of Cyt-c (denoted as state B1), with variable contributions of the reduced and oxidized forms (Figure 1). The relative contributions of the component spectra of reduced and oxidized forms obtained in this way were converted to relative surface concentrations by using proportionality factors determined by RR spectroscopy of the pure species in solution.[43] The resultant potential-dependent changes of the relative concentrations were then analyzed in terms of the Nernst equation for determining the standard reduction potentials E°. As summarized in Table 1, Cyt-c electrostatically adsorbed to the different SAMs exhibits nearly ideal Nernst behavior with E° values slightly more negative than determined for Cyt-c in solution. These negative shifts can be ascribed to the potential drop across the SAMs.[40]

The SERR spectra recorded at very negative potentials reveal a small contribution (<5%) of native but redox-inactive species which are attributed to proteins immobilized with orientations of very weak electronic coupling (Figure 2).[27,39] For electrode potentials above 50 mV, the component analysis of the SERR spectra reveals small contributions of the so-called B2 species of Cyt-c (Figure 2), in which the Met-80 axial ligand is removed from the heme iron atom to give five-coordinate high-spin heme species. This species is in equilibrium with a non-native six-coordinate low-spin form in which the Met-80 ligand is replaced by a His residue.[3,40] This structural transition to the B2 state is only observed for the ferric protein, whereas upon reduction the B1 form is recovered.

Cyt-c was covalently attached to the various SAMs described above by using two different cross-linking reagents and procedures (A and B; see Experimental Section) that are expected to yield differently oriented samples. In both cases the final step consists of removal of the residual physisorbed Cyt-c by thorough washing with buffered KCl solutions. The desorption procedure was optimized by monitoring the SERR signal as a function of time after dipping the Cyt-c-loaded electrodes into KCl solutions of different concentrations (Figure 3). Accordingly, immersion of the electrodes in 2 M KCl solution for 15 min, followed by gentle rinsing with the buffer solution, was found to remove 95% of the physisorbed species from the electrode surface. This protocol was applied to the electrode loaded with Cyt-c immobilized by covalent cross-linking such that the contribution of electrostatically bound Cyt-c to the resultant SERR spectra was always negligibly small. Treatment with a sulfate-containing solution of the same ionic strength did not cause complete desorption of the physisorbed proteins.

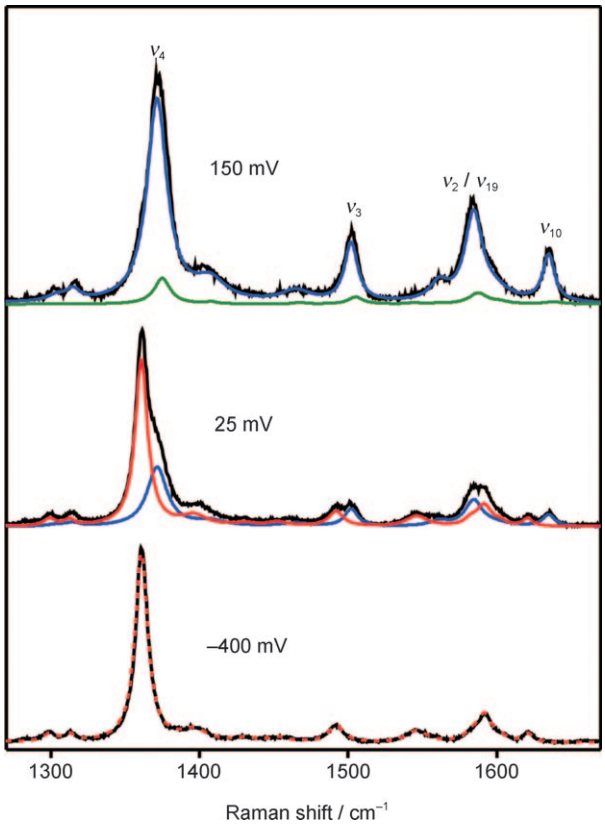

Figure 1. Soret-band SERR spectra measured at various potentials for Cyt-c electrostatically adsorbed on a Ag electrode coated with a 1:1 C10-COOH/C11-OH SAM. The experimental spectra are given by the black lines, whereas the component spectra of the oxidized B1, the reduced B1, and the oxidized B2 states are represented by the blue, red, and green lines, respectively.

Table 1. Thermodynamic and kinetic parameters obtained by SERR for Cyt-c in electrostatic and covalent complexes with different SAMs. Kinetic constants for C10 and C5 SAMs refer to potential jumps from 41 to −200 mV and from 50 to −50 mV, respectively.

SAM	Electrostatic binding				Covalent binding[a]			
	C5-X		C10-X		C5-X		C10-X	
tail group (X)	CO_2H	CO_2H/CH_2OH	CO_2H	CO_2H/CH_2OH	CO_2H	CO_2H/CH_2OH	CO_2H	CO_2H/CH_2OH
E^0 [mV]	15±5	19±3	20±2	21±2	6±5	21±5	3±5	18±4
n	0.8	0.9	0.9	0.9	0.6	0.5	0.6	0.5
k_{redox} [s^{-1}][b]	220±20	113±10	160±20	170±20	120±25	125±10	125±30	120±20
$^{b}k_{orient}$ [s^{-1}][c]	250±25	170±40	400±100	250±50	n.d.[d]	n.d.[d]	n.d.[d]	n.d.[d]

[a] Covalent complexes prepared according to procedure A. [b] Determined by TRSERR with Soret-band excitation. [c] Determined by TRSERR with Q-band excitation; [d] n.d. = not determined

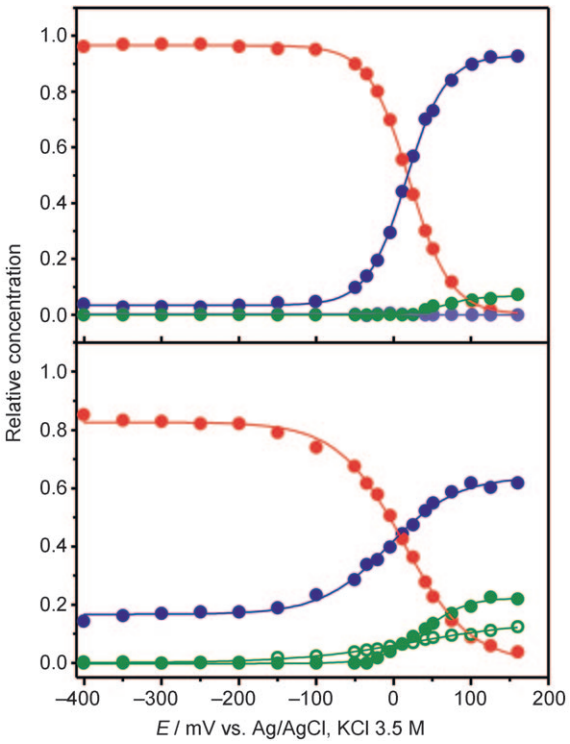

Figure 2. Relative concentrations of the different states of Cyt-c electrostatically (top) and covalently bound (bottom) to C10-COOH/C11-OH SAMs, as determined from Soret-band SERR spectra recorded as a function of the applied potential. The solid blue, red, green, and the open green symbols refer to the oxidized B1, the reduced B1, the oxidized B2(6cLS), and the oxidized B2(5cHS) states, respectively.

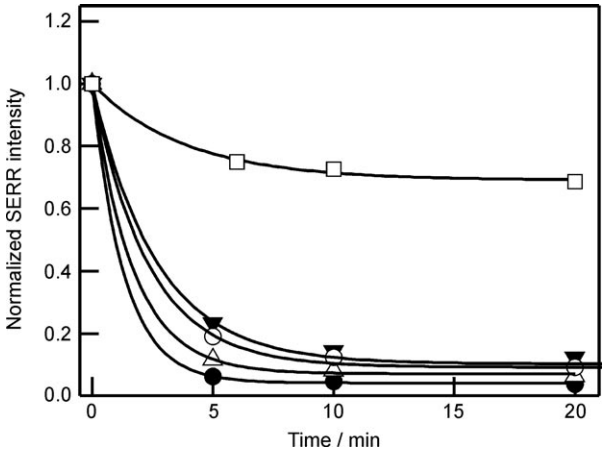

Figure 3. Normalized SERR intensities of the ν_4 band of reduced Cyt-c (B1) as a function of the time of immersion in KCl solution of different concentrations after immobilization by procedure A. Concentrations of KCl: 0.2 M (open squares), 1.0 M (filled black triangles), 2.0 M (open circles), 3.0 M (open triangles), saturated solution (filled black circles).

Potential-dependent SERR spectra of Cyt-c covalently attached to the various SAMs were measured in the potential range from −400 to 50 mV, and their analysis in terms of different contributions of the ferric and ferrous forms of state B1 indicated that the chemical immobilization procedure does not affect the structure of the redox center. However, about 10–15% of the bound protein could not be reduced even at the most negative potentials used (Figure 2). We ascribe this observation to the nonspecificity of the coupling reaction, which in principle can lead to Cyt-c binding through any of the 11 lysine residues on the protein surface, so that a subpopulation of protein molecules that are not able to establish efficient electron pathways to the electrode results. Accordingly, Nernst plots of covalently attached Cyt-c deviate from ideality with a number of transferred electrons of 0.5–0.6 and slightly more negative reduction potentials than observed for electrostatic adsorption (Table 1 and Figure 2). As in the case of electrostatic adsorption, SERR spectra indicate the formation of small amounts of B2 species for potentials above 50 mV.

2.2. Orientation of the Immobilized Protein

For symmetric molecules, the surface-enhanced Raman (SER) spectrum includes information about the orientation with respect to the surface,[44] because for modes of different symmetry the individual components of the scattering tensor are modified to different extents depending on their relative orientation with respect to the electric field vector. As a consequence, vibrational modes of different symmetry may experience different enhancements. In the specific case of the heme group which, in a first approximation, has D_{4h} symmetry, it can be shown that the totally symmetric A_{1g} modes will experience preferential enhancement when the heme plane is parallel to the surface, while for a perpendicular orientation the A_{1g} modes as well as the nontotally symmetric A_{2g}, B_{1g}, and B_{2g} modes will be enhanced to the same extent.[30] Therefore, different orientations of the adsorbed heme protein are expected to lead to different intensity ratios of modes of different symmetries, for example, $\nu_{10}(B_{1g})/\nu_4(A_{1g})$. This is strictly true only under nonresonant excitation conditions which, however, would imply the loss of selectivity in probing the cofactor spectrum. A reasonable compromise between an acceptable molecular resonance enhancement and qualitatively predictable selection rules may be achieved upon excitation close to the weak Q bands of the heme group. This approach was previously used to monitor orientational changes of Cyt-c electrostatically adsorbed on electrodes coated with single-component SAMs of ω-carboxyl alkanethiols.[27,30] In that work, it was shown that the orientation of the protein in the SAM/Cyt-c electrostatic complexes is dependent on the electric field and thus varies with the chain length of the ω-carboxyl alkanethiol and the applied electrode potential. Use of this method in the present study indicated that dilution of the carboxyl-terminated thiols by addition of ω-hydroxyl alkanethiols does not have a significant impact on the average orientation of Cyt-c electrostatically adsorbed on the SAMs. Both the absolute $\nu_{10}(B_{1g})/\nu_4(A_{1g})$ ratios and their dependence on potential are very similar to those of the pure carboxyl-terminated SAMs (Figure 4). Similar to single-component SAMs,[27,30] the $\nu_{10}(B_{1g})/\nu_4(A_{1g})$ ratios decrease for the longer SAMs, which is consistent with the proposed electric-field dependence of the orientation and indicates a more perpendicular average orientation of the

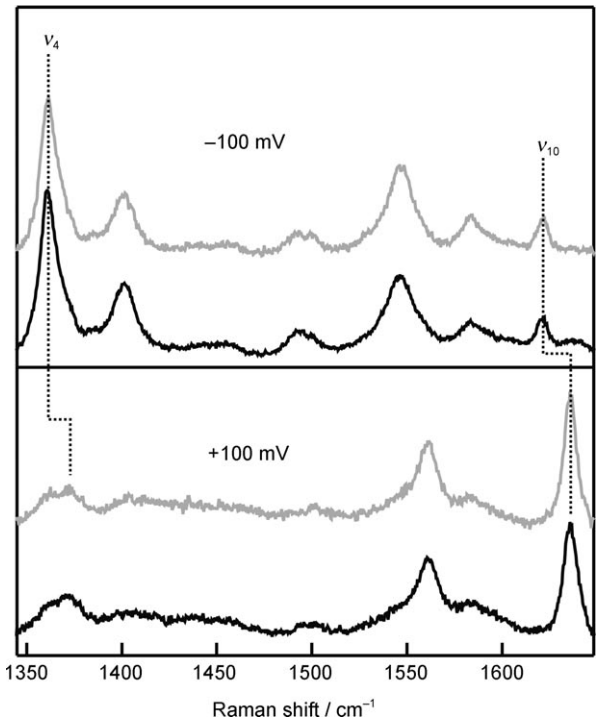

Figure 4. Q-band SERR spectra of Cyt-c in electrostatic complexes with C5-COOH (black) and C5-COOH/C6-OH (gray) SAMs recorded at −0.1 (top) and +0.1 V (bottom).

heme group with respect to the electrode surface for shorter SAMs, that is, at higher electric fields.

Upon covalent binding of the protein to the SAMs by using cross-linking procedure A, the $\nu_{10}(B_{1g})/\nu_4(A_{1g})$ intensity ratio drops with respect to the corresponding electrostatic complexes by factors of about 2 and 1.3 for the shorter and longer SAMs, respectively. These results indicate that, in the covalent complexes, ferric Cyt-c is oriented with the heme group less perpendicular to the surface than upon electrostatic binding. At first sight, a different average orientation of the electrostatically bound and the covalently attached Cyt-c may be surprising, since protocol A for covalent cross-linking is based on electrostatic pre-adsorption of the protein to the SAM. However, the lysine residues directly interacting with the carboxyl functions of the SAM are less accessible for the cross-linker EDC, such that amide bond formation may be favored for adjacent lysine residues. Furthermore, these steric constraints may lead to a less homogeneous average orientation of the covalently bound Cyt-c, which is consistent with the broad redox transitions (see above). It appears that covalent attachment according to procedure A lowers the stability of the protein. When the electrode potential is set to $E > E^0$, slow and partially irreversible transition to the B2 or a B2-like state is observed with time constants on the order of seconds or minutes even for thick C11-SAMs (see Supporting Information, Figure S1). Such a transition has not been noted for Cyt-c electrostatically bound to SAMs of the same thickness. Covalent attachment of Cyt-c by procedure A does not inhibit reorientation of the protein, as demonstrated by the dependence of the $\nu_{10}(B_{1g})/\nu_4(A_{1g})$ intensity ratio on potential, although the variation with potential is weaker than for electrostatically bound Cyt-c (Figure 5). The situation is different when Cyt-c is covalently attached by cross-linking procedure B. Here, the average orientation of the heme group with respect to the electrode surface appears to be even less perpendicular and, in contrast to covalent immobilization by procedure A, it is independent of the applied potential (Figure 5).

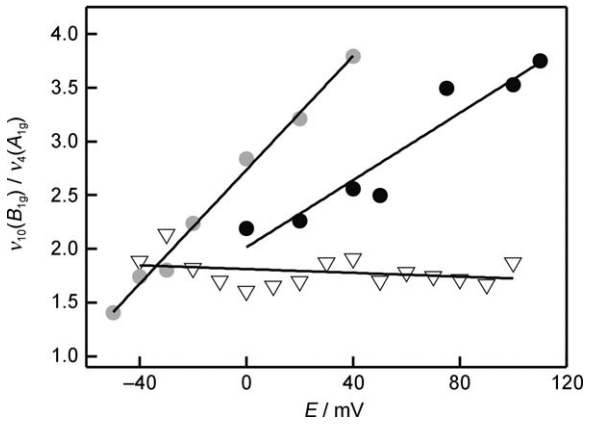

Figure 5. Potential dependence of the $\nu_{10}(B_{1g})/\nu_4(A_{1g})$ intensity ratio as determined by Q-band SERR for oxidized Cyt-c immobilized on C10-COOH SAMs by different strategies. Gray filled circles: electrostatic adsorption; black filled circles: cross-linking procedure A; empty triangles: cross-linking procedure B.

2.3. Electron Transfer and Orientation Dynamics

It is well established that the heterogeneous ET rate constant of Cyt-c in electrostatic complexes with SAMs of long chain ω-carboxy alkanethiols exhibits the exponential dependence on distance characteristic of the tunneling mechanism, but it levels off when the number of methylene groups of the thiol is reduced to less than ten.[2,3,23,31–36] This behavior is confirmed by the present TRSERR experiments on electrostatically bound Cyt-c carried out with an overpotential of −100 mV (Figure 6).

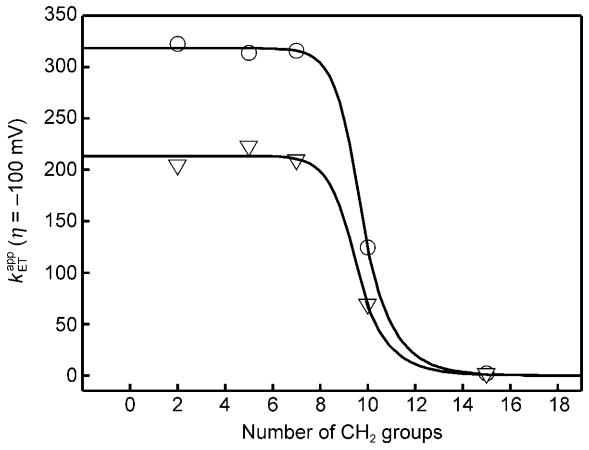

Figure 6. Distance dependence of the apparent ET rate constants k_{ET}^{app} of Cyt-c immobilized on C11-COOH SAMs, as determined by TRSERR spectroscopy for overpotentials of −100 mV. Empty circles: electrostatically adsorbed protein; empty triangles: protein cross-linked by procedure B.

The spectral analysis did not provide any indication for involvement of species other than the reduced and oxidized form B1 in the interfacial redox process.[3,40,43] Essentially the same kinetic behavior is observed when the protein is electrostatically adsorbed on mixed C10-COOH/C11-OH SAMs; the TRSERR experiments yield very similar results (Table 1), in line with previous findings by Davis et al.[42] For the shorter SAMs, however, we observe a drop of the apparent ET rate by a factor of two when comparing C5-COOH with C5-COOH/C6-OH (Table 1). Q-band-excited TRSERR spectra of electrostatically bound Cyt-c reveal that, regardless of the SAM composition, thinner films yield reorientation rates that are nearly identical to the ET rates obtained from TRSERR experiments with Soret-band excitation. These results are consistent with a gated mechanism, as recently proposed for single-component SAMs,[2,27,30] in which the overall redox process is controlled by the electron-tunneling probability at long distances, but protein reorientation becomes rate-limiting for the thinner films.

Covalent binding of Cyt-c to single-component or mixed SAMs by cross-linking procedure A has a relatively small effect on k_{ET}^{app} compared to the analogous electrostatic complexes (Table 1), except for C_5-COOH SAMs, for which a value nearly two times smaller is determined. The overall similar kinetic behavior suggests that also for the covalent Cyt-c-SAM complexes prepared according to procedure A the same gated mechanism holds, even though the kinetics of the reorientation process could not be determined in an equally reliable manner, mainly due to the smaller potential-dependent changes of the $\nu_{10}(B_{1g})/\nu_4(A_{1g})$ intensity ratio compared to the electrostatic complexes (Figure 5). In this respect, the results obtained for the covalently bound Cyt-c obtained by procedure B are quite unexpected. Despite the lack of any detectable potential-dependent orientational changes, reflected by the essentially constant $\nu_{10}(B_{1g})/\nu_4(A_{1g})$ intensity ratio (Figure 5), the k_{ET}^{app} values determined from the TRSERR experiments display qualitatively the same distance dependence as the electrostatically adsorbed protein (Figure 6), albeit with generally lower k_{ET}^{app} values. Also the overpotential dependence of k_{ET}^{app} for C10-COOH SAMs is qualitatively similar to that the electrostatic complexes (Figure 7), again with a limiting value that is ca. 30% lower. When the relative viscosity of the solution is increased to 1.5 cP by addition of sucrose, the k_{ET}^{app} values show a decrease at the higher overpotentials which is more severe than for the covalent complex obtained by procedure A. A fit of Equation (2) to the experimental data for the overpotential dependence of k_{ET}^{app} affords an apparent reorganization energy of $\lambda_{app} = 0.23$ eV for Cyt-c electrostatically adsorbed to C10-COOH SAMs. This value is in good agreement with that previously determined for Cyt-c at C15-COOH, for which electron tunneling is the rate limiting step. This finding is consistent with the fact that the reorientation rate is almost independent of the applied overpotential (within the applied range) and that k_{reor}^{app} is larger than the limiting value of k_{ET}^{app} (Figure 7). A 50% increase in solution viscosity causes a drop of the reorientation rate of the electrostatically adsorbed protein that results in a slight decrease of the k_{ET}^{app} values at the higher overpotentials. As a consequence a slightly lower value of 0.19 eV is determined for λ_{app}. For the protein covalently bound by following procedure B, the overpotential dependence of k_{ET}^{app} yields $\lambda_{app} = 0.20$ eV at $\rho = 1$ cP, that is, a lower value than for the electrostatic complex at 1 cP and very close to the value obtained at 1.5 cP.

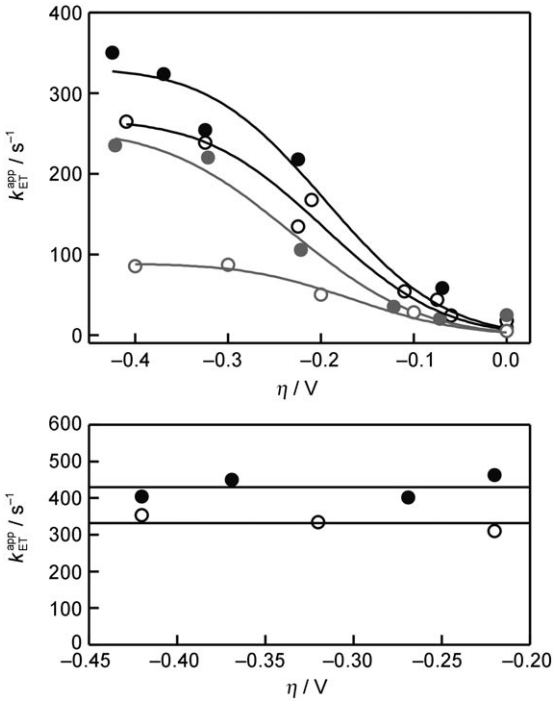

Figure 7. Top: Overpotential dependence of k_{ET}^{app} for Cyt-c immobilized on C10-COOH SAMs in normal phosphate buffer ($\rho = 1$ cP; filled symbols) and phosphate buffer with addition of sucrose ($\rho = 1.5$ cP; empty symbols). Black circles: electrostatically adsorbed protein; gray circles protein cross-linked by method B. Bottom: Overpotential dependence of k_{reor}^{app} for C10-COOH/Cyt-c electrostatic complexes at 1 cP (filled circles) and 1.5 cP (open circles).

2.4. Molecular Dynamics Simulations

In previous computational work we studied the adsorption, dynamics, and electronic coupling of Cyt-c on metal surfaces coated with SAMs of ω-carboxyl alkanethiols.[27,39] It was shown that the protein exhibits three main binding domains of different affinity. Binding through any of the domains does not lead to rigid electrostatic complexes, and instead the protein exhibits significant mobility that modulates the electronic coupling. The simulations predict that small-amplitude motions of the protein may have a substantial effect on the heterogeneous ET rate. For instance, changes of the tilt angle of the heme plane with respect to the electrode surface as small as 5° may result in a variation of the electronic coupling of one order of magnitude, corresponding to variations of k_{ET} by two orders of magnitude. Furthermore, large-amplitude rotations of the protein on the SAM surface are strongly suggested, although they cannot be captured within the timescale of the simulations. Such rotations have a direct impact on the order of magnitude of the electronic coupling, while fine tuning is exerted by

structural thermal fluctuations of the proteins and solvent molecules.[27,39]

Herein, we applied the same methodology for investigating the ET properties of Cyt-c covalently bound to similar SAMs. For the in silico covalent linkage we selected as representative examples four different lysine residues: lysines 79 and 86, which are included in the main binding domains MZI and MZII of the ferric protein, and lysines 13 and 72, which are included in MZI and MZII of ferrous Cyt-c.[27,39] Single amide bonds with the SAM were formed in each case. For all binding configurations, MD simulations were run in explicit water environment for 10 ns and optimal electronic couplings V^{max} were computed every 10 ps by using the pathway algorithm. Figure 8 shows the mobility of the protein in terms of the angles α and ϕ that describe the orientation of the heme group with respect to the metal surface (see Experimental Section for definition of α and ϕ and further computational details). The high-frequency mobility of the covalently attached protein is very similar to that observed for electrostatic adsorption through the same region, and thus leads to comparable fluctuations of the electronic coupling along the simulation. Similarities and differences can be better appreciated in the histograms shown in Figure 9. For the angle α, the electrostatic and covalent complexes have almost identical distributions centered at 112°, while for ϕ the covalent complex is slightly shifted to lower values (maxima at 170 and 172°, respectively). Note that the dynamics of Cyt-c in electrostatic and covalent complexes shown in Figure 8 are rather similar during the first 8 ns. At this point in time the electrostatically adsorbed protein rotates by 10 and 20° in α and ϕ directions, respectively, which is also evident as a shoulder in Figure 9. The resulting orientation exhibits a lower average coupling, and no large amplitude peaks are detected for the remaining 2 ns. As a consequence, the ET rate in this orientation is expected to be significantly lower. This large-amplitude rotation is impeded in the covalent complex. Similar results were obtained for all cases studied.

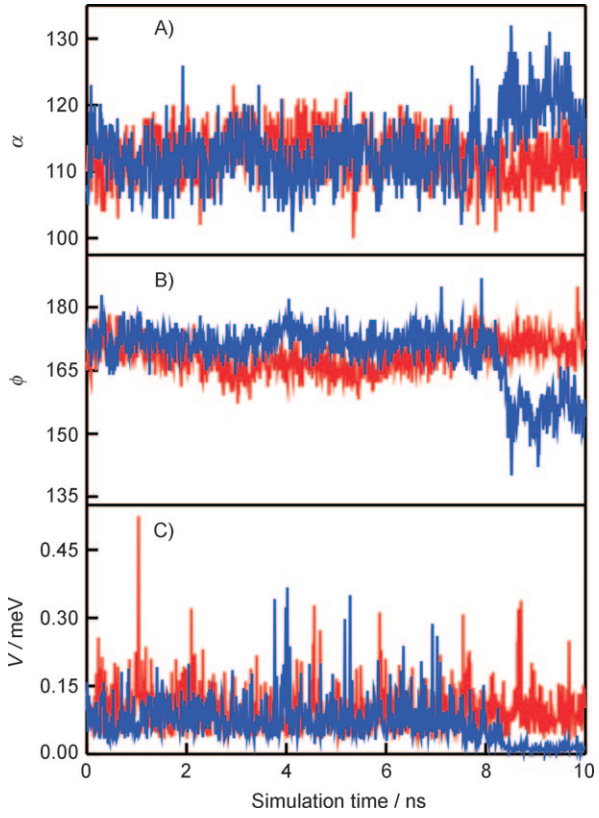

Figure 8. Variation of α (A), ϕ (B), and V (C) as a function of simulation time for oxidized Cyt-c cross-linked to a SAM through Lys86 (red) compared with the variations of the same parameters for the equivalent electrostatic complex (blue).

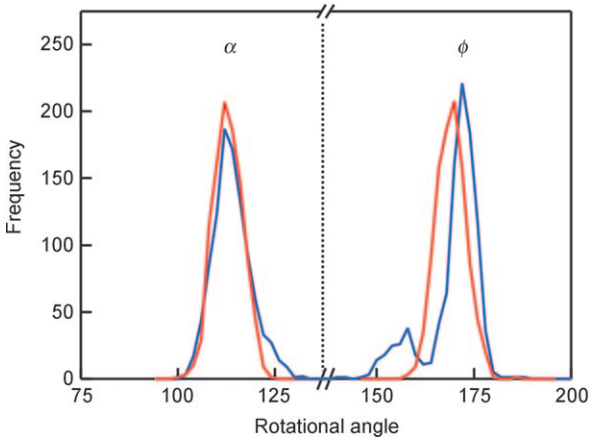

Figure 9. Histograms of the angles α and ϕ determined along the 10 ns simulations for electrostatic (blue) and covalent (red) SAM/Cyt-c complexes.

A summary of the results obtained for the different binding configurations and redox states is presented in Table 2. In all cases the adsorbed and covalently attached proteins exhibit

Table 2. Average values of α, ϕ, and V, maximum coupling V^{MAX} and optimal electron pathways obtained for the different immobilization modes of Cyt-c, as obtained by MD simulations.

Redox state	Binding site	$<\alpha>$	$<\phi>$	$\langle V\rangle$ [meV]	V^{MAX} [meV]	ET path[a]
Covalent binding						
Fe^{2+}	Lys13	93.8	172	0.14 ± 0.075	0.61	Hec–Cys–SAM
	Lys72	96	186	0.72 ± 0.36	2.18	Hec–Cys–SAM
Fe^{3+}	Lys79	112	168	0.095 ± 0.046	0.52	Hec–Vinyl–SAM
	Lys86	101	193	0.31 ± 0.12	0.88	Hec–Vinyl–SAM
Electrostatic binding						
Fe^{2+}	MZI (Lys13)	87	183	0.44 ± 0.20	1.44	Hec-Cys-SAM
	MZII (Lys72)	92	185	0.50 ± 0.25	1.71	Hec–Cys–SAM
Fe^{3+}	MZI (Lys79)	113	171	0.067 ± 0.045	0.36	Hec–Wat–SAM
	MZII (Lys86)	105	195	0.41 ± 0.20	1.74	Hec–Methyl–SAM

[a] Hec: heme tetrapyrrole ring, Cys: cysteine 17, Methyl: methyl substituent of ring D, Wat: water molecule.

comparable average and maximum couplings as well as standard deviations.

2.5. Interplay of Electron Transfer and Protein Dynamics

The TRSERR results presented here show that the distance dependence of the heterogeneous ET rate of Cyt-c on SAM-coated electrodes follows qualitatively the same tendency whether the protein is electrostatically adsorbed or cross-linked to the SAMs. The kinetic behavior includes the characteristic exponential variation for long SAMs and little or no variation for the shorter ones. In quantitative terms, however, k_{ET}^{app} for the covalently attached protein is lower in the plateau region. In all cases, k_{ET}^{app}, measured for short SAMs or high driving forces, drops upon increasing the viscosity of the solution in contact with the immobilized protein, and this suggests that under these conditions the rate-limiting event is related to protein motion. Stationary SERR experiments performed under Q-band excitation show a distinct potential dependence of the average protein orientation for electrostatically bound Cyt-c and for covalent SAM/Cyt-c complexes prepared according to procedure A, although in that case the variation is smaller. At first sight this result is surprising, since formation of the amide bond between the protein and the SAM is expected to restrict the mobility. Although this is true for large-amplitude motion, MD simulations show that the low-amplitude mobility (thermal fluctuations) in the complexes formed through electrostatic interactions and through equivalent single covalent bonds are rather similar and, furthermore, that these subtle fluctuations are sufficient for producing significant changes of the tunneling probabilities. Thus, the present experimental results for the covalently bound Cyt-c prepared according to procedure A are consistent with formation of a single amide bond that allows for a similar orientation and low-amplitude mobility as in the electrostatic complex. Small populations of differently oriented protein or multibond formation cannot be discarded and, in fact, are strongly suggested by the less ideal electrochemical response and the slightly lower variation of the $\nu_{10}(B_{1g})/\nu_4(A_{1g})$ ratio with the potential in comparison with the electrostatic complex. For electrostatically bound Cyt-c the transition from the tunneling-controlled to the orientation-controlled ET regime has been proposed to be governed by the increasing interfacial electric field with decreasing SAM length, which slows down the mobility of the protein. The experimentally determined rate of reorientation of Cyt-c in electrostatic complexes with C5-COOH SAMs is about two orders of magnitude slower than that for C15-COOH SAMs,[30] corresponding to an approximately twofold increase of the interfacial electric field.[45] In agreement with this interpretation, MD simulations on similar SAM/Cyt-c electrostatic complexes suggest that the rate of reorientation from the high-affinity domain with low electronic coupling configuration to the optimal orientation for ET decreases by more than one order of magnitude in the presence of an electric field strength of 0.01 V Å^{-1} and more than 11 orders of magnitude when the field strength is 0.1 V Å^{-1}.[39] In view of the quite similar overall kinetic behavior compared to electrostatically bound Cyt-c, we conclude that, also for the covalent Cyt-c/SAM complex obtained by procedure A, the local electric field strength determines the protein mobility, despite partial neutralization of surface charges by the cross-linking procedure.

According to the MD calculations, one would further expect that, at sufficiently high fields, k_{ET}^{app} should decrease after reaching a maximum. This behavior has not been observed for SAMs of ω-carboxyl alkanethiols, evidently because even for the shortest possible chain length with only one methylene group, the electric field is not sufficiently strong. A decrease of k_{ET}^{app}, however, has in fact been observed upon replacing the carboxyl group by divalent anions to increase the charge density at the interface and thus the electric field for the electrostatically bound Cyt-c.[3] The distance dependence of k_{ET}^{app} for Cyt-c covalently bound according to procedure B is qualitatively similar to the two modes of protein immobilization discussed above (electrostatic and covalent through procedure A), including the viscosity sensitivity in the plateau region. However, SERR experiments performed with Q-band excitation do not show any appreciable variation of the $\nu_{10}(B_{1g})/\nu_4(A_{1g})$ ratio with potential. This striking discrepancy indicates that procedures A and B lead to different covalent Cyt-c/SAM complexes. According to protocol A, cross-linking is carried out with the electrostatic ferrous Cyt-c/SAM complex formed at a negative potential, while in protocol B the SAM is activated prior to coupling of ferric Cyt-c at open circuit. Thus, procedures A and B yield slightly different distributions of orientations, as reflected by the different $\nu_{10}(B_{1g})/\nu_4(A_{1g})$ intensity ratios. In addition, protocol B includes the addition of NHS and significantly longer incubation times, and thus is expected to afford higher protein coverage, as indicated by the stronger SERR signals. On the other hand, albeit not verified experimentally, it is reasonable to assume that protocol B should lead to the formation of more than one amide bond per Cyt-c molecule.[42] If this were the case the covalently attached protein would exhibit a much more restricted mobility consistent with a potential-independent $\nu_{10}(B_{1g})/\nu_4(A_{1g})$ intensity ratio. However, low-amplitude motions that refers to thermal fluctuations of the protein and interfacial solvent molecules are not inhibited and may result in a distinct modulation of the optimum electron pathways and thus of the ET rate.[27,39] Moreover, depending on the positions of the amide bonds the mobility of the protein can be restricted with respect to the angle α, ϕ, or both. If the protein were attached through two bonds that are contained in a plane perpendicular to the heme group, then rotation with respect to α, but not to ϕ, would be largely restricted. As a consequence, SERR experiments would reveal no changes of the $\nu_{10}(B_{1g})/\nu_4(A_{1g})$ intensity ratio that are only sensitive to variation of α. Conversely, thermal fluctuations and low-amplitude rotations with respect to ϕ that are not detectable in SERR experiments may still occur and modulate the electronic coupling. Then, as in the previous cases, protein dynamics is expected to be rate-limiting for thin SAMs, that is, at high electric fields, as suggested by the large viscosity effects observed for short SAMs or high driving forces.

Consistent with this interpretation are previous findings by Jin et al., who showed that, in contrast to electrostatically im-

mobilized Cyt-c, the covalently bound protein prepared according to procedure A is not capable of shuttling electrons between the electrode and NADPH cytochrome P450 reductase in the solution phase.[46] Here a major reorientation is required to switch between electron exchange with the electrode and the reductase, a movement of Cyt-c that is blocked upon covalent attachment already under "mild" conditions.

Conclusions

The results presented here show that the experimentally determined rate constants for the heterogeneous ET of Cyt-c immobilized on SAM-coated electrodes represent a convolution of orientation-dependent tunneling probabilities and the orientational distribution and dynamics of the protein ensemble. In electrostatic complexes with negatively charged SAMs, the relatively narrow orientational distribution leaves the vast majority of molecules in an orientation that is not optimized for ET. A qualitatively similar conclusion is reached for the protein cross-linked to these SAMs, although in this case the distribution of orientations is broader and the mobility is restricted specifically when the protein is attached by more than one covalent amide bond. However, even in the covalent complexes, low-amplitude motions of the proteins and interfacial water molecules guarantee transient pathways of sufficiently high electronic coupling. For thick SAMs, electron tunneling is significantly slower than protein and solvent dynamics, and thus the measured rates represent a true ET rate that exhibits the characteristic exponential dependence on distance. For thinner SAMs, that is, higher charge densities and stronger electric fields, protein and solvent dynamics is significantly slowed down and becomes rate-limiting. This kinetic behavior is likely to be rather general and may constitute the basis for the unusual distance dependencies of the ET rates reported for a variety of redox proteins in electrochemical studies.[21–26] A similar mechanism is likely to operate when Cyt-c exerts its electron-transport function in aerobic respiration. As suggested by various studies, the initial electrostatic complex of Cyt-c with the natural reaction partner Cyt-c oxidase is not optimized for ET and thus requires reorientation.[47] According to the results presented here, such reorientation processes can be expected to be modulated by the variable transmembrane potential, which thus would play a role in inhibitory control of the ET-driven proton translocation activity.

Experimental Section

Chemicals: 6-Mercaptohexanoic acid (C5-COOH) was purchased from Dojindo. All other chemicals, including 11-mercaptoundecanoic acid (C10-COOH), 11-mercaptoundecan-1-ol (C11-OH), 6-mercaptohexan-1-ol (C6-OH), *N*-ethyl-*N*′-(3-dimethylaminopropyl) carbodiimide (EDC), *N*-cyclohexyl-*N*′-(2-morpholinoethyl)carbodiimide methyl-*p*-toluenesulfonate (CMC), and *N*-hydroxysuccinimide (NHS), were purchased from Sigma-Aldrich and used without further purification. Horse heart cytochrome c (Cyt-c) was purchased from Sigma-Aldrich and purified by HPLC. The water used in all experiments was purified by a Millipore system and its resistance was greater than 18 MΩ.

Electrode Modification: Silver ring electrodes were mechanically polished with 3M polishing films from 30 to 1 μm grade. After washing, electrodes were subjected to oxidation–reduction cycles in 0.1 M KCl to create an SER-active nanostructured surface. Subsequently, the electrodes were incubated in 1.5 mM ethanolic solutions of the alkanethiols (pure or 1:1 mixtures) for ca. 20 h, and then rinsed and transferred to the spectroelectrochemical cell. For electrostatic adsorption Cyt-c was added to the electrochemical cell from a stock solution to form a 0.2–0.4 μM solution and allowed to incubate at room temperature for ca. 15–20 min before starting the experiments.

Covalent Binding: Two different procedures were used for cross-linking of Cyt-c to the SAMs. In procedure A, the protein was adsorbed on the SAM-coated working electrode for about 20 min. at −100 mV as in the case of electrostatic binding. Subsequently, EDC was added to the cell from a stock solution to obtain a 5 mM concentration. The resulting solution was stirred for 45 min while maintaining the applied potential (−100 mV). The electrode was then rinsed with water and exposed to a 2–3 M KCl solution for 15 min at open circuit to remove remaining electrostatically adsorbed protein.

In procedure B, The SAM-coated electrodes were incubated for 2 h in a de-aerated solution of CMC (20 mg/10 mL) and NHS (6 mg/10 mL). After activation of the carboxyl groups, the electrode was rinsed thoroughly and immersed in a 10 mM Cyt-c solution containing 30 mM phosphate buffer solution (pH 7) overnight. Finally, the electrode was thoroughly rinsed with water and then immersed in a 2–3 M KCl solution for 10 min to desorb the remaining physisorbed protein. In contrast to procedure A, all steps were performed at open circuit.

Surface-Enhanced Resonance Raman Spectroscopy: The spectroelectrochemical cell for SERR spectrosocpy has been described elsewhere.[40] Briefly, a Pt wire and a Ag/AgCl electrode were used as counter- and reference electrodes, respectively. All potentials cited in this work refer to the Ag/AgCl (3 M KCl) electrode. The working electrode was a silver ring of 8 mm diameter and 2.5 mm height mounted on a shaft that is rotated at about 5 Hz to avoid laser-induced sample degradation.

The electrolyte solution (30 mM phosphate buffer, pH 7.0) was bubbled with catalytically purified oxygen-free argon prior to the measurements, and Ar overpressure was maintained throughout the experiments. The viscosity of the solution was adjusted by addition of sucrose to the same buffer, which has been shown not to affect significantly the dielectric constant.[33]

SERR spectra were measured in backscattering geometry by using a confocal microscope coupled to a single-stage spectrograph (Jobin Yvon, LabRam 800 HR or XY 800) equipped with a liquid-nitrogen-cooled back-illuminated CCD detector. Elastic scattering was rejected with notch or edge filters. The 413 nm line of a cw krypton ion laser (Coherent Innova 300c) or the 514 nm line of a cw argon laser (Coherent Innova 70c) was focused onto the surface of the rotating Ag electrode by means of a long-working-distance objective (20×, N.A. 0.35). Typically, experiments were performed with laser powers of about 1 mW (413 nm) and 5–12 mW (514 nm) at the sample. Effective acquisition times were between 3 and 10 s. All experiments were repeated several times to ensure reproducibility.

For TRSERR experiments, potential jumps of variable height and duration were applied to trigger the reaction. The SERR spectra were measured at different delay times following the potential

jump. Synchronization of potential jumps and probe laser pulses was achieved by a pulse-delay generator (BNC). The probe pulses were generated by passing the cw laser beam through two consecutive laser intensity modulators (Linos), which give a total extinction better than 1:50 000 and a time response of ca. 20 ns. Details of the TRSERR measurements are described elsewhere.[23,30]

After background subtraction the spectra were treated by single-band (514 nm) or component analysis[43] (413 nm) in which the spectra of the individual species were fitted to the measured spectra by using a home-made analysis software. The time-dependent changes of the relative concentrations of the species involved were subsequently analyzed in terms of relaxation kinetics to yield reciprocal relaxation time constants.[24]

Molecular Dynamics Simulations: The computational methods for comparing the covalent and electrostatic SAM/Cyt-c complexes have been presented and discussed previously,[27,39] and therefore they will be only briefly described here.

Initial Cyt-c structures were obtained from the PDB database (PDB 26IW and PDB 1HRC for the reduced and oxidized form, respectively). For simulating the SAMs, an infinite array of fixed Au atoms with lattice structure 111 was built in silico, and each of them was linked to a C5-COOH molecule through the S atom. SAM and lattice parameters were adopted from the literature.[27,39] The infinite array consisted of a periodic boundary condition (PBC) cell of 13×14 Au atoms in the *X* and *Y* directions, with their corresponding alkanethiols. In the *Z* direction periodicity is achieved by using periodic boxes of 80 Å width, which leaves sufficient space between the Cyt-c surface and the next (upper) gold layer to avoid direct interaction. Cross-linking of Cyt-c to the SAMs was performed by in silico modification of selected protein Lys residues and SAM carboxylate groups to an amide bond.

The production simulations of each complex were performed by immersing the SAM/Cyt-c structures contained in a TIP3P water box. For each case, an initial constant-volume MD was performed to heat the system to 300 K, and subsequently a constant-pressure simulation was performed to equilibrate the system density. Finally, production MDs were performed. Temperature and pressure were kept constant using the Berendsen thermostat and barostat. For the PBC simulations, Ewald summations were employed to compute the electrostatic energy terms by using the default parameters in the Sander module of the AMBER package.

The orientation of Cyt-c with respect to the Au/SAM surface was defined based on the relative heme orientation in terms of two angles: the angle α between the Fe–S(Met80) bond, which is perpendicular to the heme plane, and the *Z* axis of the system, which is perpendicular to the Au/SAM surface. Values of α close to 0 or 180° imply that the heme group lies parallel to the SAM, whereas a value of 90° corresponds to perpendicular orientation of the heme plane with respect to the surface. The angle ϕ is determined by the vector defining the Fe–N_A bond (where N_A is the nitrogen atom of the pyrrolic ring) and the vector pointing towards the SAM, which lies in the heme plane. This angle describes the rotational orientation of the heme group and thus of the entire Cyt-c. Values between 0 and 90° correspond to protein orientations in which the heme propionate groups are closer to the SAM surface, whereas for values between 180 and 270° the propionate groups point away from the SAM surface. Note that for α values close to 0 or to 180° changes of the ϕ value do not correspond to significant variations of protein orientation since the heme group lies parallel to the SAM surface.

Coupling Matrix calculation: The electronic coupling between the heme iron atom and any of the Au atoms that represent the electrode surface were estimated by using the pathway algorithm developed by Beratan et al.,[48] specifically modified for the present system.[27,39]

Acknowledgements

Financial support by the DFG (Sfb498-A8; PH, D.H.M.), the Fond der Chemischen Industrie (I.M.W.) and the ANPCyT (PICT2006-459; PICT2007-00314) is gratefully acknowledged. M.A.M. and D.H.M. are members of CIC-CONICET. D.F.M. and D.A.P. are CONICET fellows.

Keywords: electron transfer · molecular dynamics · monolayers · proteins · time-resolved spectroscopy

[1] F. A. Armstrong, *Curr. Opin. Chem. Biol.* **2005**, *9*, 110.
[2] D. H. Murgida, P. Hildebrandt, *Chem. Soc. Rev.* **2008**, *37*, 937.
[3] D. H. Murgida, P. Hildebrandt, *Acc. Chem. Res.* **2004**, *37*, 854.
[4] K. K. Chohan, M. Jones, J. G. Grossmann, F. E. Frerman, N. S. Scrutton, M. J. Sutcliffe, *J. Biol. Chem.* **2001**, *276*, 34142.
[5] V. L. Davidson, *Acc. Chem. Res.* **2000**, *33*, 87.
[6] T. Z. Grove, N. M. Kostic, *J. Am. Chem. Soc.* **2003**, *125*, 10598.
[7] L. J. C. Jeuken, *Biochim. Biophys. Acta Bioenerg.* **2003**, *1604*, 67.
[8] S. A. Kang, B. R. Crane, *Proc. Natl. Acad. Sci. USA* **2005**, *102*, 15465.
[9] H. J. Lee, J. Basran, N. S. Scrutton, *Biochemistry* **1998**, *37*, 15513.
[10] H. K. Mei, K. F. Wang, N. Peffer, G. Weatherly, D. S. Cohen, M. Miller, G. Pielak, B. Durham, F. Millett, *Biochemistry* **1999**, *38*, 6846.
[11] F. Millett, B. Durham, *Photosynth. Res.* **2004**, *82*, 1.
[12] J. M. Nocek, S. L. Hatch, J. L. Seifert, G. W. Hunter, D. D. Thomas, B. M. Hoffman, *J. Am. Chem. Soc.* **2002**, *124*, 9404.
[13] J. N. Onuchic, C. Kobayashi, O. Miyashita, P. Jennings, K. K. Baldridge, *Philos. Trans. R. Soc. London Ser. B* **2006**, *361*, 1439.
[14] H. Y. Wang, S. Lin, J. P. Allen, J. C. Williams, S. Blankert, C. Laser, N. W. Woodbury, *Science* **2007**, *316*, 747.
[15] A. V. Zhuravleva, D. M. Korzhnev, E. Kupce, A. S. Arseniev, M. Billeter, V. Y. Orekhov, *J. Mol. Biol.* **2004**, *342*, 1599.
[16] F. A. Armstrong, N. A. Belsey, J. A. Cracknell, G. Goldet, A. Parkin, E. Reisner, K. A. Vincent, A. F. Wait, *Chem. Soc. Rev.* **2009**, *38*, 36.
[17] J. A. Cracknell, K. A. Vincent, F. A. Armstrong, *Chem. Rev.* **2008**, *108*, 2439.
[18] I. Willner, E. Katz, *Angew. Chem.* **2000**, *112*, 1230; *Angew. Chem. Int. Ed.* **2000**, *39*, 1180.
[19] C. E. D. Chidsey, *Science* **1991**, *251*, 919.
[20] R. A. Marcus, *J. Chem. Phys.* **1965**, *43*, 679.
[21] J. Q. Chi, J. D. Zhang, J. E. T. Andersen, J. Ulstrup, *J. Phys. Chem. B* **2001**, *105*, 4669.
[22] K. Fujita, N. Nakamura, H. Ohno, B. S. Leigh, K. Niki, H. B. Gray, J. H. Richards, *J. Am. Chem. Soc.* **2004**, *126*, 13954.
[23] D. H. Murgida, P. Hildebrandt, *J. Am. Chem. Soc.* **2001**, *123*, 4062.
[24] A. Kranich, H. Naumann, F. P. Molina-Heredia, H. J. Moore, T. R. Lee, S. Lecomte, M. A. de La Rosa, P. Hildebrandt, D. H. Murgida, *Phys. Chem. Chem. Phys.* **2009**, *11*, 7390.
[25] P. Zuo, T. Albrecht, P. D. Barker, D. H. Murgida, P. Hildebrandt, *Phys. Chem. Chem. Phys.* **2009**, *11*, 7430.
[26] J. J. Feng, D. H. Murgida, U. Kuhlmann, T. Utesch, M. A. Mroginski, P. Hildebrandt, I. Weidinger, *J. Phys. Chem. B* **2008**, *112*, 15202.
[27] D. A. Paggi, D. F. Martin, A. Kranich, P. Hildebrandt, M. A. Marti, D. H. Murgida, *Electrochim. Acta* **2009**, *54*, 4963.
[28] D. H. Murgida, P. Hildebrandt, *J. Phys. Chem. B* **2002**, *106*, 12814.
[29] L. Rivas, D. H. Murgida, P. Hildebrandt, *J. Phys. Chem. B* **2002**, *106*, 4823.
[30] A. Kranich, H. K. Ly, P. Hildebrandt, D. H. Murgida, *J. Am. Chem. Soc.* **2008**, *130*, 9844.
[31] J. S. Xu, E. F. Bowden, *J. Am. Chem. Soc.* **2006**, *128*, 6813.

[32] K. Niki, W. R. Hardy, M. G. Hill, H. Li, J. R. Sprinkle, E. Margoliash, K. Fujita, R. Tanimura, N. Nakamura, H. Ohno, J. H. Richards, H. B. Gray, *J. Phys. Chem. B* **2003**, *107*, 9947.
[33] A. Avila, B. W. Gregory, K. Niki, T. M. Cotton, *J. Phys. Chem. B* **2000**, *104*, 2759.
[34] A. El Kasmi, J. M. Wallace, E. F. Bowden, S. M. Binet, R. J. Linderman, *J. Am. Chem. Soc.* **1998**, *120*, 225.
[35] H. J. Yue, D. Khoshtariya, D. H. Waldeck, J. Grochol, P. Hildebrandt, D. H. Murgida, *J. Phys. Chem. B* **2006**, *110*, 19906.
[36] J. J. Wei, H. Y. Liu, K. Niki, E. Margoliash, D. H. Waldeck, *J. Phys. Chem. B* **2004**, *108*, 16912.
[37] D. H. Murgida, P. Hildebrandt, J. Wei, Y. F. He, H. Y. Liu, D. H. Waldeck, *J. Phys. Chem. B* **2004**, *108*, 2261.
[38] D. E. Khoshtariya, J. J. Wei, H. Y. Liu, H. J. Yue, D. H. Waldeck, *J. Am. Chem. Soc.* **2003**, *125*, 7704.
[39] D. Alvarez-Paggi, D. F. Martin, P. M. De Biase, P. Hildebrandt, M. A. Marti, D. H. Murgida, unpublished results.
[40] D. H. Murgida, P. Hildebrandt, *J. Phys. Chem. B* **2001**, *105*, 1578.
[41] P. M. De Biase, D. Alvarez-Paggi, F. Doctorovich, P. Hildebrandt, D. A. Estrin, D. H. Murgida, M. A. Marti, *J. Am. Chem. Soc.* **2009**, *131*, 16248.
[42] K. L. Davis, D. H. Waldeck, *J. Phys. Chem. B* **2008**, *112*, 12498.
[43] S. Döpner, P. Hildebrandt, A. G. Mauk, H. Lenk, W. Stempfle, *Spectrochim. Acta Part A* **1996**, *52*, 573.
[44] *Surface-Enhanced Raman Scattering: Physics and Applications* (Eds.: K. Kneipp, H. Kneipp, M. Moskovits), Springer, Berlin, **2006**.
[45] S. Todorovic, C. Jung, P. Hildebrandt, D. H. Murgida, *J. Biol. Inorg. Chem.* **2006**, *11*, 119.
[46] W. Jin, U. Wollenberger, E. Kärgel, W. H. Schunck, F. W. Scheller, *J. Electroanal. Chem.* **1997**, *433*, 135.
[47] B. Michel, H. R. Bosshard, *Biochemistry* **1989**, *28*, 244.
[48] D. N. Beratan, J. N. Onuchic, J. N. Betts, B. E. Bowler, H. B. Gray, *J. Am. Chem. Soc.* **1990**, *112*, 7915.

Received: December 8, 2009
Published online on April 7, 2010

7

Electric Field Effects on the Interfacial Electron Transfer and Protein Dynamics of Cytochrome *c*

Ly, H. K.; Wisitruangsakul, N.; Sezer, M.; Feng, J. J.; Kranich, A.; Weidinger, I.; Zebger, I.; Murgida, D. H.; Hildebrandt, P. *J. Electroanal. Chem.* **2011**, 660, 367-376.

Journal of Electroanalytical Chemistry 660 (2011) 367–376

Contents lists available at ScienceDirect

Journal of Electroanalytical Chemistry

journal homepage: www.elsevier.com/locate/jelechem

Electric-field effects on the interfacial electron transfer and protein dynamics of cytochrome c

H. Khoa Ly [a], Nattawadee Wisitruangsakul [a,b], Murat Sezer [a], Jiu-Ju Feng [a,c], Anja Kranich [a], Inez M. Weidinger [a], Ingo Zebger [a], Daniel H. Murgida [d], Peter Hildebrandt [a,*]

[a] Technische Universität Berlin, Institut für Chemie, Sekr. PC 14, Straße des 17. Juni 135, D-10623 Berlin, Germany
[b] Iron and Steel Institute of Thailand, 1st-2nd Floor, Bureau of Industrial Sectors Development Building, Trimitr Soi., Pharam 4 Rd. Phakhanong, Klongtoey Bangkok 10110, Thailand
[c] School of Chemistry and Environmental Science, Henan Normal University, Xinxiang, Henan 453007, China
[d] Departamento de Química Inorgánica, Analítica y Química Física/INQUIMAE-CONICET, Facultad de Ciencias Exactas y Naturales, Universidad de Buenos Aires, Ciudad Universitaria, Pab. 2, Piso. 1, C1428EHA-Buenos Aires, Argentina

ARTICLE INFO

Article history:
Received 18 May 2010
Received in revised form 8 October 2010
Accepted 15 December 2010
Available online 21 December 2010

Keywords:
Surface enhanced Raman spectroscopy
Surface enhanced infrared spectroscopy
Electron transfer
Cytochrome c
Electric field

ABSTRACT

Time-resolved surface enhanced resonance Raman and surface enhanced infrared absorption spectroscopy have been employed to study the interfacial redox process of cytochrome *c* (Cyt-c) immobilised on various metal electrodes coated with self-assembled monolayers (SAMs) of carboxyl-terminated mercaptanes. The experiments, carried out with Ag, Au and layered Au–SAM–Ag electrodes, afford apparent heterogeneous electron transfer constants (k_{relax}) that reflect the interplay between electron tunnelling, redox-linked protein structural changes, protein re-orientation, and hydrogen bond re-arrangements in the protein and in the protein/SAM interface. It is shown that the individual processes are affected by the interfacial electric field strength that increases with decreasing thickness of the SAM and increasing difference between the actual potential and the potential of zero-charge. At thick SAMs of mercaptanes including 15 methylene groups, electron tunnelling (k_{ET}) is the rate-limiting step. Pronounced differences for k_{ET} and its overpotential-dependence are observed for the three metal electrodes and can be attributed to the different electric-field effects on the free-energy term controlling the tunnelling rate. With decreasing SAM thickness, electron tunnelling increases whereas protein dynamics is slowed down such that for SAMs including less than 10 methylene groups, protein re-orientation becomes rate-limiting, as reflected by the viscosity dependence of k_{relax}. Upon decreasing the SAM thickness from 5 to 1 methylene group, an additional H/D kinetic isotope effect is detected indicating that at very high electric fields re-arrangements of the interfacial or intra-protein hydrogen bond networks limit the rate of the overall redox process.

1. Introduction

Interfacial electron transfer (ET) reactions play a key role in various processes of technological importance such as catalysis, corrosion and energy conversion or storage [1–3]. Furthermore, they are constitutive for a large number of biological functions and essential for most of the biotechnological applications that utilize redox enzymes [4]. This wide range of fundamental and applied aspects of heterogeneous ET has motivated numerous experimental and theoretical studies for decades. It is, therefore, quite surprising that these elementary reactions are yet not comprehensively understood.

One reason for this quite remarkable gap is related to methodological shortcomings. For a long time, electrochemical methods have been the only techniques for determining thermodynamic and kinetic data of redox processes although the nature of the participating molecules could not be directly identified [5,6]. Thus, analyses of mechanistic aspects of interfacial redox processes had to rely upon indirect evidences.

In this respect, surface enhanced Raman (SER) and surface enhanced infrared absorption (SEIRA) spectroscopy represent powerful complementary techniques since the vibrational spectra of molecules in close vicinity of metal electrodes can be selectively probed due to the resonant coupling of the radiation field with the surface plasmons of the metallic support, which may be Ag or Au [7,8]. These methods can be coupled with the potential jump technique such that they provide information of the kinetics and thermodynamics of the interfacial processes and the nature of the molecule species involved [9–13].

SER and SEIRA spectroscopy have been employed to study interfacial processes of redox proteins [14–17]. In these studies, the SER

* Corresponding author. Tel.: +49 30 314 21419; fax: +49 30 314 21122.
E-mail address: hildebrandt@chem.tu-berlin.de (P. Hildebrandt).

1572-6657/$ - see front matter © 2010 Elsevier B.V. All rights reserved.
doi:10.1016/j.jelechem.2010.12.020

effect is combined with the molecular resonance Raman (RR) effect (surface enhanced resonance Raman – SERR) such that it is possible to selectively probe the redox site solely of the immobilised proteins by tuning the excitation line in resonance with both the electronic transition of the cofactor *and* the surface plasmons of the metal [7,8]. The sensitivity and selectivity of SEIRA spectroscopy is increased upon operating in the difference mode such that only potential-dependent changes of the vibrational bands of the protein *and* the cofactor are detected [13,16,17].

A widely used model system, appropriate for employing SERR and SEIRA spectroscopy as well as electrochemical methods, is based on Au or Ag electrodes coated by self-assembled monolayers (SAM) of mercaptanes [14,15]. Such coatings on Au surfaces have been first characterised by Nuzzo and Allara [18] and later used for biocompatible immobilisation of redox proteins [19–21]. The terminal tail groups of the mercaptanes can be varied to allow for different modes of protein binding and the thickness of the SAM is defined by the number of methylene groups in the alkyl chain of the mercaptanes. These devices allow systematic variation of important parameters controlling the heterogeneous ET, such as the ET distance, driving force, charge distribution in the SAM/protein interface, and ionic strength, viscosity, and pH in the bulk solution.

A particularly large body of experimental and theoretical data has been accumulated for the redox process of the heme protein cytochrome *c* (Cyt-c) electrostatically immobilised on electrodes coated with carboxyl-terminated SAMs [11–17,20–50]. The results obtained so far indicate that the overall redox process is determined by the coupling of protein dynamics with electron tunnelling [42,46–48]. This coupling results from the fact that the energetically preferred electrostatic binding domain corresponds to an orientation of the bound protein that exhibits a distinctly lower tunnelling probability than a lower affinity binding site [46,48]. Optimum electron tunnelling efficiency, therefore, requires rotational motions of the protein on the SAM. This conclusion seems to provide a satisfactory explanation for the unique distance-dependence of the experimentally observed ET rate which first increases exponentially with decreasing distance, i.e. the SAM thickness, but then levels off to a plateau region for SAMs shorter than 10 methylene groups [12–15,23,25,27,29–32,42]. This region has, hence, been attributed to a kinetic regime in which protein-re-orientation becomes the rate-limiting step [42]. This interpretation is consistent with the experimental finding that the relaxation constants for protein re-orientation decrease substantially with decreasing distance in contrast to the exponential increase of the electron tunnelling rate. The slow-down of the protein dynamics with decreasing distance has been attributed to the concomitant increase of the electric field strength at Cyt-c/SAM interface, thereby increasing the activation energy for protein re-orientation. Thus, the interfacial redox process *in toto* has been suggested to be modulated by the electric field. Evidently, this scenario holds for quite different proteins which have been shown to exhibit a similar non-exponential distance dependence of the heterogeneous ET rate constant [51–55].

However, there are still some observations which do not fully fit into this scheme. First, in the limit of highly restricted protein mobility, one would expect at least a slight increase of the ET rate with further decreasing the electron tunnelling distance due to the exponential increase of the electronic coupling parameter in each protein orientation. However, all experimental data reported so far indicate an essentially distance-independent regime for short distances, i.e. high electric fields. Second, although experimental data obtained for SAM-coated Au and Ag electrodes display a qualitatively similar distance dependence, even for the same protein (i.e. Cyt-c) the absolute values for the experimentally determined ET rate constants are generally higher for Au than for Ag [12,13,23,25,27–29,36,38,45]. Third, in the plateau region, the ET rate constants have been shown to be lower in D_2O compared to H_2O, which has been ascribed to a kinetic isotope effect due to the coupling of electron transfer with redox-linked proton translocation in the protein or in the protein/SAM interface [12,43]. Although recently a part of this isotope effect was attributed to the intrinsically higher viscosity of D_2O solutions [43], it remains to be clarified why the ratio of the rate constants in H_2O and D_2O increases with decreasing distance to the electrode.

In the present work we have addressed these three questions by employing time-resolved (TR) SERR and SEIRA spectroscopy to probe the distance- and overpotential-dependence of the interfacial ET on Ag, Au, and Au–SAM–Ag hybrid electrodes. Special emphasis is laid on the analysis of viscosity and H/D effects on the kinetic constants. The results lead to the conclusion that not only protein re-orientation but also the electron tunnelling step itself is controlled by the interfacial electric field.

2. Experimental

2.1. Materials

6-mercaptohexanoic acid (C_5) from Dojindo, 16-mercaptohexadecanoic acid (C_{15}), 11-mercaptoundecanoic acid (C_{10}), and mercaptoacetic acid (C_1), all purchased from Sigma–Aldrich, were used without further purification. Formation of SAMs on the metal electrode followed the protocol described previously [26]. Horse heart Cyt-c from Sigma–Aldrich was purified by HPLC. The water used in all experiments was purified by a Millipore system and its resistance was more than 18 MΩ. All other chemicals were of highest purity grade available.

2.2. Surface Enhanced Resonance Raman spectroscopy

The spectroelectrochemical cell for SERR spectrosocpy has been described elsewhere [26]. All potentials cited in this work refer to the Ag/AgCl (3 M KCl) electrode. A rotating Ag ring served as the working electrode. SER-activation, coating of the electrode by SAMs and subsequent protein immobilization followed the protocol described previously with minor modifications [10,26]. Briefly, prior to the spectroscopic experiments, the electrolyte solution (30 mM phosphate buffer, pH = 7.0) was bubbled with catalytically purified oxygen-free argon for ca. 20 min. Consecutively, Cyt-c solution was added yielding a final concentration of ca. 0.2 μM. Protein adsorption was achieved by incubating the working electrode for 30 min into the protein containing buffer solution at open circuit potential. All experiments were performed in the presence of protein in solution and Ar overpressure.

For experiments in D_2O, the protein was dissolved in buffered D_2O solutions adjusted to pD = 7.0 [12] and subsequently incubated for further 18–24 h for complete H/D exchange. To account for the intrinsically higher viscosity of D_2O, comparative experiments in H_2O buffer were carried out at a viscosity of 1.2 cp adjusted by addition of sucrose [42]. All SERR measurements were carried out with a roughened Ag electrode [10] or an Au–SAM–Ag electrode fabricated as described previously [45].

SERR spectra were measured in back-scattering geometry using a confocal microscope coupled to a single stage spectrograph (Jobin Yvon, LabRam 800 HR) equipped with a liquid-nitrogen cooled back illuminated CCD detector. The 413-nm line of a cw Krypton ion laser (Coherent Innova 300c) was focused onto the surface of the rotating Ag electrode by means of a long working distance objective (20×; NA 0.35). Typically, experiments were performed with laser powers of ca. 1 mW. Effective acquisition times were between 3 and 10 s. All experiments were repeated several times to

ensure reproducibility. For TR-SERR experiments, potential jumps of variable height and duration were applied to trigger the reaction. The SERR spectra were measured at different delay times following the potential jump. Further details of the stationary and TR-SERR experiments are given elsewhere [11,15,27]. After background subtraction the spectra were treated by a component analysis in which the spectra of the individual species were fitted to the measured spectra using a home-made analysis software [56,57].

2.3. Surface enhanced infrared absorption measurements

SEIRA measurements were performed with a Kretschmann-ATR configuration using a semi-cylindrical shaped silicon crystal. Thin gold (Au) films were formed on the flat surface of the silicon substrate by electroless (chemical) deposition technique [13]. For Cyt-c adsorption, SAM-coated electrodes were immersed in Cyt-c solution using a concentration of 2 μM. The SEIRA spectra were recorded from 4000 to 1000 cm^{-1} with a spectral resolution of 4 cm^{-1} on a Bruker IFS66v/s spectrometer equipped with a photoconductive MCT detector. Four hundred scans were co-added for a spectrum. For the spectro-electrochemical measurements, the ATR crystal was incorporated into a three-electrode home-built cell [13].

TR SEIRA experiments were carried out using the potential jump technique [13]. Spectra acquisition was synchronized with the potential jumps controlled by a home-made pulse delay generator. Series of time dependent single-channel spectra of Cyt-c were collected when a potential jump was carried out from the reference potential at which Cyt-c was either largely reduced (−0.1 V) or oxidised (+0.125 V) to the final potential, and for the reverse jump. Depending on the time scale under examination, either step-scan or rapid-scan TR SEIRA measurements were carried out. The photoconductive MCT detector with a fast amplifier was used in the DC-coupled mode for the step-scan measurements. In the case of the rapid-scan measurements, the AC-coupled mode was utilized. Details of the set-up as well as of the stationary and TR SEIRA experiments have been described previously [13].

3. Results

3.1. Stationary SERR spectra and spectra analysis

SERR spectra of Cyt-c were measured from Ag electrodes coated with carboxyl-terminated thiols of different chain lengths (C_x-SAM), expressed by the number of methylene groups x. For chain lengths with $x = 15$, 10, 5, SERR spectra do not provide any indication for contributions from species other than the native state (denoted as B1). Thus, these spectra could be well described by a superposition of the reduced and oxidised forms of state B1 using component analysis. For shorter SAMs, however, there are non-negligible contributions from non-native species (denoted as state B2) which increase upon approaching potentials above the redox potential of the native state [57,58], as reflected, *inter alia*, by a broadening of the peaks in the ν_4 and ν_3 band region (Fig. 1). These species include a five-coordinated high spin (5cHS) and a six-coordinated low spin (6cLS) ferric heme in which the native Met80 ligand is removed from the heme iron and this coordination site remains vacant or is replaced by a His, respectively [57]. The formation of these species is most likely related to the weakening of the Fe-Met80 bond of native ferric Cyt-c (B1) by the high electric fields in close proximity to the electrode as concluded from previous experimental and theoretical studies [57–59]. Thus, the analysis of the SERR spectra measured under these conditions has to consider the involvement of four different species, i.e., $B1_{red}$, $B1_{ox}$, $B2_{ox}$ [5cHS], and $B2_{ox}$ [6cLS]. Then, the component analysis provides a consistent description of all experimental spectra, yielding the relative spectral contributions of each component to the individual experimental spectra. These spectral contributions were subsequently converted to relative concentrations [57]. The results of the analysis of the SERR spectra of Cyt-c at a C_1-SAM-coated Ag electrode, measured as a function of the electrode potential, are shown in Fig. 2. The only redox transition refers to the native state B1 as demonstrated by a fit of the Nernstian equation to the data, allowing for the determination of the redox potential E^0 and the number of transferred electrons n (Table 1). No effect on the redox equilibrium was observed upon increasing the viscosity of the solution or upon H/D exchange.

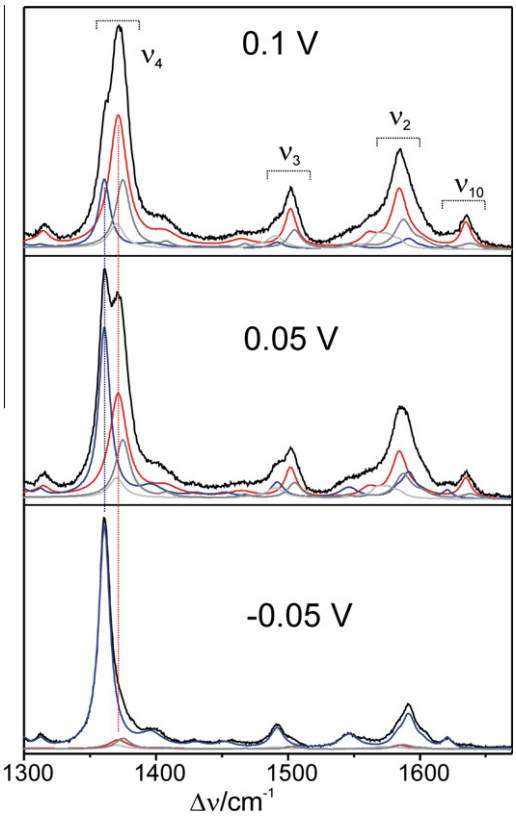

Fig. 1. SERR spectra of Cyt-c immobilised on a C_1-SAM-coated Ag electrode at different electrode potentials. The blue, red, dark gray, and light gray lines represent the component spectra of the reduced B1, oxidised B1, oxidised B2[6cLS], and oxidised B2[5cHS] state, respectively. Further experimental details are given in the text. (For interpretation of the references to colour in this figure legend, the reader is referred to the web version of this article.)

The non-native species are only present in the oxidised forms. The corresponding reduced counterparts are formed with electrode potentials below −0.3 V and are then rapidly converted to the native reduced B1 state [58,60], such that they are not detectable under equilibrium conditions in the stationary measurements.

3.2. Distance-dependence of the apparent electron transfer rate constant

TR-SERR experiments were first performed employing potential jumps from negative potentials (−0.1 V) to the redox potential such that relaxation processes include the ET of the immobilised Cyt-c at zero-driving force ($\Delta G = 0$ eV). These experiments were carried out as a function of the SAM thickness for $x = 15$, 10, 5, and 1 on Ag electrodes. As in the stationary experiments, spectra for $x \geqslant 5$ only include the native species whereas at $x = 1$ also the component spectra of the two B2 species were required for a

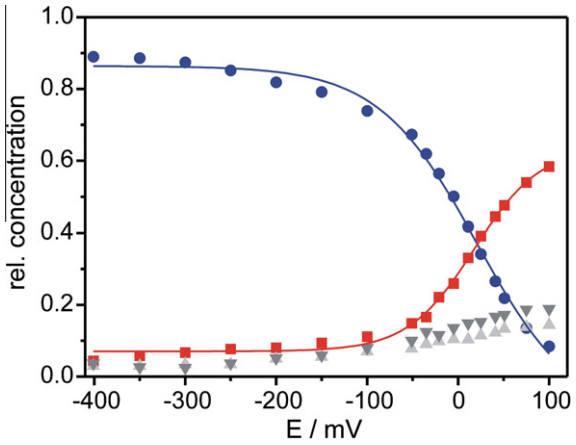

Fig. 2. Potential-dependent distribution of the relative concentrations of the various species of Cyt-c immobilised on a C_1-SAM-coated Ag electrode, as determined by SERR spectroscopy. The blue(circles), red(squares), dark gray(down-pointing triangle), and light gray(up-pointing triangle) symbols represent the reduced B1, oxidised B1, oxidised B2[6cLS], and oxidised B2[5cHS] state, respectively. The solid lines refer to a fit of the Nernst equation to the experimental data. Further experimental details are given in the text. (For interpretation of the references to colour in this figure legend, the reader is referred to the web version of this article.)

Table 1
Redox potentials and relaxation constants at zero-driving force for the interfacial redox process of Cyt-c immobilised on Ag electrodes coated with different SAMs.[a]

SAM	Buffer	E^0 (V)	k_{relax} (s^{-1})
C_{10}	H_2O	0.021	53
	H_2O, 1.2 cp	0.019	45
	D_2O	0.020	48
C_5	H_2O	0.018	130
	H_2O, 1.2 cp	0.010	100
	D_2O	0.015	100
C_1	H_2O	0.033	40
	H_2O, 1.2 cp	0.031	30
	D_2O	0.030	16

[a] The data were obtained by TR-SERR experiments with potential jumps from −0.1 V to the redox potential. The average error associated with the determination of E^0 and k_{relax} was determined to be ±005 V and ±10%.

satisfactory global fit to the experimental TR SERR spectra. Representative example spectra of experiments with Cyt-c on a C_1-SAM-coated Ag electrode are shown in Fig. 3. The time-dependent relative concentration changes of the various species indicate a clear correlation between the decay of the reduced and the increase of the oxidised B1 state (Fig. 4). The non-native species initially grow in and then reach a constant level after ca. 20 ms. Thus, the kinetic analysis cannot be restricted to the redox process of the native state but must also include the formation of the B2 species. A qualitatively similar kinetic behaviour has been recently observed for Cyt-c covalently attached to SAM-coated Ag electrodes, and found to be adequately described by the scheme in which $B1_{ox}$ exhibits a reaction channel to $B2_{ox}$[5cHS] in equilibrium with $B2_{ox}$[6cLS] [47]. In a similar way, we have considered the temporal evolution of the B2 species in the present kinetic analysis which thus allowed determining the relaxation constant k_{relax} of the redox process of B1 (Table 1).

For the C_{15}-SAM, k_{relax} was identical to the previously determined value [12] but with decreasing chain length the relaxation constants obtained in this work were found to be smaller than the constants reported earlier, specifically for the C_1-SAM. As a consequence, the distance-dependence of k_{relax} does not display a plateau for $x < 10$ but even a decrease at $x < 5$ (Fig. 5).

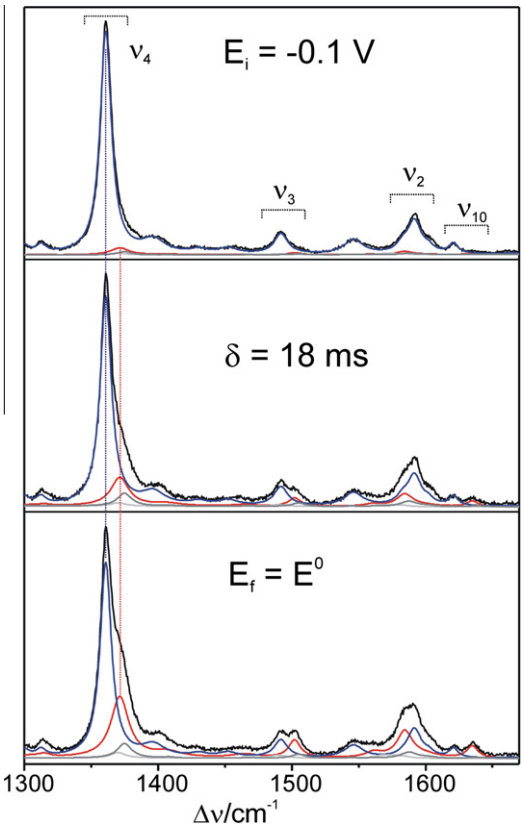

Fig. 3. Selection of SERR spectra of a time-resolved experiment of Cyt-c immobilised on a C_1-SAM-coated Ag electrode, including the stationary SERR spectra at the initial potential $E_i = -0.1$ V and the final potential $E_i = E^0$, and a TR SERR spectrum obtained after a delay time $\delta = 18$ ms subsequent to the potential jump. The blue, red, dark gray, and light gray lines represent the component spectra of the reduced B1, oxidised B1, oxidised B2[6cLS], and oxidised B2[5cHS] state, respectively. Further experimental details are given in the text. (For interpretation of the references to colour in this figure legend, the reader is referred to the web version of this article.)

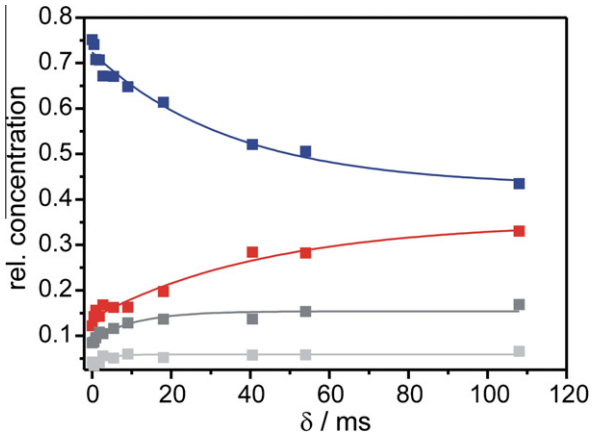

Fig. 4. Time-dependent changes of the relative concentrations of the various species of Cyt-c immobilised on a C_1-SAM-coated Ag electrode, following a potential jump from $E_i = -0.1$ V to the $E_i = E^0$. The experimental data were determined by TR SERR spectroscopy. The blue, red, dark gray, and light gray symbols represent the reduced B1, oxidised B1, oxidised B2[6cLS], and oxidised B2[5cHS] state, respectively. The solid lines refer to a fit of exponentials to the experimental data. Further details of the experiments and the data analysis are given in the text. (For interpretation of the references to colour in this figure legend, the reader is referred to the web version of this article.)

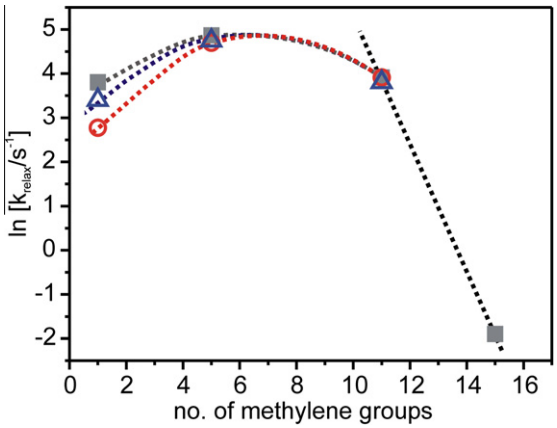

Fig. 5. Relaxation constants for the interfacial redox process of Cyt-c at zero-driving force at Ag electrodes coated with SAMs of different thickness, expressed by the number of methylene groups. The solid squares (dark gray), open triangles (blue), and open circles (red) symbols refer to the data obtained in H_2O, H_2O/sucrose (1.2 cp), and D_2O buffer, respectively. The dotted lines are just to guide the eye. Further details of the experiments and the data analysis are given in the text. (For interpretation of the references to colour in this figure legend, the reader is referred to the web version of this article.)

3.3. Kinetic isotope and viscosity effects of the apparent electron transfer rate constant

Preliminary SEIRA experiments monitoring the amide I band changes indicated that a complete H/D exchange requires incubation times for more than 24 h which is consistent with previous studies revealing a wide dynamic range for the substitution of the exchangeable protons [61,62]. Here we have chosen two different protocols for the H/D exchange. First, ferric Cyt-c was incubated in D_2O buffer solutions (pD 7.0) for different periods of time from 1 h to 24 h. Second, to achieve an exchange of protons that are hardly accessible in the folded form, the protein was first unfolded in the presence of GuHCl at pH 2.0 in D_2O and subsequently refolded in neutral (buffered) D_2O solution [63]. However, in all cases, the kinetic constants, determined for a potential jump to the redox potential at a given SAM by SERR spectroscopy, were found to be the same.

TR-SERR experiments on Ag electrodes coated with SAMs with $x \geqslant 10$ in D_2O afforded relaxation constants equal to those determined in H_2O whereas for C_5-SAM-coated Ag electrode, the experiments yielded a 1.3 times smaller value in D_2O (Table 1). At C_1-SAM, the relaxation constant was found to be smaller by a factor of 2.5 as compared to the value in H_2O. Next, we carried out distance-dependent TR SERR measurements in H_2O buffer solution including 6.5% sucrose to match the viscosity of D_2O. Again, no changes of the relaxation constants were noted at long chain lengths whereas at C_5-SAM a value of 100 s^{-1} was determined that is smaller by a factor of 1.3 than in H_2O buffer in the absence of sucrose. The same ratio of the relaxation constants was found for C_1-SAM in the presence and in the absence of sucrose.

On the other hand, step-scan SEIRA experiments on C_5-SAM-coated Au electrodes afford a value for k_{relax} of 800 s^{-1} that does not exhibit H/D or viscosity sensitivity within the experimental error of 10%.

3.4. Overpotential-dependence of the heterogeneous electron transfer rate constant

The relaxation constants of the interfacial redox process of Cyt-c, k_{relax}, were determined as a function of the overpotential for C_{15}-SAM-coated electrodes in H_2O buffer. Here, we have employed potential jumps from an initial potential $E_i \geqslant E^0$ to a final potential $E_f < E^0$ such that the amount of the overpotential $\eta = E_f - E^0$ was stepwise increased. Such measurements have been previously carried out with Cyt-c immobilised on SAM-coated Ag electrodes (Table 2) [27]. In this work, we have extended the experiments to C_{15}-SAM-coated Au and Au–SAM–Ag hybrid electrodes, probing the relaxation process by rapid-scan SEIRA and TR SERR spectroscopy, respectively. SEIRA spectroscopy allows monitoring the redox process of the immobilised Cyt-c on the basis of various redox-sensitive amide I bands at 1693 and 1673 cm^{-1} which have been assigned to the β-turn type III segment 67–70 of the reduced and oxidised Cyt-c, respectively (Figs. 6 and 7) [13]. For zero-driving force ($\eta = 0$ V), k_{relax} was determined to be 0.29 s^{-1} using the average of the relaxation constants derived from the intensity changes of the individual redox-sensitive amide bands (Table 2). This value is by a factor of 2 larger than the corresponding value determined for Ag electrodes under otherwise identical conditions. Increasing the driving force, however, leads to a much smaller increase of k_{relax} as compared to the C_{15}-SAM-coated Ag electrode with 0.35 and 0.77 s^{-1} at $\eta = -0.24$ V and $\eta = -0.44$ V, respectively. A further increase of the driving force ($\eta = -0.49$ V) causes only a slight increase of k_{relax} (Table 2). These observations are in sharp contrast to the results obtained for the C_{15}-SAM-coated Ag electrode for which a substantially larger overpotential-dependent increase of k_{relax} was noted [27].

A comparably unprecedented behaviour is found for the Au–SAM–Ag hybrid electrode [45,50]. This device is based on an electrochemically roughened Ag electrode, coated by a SAM of 11-amino-1-undecanethiol (AUT) which in turn is covered by a 15-nm thick Au film. The Au surface is then functionalised by a (carboxyl-terminated) C_{15}-SAM to allow for Cyt-c binding. The hybrid electrodes offer the advantage of combining the optical properties of Ag with the electrochemical stability of Au [45]. Moreover, the dielectric spacer between the two metals promotes plasmon excitation such that the intensity of the SERR spectrum of Cyt-c immobilised on the outer C_{15}-SAM layer of the Au film is comparable to that observed for Cyt-c at C_{15}-SAM Ag electrodes. The SERR spectra with 413-nm excitation afford qualitatively the same results as observed for the Ag-only electrode system, i.e. with no contribution from non-native species at long chain lengths [45,50]. ET of the immobilised Cyt-c on C_{15}-SAM-coated

Table 2
Relaxation constants for the interfacial redox process as a function of the overpotential of Cyt-c immobilised on different electrode systems.[a]

SAM	Ag (SERR)[b]		Au (SEIRA)		Au–SAM–Ag (SERR)	
	$-\eta$ (V)	k_{relax} (s^{-1})	$-\eta$ (V)	k_{relax} (s^{-1})	$-\eta$ (V)	k_{relax} (s^{-1})
C_{15}	0	0.15	0	0.29	0	0.77
	−0.05	0.26			−0.05	1.2
	−0.1	0.60			0.1	1.2
	−0.13	0.80				
	−0.2	1.5	−0.24	0.35	−0.2	4.9
	−0.3	2.88			−0.3	8.2
	−0.4	3.73	−0.44	0.77	−0.45	9.0
	−0.6	3.91	−0.49	0.83	−0.5	9.6
C_{10}	0	53	0	72	0	45
	−0.19	240				
	−0.22	320	−0.25	180	−0.2	167
	−0.29	370				
	−0.39	500			−0.4	313
	−0.44	550				

[a] The data were obtained by TR-SERR experiments with potential jumps from +0.1 V to different final potentials E_f corresponding to an overpotential of $\eta = E_f - E^0$. The average error associated with the determination of k_{relax} was ±10%. The k_{ET} values for Cyt-c on C_{15}-SAM-coated electrodes as discussed in the text were calculated according to Eq. (2).

[b] Data taken from Refs. [27,42].

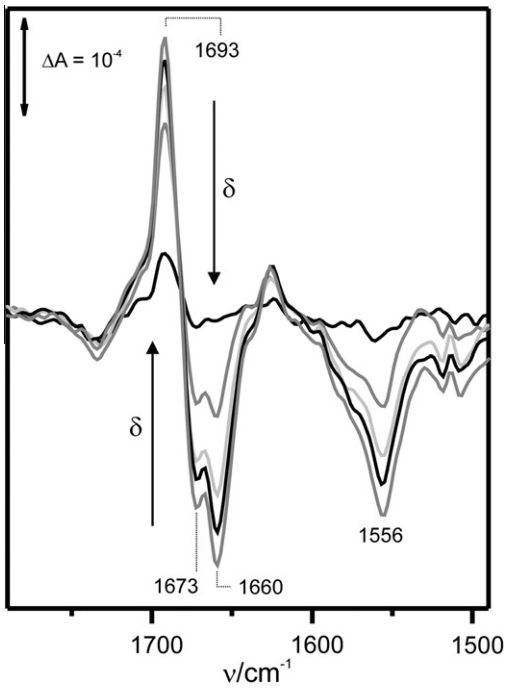

Fig. 6. Rapid scan SEIRA difference spectra of Cyt-c immobilised on a C_{15}-SAM-coated Au electrode for a potential jump from +0.125 V to −0.4 V. The reference spectrum refers to the initial potential of +0.125 V. The individual spectra that are displayed refer to delay times of 0.5, 1, 2.5, 5, and 15 s. The solid arrows indicate the direction of increasing delay times. Further details of the experiments are given in the text.

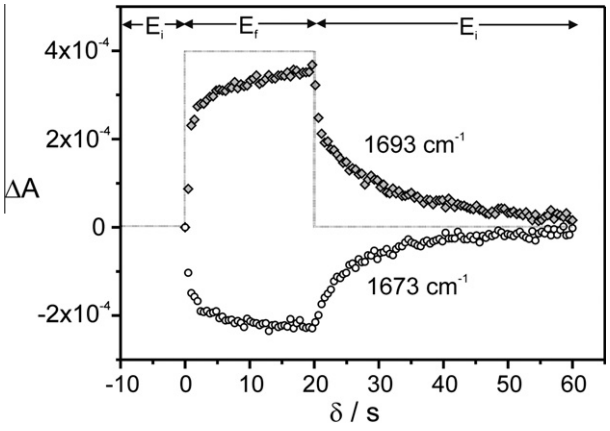

Fig. 7. Time-dependent changes of the intensities of the 1693 and 1673-cm^{-1} bands determined from rapid-scan SEIRA difference spectroscopy of Cyt-c on C_{15}-SAM-coated Au electrode. The data were obtained from potential jump experiments from +0.125 V (E_i) to −0.4 V (E_f). The reference spectrum refers to the initial potential of +0.125 V. Further details of the experiments are given in the text.

Au–SAM–Ag electrodes proceeds via different regimes. For the oxidation reaction, the first step is electron tunnelling from Cyt-c through the outer C_{15}-SAM coating to the Au film, followed by metallic conductance across the Au film in the second step, and, in the third step, again by electron tunnelling through the AUT SAM to the Ag electrode. The electron transport through the metallic Au film is much faster than the tunnelling processes for which the rates depend on the thickness of the respective SAMs. Thus, one intuitively expects that the ultimate rate-limiting step is tunnelling through the outer C_{15}-SAM coating. This conclusion is in fact confirmed by a recent systematic analysis of the ET processes of Cyt-c at C_x-SAM-coated Au–SAM–Ag devices in which the thickness of the inner and the outer SAMs was varied [50]. Consequently, we can compare the ET dynamics of Cyt-c on C_{15}-SAM-coated Au–SAM–Ag electrodes directly with those at C_{15}-SAM-coated Au and Ag electrodes. In this respect, the experimentally determined rate constant is found to be higher by a factor of ca. 2.6 and 5.1 than for the Au and Ag electrode system, respectively. However, the overpotential is weaker than for Ag albeit more pronounced than for Au (Table 2).

Analogous experiments were carried out with Cyt-c immobilised on C_{10}-SAM coatings for all three electrode systems. The corresponding values for k_{relax} are listed in Table 2.

4. Discussion

Electrostatic binding of Cyt-c to electrodes coated with carboxyl-terminated SAMs proceeds mainly via two binding domains [46,48]. The high affinity domain (BD3), involving the lysine residues 72, 73, 79, 86, and 87, is, however, associated with a distinctly lower average electron tunnelling probability than the medium-affinity binding domain (BD2), defined by lysine residues 25 and 27. Thus, optimum electron tunnelling requires the rotational diffusion of the immobilised Cyt-c, which at C_{15}-SAM-coated Ag electrodes proceeds with the rate constant k_{orient} larger than 6000 s^{-1} as determined by TR SERR spectroscopy with 514 nm excitation [42]. This approach is based on the orientation-dependent preferential enhancement of heme modes of different symmetry under Q-band excitation. In contrast, the kinetic data obtained by TR SERR spectroscopy with 413-nm (Soret band) excitation as used in this work represent relaxation constants k_{relax} describing the reduction and oxidation of the heme. The latter experiments afford the relaxation of the individual oxidised and reduced Cyt-c species A_i following a potential jump. This relaxation is generally described by a mono-exponential function

$$A_i(\delta) = A_i(E_i) \cdot \exp(-k_{relax} \cdot \delta) \quad (1)$$

where $A_i(\delta)$ and $A_i(E_i)$ are the concentration of the species under consideration at the delay time δ and at the initial potential E_i (δ = 0 s). For C_{15}-SAM-coated Ag electrodes, k_{relax} is 0.15 s^{-1} at zero-driving force and it increases to nearly 4 s^{-1} upon raising the modulus of the overpotential [27]. Thus, k_{orient} is always distinctly larger than k_{relax} implying that at C_{15}-SAM-coated Ag electrodes the TR-SERR experiments directly probe electron tunnelling. In a first approximation, this is also true for C_{10}-SAM coatings where, at zero-deriving force, k_{relax} is ca. 50 s^{-1} compared to k_{orient} = 390 s^{-1} [42]. However, with increasing driving force, k_{relax} approaches k_{orient} which becomes the limiting value of the overpotential-dependence of k_{relax}. For C_5-SAM coatings, even at zero-driving force, the same values were determined for k_{relax} and k_{orient} [42]. Under these conditions, the overall kinetics of the interfacial ET is the result of the convolution of protein dynamics and electron tunnelling and should, in fact, follow a more complex kinetic behaviour that deviates from a mono-exponential decay [49]. However, within the experimental accuracy and due to the limited time-resolution of the TR-SERR experiments, the description of the relaxation processes does not justify fit functions that are more complex than a single exponential.

On the other hand, the increasing deviations for the values of k_{relax} for C_x-SAM coatings with $x \leqslant 10$ determined in this work and those obtained earlier in our group (Table 2, [12]) may be related to the fact that the mono-exponential approximation becomes less accurate for thinner SAM coatings. In contrast to the fit of Eq. (1) to the data in this work, we have previously employed a fit of the linearized Eq. (1) [12], which might overestimate fast events in the case of a complex kinetic behaviour. As a consequence, the previous study afforded increasingly larger k_{relax} values for C_x-SAM coatings with $x \leqslant 10$, compared to the present results.

In addition, the present spectra analysis is not restricted to the ν_4 and ν_3 band region as previously [12] but covers a wider spectral range, thereby increasing the accuracy specifically for thinner SAMs where contributions from the non-native states gain importance. This different spectra analysis may also account for the slight differences of the redox potentials determined from stationary SERR experiments (Table 1, [26]).

4.1. Electric-field effects on electron tunnelling

At C_{15}-SAM-coated Ag electrodes, i.e. in the tunnelling regime, k_{relax} determined from the TR-SERR experiments is related to the electron tunnelling rate constant k_{ET} for the reduction of the heme according to

$$k_{ET} = \frac{k_{relax} \cdot K_{eq}}{(1 + K_{eq})} \tag{2}$$

where K_{eq} is the redox equilibrium constant

$$K_{eq} = \exp\left(-\frac{(E - E^0) \cdot n \cdot e}{k_B T}\right) \tag{3}$$

with E, e, k_B, and T denoting the electrode potential, the elementary charge, the Boltzmann constant, and the temperature, respectively. Thus, for zero-driving force corresponding to $\eta = E - E^0 = 0$ V, we obtain $k_{ET} = 2k_{relax}$.

Eqs. (2) and (3) also hold for the relaxation constants derived from the mono-exponential fits to intensity changes of the SEIRA bands at 1693 and 1673 cm^{-1} measured for Cyt-c on C_{15}-SAM-coated Au electrodes, since these changes seem to proceed instantaneously with the heterogeneous ET [13]. This conclusion is very plausible as the amide I band changes most likely reflect the redox-linked protein structural changes, i.e. the protein reorganisation, which occurs much faster than long-distance electron tunnelling considered in this work. Furthermore, even for C_5-SAM-coated Au electrodes, k_{relax} at zero-driving force was found to be unaffected by an increase of the viscosity to 1.2 cp, implying that protein reorientation is faster than electron tunnelling. Thus, we can safely conclude for both the Ag and the Au electrode, the C_{15}-SAM coating refers to a regime, in which, regardless of the overpotential, electron tunnelling is the rate-limiting step. The same considerations hold for the Au–SAM–Ag electrode.

Electron tunnelling between an immobilised redox site and the electrode can be described according to Eq. (4) [64,65]

$$k_{ET}(\eta) \approx \frac{\pi}{\hbar} \cdot |V|^2 \cdot \rho \cdot \exp(-\beta \cdot d) \cdot erfc\left(\frac{\lambda + e\eta}{\sqrt{4\lambda k_B T}}\right) \tag{4}$$

where λ, V, and ρ are the reorganisation energy, the electronic coupling parameter, and the density of states in the electrode, respectively, and $erfc(z)$ is the complementary error function. The exponential function in Eq. (4) represents the distance-dependence of the electronic coupling parameter with d and β denoting the ET distance and the tunnelling decay parameter. Upon relating the ET rate constant at a given overpotential $k_{ET}(\eta)$ with the rate constant at zero-driving force ($\eta = 0$ V), $k_{ET}(0)$, one obtains

$$\frac{k_{ET}(\eta)}{k_{ET}(0)} = \frac{erfc\left(\frac{\lambda + e\eta}{\sqrt{4\lambda k_B T}}\right)}{erfc\left(\frac{\lambda}{\sqrt{4\lambda k_B T}}\right)} \tag{5}$$

which has been employed to determine the reorganisation energy for the electron tunnelling process of Cyt-c immobilised on a C_{15}-SAM-coated Ag electrode (Fig. 8) [27]. In this way, a reorganisation of 0.22 eV has been determined.

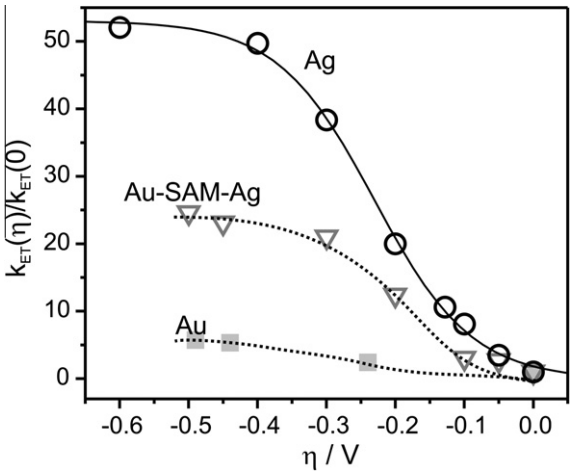

Fig. 8. Overpotential-dependence of the heterogeneous electron transfer rate constant k_{ET} for Cyt-c immobilised on C_{15}-SAM-coated electrodes. The black (open circles), dark gray (open triangles), and light gray (solid squares) symbols refer to the data obtained from an Ag (TR SERR), Au–SAM–Ag (TR SERR), and Au electrode (rapid-scan SEIRA) (Table 2). The solid line represents a fit of Eq. (5) to the experimental data for the Ag electrode, taken from Ref. [27], whereas in the case of Au and Au–SAM–Ag, dotted lines are included to guide the eyes. Further details of the experiments and the data analysis are given in the text.

We now consider the overpotential-dependence of k_{ET} determined for Cyt-c on C_{15}-SAM-coated Au and Au–SAM–Ag hybrid electrodes, determined by rapid-scan SEIRA and TR SERR spectroscopy, respectively. In both cases, k_{ET} displays a drastically weaker increase with increasing $|\eta|$ (Fig. 8). This discrepancy with respect to Ag can hardly be rationalised on the basis of Eq. (5) since it would imply a physically meaningless low value for reorganisation energy, specifically for the SAM-coated Au electrode. Instead, in a first approximation, one may expect that λ should be similar for Cyt-c, independent of the kind of the supporting metal (*vide infra*).

The crucial electrochemical property that is different for SAM-coated Au and Ag electrodes is the potential of zero-charge E_{pzc}. This quantity depends of the crystalline structure of the metal and the type of SAM-coating and has been determined to be –0.45 and –0.2 V for C_{10}-SAM-coated Ag and Au–SAM–Ag electrodes [50]. It is reasonable to assume that the values for the respective C_{15}-coated electrodes are very similar [66]. Correspondingly, we assume $E_{pzc} = -0.05$ V for C_{15}-SAM-coated Au electrodes taking into account literature data [66]. The difference between the actual electrode potential E and E_{pzc} is proportional to the electric field in the SAM/Cyt-c interface [26,54]. Thus, the ET reactions of Cyt-c at Au and Ag electrodes take place under the action of opposite electric fields, and moreover, experience increasing field strengths for Au but decreasing strengths for Ag upon increasing the driving force for reduction, i.e. with increasingly negative overpotential $\eta = E - E^0$, taking into account the redox potentials of −0.01 V and +0.04 V for Cyt-c on C_{15}-SAM-coated Ag and Au electrodes, respectively [12,13]. Accordingly, the electric field variation for the Au–SAM–Ag electrode lies in between those for the Ag and Au electrode as it first decreases until $E = E^0$ ($E^0 = +0.04$ V [50]) and then increases again for $E < E_{pzc}$.

As shown previously for the charge recombination in photosynthetic systems, ET transfer reactions may be accelerated or slowed down by an externally applied electric field (e.g. [67–69]). These and related experimental data have been attributed to an electric-field dependent variation of the free-energy term of the Marcus equation [67,70], as the electric-field dependence of the electronic parameter is usually very small [71]. Accordingly, we have adopted these approximations and used a simple electric-field dependent correction to the free-energy term to rationalise

the present kinetic data. These approximations imply that, due to the fast protein re-orientation at C_{15}-SAM coatings (*vide supra*), any electric-field dependent differences in the orientational distribution of the immobilised Cyt-c on the three electrode systems have no effect on the ET kinetics, i.e. ET always takes place via the optimum electron coupling.

Assuming a linear relationship between E_{pzc} and the electric field strength [26,54], the actual driving force may be given by an effective overpotential η_{eff} according to Eq. (6)

$$\eta_{eff} = \eta + [a_0 + a_1 \cdot (E - E_{pzc})] = (E - E^0) + [a_0 + a_1 \cdot (E - E_{pzc})] \quad (6)$$

where a_0 and a_1 are constants. Then Eq. (5) is modified to

$$\frac{k_{ET}(E)}{k_{ET}(0)} = \frac{erfc\left(\frac{\lambda + e(E-E^0) + e[a_0 + a_1(E-E_{pzc})]}{\sqrt{4\lambda k_B T}}\right)}{erfc\left(\frac{\lambda + e[a_0 + a_1(E^0 - E_{pzc})]}{\sqrt{4\lambda k_B T}}\right)} \quad (7)$$

Eq. (7) is then fitted to the experimental data for C_{15}-SAM-coated Ag and Au–SAM–Ag electrodes setting $\lambda = 0.22$ eV [27] in both cases and using the experimentally determined redox potentials of −0.01 and +0.04 V for Cyt-c on C_{15}-SAM-coated Ag and Au–SAM–Ag electrodes, respectively [26,50]. Thus, a good and consistent description is achieved with the same value for a_1 (ca. 0.01) and a_0 of ca. −0.004 and −0.04 V for Ag and Au–SAM–Ag, respectively (Fig. 9). With these parameters, the ratio of the ET rate constants at zero-driving force for Cyt-c at C_{15}-SAM-coated Ag and Au–SAM–Ag, $k_{ET}(0, Ag)/k_{ET}(0, AuAg)$, is calculated to be ca. 0.4 which is in qualitative agreement with the experimental value of 0.2 (Table 2).

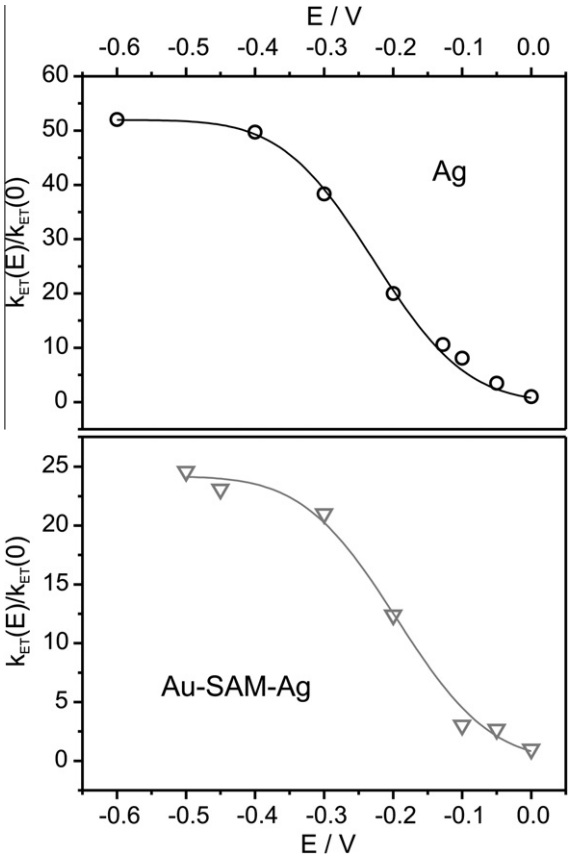

Fig. 9. Potential-dependence of the heterogeneous electron transfer rate constant k_{ET} for Cyt-c immobilised on C_{15}-SAM-coated Ag (top) and Au–SAM–Ag (bottom) electrodes. The black (open circles) and dark gray (open triangles) symbols refer to the data obtained from a Ag and Au–SAM–Ag electrode, respectively. The solid lines represent fits of Eq. (7) to the experimental data. Further details of the experiments and the data analysis are given in the text.

The low number of experimental values for $k(\eta)$ of Cyt-c at the C_{15}-SAM-coated Au electrode does not justify a fit of Eq. (7) with two adjustable parameter but introducing the additional constraint of $k_{ET}(0, Ag)/k_{ET}(0, Au) = 0.5$ (Table 2), it turns out that a reasonable reproduction of the experimental data may be achieved by a similarly low value of a_0 as for Ag and Au–SAM–Ag but a distinctly more negative value for a_1.

Despite the crudeness of the present approach, the results allow concluding that electron tunnelling is controlled by the interfacial electric field. This electric-field dependence does not only account for the different overpotential-dependencies at the various electrodes. In addition, it provides a satisfactory explanation also for the different $k_{ET}(0)$ values although for this quantity, electrode-specific differences of ρ and V cannot be neglected *a priori*. However, the differences for the electronic densities of states ρ of the three electrode systems are expected to be relatively small [72,73] and, in particularly, cannot account for variations of $k_{ET}(0)$ by factor of more than 5. This is also true for the effect of the different tilt angles of the mercaptanes on Ag and Au surfaces [74–76], which in principle might alter the electronic coupling V. However, in particular the 2.5 larger $k_{ET}(0)$ for Au–SAM–Ag compared to Au argues against this interpretation. Thus, we conclude that also differences for $k_{ET}(0)$ at the various electrodes are largely due to the different interfacial electric fields.

Note that for all three electrodes, the parameter a_0 was found to be very small. Since this quantity can be considered a correction term for the reorganisation energy, it implies that λ is largely the same for all three systems and thus independent of the electric field (*vide supra*) [70]. A more specific and quantitative description of the electric-field effect, however, would require a more elaborate description of the interfacial electric field which is beyond the scope of the present work.

Extending this analysis to the overpotential measurements to C_{10}-SAM-coated electrodes (Table 2) is problematic due to the interferences of electron tunnelling with protein dynamics which for Ag has been shown to proceed on comparable time scales already at moderate overpotentials [42].

4.2. Protein re-orientation and reorganisation of the hydrogen bond network in the protein/SAM interface

At C_x-SAM coatings at Ag electrodes with $x \leqslant 5$, the interfacial ET is controlled by the orientational distribution and dynamics of the immobilised protein. In fact, the dynamics of the overall redox process is viscosity-dependent as reflected by the decrease of k_{relax} by a factor of 1.3 from the pure H_2O buffer to the sucrose containing solution at 1.2 cp. This decrease is the same for C_5-SAM and C_1-SAM coatings at the Ag electrode, implying that a potential electric-field dependence of the viscosity effect is beyond the detection limit.

Conversely, the decrease of k_{relax} induced by substituting H_2O against D_2O buffer varies with the thickness of the SAM. Whereas at C_5-SAM coatings on Ag electrodes $k_{relax}(H_2O)/k_{relax}(D_2O)$ is 1.3 and thus identical to the viscosity-induced decrease of the relaxation constant, the ratio increases to 2.5 at C_1-SAM coatings. Taking into account the intrinsically higher viscosity of D_2O buffer solution that corresponds to that of a H_2O buffer/sucrose solution at 1.2 cp, one may evaluate a true H/D kinetic isotope effect (KIE) at C_1-SAM coatings of ca. 2.0. At C_5-SAM coatings, however, the observed decrease of k_{relax} in D_2O appears to be largely a viscosity effect. An upper limit of the H/D KIE in that case, however, may be estimated to be 1.1, taking into account the experimental accuracy of the determination of k_{relax}. In this respect, the KIEs determined in this work are actually somewhat smaller than the previously reported values for which the viscosity contribution was not

considered [12]. For C_5-SAM-coated Au electrodes, TR SEIRA experiments reveal no viscosity dependence and no H/D KIE for k_{relax}, which in addition is distinctly larger ($800\ s^{-1}$) than for Ag. This finding indicates that at C_5-SAM-coated Au electrodes protein re-orientation is much faster than on the Ag electrode and does not appear to constitute the rate-limiting step of the interfacial redox process.

An increased viscosity is likely to slow-down the large-scale motions of the immobilised protein, specifically the change of the binding site via rotational diffusion [42,46]. However, also small-amplitude fluctuations of water molecules in the Cyt-c/SAM contact region are affected as concluded from recent studies on covalently attached Cyt-c that as well reveals a viscosity effect of k_{relax} in the non-tunnelling regime [47].

The molecular origin of the H/D KIE may be based on two different processes. First, the above-mentioned fluctuations of water molecules in the interface between Cyt-c and the SAM have been shown to be important for a fine adjustment of the protein orientation with respect to the surface and thus for a more efficient electronic coupling [46,48]. Such motions inevitably include a re-arrangement of the hydrogen bond network, which is part of the thermal fluctuations of the system and is not a pre-requisite for the ET although they may affect the rate of electron tunnelling. Second, the change of the charge distribution at the redox site associated with the ET requires a re-arrangement of the hydrogen bond network, specifically albeit not exclusively, in the immediate surroundings of the heme as a part of the structural reorganisation [12,27]. It might be that this process involves short-range proton translocations, corresponding to a proton-coupled electron transfer mechanism. Such a mechanism has been proposed in our previous study [12,27] and, recently, discussed in more detail by Davis and Waldeck [43] in the context of further experimental and theoretical data [30,77,78]. In any case, the fact that the same KIE is observed regardless of the H/D exchange method (*vide supra*) implies that the kinetically relevant protons are easily exchanged.

Both processes, the fluctuations of the hydrogen bond network in the Cyt-c/SAM interface, and the redox-linked re-arrangement of the internal hydrogen bond network, may account for the H/D KIE effects observed in this work. In each case, displacements of (partially) charged groups and protons are involved which are likely to be affected by the interfacial electric field. The decrease of the H/D-sensitive relaxation constant from C_5-SAMs to C_1-SAMs points to an electric-field dependent increase of the activation energy required for the underlying processes. Moreover, also the KIE itself increases with increasing field strength (i.e., from C_5- to C_1-SAMs).

4.3. Overall electric-field effect on the interfacial electron transfer process

Due to the electric-field dependent decrease of the protein re-orientation rate, the experimentally determined values for k_{orient} and k_{relax} are essentially the same for C_5-SAM-coated Ag electrodes [42]. Under these conditions, the interfacial redox process may be described by a convolution of protein re-orientation and orientation-dependent electron tunnelling probabilities [42,48]. Most likely, the majority of the proteins is bound to the SAM surface via the high affinity domain BD3 for which the average electronic coupling parameter is predicted to be lower by a factor of ca.10 as compared to the medium-affinity binding domain BD2 for which the largest average electron coupling parameter has been calculated [46]. As a consequence, electron tunnelling should be faster by a factor of 100 for Cyt-c bound via BD2 than via BD3. Thus, the lower limit for the heterogeneous ET rate (slow protein re-orientation) should be given by the average electron tunnelling rates via BD3 whereas the upper limit (fast protein re-orientation) results from electron tunnelling via BD2. Then, the upper limit of the ET rate at C_5-SAM coatings may be estimated on the basis of distance-dependent term in Eq. (4) by extrapolating the rate constants in the electron tunnelling regime (C_{15}- and C_{10}-SAMs) to the C_5-SAM system [12]. This leads to a limiting rate constant of $6 \times 10^5\ s^{-1}$ that is four orders of magnitude larger than the experimentally observed value for k_{relax}. This difference has to be compared with the gap of two orders of magnitude between the lower and upper limit for orientation-dependent tunnelling as derived from the MD simulations. Moreover, this discrepancy is even more severe considering the kinetics at the C_1-SAM since the experimental value for k_{relax} even drops compared to the C_5-SAM. Just due to the distance dependence one would have expected an increase of the rate constant by a factor ca. 500, independent of the protein orientation and orientational dynamics.

These considerations imply that with increasing electric field strength at short distances the electron tunnelling rate is drastically slowed down. Most likely, in this high-field regime, the electric-field dependence of the tunnelling rate is more complex than included in Eqs. (7) and (6). Specifically, the assumption of an electric-field independent electronic coupling parameter (Eq. (4)) might not be justified. In fact, the effect of the interfacial electric field on the electronic coupling parameter has not been considered in the previous calculations of the electron tunnelling probabilities for the various orientations of Cyt-c [46,48].

On the basis of this interpretation one can also understand the ca. 1000 times smaller relaxation constant for SAMs of the same length as C_{10} but which carry a phosphonate instead of a carboxylate head group [15]. Due to the significantly higher charge density on the phosphonate-terminated SAM, the interfacial electric field strength is larger than for the carboxyl-terminated SAM, causing the drastic decrease of the electron tunnelling rate constant. The same explanation holds for the ca. 40 times lower k_{ET} at Ag electrodes covered with sulphate anions compared to the C_1-coated Ag electrode [58].

The interfacial redox process of Cyt-c on electrodes involves four different elementary steps, that are electron tunnelling coupled with the reorganisation of the protein structure, protein re-orientation on the SAM surface, and the re-arrangement of the hydrogen bond network in the protein/SAM interface and possibly also inside the protein. The individual steps depend on the local electric field, which in turn is controlled by the distance- and potential-dependence of the surface charge density on the SAM σ_S and of the quantity $(E - E_{pzc})$ [26,54]. The interplay of these electric-field dependent steps results in a complex overall potential- and distance-dependent kinetic behaviour.

Since the surface change density σ_S and $(E - E_{pzc})$ are different for different metals (i.e. Ag and Au) and the different types of coatings (i.e., charged, polar, or hydrophobic SAM surfaces) one may readily understand why the experimentally determined rate constants may differ among the various electrode/SAM systems but display, *in toto*, a similarly shaped distance-dependence [12,15,23,25,29–32,36]. At C_5-SAM-coated Au electrodes, for instance, k_{relax} at zero-driving force ($E = E^0$) is more than 6 times larger than in the case of Ag. This difference can be attributed to the fact that $|E^0 - E_{pzc}|$ is smaller for Au and, hence, also the electric field is weaker for Au than for Ag (*vide supra*) such that both electronic tunnelling and, as supported by the lack of a significant viscosity and H/D KIE effect, also protein re-orientation and hydrogen bond fluctuations are faster. On the other hand, an electrochemical investigation by Davis and Waldeck [43] reported a viscosity-corrected H/D KIE of ca. 1.2 for Cyt-c immobilised on Au electrodes coated by mixed carboxyl- and hydroxyl-terminated SAMs of 5 and 4 methylene groups, respectively. This difference compared to the present results is evidently due to the mixed monolayer that, compared to the pure carboxyl-terminated SAM used in this work,

affords a ca. 6 times larger k_{relax}, close to the rate constants of the viscosity- and H/D-dependent processes.

5. Conclusions

We have shown that the electric-field effects on protein motion, electron tunnelling, and hydrogen bond re-arrangements provide the basis for a consistent description of the present and previous experimental findings on the heterogeneous ET reaction of Cyt-c obtained for different electrode systems and SAM-coatings [12,15,23,25,29–32,36]. Moreover, these electric-field effects seem to constitute a general mechanism for interfacial processes of quite different redox proteins, since in each case the same elementary steps are involved. Details may be different depending on the surface charge of the protein's binding domains that may be either cationic, anionic, or hydrophobic and may contain heme or copper redox centers [51–55].

Acknowledgement

The work was supported by the DFG (Cluster of Excellence – UniCat).

References

[1] J.Ó.M. Bockris, A.K.N. Reddy, M. Gamboa-Aldeco, Modern Electrochemistry, vol. 2A, Kluwer, Academic, New York, 2000.
[2] J.Ó.M. Bockris, A.K.N. Reddy, Modern Electrochemistry, vol. 2B, Kluwer Academic, New York, 2000.
[3] A.M. Kuznetsov, J. Ulstrup, Electron Transfer in Chemistry and Biology an Introduction to the Theory, Wiley-VCH, Weinheim, 1998.
[4] O. Hammerich, J. Ulstrup, Bioinorganic Electrochemistry, Springer, New York, 2008.
[5] A.J. Bard, L.R. Faulkner, Electrochemical Methods: Fundamentals and Applications, Dekker, New York, 2000.
[6] F.A. Armstrong, Curr. Opin. Chem. Biol. 9 (2005) 110.
[7] K. Kneipp, M. Moskovits, H. Kneipp (Eds.), Surface-enhanced Raman Scattering: Physics and Applications, Springer, Berlin, 2006.
[8] F. Siebert, P. Hildebrandt, Vibrational Spectroscopy in Life Science, Wiley-VCH, Weinheim, 2007.
[9] S. Lecomte, H. Wackerbarth, T. Soulimane, G. Buse, P. Hildebrandt, J. Am. Chem. Soc. 120 (1998) 7381.
[10] H. Wackerbarth, U. Klar, W. Günther, P. Hildebrandt, Appl. Spectrosc. 53 (1999) 283.
[11] D.H. Murgida, P. Hildebrandt, Angew. Chem. Int. Ed. 40 (2001) 728.
[12] D.H. Murgida, P. Hildebrandt, J. Am. Chem. Soc. 123 (2001) 4062.
[13] N. Wisitruangsakul, I. Zebger, K.H. Ly, D.H. Murgida, S. Egkasit, P. Hildebrandt, Phys. Chem. Chem. Phys. 10 (2008) 5276.
[14] D.H. Murgida, P. Hildebrandt, Chem. Soc. Rev. 37 (2008) 937.
[15] D.H. Murgida, P. Hildebrandt, Phys. Chem. Chem. Phys. 7 (2005) 3773.
[16] K. Ataka, J. Heberle, J. Am. Chem. Soc. 126 (2004) 9445.
[17] K. Ataka, J. Heberle, Anal. Bioanal. Chem. 388 (2007) 47.
[18] R.G. Nuzzo, D.L. Allara, J. Am. Chem. Soc. 105 (1983) 4481.
[19] L.K. Prime, G.M. Whitesides, Science 252 (1991) 1164.
[20] M.J. Tarlov, E.F. Bowden, J. Am. Chem. Soc. 113 (1991) 1847.
[21] S. Song, R.A. Clark, E.F. Bowden, M.J. Tarlov, J. Phys. Chem. 97 (1997) 6564.
[22] T.M. Nahir, R.A. Clark, E.F. Bowden, Anal. Chem. 66 (1994) 2595.
[23] Z.Q. Feng, S. Imabayashi, T. Kakiuchi, K. Niki, J. Chem. Soc. Faraday Trans. 93 (1997) 1367.
[24] A. El Kasmi, J.M. Wallace, E.F. Bowden, S.M. Binet, R.J. Linderman, J. Am. Chem. Soc. 120 (1998) 225.
[25] A. Avila, B.W. Gregory, K. Niki, T.M. Cotton, J. Phys. Chem. B 104 (2000) 2759.
[26] D.H. Murgida, P. Hildebrandt, J. Phys. Chem. B 105 (2001) 1578.
[27] D.H. Murgida, P. Hildebrandt, J. Phys. Chem. B 106 (2002) 12814.
[28] C.E. Nordgren, D.J. Tobias, M.L. Klein, J.K. Blasie, Biophys. J. 83 (2002) 2906.
[29] K. Niki, W.R. Hardy, M.G. Hill, H. Li, J.R. Sprinkle, E. Margoliash, K. Fujita, R. Tanimura, N. Nakamura, H. Ohno, J.H. Richards, H.B. Gray, J. Phys. Chem. B 107 (2003) 9947.
[30] D.E. Khoshtariya, J.J. Wei, H.Y. Liu, H.J. Yue, D.H. Waldeck, J. Am. Chem. Soc. 125 (2003) 7704.
[31] D.H. Murgida, P. Hildebrandt, J. Wei, Y.F. He, H.Y. Liu, D.H. Waldeck, J. Phys. Chem. B 108 (2004) 2261.
[32] J.J. Wei, H.Y. Liu, K. Niki, E. Margoliash, D.H. Waldeck, J. Phys. Chem. B 108 (2004) 16912.
[33] J. Petrovic, R.A. Clark, H.J. Yue, D.H. Waldeck, E.F. Bowden, Langmuir 21 (2005) 6308.
[34] H.J. Yue, D.H. Waldeck, Curr. Opin. Solid State Mater. Sci. 9 (2005) 28.
[35] J.S. Xu, E.F. Bowden, J. Am. Chem. Soc. 128 (2006) 6813.
[36] H.J. Yue, D. Khoshtariya, D.H. Waldeck, J. Grochol, P. Hildebrandt, D.H. Murgida, J. Phys. Chem. B 110 (2006) 19906.
[37] K.B. Holt, Langmuir 22 (2006) 4298.
[38] M.T. de Groot, M. Merkx, M.T.M. Koper, Langmuir 23 (2007) 3832.
[39] X.U. Jiang, K. Ataka, J. Heberle, J. Phys. Chem. C 112 (2008) 813.
[40] K.L. Davis, B.J. Drews, H. Yue, D.H. Waldeck, K. Knorr, R.A. Clark, J. Phys. Chem. C 112 (2008) 6571.
[41] J.J. Feng, D.H. Murgida, T. Utesch, M.A. Mroginski, P. Hildebrandt, I. Weidinger, J. Phys. Chem. B 112 (2008) 15202.
[42] A. Kranich, H.K. Ly, P. Hildebrandt, D.H. Murgida, J. Am. Chem. Soc. 130 (2008) 9844.
[43] K.L. Davis, D.H. Waldeck, J. Phys. Chem. B 112 (2008) 12498.
[44] D. Millo, A. Ranieri, P. Gross, M. Borsari, H.K. Ly, P. Hildebrandt, G.J.L. Wuite, C. Gooijer, G. van der Zwan, J. Phys. Chem. C 113 (2009) 2861.
[45] J.J. Feng, U. Gernert, M. Sezer, U. Kuhlmann, D.H. Murgida, C. David, M. Richter, A. Knorr, P. Hildebrandt, I. Weidinger, Nano Lett. 9 (2009) 298.
[46] D.A. Paggi, D.F. Martín, A. Kranich, P. Hildebrandt, M. Martí, D.H. Murgida, Electrochim. Acta 54 (2009) 4963.
[47] H.K. Ly, M. Marti, D.F. Martin, D.A. Paggi, W. Meister, A. Kranich, I.M. Weidinger, P. Hildebrandt, D.H. Murgida, Chem. Phys. Chem. 11 (2010) 1225.
[48] D.A. Paggi, D.F. Martín, P.M. Biase, P. Hildebrandt, M.A. Martí, D.H. Murgida, J. Am. Chem. Soc. 132 (2010) 5769.
[49] S. Georg, J. Kabuss, I.M. Weidinger, D.H. Murgida, P. Hildebrandt, A. Knorr, M. Richter, Phys. Rev. E 81 (2010) 046101.
[50] M. Sezer, J.J. Feng, H.K. Ly, Y. Shen, T. Nakanishi, U. Kuhlmann, H. Möhwald, P. Hildebrandt, I. Weidinger, Phys. Chem. Chem. Phys. 12 (2010) 9822.
[51] J.Q. Chi, J.D. Zhang, J.E.T. Andersen, J. Ulstrup, J. Phys. Chem. B 105 (2001) 4669.
[52] K. Fujita, N. Nakamura, H. Ohno, B.S. Leigh, K. Niki, H.B. Gray, J.H. Richards, J. Am. Chem. Soc. 126 (2004) 13954.
[53] A. Kranich, H. Naumann, F.P. Molina-Heredia, H.J. Moore, T.R. Lee, S. Lecomte, M.A. de la Rosa, P. Hildebrandt, D.H. Murgida, Phys. Chem. Chem. Phys. 11 (2009) 7390.
[54] P. Zuo, T. Albrecht, P.D. Barker, D.H. Murgida, P. Hildebrandt, Phys. Chem. Chem. Phys 11 (2009) 7430.
[55] M.L. Vargo, C.P. Gulka, J.K. Gerig, C.M. Manieri, J.D. Dattelbaum, C.B. Masrks, N.T. Lawrence, M.L. Trawick, M.C. Leopold, Langmuir 26 (2010) 560.
[56] S. Döpner, P. Hildebrandt, A.G. Mauk, H. Lenk, W. Stempfle, Spectrochim. Acta A – Mol. Biomol. Spectrosc. 52 (1996) 573.
[57] S. Oellerich, H. Wackerbarth, P. Hildebrandt, J. Phys. Chem. B 106 (2002) 6566.
[58] H. Wackerbarth, P. Hildebrandt, Chem. Phys. Chem. 4 (2003) 714.
[59] P.M. De Biase, D.A. Paggi, F. Doctorovich, P. Hildebrandt, D.A. Estrin, D.H. Murgida, M.A. Marti, J. Am. Chem. Soc. 131 (2009) 16248.
[60] L. Rivas, D.H. Murgida, P. Hildebrandt, J. Phys. Chem. B 106 (2002) 4823.
[61] L. Mayne, Y. Patterson, D. Cesaroli, S.W. Englander, Biochemistry 31 (1992) 10678.
[62] S. Döpner, P. Hildebrandt, G.E. Heibel, F. Vanhecke, A.G. Mauk, J. Mol. Struct. 349 (1995) 125.
[63] J.E. Kim, M.A. Pribisko, H.B. Gray, J.R. Winkler, Inorg. Chem. 43 (2004) 7953.
[64] R.A. Marcus, J. Chem. Phys. 43 (1965) 679.
[65] C.E.D. Chidsey, Science 251 (1991) 919.
[66] P. Ramirez, R. Andreu, A. Cuesta, C.J. Calzado, J.J. Calvente, Anal. Chem. 79 (2007) 6473.
[67] D.J. Lockhart, C. Kirmaier, D. Holten, S.G. Boxer, J. Phys. Chem. 94 (1990) 6987.
[68] K. Lao, S. Franzen, M. Steffen, D. Lambright, R. Stanley, S.G. Boxer, Chem. Phys. 197 (1995) 259.
[69] M. Bixon, J. Jortner, J. Phys. Chem. 92 (1989) 7148.
[70] K. Seki, Traytak, M. Tachiya, J. Chem. Phys. 118 (2003) 679.
[71] S.H. Lin, C.Y. Yeh, G.Y.C. Wu, Chem. Phys. Lett. 166 (1990) 195.
[72] R.J. Forster, P. Loughman, T.E. Keyes, J. Am. Chem. Soc. 122 (2000) 11948.
[73] R.R. Ford, J. Pritchard, Trans. Faraday Soc. 67 (1971) 216.
[74] J.C. Love, L.A. Estroff, J.K. Kriebel, R.G. Nuzzo, G.M. Whitesides, Chem. Rev. 105 (2005) 1103.
[75] P.E. Laibinis, G.M. Whitesides, D.L. Allara, Y.T. Tao, A.N. Parikh, R.G. Nuzzo, J. Am. Chem. Soc. 113 (1991) 7152.
[76] C.D. Bain, E.B. Troughton, Y.T. Tao, J. Evall, G.M. Whitesides, R.G. Nuzzo, J. Am. Chem. Soc. 111 (1989) 321.
[77] S.A. Kang, K.R. Hoke, B.R. Crane, J. Am. Chem. Soc. 128 (2006) 2346.
[78] H. Decornez, S. Hammes-Schiffer, J. Phys. Chem. A 104 (2000) 9370.

8

Perturbation of the Redox Site Structure of Cytochrome *c* upon Tyrosine Nitration

Ly, H. K.; Utesch, T.; Díaz-Moreno, I.; Garía-Heredia, J. M.; Rósa, M. A. d. l.; Hildebrandt, P. Pertubation of the Redox Site Structure of Cytochrome *c* upon Tyrosine Nitration. *J. Phys. Chem. C* **2012**, 116, 5694–5702.

THE JOURNAL OF PHYSICAL CHEMISTRY B

Article

pubs.acs.org/JPCB

Perturbation of the Redox Site Structure of Cytochrome *c* Variants upon Tyrosine Nitration

H. Khoa Ly,[†] Tillmann Utesch,[†] Irene Díaz-Moreno,[‡] José M. García-Heredia,[‡] Miguel Ángel De La Rosa,[‡] and Peter Hildebrandt*[,†]

[†]Institut für Chemie, Technische Universität Berlin, Sekr. PC14, Straße des 17 Juni 135, D-10623 Berlin, Germany

[‡]Instituto de Bioquímica Vegetal y Fotosíntesis, cicCartuja, Universidad de Sevialla-CSIC, Avda Americo Vespucio 49, Sevilla 41092, Spain

Supporting Information

ABSTRACT: Post-translational nitration of tyrosine is considered to be an important step in controlling the multiple functions of cytochrome *c* (Cyt-*c*). However, the underlying structural basis and mechanism are not yet understood. In this work, human Cyt-*c* variants in which all but one tyrosine has been substituted by phenylalanine have been studied by resonance Raman and electrochemical methods to probe the consequences of tyrosine nitration on the heme pocket structure and the redox potential. The mutagenic modifications of the protein cause only subtle conformational changes of the protein and small negative shifts of the redox potentials which can be rationalized in terms of long-range electrostatic effects on the heme. The data indicate that the contributions of the individual tyrosines for maintaining the relatively high redox potential of Cyt-*c* are additive. Nitration of individual tyrosines leads to a destabilization of the axial Fe−Met80 bond which causes the substitution of the native Met ligand by a water molecule or a lysine residue for a fraction of the proteins. Electrostatic immobilization of the protein variants on electrodes coated by self-assembled monolayers (SAMs) of mercaptounadecanoic acid destabilizes the heme pocket structure of both the nitrated and non-nitrated variants. Here, the involvement of surface lysines in binding to the SAM surface prevents the replacement of the Met80 ligand by a lysine but instead a His-His coordinated species is formed. The results indicate that structural perturbations of the heme pocket of Cyt-*c* due to tyrosine nitration and to local electric fields are independent of each other and occur via different molecular mechanisms. The present results are consistent with the view that either tyrosine nitration or electrostatic binding to the inner mitochondrial membrane, or both events together, are responsible for the switch from the redox to the peroxidase function.

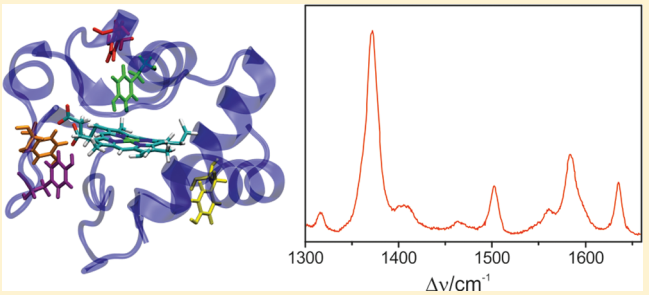

INTRODUCTION

Post-translational modifications of tyrosine residues in proteins represent essential steps for controlling biological functions, frequently related to signaling pathways of cells. Phosphorylation is known to play a key role in a variety of regulatory processes in cell growth, differentiation, and metabolism.[1,2] Nitration of tyrosines has been shown to occur in response to oxidative stress, induced by reaction with NO species.[2−4] The heme protein cytochrome *c* (Cyt-*c*) is one of the target proteins for which both types of tyrosine modifications have been demonstrated and the effects on Cyt-*c*'s biological functions have been widely studied.[5−19]

Cyt-*c* serves as an electron carrier in the mitochondrial intramembrane space transferring electrons from the membrane-bound cytochrome *c* reductase to cytochrome *c* oxidase where molecular oxygen is reduced to water.[20] In addition, Cyt-*c* has been shown to play crucial roles in programmed cell death. In one case, Cyt-*c* binds to the Apaf-1 protein, thereby causing its oligomerization and the subsequent activation of caspases.[21] Prior to this reaction sequence, however, Cyt-*c* has to be transferred through the mitochondrial membrane to the cytosol, a process that is most likely related to the function of Cyt-*c* as a catalyst of H_2O_2-dependent peroxidation of the mitochondria-specific cardiolipin.[22−24]

Nitration of tyrosine residues in Cyt-*c* has been proposed to be the initial event that triggers the change from the biological function in the respiratory chain to apoptosis.[6,14] In fact, in vitro studies revealed an enhanced peroxidase activity for Cyt-*c* upon Tyr nitration,[7,8,13] suggesting a transition from the electron-transfer to cardiolipin-peroxidation function. On the other hand, Tyr nitration inhibits caspase-9 activation and thus blocks the apoptosis signaling pathway.[9,13,15] In this respect, nitration may exert a similar inhibitory effect on caspase as phosphorylation as judged from studies on phosphomimetic Tyr mutants.[18,19]

Received: March 9, 2012
Revised: April 26, 2012
Published: April 27, 2012

   dx.doi.org/10.1021/jp302301m | *J. Phys. Chem. B* 2012, 116, 5694−5702

Peroxidase activity requires the accessibility of the heme iron by peroxide which is prohibited by the "native" closed heme pocket structure of Cyt-*c* with the axial coordination sites occupied by His18 and Met80. It is thus tempting to relate the catalytically active state of Cyt-*c* to a five-coordinated species lacking the Met80 ligand as it is formed upon electrostatic binding to model membranes.[25−27] Thus, strong electrostatic interactions, possibly in concert with Tyr nitration, have also been suggested to play a key role for the transformation of Cyt-*c* from an electron carrier to a catalyst.[27]

Clearly, a deeper understanding of the functional switch of Cyt-*c* as well as the molecular processes of the protein in apoptosis requires a profound knowledge of the structural consequences of Tyr nitration in Cyt-*c*. Following a previously established approach,[11,13−15] mutants of human Cyt-*c* have been expressed in which four out of five Tyr were substituted by Phe, allowing for a selective nitration of the remaining Tyr (Figure 1). In this work, we have employed resonance Raman

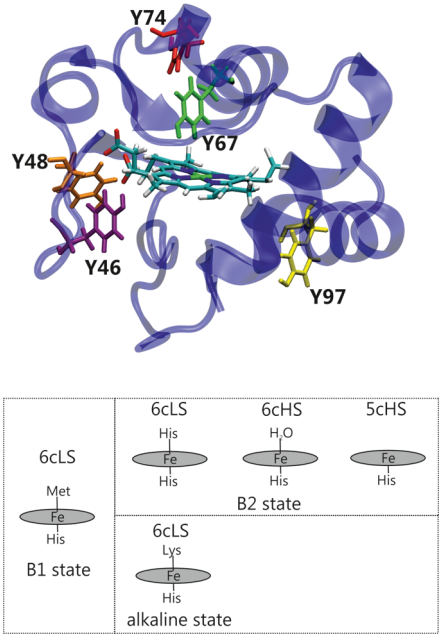

Figure 1. (Top) Three-dimensional structure of human Cyt-*c* (WT)[30] highlighting the heme and the tyrosine residues 46 (violet), 48 (orange), 67 (green), 74 (red), and 97 (yellow). (Bottom) Coordination patterns of the various states of Cyt-*c*.

(RR) spectroscopy to analyze the effect of the mutagenic and chemical modifications on the redox center, specifically the nitration-induced changes in the coordination pattern of the heme. Furthermore, the protein variants were electrostatically immobilized on electrodes coated by self-assembled monolayers (SAMs) of amphiphiles to mimic interactions with negatively charged membranes. Using surface-enhanced resonance Raman (SERR) spectroscopy and cyclic voltammetry (CV), these studies aim at investigating the combined effect of Tyr nitration and electrostatic fields on the heme structure as well as on the redox properties.

MATERIALS AND METHODS

Materials. 11-Mercaptoundecanoic acid (MUA) and sodium peroxodisulfate were purchased from Sigma Aldrich. Potassium hydrogen phosphate, potassium dihydrogen phosphate, potassium hydroxide and sodium dithionite were provided by Fluka (Merck, Germany). Ethanol (99.9%) was obtained from Fischer Scientific Company (Germany). Buffer solutions were prepared using Millipore water (Eschborn, Germany) with a resistance >18 MΩ. All chemicals were used as received.

Expression of Cyt-*c* Mutants. Recombinant human Cyt-*c*, either the *wild-type* species or the monotyrosine mutants in which all tyrosine residues but one (just that at the indicated numbered position, Figure 1) were substituted by phenylalanines, were expressed in *E. coli* DH5α and further purified by ionic exchange chromatography, as previously described.[11,13]

Nitration. Peroxynitrite synthesis and nitration of the different Cyt-*c* samples were carried out as reported previously,[11,13,14] with the following modifications: Fe^{3+}-EDTA concentration and the number of peroxynitrite additions were increased up to 1.5 mM and 10 bolus additions, respectively. The nitration reaction was performed under acidic conditions (pH 5.0). The resulting nitrated Cyt-*c* species were intensively washed with 10 mM potassium phosphate (pH 6.0). Nitrated monotyrosine Cyt-*c* mutants were separated from non-nitrated protein in a CM-cellulose column equilibrated with 1.5 mM borate, pH 9.0, using a 0−100 mM NaCl gradient. Nitrated Cyt-*c* eluted at a much lower salt concentration than native protein because of the extra negative charge of deprotonated tyrosyl anions, whose pK_a is modified by the strong electron-withdrawing effect of the NO_2 substituent at the 3-position.[5] The purity to 95% homogeneity of nitrated Cyt-*c* preparations was corroborated by SDS-Page and Western Blot using antibodies antinitrotyrosine (Biotem) to detect the presence of the NO_2 group. In addition, the molecular mass and the specifically nitrated tyrosine residue of each mutant were confirmed by tryptic digestion and MALDI-TOF (Bruker-Daltonics, Germany) analyses. Samples were concentrated up to 0.2−2.0 mM in 5 mM sodium phosphate buffer (pH 6.0).

Resonance Raman and Surface-Enhanced Resonance Raman Spectroscopy. RR and SERR spectra were acquired using the 413 nm line of a krypton ion laser (Coherent Innova 300c) coupled to a single-stage spectrograph (Jobin Yvon, LabRam 800 HR) equipped with a liquid-nitrogen-cooled back-illuminated CCD detector. The laser beam was focused using a Nikon 20× objective (N.A. 0.35) with a working distance of 20 mm. The laser power on the sample was 1 mW. Acquisition times ranged from 5 to 30 s depending on spectral quality and sample concentration.

RR measurements were carried out in a rotating quartz cuvette. Protein solutions were oxidized and reduced chemically using sodium peroxodisulfate and sodium dithionite, respectively. SERR measurements were conducted in a spectroelectrochemical cell described previously.[28] An electrochemically roughened silver ring (99%, Götz, Germany) coated with a SAM of MUA served as a working electrode. SER activation, SAM coating of the electrode, and subsequent protein immobilization followed the protocol described previously with minor modifications.[28,29] Briefly, prior to experiments the electrolyte solution (50 mM phosphate buffer at pH = 7.0, 9.0, or 12.0) was purged with catalytically purified oxygen-free argon for ca. 20 min. Then, the protein solution was added, yielding a final concentration of ca. 0.2 μM. Protein adsorption was achieved by incubating the working electrode for 30 min into the protein containing buffer solution at open circuit. All SERR experiments were performed in the presence of protein in solution and under Ar overpressure. Potentials cited in this

dx.doi.org/10.1021/jp302301m | J. Phys. Chem. B 2012, 116, 5694−5702

worked refer to an Ag/AgCl (3 M KCl) reference electrode (+0.21 V vs NHE).

Electrochemistry. CV experiments were performed in the spectroelectrochemical SERR cell (vide supra) connected to a CH Instrument 660 C potentiostat (Austin, TX). Determination of peak maxima and baseline subtraction were executed using the CHI software (CHI Electrochemical workstation, Version 6.13).

Molecular Dynamics Simulation. The crystallographic structure of human Cyt-*c* (3NWV)[30] served as template for the molecular dynamics (MD) simulations. The desired mutations and chemical modifications (nitration) were incorporated with VMD 1.8.7.[31] In addition to these sequence changes, each mutant carried a glycine instead of a serine at position 41, which is a naturally occurring apoptosis enhancing mutant.[30] Details of the MD simulations are given in the Supporting Information.

RESULTS

Resonance Raman Spectroscopy. RR spectroscopy is an ideal tool to probe the consequences of protein modifications on the redox center of Cyt-*c*. The present study is restricted to the ferric form of Cyt-*c*, generated by the addition of sodium peroxodisulfate, although in some cases a complete oxidation was not achieved. However, remaining traces of ferrous Cyt-*c* could readily be identified in the experimental spectra on the basis of its strongest band at ca. 1360 cm^{-1}. Besides this minor interference by the ferrous form, the experimental spectra particularly of the Tyr-nitrated protein variants display a substantial heterogeneity as reflected by asymmetric band shapes, shoulders, and extra bands not present in the RR spectrum of the native Cyt-*c* (Figure 2).

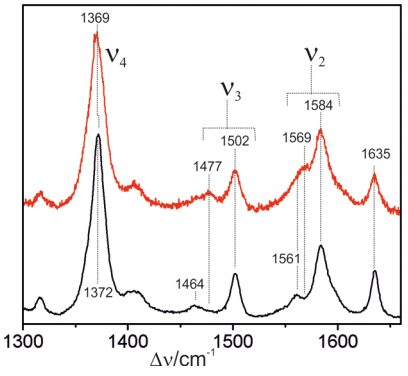

Figure 2. RR spectra of WT Cyt-*c* (bottom) and the Y48-NO_2 variant (top) in the marker band region.

These spectral changes specifically in the region of the modes ν_4, ν_3, and ν_2 indicate contributions from spin and coordination states that differ from the His-Met-coordinated low-spin configuration of the native protein, denoted as state B1.[26] For instance, the broad 1477 and 1569 cm^{-1} bands point to six- and five-coordinated high-spin (6cHS, 5cHS) species and the broadening of the bands at 1502 and 1584 cm^{-1} may originate from non-native six-coordinated low-spin (6cLS) configurations.[26]

In a first attempt to analyze these spectral changes quantitatively, we assumed that mutations and the respective tyrosine nitration solely affect the distribution among different spin and coordination states of the heme whereas the spectra of the individual components are the same in the various protein variants, i.e., the native 6cLS state B1 and the non-native 6cLS, 6cHS, and 5cHS species.[26] However, this component analysis failed to provide a satisfactory global fit to all experimental RR spectra (see Supporting Information). Each of the amino acid substitutions and the respective chemical modification of the single tyrosines cause subtle spectral alterations with frequency changes of ca. ±2 cm^{-1} and intensity variations of ca. 20% for nearly each of the component spectra. Such variations cannot be neglected within a global fit, although they are distinctly smaller than the differences between the component spectra of the individual spin and coordination states.

Thus, we have restricted the RR spectra analysis to the ν_3 band, which is most sensitive to changes of the spin and coordination state of the heme iron, and hence allows for a quantitative analysis in terms of the various coordination states involved. On the basis of a large body of experimental data, the frequency ranges of this band of 1478−1481, 1488−1491, 1500−1502, and 1504−1506 cm^{-1} in the ferric state are indicative of a 6cHS, 5cHS, a Met-His 6cLS, and a "N"-His (N = His, Lys) 6cLS configuration, respectively.[26,32] We thus have employed a band-fitting analysis to this spectral region using four bands with frequencies that were allowed to vary in the above-mentioned ranges in order to take into account the specific effects of the individual mutations and nitration (vide supra) (Figure 3; further details of the band fitting are given in

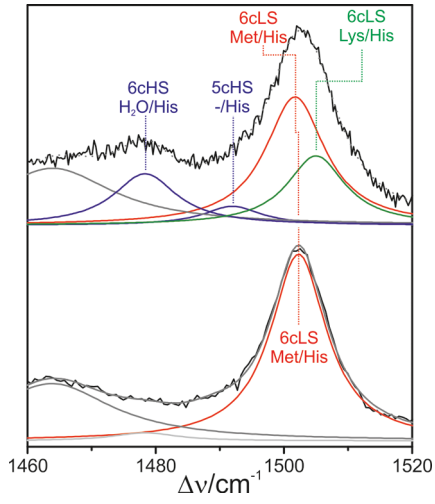

Figure 3. RR spectra in the ν_3 band region of the WT Cyt-*c* (bottom) and the Y46-NO_2 variant (top), including the fitted Lorentzian band shapes.

the Supporting Information). This procedure is associated with a relatively large error for determining weak contributions of the 6cHS state in the presence of a prevailing B1 contribution since the latter species gives rise to a broad band at 1465 cm^{-1} (ν_{28}) that overlaps with the ν_3 mode of the 6cHS state. After taking into account this interference, the relative intensities obtained by the fitting procedure were then converted into relative concentrations (Supporting Information)[33] as listed in Table 1.

The data for the non-nitrated protein variants indicate no changes of the coordination and spin state when all five Tyr (null mutant) are substituted by Phe. This is also true for the monotyrosine variants Y46 and Y74. However, a small but clearly detectable decrease of the native state B1 by ca. 15% is

dx.doi.org/10.1021/jp302301m | J. Phys. Chem. B 2012, 116, 5694−5702

Table 1. Relative Contributions of the Various Spin and Coordination States in Nitrated and Non-nitrated Cyt-*c* Variants (in %)

	native	non-native		
	B1 6cLS (Met-His)	6cLS (Lys-His)	HS[a]	nitration-induced destabilization of the native state B1[b]
WT	100	0	0	–
null	100	0	0	–
Y46	100	0	0	–
Y46-NO_2	42		42	2.4
Y48	85	4	11	–
Y48-NO_2	40	13	47	2.1
Y67	86	0	14	–
Y67-NO_2	57	12	31	1.5
Y74	100	0	0	–
Y74-NO_2	63	13	24	1.6
Y97	92	1	7	–
Y97-NO_2	90	4	6	1.0

[a]The contribution of the 5cHS (-His) and 6cHS (H_2O-His) were combined. [b]Ratio of the contributions of the native state in the non-nitrated and nitrated forms

noted for Y67 and Y48 and by 8% for Y97. The situation is different when the single Tyr residues are nitrated. These modifications lead to a significant population of a non-native 6cLS and a HS configuration (predominantly 6cHS) with a relative contribution of ca. 15% and between 25 and 45%, respectively. The only exception refers to Y97-NO_2, in which the nitration site (i.e., the tyrosine) is most remote from the heme (Supporting Information). Here the relative contributions of the non-native species are distinctly lower and are, within the fitting accuracy, unchanged compared to the non-nitrated protein.

The non-native 6cLS state is of particular interest since the nature of the "new" axial ligand that has replaced Met80 is not clear a priori. The position of the marker bands ν_3 (vide supra) or ν_{10} indicate the coordination via a nitrogen atom that may either be provided by a His or by a Lys. In the former case, His33 or His26 may be potential candidates since these amino acids have been identified as axial ligands in an (metastable) intermediate formed during unfolding or refolding.[34] This coordination pattern is also found in Cyt-*c* electrostatically bound to negatively charged surfaces, denoted as state B2 in distinction to state B1 as the native state.[26] Alternatively, a Lys (72, 73, or 79) may bind to the heme iron corresponding to the "alkaline" state typically formed for WT Cyt-*c* at a pH above 10.[35,36]

We have, therefore, examined the low-frequency region of the RR spectra to distinguish between both possibilities. In this region, the alkaline state and state B2 each exhibits a unique band pattern that differs from the characteristic RR spectrum of the native Met-His coordinated 6cLS state (B1) and are not superimposed by the intrinsically weak RR bands of the HS species.[35,37] Nevertheless, the relatively low relative contributions of the non-native 6cLS form require a difference procedure to enhance the spectral changes with respect to the native state.

First, the WT protein was measured at pH 7 and pH 12 to obtain the native B1 state and a largely pure alkaline state. The

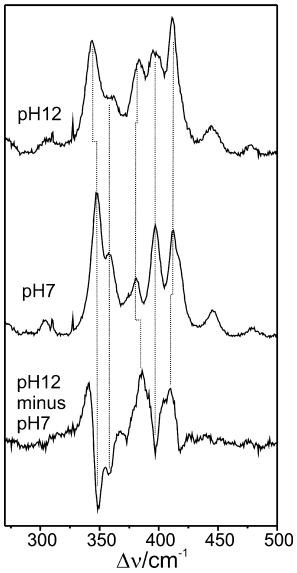

Figure 4. Low-frequency RR spectra of WT Cyt-*c* at pH 12 and at pH 7. The third trace displays the difference spectrum "pH 12 minus pH 7".

difference spectrum "pH12 minus pH7" in this region displays a characteristic pattern of positive and negative signals (Figure 4), which is also found for the null mutant and all non-nitrated Cyt-*c* variants, indicating that in each mutant the alkaline form with its characteristic Lys/His axial coordination pattern of the heme prevails at pH 12. To find out whether the non-native 6cLS state, which is partially populated upon Tyr nitration in neutral solutions, exhibits the same Lys/His coordination as the alkaline form, we have constructed the difference spectra "nitrated monotyrosine mutant minus non-nitrated monotyrosine mutant" from the spectra measured at pH 7. In fact, the difference spectra for all tyrosine mutants (i.e., "nitrated" minus "non-nitrated") display band patterns, which are similar to that of the "pH12 minus pH7" difference spectrum of WT Cyt-*c* or the "null" mutant (Figure 5). These findings suggest that in the nitrated variants the N-containing ligand of the "N"/His 6cLS species is a Lys.

UV−Vis Absorption Spectroscopy. The effect of the Tyr-to-Phe substitutions on the absorption spectra of the non-nitrated Cyt-*c* variants in the Soret band region is relatively small (ca. <3 nm), whereas upon nitration the peak maximum is shifted more significantly to the blue by up to 6 nm (Supporting Information). These shifts mainly reflect the coexistence of different spin and coordination states and specifically the formation of a HS species which is known to exhibit a Soret band maximum at wavelengths shorter than the 6cLS forms. Thus, the UV−vis absorption data are in agreement with the RR spectroscopic results inasmuch as the largest blue shift of the Soret maximum is noted for Y46-NO_2 and Y48-NO_2 which includes the largest HS contribution, in agreement with previous reports.[14,15]

Surface-Enhanced Resonance Raman Spectroscopy. To probe electric field effects on the protein stability, Cyt-*c* variants were electrostatically immobilized on an Ag electrode coated with a carboxyl-terminated SAM of MUA and studied by SERR spectroscopy. The SERR spectrum of WT Cyt-*c* is

dx.doi.org/10.1021/jp302301m | J. Phys. Chem. B 2012, 116, 5694−5702

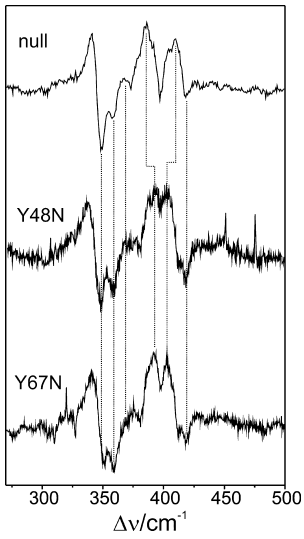

Figure 5. Difference spectrum "pH 12 minus pH 7" of the null mutant compared with the difference spectra of Y48-NO_2 and Y67-NO_2 obtained from the spectra of the respective nitrated mutants and the non-nitrated mutant, all measured at pH 7.

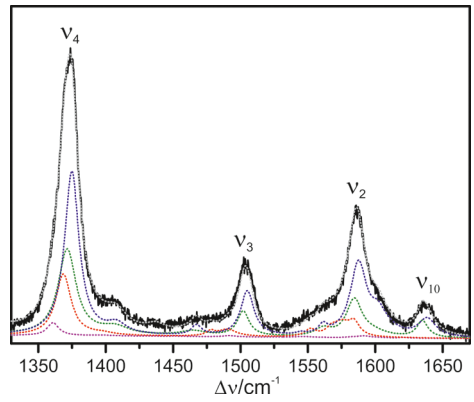

Figure 6. SERR spectrum of the null variant of Cyt-*c* obtained from a MUA-coated Ag electrode, including the component spectra obtained by a global fit. The component spectra of the oxidized B1, reduced B1, the oxidized B2[6cLS], and the oxidized B2[HS] (sum of the 5cHS and 6cHS species) are given by the dotted lines in green, magenta, blue, and red, respectively. The dotted gray line represents the sum of the component spectra.

dominated by the component spectrum of the native state B1 which is nearly identical to the RR spectrum of the protein in solution. This state could be reversibly oxidized and reduced by varying the electrode potential. Thus, the behavior of the human WT Cyt-*c* on MUA-coated electrodes is similar to that of horse heart protein except for a higher contribution of non-native states in the SERR spectrum of human Cyt-*c*.[28]

Unlike the RR spectroscopic analysis of the proteins in solution, a global component analysis could be applied starting with the component spectra previously determined for horse heart Cyt-*c*.[26,28] Only minor adjustments of a few spectral parameters (i.e., intensities in the ν_2 region) were required to improve the global fit. Thus, all experimental spectra could be simulated by the same set of component spectra, i.e., the spectra of the native reduced and oxidized B1 state (6cLS with Met-His ligation) and the oxidized B2 species including the 5cHS (−/His) and 6cHS (H_2O/His) configuration as well as the 6cLS ("N"/His) configuration (see Supporting Information). The component spectrum of the latter is nearly identical to that of the bis(histidine)-coordinated 6cLS state of horse heart Cyt-*c* implying that, unlike the proteins in solution, an additional His (instead of a Lys) serves as the sixth ligand in the immobilized nitrated and non-nitrated Tyr variants. Spectra of the reduced forms of the B2 species were not required for the global fit since the experiments were carried out above the respective reduction potentials between −0.25 and −0.4 V (vs AgCl).[38] Figure 6 shows an example of a SERR spectrum analyzed in this way. The resultant relative weights of the individual component spectra were then converted into relative concentrations (Table 2) according to the procedure described previously (Supporting Information)[33] such that the data can be directly compared with those obtained for Cyt-*c* in solution on the basis of the ν_3 band fitting (Table 1). However, the accuracy of the component analysis is significantly higher than for a simple band fitting analysis since complete spectra of the individual components are fitted to the experimental spectra and the degrees of freedom in the fitting procedure are restricted to the number of components.[39] Further data on the distribution among the various states at open circuit of the electrode are given in the Supporting Information.

Table 2. Relative Contributions (in %) of the Various Spin and Coordination States of Cyt-*c* Variants Immobilized on SAM-Coated Electrodes at +0.15 V

	B1 6cLS (Met-His)	B2 6cLS (His-His)	B2HS[a]	electric-field-induced destabilization of the native state B1[b]
WT	76	16	8	1.3
null	49	39	12	2.0
Y46	42	17	41	2.3
Y46-NO_2	30	24	46	1.4
Y48	42	42	16	2.0
Y48-NO_2	43	43	14	0.9
Y67	51	41	8	1.7
Y67-NO_2	42	43	15	1.4
Y74	64	20	16	1.6
Y74-NO_2	45	42	13	1.4
Y97	42	26	32	2.2
Y97-NO_2	33	21	46	2.7

[a]The contributions of the 5cHS (-His) and 6cHS (H_2O-His) were combined. [b]Ratio of the contributions of the native state in solution (Table 1) and in the immobilized state.

Electrochemistry. The formal midpoint potential and the electron-transfer rate constants of the various Cyt-*c* variants immobilized on SAM-coated Ag electrodes were measured by CV using a potential range from +0.15 to −0.2 V. Under these conditions, CV solely probes the redox potentials of the native B1 state since, according to the previous findings for horse heart Cyt-*c*, the B2 species should give rise to redox potentials lower than −0.2 V.[38] Extending this conclusion from horse heart to human Cyt-*c* is justified in view of the far-reaching similarities in the three-dimensional structures[30,40] and the spectral properties, including the RR spectra (vide supra). Also, the midpoint potentials of the immobilized WT proteins have been found to be essentially the same with 22 and 23 mV for horse heart and human Cyt-*c*, respectively.[28,41]

dx.doi.org/10.1021/jp302301m | J. Phys. Chem. B 2012, 116, 5694−5702

The CVs afforded well-resolved peaks and a quasi-reversible electron transfer (ET), reflected by a full width at half-height of

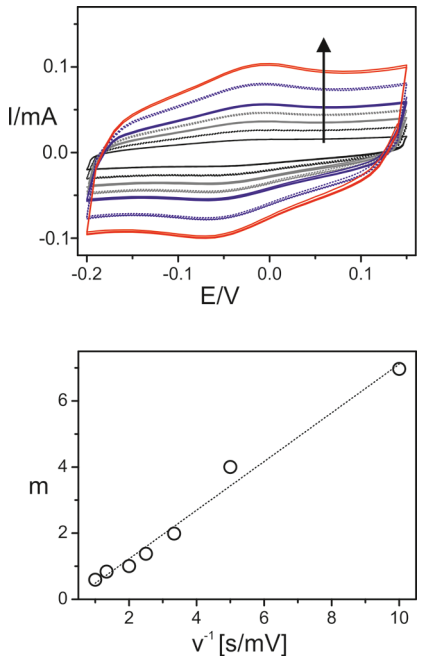

Figure 7. CVs of WT human Cyt-*c* (top) obtained with increasing scan rates (in the direction of the arrow, 100, 200, 300, 400, 500, 750, and 1000 mV/s) and the Laviron plot (bottom).

Table 3. Redox Properties of the Non-nitrated and Nitrated Cyt-*c* Variants Immobilized on a MUA-Coated Ag Electrode

protein	E^0/mV	k_{ET}/s^{-1}
WT	22	4
null	−33	29
Y46	−24	59
Y46-NO_2	−46	31
Y48	−13	10
Y48-NO_2	−61	28
Y67	−2	7
Y67-NO_2	−5	27
Y74	−28	60
Y74-NO_2	−20	40
Y97	−22	32
Y97-NO_2	−31	53

80−100 mV (Figure 7). Upon mutation the redox potential is significantly lowered by up to 50 mV (Table 3). Additional downshifts of the redox potential were noted upon tyrosine nitration except for the Y74 protein which displays a small upshift in the Y74-NO_2 variant.

Upon varying the scan rate, the ET kinetics of the immobilized Cyt-*c* variants has been determined by applying the Laviron method (Figure 7). The ET rate constant of the WT protein was found to be distinctly smaller compared to that determined for horse heart Cyt-*c* under otherwise the same conditions (4 vs 40 s^{-1}).[41] The mutation of the individual tyrosines leads to a strong increase of the ET rate constant whereas nitration either accelerates or slows down the heterogeneous ET.

DISCUSSION

Effect of Phe-to-Tyr Mutations on the Redox Center.

The most striking result of the RR spectroscopic analysis of the non-nitrated Cyt-*c* is the fact that substitutions of all Tyr by Phe leaves the redox site structure essentially unchanged whereas preservation of a single Tyr residue in position 48, 67, or 97 causes a weakening of the Fe−Met bond and thus leads to small contributions of non-native states. These results are difficult to rationalize since one intuitively expects that specifically Tyr67, due to its proximity to the heme, exerts a stabilizing function on the heme pocket. We thus conclude that the small effects on the coordination state of Cyt-*c* (as well as on the small spectral modifications of the respective native B1 state) are largely due to long-range perturbations of the electrostatics in the heme pocket. In some cases, such as the null mutant, the structural consequences of individual Tyr-to-Phe substitutions may accidentally compensate each other. However, it should be noted that this conclusion solely refers to the structure of the heme site as the RR spectra do not provide information about structural changes of protein.

The situation is different for the effect of the individual tyrosine residues on the redox potential of the heme in the native state B1. All the monotyrosine mutants, including the null variant, display negative shifts of the redox potential with respect to the WT protein (Table 3). Assuming that each Tyr residue exerts an incremental contribution to the redox potential, one may express the redox potential shift ΔE_i for each variant i according to

$$\Delta E_i = E_i^0 - E_{WT}^0 = \sum_j \varepsilon_{i,j} \quad (1)$$

where E_{WT}^0 and E_i^0 are the redox potentials of the WT protein and mono-Tyr variant i, respectively, and $\varepsilon_{i,j}$ represents the incremental redox potential shift due to the Tyr-to-Phe substitution at the amino acid position j; i.e., $\varepsilon_{i,j}$ is zero for $i = j$ but nonzero for $i \neq j$. Correspondingly, one obtains a set of five equations according to the scheme in Table 4 that can be solved to afford the individual values for ε_j. This approach is justified a posteriori since the sum of all ε_j values is very similar

Table 4. Shifts of the Redox Potential of Non-nitrated Protein Variants and Contributions of the Individual Tyr Residues[a]

	tyrosine residues					
protein	67	48	46	74	97	ΔE^0/mV
WT	x	x	x	x	x	0
Y67	x	–	–	–	–	−24
Y48	–	x	–	–	–	−35
Y46	–	–	x	–	–	−46
Y74	–	–	–	x	–	−50
Y97	–	–	–	–	x	−44
null	–	–	–	–	–	−55
	ε_{67}	ε_{48}	ε_{46}	ε_{74}	ε_{97}	$\sum_j \varepsilon_j$
contribn to ΔE^0 (in mV)	−25.75	−14.75	−3.75	0.25	−5.75	−49.75
contribn to ΔE^0 (in mV) for the nitrated Tyr	−41.25	+14.75	−0.25	−26.25	−15.25	−68.25
distance to the heme (Å)	6.5	10.2	9.4	12.6	14.0	

[a]Determined according to eq 1.

dx.doi.org/10.1021/jp302301m | J. Phys. Chem. B 2012, 116, 5694−5702

(−50 mV) to the redox potential shift of the null mutant of −55 mV. This finding suggests that the main origin of the redox potential shifts lies in a change of the polarity and electrostatics of the protein environment rather than a mutation-induced structural perturbation of the redox center. This conclusion is consistent with the appreciable long-range effect of the most remote Tyr residue at position 97, although those residues that are in closest proximity to the heme (i.e., at positions 67 and 48) exert the strongest influence on the redox potential.

The redox potentials determined in this work refer to the native B1 state of the proteins immobilized on the MUA-coated Ag electrode. Taking into account the interfacial potential drop which leads to a small apparent negative shift of the redox potentials,[28] the values for the WT protein and the null variant are in good agreement with those in solution.[11] However, redox potential shifts of the mono-Tyr mutants differ slightly for the protein in solution and on the electrode (Supporting Information) which may be attributed to the distance- and orientation-dependent modulation of ε_j by the interfacial electric field.[42]

Effect of Tyrosine Nitration on the Redox Center. Upon nitration, a considerable fraction of the individual Tyr variants is converted into states with non-native heme coordination. Among them, a new 6cLS species is formed with ca. 15% in all nitrated Cyt-*c* variants except for Y97-NO_2 (<10%). RR spectra indicate that this 6cLS species is closely related the alkaline form of Cyt-*c* in which Met80 is replaced by a Lys (72, 73, or 79). These findings are in agreement with previous spectroscopic data on the nitrated Tyr mutants.[12−14] In WT Cyt-*c*, this alkaline species is formed at a pH above 9.5,[13] corresponding to the pK_a of the surface-exposed lysine residues. Thus, deprotonation of the Lys side chain is likely to be the crucial step of this conformational transition and the stronger binding affinity of the Lys amino group to the ferric heme compared to the thioether group of Met80 may constitute a significant thermodynamic driving force. However, formation of the Lys/His coordinated species in the nitrated Tyr mutants of Cyt-*c* at pH 7 seems to follow a different mechanism in view of the concomitant formation of the prevailing 6cHS species which is attributed to a H_2O/His heme (Table 1). The coexistence of the 6cLS and the HS form detected in the present RR spectroscopic study suggests that the primary effect of tyrosine nitration is the destabilization of the native state B1, specifically the weakening of Fe−S(Met80) bond, rather than a lowering of the pK_a of one of the surface lysines.

Nitration of the tyrosines does not display a uniform tendency for the individual redox potential shifts of the B1 state of immobilized protein (Table 3) which can be analyzed according to eq 1. Whereas ε_j for the nitrated Tyr at positions 67, 74, and 97 is distinctly more negative than for the non-nitrated form, the value for ε_{46} remains small. Most strikingly, however, there is a large positive shift for ε_{48} by 30 mV compared to the non-nitrated Tyr. Note that in solution most of the nitrated mono-Tyr mutants display a positive redox potential shift compared to the non-nitrated forms.[11]

Coordination State Changes and Peroxidase Activity. Previous studies have shown that Tyr nitration leads to an increase of the peroxidase activity.[7,13] Intuitively, one might expect a direct correlation between the peroxidase activity and the relative contribution of the HS species with its vacant (or only weakly bound) axial coordination site, which increases in the order Y48-NO_2 ≈ Y46-NO_2 > Y74-NO_2 ≈ Y67-NO_2 > Y97-NO_2 (Table 1). The same order holds for the nitration-induced destabilization of the native B1 state in general. For Y46-NO_2, Y48-NO_2 and Y74-NO_2 but not for Y67-NO_2 a significantly increased peroxidase activity was found.[13,14] Also, the comparison with the enzymatic data for the site-specifically nitrated wild-type Cyt-*c* reported by Batthány et al.[7] does not provide an unambiguous correlation with the present spectroscopic results on the corresponding monotyrosine mutants inasmuch as the peroxidase activity follows the order Y74-NO_2 > Y67-NO_2 ≈ Y97-NO_2. Accordingly, it appears to be more plausible to assume that the peroxidase process is primarily controlled by the accessibility of the heme pocket for H_2O_2 which requires a destabilization of the heme crevice.[13] This conclusion is in line with a previous UV RR study by Spiro and co-workers.[43] These structural changes are accompanied by a weakening of the Fe-Met bond which eventually may lead to the removal of the ligand from the heme.[14]

Effect of the Electric Field on the Redox Site. The relationship between destabilization of the heme crevice and the distortion of the axial heme coordination has been observed for Cyt-*c* bound to negatively charged liposomes including cardiolipin or other anionic phospholipids,[23,25,26,44,45] or even more simple membranes models such as an electrode coated by a SAM with anionic head groups.[26−28,41] Thus, it has been assumed that also electrostatic interactions, which govern Cyt-*c* binding to the cardiolipin-rich inner mitochondrial membrane, may promote the switch from the redox to the peroxidase function.[41] In these electrostatic complexes, however, the weakening of the Fe-Met leads to a 5cHS and a new non-native 6cLS state in which a His (33 or 26) replaces the Met80 ligand of the heme iron (B2 states).[26−28] In fact, also the non-nitrated and nitrated protein variants of human Cyt-*c* immobilized on SAM-coated electrodes show a similar behavior. The component spectrum of the 6cLS species in the present SERR spectra is essentially identical to that of the B2 6cLS state of horse heart Cyt-*c*.[26] Conversely, the alternative assignment of this species to the alkaline state is rather unlikely since the Lys residues that might substitute the Met80 ligand are involved in electrostatic binding of the protein to the SAM surface.[46]

The extent of B2 formation, including both the 6cLS and the HS forms, is higher for the human WT Cyt-*c* protein than for the WT Cyt-*c* from horse heart under similar experimental conditions but it is further increased for the various Tyr mutants, including the null mutant. For the non-nitrated variants, the interfacial electric field induces a decrease of the B1 content by a factor of ca. 2. This factor is distinctly higher than for the WT protein and the average value for the nitrated Tyr mutants (1.3), except for Y97-NO_2, such that the contribution of the native B1 state has dropped to a similar value of ca. 40% in all nitrated and non-nitrated mutants. These findings suggest that the electric-field-induced destabilization of the redox site is largely independent of the site of the Tyr → Phe substitutions and the Tyr nitration. In fact, the strength of the electrostatic interactions and thus the electric field experienced by the bound proteins seem to remain largely unchanged since the various Tyr → Phe substitutions and the respective nitrations do not affect the charge distribution in the binding domain and do not significantly alter the dipole moment of the protein (Supporting Information).

The dipole moment of ferric human WT Cyt-*c* has been calculated to be 254 D in the present work (Supporting Information) and thus is distinctly higher than that of horse WT horse heart Cyt-*c* (184 D),[47] implying that electrostatic

dx.doi.org/10.1021/jp302301m | J. Phys. Chem. B 2012, 116, 5694−5702

interactions on the MUA-coated Ag electrode are much stronger for the human protein. One consequence refers to the electric-field-induced stabilization of the heme pocket which is more severe for human WT Cyt-*c* (24% B2; Table 2) than for horse heart Cyt-*c* (~0% B2)[28] under the same immobilization conditions. Consistently, destabilization of yeast iso-1 Cyt-*c*, which exhibits a dipole moment 544 D in the ferric form,[47] is even more severe than for human Cyt-*c*. The second consequence is related to the electron-transfer process in the immobilized state which has been shown to be controlled by the interplay between protein dynamics and electron tunneling.[27,41,46,48] Since the thermodynamically preferred binding domain of Cyt-*c* does not correspond to the orientation that is optimum for electron transfer, a reorientation of the bound protein must precede electron tunneling which is the rate-limiting step for horse heart Cyt-*c* on a MUA-coated Ag electrode (k_{ET} = 40 s^{-1}). With increasing strength of electrostatic binding, reorientation is slowed down and may become the rate-limiting step as it is most likely the case for WT human Cyt-*c* (k_{ET} = 4 s^{-1}; Table 3). For yeast iso-1 Cyt-*c*, the strong electrostatic binding to the MUA surface even impairs the spectroelectrochemical determination of the interfacial electron transfer.[47] On the other hand, the increase of the electron-transfer rate constant upon Tyr → Phe substitution and Tyr nitration cannot be related to the relatively small changes of the dipole moment by less than 10% compared to the WT protein (Supporting Information). More detailed experimental and theoretical studies are required to explore the impact of the mutational and chemical modifications of Cyt-*c* on the dynamics and the electron tunneling pathways in the immobilized state.

CONCLUSIONS

The effect of Tyr nitration on the structural and redox properties of the heme site of Cyt-*c* was studied on the basis of mono-Tyr mutants. This approach is based on the approximation that the replacement of Tyr by Phe only causes minor perturbations of the protein structure and the redox potential. This assumption seems to be largely justified since crucial structural parameters of the heme pocket are preserved, including the sensitive Fe−Met axial bond. The RR spectroscopic analysis reveals subtle conformational changes beyond the level of heme ligand exchange, which are, however, accompanied by redox potential shifts by up to −55 mV. Most surprisingly, the effects of the individual Tyr → Phe substitutions on the redox potential are additive, pointing to long-range electrostatic perturbations of the redox potential.

Nitration of the individual tyrosines causes more severe structural changes of the heme pocket including a substantial weakening of the Fe-Met axial bond which eventually leads to partial formation of non-native ligation states. These states include HS species and a Lys-His coordinated 6cLS species at pH 7.0 with the same coordination pattern as the alkaline form of the WT and the non-nitrated Cyt-*c* variants formed above pH 10.0. There is no direct correlation between the peroxidase activity determined previously[7,13] and the relative contribution of the HS forms or with the extent of coordination state changes in toto. These findings support the view that nitration-induced peroxidase activity is primarily due to the increased accessibility of H_2O_2 which results from the perturbation of the heme crevice.

Upon electrostatic binding to SAM-coated electrodes, the Fe−Met axial bond is weakened for both the nitrated and non-nitrated protein variants to a comparable extent implying that the electric-field-induced destabilization of the heme pocket structure is largely independent of the effect of tyrosine nitration. In the immobilized state, a Lys-His coordinated species is not formed due to the involvement of Lys residues in electrostatic binding to the SAM surface, but instead His33 (or His26) evidently replaces Met80 to form a non-native 6cLS state. The same structural changes, albeit not so pronounced, are also observed for the WT protein.

Both Tyr nitration and membrane binding cause similar albeit not identical destabilizations of the heme pocket, leading to a decrease of the native B1 conformation. In both cases, the non-native states, i.e., the HS forms, the alkaline-like species in solution, and the His-His coordinated 6cLS form in the immobilized state, display a strongly negatively shifted redox potential[25,28,38,49] that impairs electron acceptance from cytochrome *c* reductase. Thus, the present results are consistent with the view that either Tyr nitration or electrostatic binding to the anionic cardiolipin-rich inner mitochondrial membrane, or the combination of both events, may trigger the functional switch from the redox to the peroxidase function of Cyt-*c*.

ASSOCIATED CONTENT

Supporting Information

The material includes a description of the RR and SERR spectroscopic analysis, UV−vis absorption spectra, and details of the MD simulations. This material is available free of charge via the Internet at http://pubs.acs.org.

AUTHOR INFORMATION

Corresponding Author

*E-mail: hildebrandt@chem.tu-berlin.de. Tel.: +49-30-314-21419.

Notes

The authors declare no competing financial interest.

ACKNOWLEDGMENTS

The authors thank the Spanish Ministry of Science and Innovation (BFU2009-07190) and the Andalusian Government (BIO198) for financial support. The work was further supported by the Cluster of Excellence "Unifying Concepts in Catalysis" funded by the DFG.

ABBREVIATIONS

CV, cyclic voltammetry; Cyt-*c*, cytochrome *c*; HS, high spin; LS, low spin; MD, molecular dynamics; MUA, mercaptoundecanoic acid; RR, resonance Raman; SAM, self-assembled monolayer; SERR, surface enhanced resonance Raman

REFERENCES

(1) Tarrant, M. K.; Cole, P. A. *Annu. Rev. Biochem.* **2009**, *78*, 797−825.
(2) Monteiro, H. P.; Arai, R. J.; Travassos, L. R. *Antiox. Red. Sign.* **2008**, *10*, 843−889.
(3) Ischiropoulos, H. *Biochem. Biophys. Res. Commun.* **2003**, *305*, 776−783.
(4) Koeck, T.; Fu, X.; Hazen, J. W.; Crabb, J. W.; Stuehr, D. J.; Aulak, K. S. *J. Biol. Chem.* **2004**, *279*, 27257−27262.
(5) Cassina, A. M.; Hodara, R.; Souza, J. M.; Thomson, L.; Castro, L.; Ischiropoulos, H.; Freeman, B. A.; Radi, R. *J. Biol. Chem.* **2000**, *275*, 21409−21415.
(6) Radi, R. *Proc. Natl. Acad. Sci. U.S.A.* **2004**, *101*, 4003−4008.

(7) Batthyány, C.; Souza, J. M.; Durán, R.; Cassina, A.; Cerveñansky, C.; Radi, R. *Biochemistry* **2005**, *44*, 8038−8046.
(8) Jang, B.; Han, S. *Biochimie* **2005**, *88*, 53−58.
(9) Nakagawa, H.; Komai, N.; Takusagawa, M.; Miura, Y.; Toda, T.; Miyata, N.; Ozawa, T.; Ikota, N. *Biol. Biol. Pharm. Bull.* **2007**, *30*, 15−20.
(10) Souza, J. M.; Castro, L.; Cassina, A. M.; Batthyány, C.; Radi, R. *Methods Enzymol.* **2008**, *441*, 197−215.
(11) Rodríguez-Roldán, V.; García-Heredia, J. M.; Navarro, J. A.; De la Rosa, M. A.; Hervás, M. *Biochemistry* **2008**, *47*, 12371−12379.
(12) Abriata, L. A.; Cassina, A.; Tórtora, V.; Marín, M.; Souza, J. M.; Castro, L.; Vila, A. J.; Radi, R. *J. Biol. Chem.* **2009**, *284*, 17−26.
(13) García-Heredia, J. M.; Díaz-Moreno, I.; Nieto, P. M.; Orzáez, M.; Kocanis, S.; Teixeira, M.; Pérez-Payá, E.; Díaz-Quintana, A.; De la Rosa, M. A. *Biochim. Biophys. Acta* **2010**, *1797*, 981−983.
(14) Díaz-Moreno, I.; García-Heredia, J. M.; Díaz-Quintana, A.; Teixeira, M.; De la Rosa, M. A. *Biochim. Biophys. Acta* **2011**, *1807*, 1616−1623.
(15) García-Heredia, J. M.; Díaz-Moreno, I.; Díaz-Quintana, A.; Orzáez, M.; Navarro, J. A.; Hervás, M.; De la Rosa, M. A. *FEBS Lett.* **2012**, *586*, 154−158.
(16) Lee, I.; Salomon, A. R.; Yu, K.; Doan, J. W.; Grossman, L. I.; Hüttemann, M. *Biochemistry* **2006**, *45*, 9121−9128.
(17) Yu, H.; Lee, I.; Salomon, A. R.; Yu, K.; Hüttemann, M. *Biochim. Biophys. Acta* **2008**, *1777*, 1066−1071.
(18) Pecina, P.; Borisenko, G. G.; Belokova, N. A.; Tyurina, Y. Y.; Pecinova, A.; Lee, I.; Samhan-Arias, A. K.; Przyklenk, K.; Kagan, V. E.; Hüttemann, M. *Biochemistry* **2010**, *49*, 6705−6714.
(19) García-Heredia, J. M.; Díaz-Quintana, A.; Salzano, M.; Orzáez, M.; Pérez-Payá, E.; Teixeira, M.; De la Rosa, M. A.; Díaz-Quintana, A. *J. Biol. Inorg. Chem.* **2011**, *16*, 1155−1168.
(20) Scott, R. A., Mauk, A. G., Eds. *Cytochrome c—a multidisciplinary approach*; University Science Books: Sausalito, CA, 1995.
(21) Ow, Y. L.; Green, D. R.; Hao, Z.; Mak, T. W. *Nat. Rev. Mol. Cell Biol.* **2008**, *9*, 532−542.
(22) Kagan, V. E.; Tyurin, V. A.; Jiang, J.; Tyurina, Y. Y.; Ritov, V. B.; Amoscato, A. A.; Osipov, A. N.; Belikova, N. A.; Kapralov, A. A.; Kini, V.; et al. *Nat. Chem. Biol.* **2005**, *4*, 223−232.
(23) Belikova, N. A.; Vladimorov, Y. A.; Osipov, A. N.; Kapralov, A. A.; Tyurin, V. A.; Potapovich, M. V.; Basova, L. V.; Peterson, J.; Kurnikov, I. V.; Kagan, V. E. *Biochemistry* **2006**, *45*, 4998−5009.
(24) Kagan, V. E.; Bayir, A.; Bayir, H.; Stoyanovsky, D.; Borisenko, G. G.; Tyurina, Y. Y.; Wipf, P.; Atkinson, J.; Greenberger, J. S.; Chapkin, R. S.; et al. *Mol. Nutr. Food Res.* **2009**, *53*, 104−114.
(25) Basova, V. L.; Kurnikov, I. V.; Wang, L.; Ritov, V. B.; Belikova, N. A.; Vlasova, I. I.; Pacheco, A. A.; Winnica, D. E.; Peterson, J.; Bayir, H.; et al. *Biochemistry* **2007**, *46*, 3423−3434.
(26) Oellerich, S.; Wackerbarth, H.; Hildebrandt, P. *J. Phys. Chem. B* **2002**, *106*, 6566−6580.
(27) Ly, H. K.; Sezer, M.; Wisitruangsakul, N.; Feng, J. J.; Kranich, A.; Millo, D.; Weidinger, I. M.; Zebger, I.; Murgida, D. H.; Hildebrandt, P. *FEBS J.* **2011**, *278*, 1382−1390.
(28) Murgida, D. H.; Hildebrandt, P. *J. Phys. Chem. B* **2001**, *105*, 1578−1586.
(29) Wackerbarth, H.; Klar, U.; Günther, W.; Hildebrandt, P. *Appl. Spectrosc.* **1999**, *53*, 283−291.
(30) Liptak, M. D.; Fagerlund, R. D.; Ledgerwood, E. C.; Wilbanks, S. M.; Bren, K. L. *J. Am. Chem. Soc.* **2011**, *133*, 1153−1155.
(31) Humphrey, W.; Dalke, A.; Schulten, K. *J. Mol. Graph.* **1996**, *14*, 33−38.
(32) Parthasarathi, N.; Hansen, C.; Yamaguchi, S.; Spiro, T. G. *J. Am. Chem. Soc.* **1987**, *109*, 3865−3871.
(33) Oellerich, S.; Wackerbarth, H.; Hildebrandt, P. *Eur. Biophys. J.* **2003**, *32*, 599−613.
(34) Yeh, S. R.; Han, S. W.; Rousseau, D. L. *Acc. Chem. Res.* **1998**, *31*, 7276−7280.
(35) Döpner, S.; Hildebrandt, P.; Rosell, F. I.; Mauk, A. G. *J. Am. Chem. Soc.* **1998**, *120*, 11246−11255.
(36) Pollock, W. B. R.; Rosell, F. I.; Twitchett, M. B.; Dumont, M. E.; Mauk, A. G. *Biochemistry* **1998**, *37*, 6124−6131.
(37) Hildebrandt, P. *Biochim. Biophys. Acta* **1990**, *1040*, 175−186.
(38) Wackerbarth, H.; Oellerich, S.; Hildebrandt, P. *Chem. Phys. Chem.* **2003**, *4*, 714−724.
(39) Döpner, S.; Hildebrandt, P.; Mauk, A. G.; Lenk, H.; Stempfle, W. *Spectrochim. Acta Part A, Biomol. Spectrosc.* **1996**, *51*, 573.
(40) Bushnell, G. W.; Louie, G. V.; Brayer, G. D. *J. Mol. Biol.* **1990**, *214*, 585−595.
(41) Ly, K. H.; Wisitruangsakul, N.; Sezer, M.; Feng, J. J.; Kranich, A.; Weidinger, I.; Zebger, I.; Murgida, D. H.; Hildebrandt, P. *J. Electroanal. Chem.* **2011**, *660*, 367−376.
(42) Rivas, L.; Soares, C. M.; Baptista, A. M.; Simaan, J.; DiPaolo, R.; Murgida, D. H.; Hildebrandt, P. *Biophys. J.* **2005**, *88*, 4188−4199.
(43) Balakrishnan, G.; Hu, Y.; Oyerinde, O. F.; Su, J.; Grooves, J. T.; Spiro, T. G. *J. Am. Chem. Soc.* **2006**, *129*, 504−505.
(44) Oellerich, S.; Lecomte, S.; Paternostre, M.; Heimburg, T.; Hildebrandt, P. *J. Phys. Chem. B* **2004**, *108*, 3871−3878.
(45) Kapralov, A. A.; Kurnikov, I. V.; Vlasova, I. I.; Belikova, N. A.; Tyurin, V. A.; Basova, L. V.; Zhao, Q.; Tyurina, Y. Y.; Jiang, J.; Bayir, H.; et al. *Biochemistry* **2007**, *46*, 14232−14244.
(46) Paggi, D. A.; Martín, D. F.; Kranich, A.; Hildebrandt, P.; Martí, M.; Murgida, D. H. *Electrochim. Acta* **2009**, *54*, 4963−4970.
(47) Feng, J. J.; Murgida, D. H.; Utesch, T.; Mroginski, M. A.; Hildebrandt, P.; Weidinger, I. *J. Phys. Chem. B.* **2008**, *112*, 15202−15211.
(48) Kranich, A.; Ly, H. K.; Hildebrandt, P.; Murgida, D. H. *J. Am. Chem. Soc.* **2008**, *130*, 9844−9848.
(49) Barker, P. D.; Mauk, A. G. *J. Am. Chem. Soc.* **1992**, *114*, 3619−3624.

9

Unraveling the Interfacial Electron Transfer Dynamics of Electroactive Microbial Biofilms Using Surface-Enhanced Raman Spectroscopy

Ly, H. K.; Harnisch, F.; Hong, S.-F.; Schröder, U.; Hildebrandt, P; Millo, D. *ChemSusChem* **2013**, DOI: 10.1002/cssc.201200626.

ChemPubSoc Europe

DOI: 10.1002/cssc.201200626

Unraveling the Interfacial Electron Transfer Dynamics of Electroactive Microbial Biofilms Using Surface-Enhanced Raman Spectroscopy

Hoang K. Ly,[a] Falk Harnisch,[b] Siang-Fu Hong,[b] Uwe Schröder,[b] Peter Hildebrandt,[a] and Diego Millo*[a, c]

The electron transfer (ET) processes of electroactive microbial biofilms have been investigated by combining electrochemistry and time-resolved surface-enhanced resonance Raman (TR-SERR) spectroscopy. This experimental approach provides selective information on the ET process across the biofilm–electrode interface by monitoring the redox-state changes of heme cofactors in outer membrane cytochromes (OMCs) that are in close vicinity (i.e., within 7 nm) to the Ag working electrode. The rate constant for heterogeneous ET of the surface-confined OMCs (sc-OMCs) of a mixed culture derived electroactive microbial biofilm has been determined to be 0.03 s^{-1}. In contrast, according to kinetic simulations the ET between sc-OMCs and their redox partners, embedded within the biofilm, is a much faster process with an estimated rate constant greater than 1.2 s^{-1}. The slow rate of heterogeneous ET and the lack of high-spin species in the SERR spectra rule out the direct attachment of the sc-OMCs to the electrode surface.

Introduction

Microbial bioelectrochemical systems (BESs) are devices using electroactive microbial biofilms that are attached to electrodes for the catalysis of bioelectrochemical oxidations (at anodes) and reductions (at cathodes). Microbial BESs are used for the production of electricity and hydrogen, as well as for other applications.[1,2] BESs have an electroactive microbial biofilm on the anode that relies upon an efficient electron transfer (ET) strategy for delivering the electrons, gathered from the oxidation of the microbial substrates, to the electrode.

The elucidation of ET mechanisms used by different microorganisms is motivating substantial research efforts.[3,4] Several studies have reported active roles of soluble redox mediators, membrane-bound redox proteins [that is, outer membrane cytochromes (OMCs)], and conducting nanowires.[5,6] Although all of these species appear to be involved in the ET process, their mutual interplay and individual contributions to the observed current densities are still unclear and under debate.[7,8] These shortcomings are mainly attributable to the lack of appropriate analytical methods for investigating the underlying ET reactions in situ, that is, on living electrocatalytic microbial biofilms.[9] The outstanding complexity of these microbial bioelectrocatalytic processes, involving several electroactive species that are difficult to probe individually, require an analytical methodology providing selective information regarding the redox and structural properties of the species promoting the ET process. We have applied a spectroelectrochemical approach to gain insight into the kinetics of the ET that is selective for the biofilm/electrode interface. Whereas electrochemistry allows the monitoring and control of electrocatalytic activity and the redox processes of the biofilm in toto, spectroelectrochemistry based on surface-enhanced resonance Raman (SERR) spectroscopy exclusively probes the heme groups of the surface-confined OMCs (sc-OMCs) and their redox processes at the interface of the biofilm and the Ag electrode.[10] The selectivity of the spectroscopic approach originates from the near-field enhancement of the resonance Raman (RR) scattering of the heme groups that are in close vicinity (<7 nm)[11] to the Ag working electrode. In contrast to other spectroelectrochemical approaches based on UV/Vis spectroscopy that probe all of the heme groups across the entire biofilm (i.e., the outer membrane and the periplasmic cytochromes over a distance of tens of micrometers);[12] cytochromes other than sc-OMCs, that is, cytochromes more distant from the electrode and periplasmic cytochromes, do not contribute to the SERR spectra. For the sc-OMCs, the SERR spectra provide information on both the oxidation state and the structure (e.g., coordination and spin state) of the heme as well as the respective changes during the redox processes of the biofilm. Moreover, the method can be employed to probe the dynamics of these processes by combining it with the electrochemical potential

[a] H. K. Ly, Prof. Dr. P. Hildebrandt, Dr. D. Millo
Institut für Chemie, Sekr. PC14
Technische Universität Berlin
Straße des 17. Juni 135, 10623 Berlin (Germany)

[b] Dr. F. Harnisch, Dr. S.-F. Hong, Prof. Dr. U. Schröder
Institute of Environmental and Sustainable Chemistry
TU Braunschweig
Hagenring 30, 38106 Braunschweig (Germany)

[c] Dr. D. Millo
Biomolecular Spectroscopy/LaserLaB Amsterdam
Vrije Universiteit Amsterdam
De Boelelaan 1083, 1081 HV Amsterdam (The Netherlands)
E-mail: d.millo@vu.nl

Supporting Information for this article is available on the WWW under http://dx.doi.org/10.1002/cssc.201200626.

step method. Here, the electrode potential is stepped from an initial (E_i) to a final potential (E_f) to perturb the original redox equilibrium at E_i. The subsequent relaxation processes towards the equilibrium state at E_f can be monitored by measuring the TR-SERR spectra at various delay times relative to the potential step. This approach has successfully been applied to the study of immobilized proteins.[13] Herein, we have applied this approach to electroactive microbial biofilms grown on Ag electrodes to selectively obtain information regarding the ET reactions and possible coupled conformational transitions of sc-OMCs. The biofilms are derived from mixed-culture inoculum; the bioelectrocatalytic activity is dominated by *Geobacteraceae* [14] In conjunction with electrochemical methods and by extending the approach to turnover and non-turnover conditions, the study provides new insight into ET dynamics of these biofilms.

Results

Under non-turnover conditions (i.e., in the absence of substrate), the redox states of the sc-OMCs can be adequately controlled by applying an appropriate potential to the biofilm-covered working electrode.[10] To explore the ET dynamics of the sc-OMCs, a potential step is applied from $E_i = -450$ to $E_f = -320$ mV [vs. Ag/AgCl (3.0 M KCl) reference electrode] to trigger the transition from a largely reduced state of the sc-OMCs (E_i) to a state of equal contributions of ferric and ferrous hemes ($E_f = E_{1/2}$) via ET from the sc-OMCs to the electrode. $E_{1/2}$ can be considered as the apparent equilibrium potential of sc-OMCs, representing the average of the macroscopic redox potentials of the individual OMCs that are centered at −280 and −360 mV (Figure S1).

TR-SERR spectra, recorded at different delay times after the potential step, displayed an increase of the band at 1375 cm^{-1} at the expense of the 1361 cm^{-1} band, which are characteristic markers for the ferric and ferrous hemes in sc-OMCs, respectively (Figure 1, upper panel). The TR-SERR spectra did not reveal any indications of the involvement of intermediate states other than the ferric and the ferrous forms in their native bis-histidine ligated, six-coordinated, low-spin configurations that were already assigned to a mixed-culture-derived electroactive biofilm.[10] Furthermore, there were no time-dependent changes of the overall SERR intensity during the potential step experiments, which implied that the arrangement of the sc-OMCs with respect to the electrode remained unchanged (Figure S2). This finding excludes the potential-dependent adsorption/desorption of sc-OMCs that has been suggested to explain the sharp cleft observed in the cyclic voltammetry (CV) trace of the *Geobacteraceae* species under non-turnover conditions, a feature that is also present in the CVs of the biofilms in this study (Figure S1).[15,16]

The spectra obtained at different delay times were subsequently subjected to a component analysis to extract the relative contributions of oxidized and reduced sc-OMCs, expressed as the molar fractions X_{Ox} and X_{Red}, respectively.[10,17] The relaxation constant $k_{relax} = (0.06 \pm 0.04)$ s^{-1}, obtained from the fitting of a single exponential function to the data, refers to the heterogeneous ET with zero-driving force ($\eta = 0$ mV). The relaxation constant was found to be independent of the magnitude of the potential step from E_i to E_f (for $E_f = E_{1/2}$) and was the same irrespective of the direction of the step (Table S1), implying that oxidation and reduction of the sc-OMCs occurred at the same rate. As k_{relax} is equal to the sum of the rate constants for oxidation (k_1) and reduction (k_2), we thus obtained $k_1 = k_2 = 0.03$ s^{-1} (vide infra). It should be noted that TR-SERR experiments carried out with shorter delay times rule out any transient changes of sc-OMCs on the millisecond time scale (Figure S3). Furthermore, an increase in the driving force by selecting $|E_f| > |E_{1/2}|$ ($\eta \neq 0$ mV) has no impact on the relaxation constant determined by TR-SERR spectroscopy (Table S1).

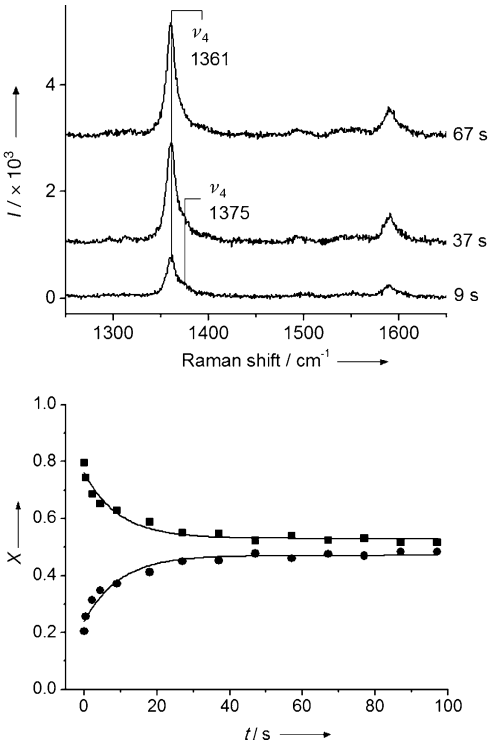

Figure 1. Upper panel: selected TR-SERR spectra of the biofilm under non-turnover conditions obtained at delay times of 9, 37, and 67 s after the applied potential step from $E_i = -450$ mV to $E_f = -320$ mV. Lower panel: time-dependent changes of the mole fractions of reduced (■) and oxidized (●) sc-OMCs determined from the TR-SERR spectra, measured under non-turnover conditions, following a potential step from $E_i = -450$ mV to $E_f = -320$ mV. The solid lines refer to the mono-exponential fits to the experimental data.

Static potential-dependent SERR spectra obtained under turnover conditions (i.e., in the presence of substrate) showed that the majority of the sc-OMCs are reduced, independent of the oxidizing electrode potential (Figure S4). Approximately only 10% of the heme cofactors remained oxidized throughout the entire potential window investigated. As a 10% fraction of sc-OMCs was shown to be redox-inactive under non-turnover conditions,[10] we concluded that such biofilms inevitably include a small portion of sc-OMCs that, possibly because of an unfavorable orientation, do not participate in electron exchange with the electrode.

TR-SERR experiments under turnover conditions, carried out with a wide dynamic range from a few milliseconds to a number of seconds, indicate that there are no transient changes of the oxidation state of the sc-OMCs (Figure S5).

The applied potential steps were also monitored by chronoamperometric measurements to record simultaneous spectroscopic signals and corresponding current (*i*) versus time (*t*) traces. Because the entire biofilm is conductive, the current flow reflects a superposition of all charge-transfer processes originating from all layers of the biofilm.[18] Separating the observed current into the different individual contributions (i.e., surface-confined and more remote OMCs, periplasmic cytochromes, conducting nanowires, and non-Faradaic processes) requires a profound knowledge of the architecture of the biofilm. Because of the lack of this information, we were unable to separate the current flow with respect to redox processes that were not directly probed by SERR spectroscopy. The *i* versus *t* traces obtained under non-turnover conditions display biphasic behavior, showing an initial current flow leveling off after a few seconds, followed by a slower relaxation phase (Figure S6). Accordingly, each *i* versus *t* trace has been fitted to a biexponential function, affording $k_{fast} > 1\ s^{-1}$ and $k_{slow} = (0.04 \pm 0.02)\ s^{-1}$ for the fast and the slow process, respectively. The rate constant of the slow process is in very good agreement with the heterogeneous ET rate constants derived from the TR-SERR experiments (Table S2 and S1, respectively).

Conversely, the fast process cannot be ascribed to redox charging/discharging processes of the sc-OMCs. Such an assignment is highly unlikely as no changes of the oxidation state of sc-OMCs could be detected by TR-SERR spectroscopy, even on the millisecond time scale. Thus, the fast component of the amperometric response to the potential step must refer to another unidentified charge-transfer process in the biofilm.

Discussion

The TR-SERR spectroscopy experiments under non-turnover conditions showed that heterogeneous ET across the sc-OMCs/electrode interface was a slow process. No oxidized sc-OMCs were transiently formed under turnover conditions, which implied that there was a rapid reduction of the sc-OMC via a fast ET from a pool of redox partners, assigned to a bulk redox center (b-RC) that was more remote from the metal surface and thus, in contrast to sc-OMCs, was not visible in the SERR spectra.

Accordingly, the experimental kinetic data obtained in this study could be explained by using a simple model that assumed a pool of two redox centers, that is, sc-OMCs and a b-RC (Figure 2). The sc-OMC was directly monitored by SERR spectroscopy and was characterized by (i) an average redox potential that defined the equilibrium between the reduced and oxidized species, and (ii) a rapid electron exchange between the heme groups within the sc-OMC. The b-RC was not directly accessible using SERR spectroscopy, but it was assumed to exchange electrons with the sc-OMC. As all of the microbial cells within the biofilm were electrically wired to the electrode, there must have been a redox species, such as b-RC,

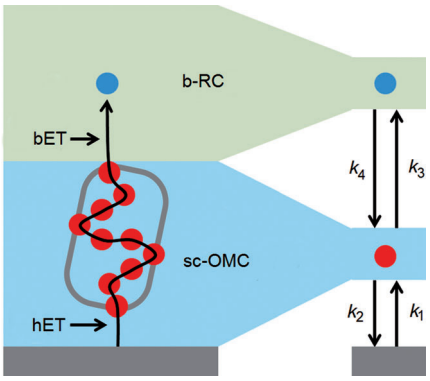

Figure 2. Representation of the scheme adopted to describe the ET across the bacteria/electrode interface and within the microbial biofilm. The red dots on the left panel represent the heme groups of the sc-OMCs. These sc-OMCs exchange electrons with the electrode (in gray), characterized by the rate constants k_1 and k_2, and with the b-RCs, described by the rate constants k_3 and k_4. The black arrow represents the route followed by the electrons in a reduction process. In the right panel, the sc-OMC depicted on the left panel is represented by the average equilibrium potential of the corresponding OMC (i.e. $E_{1/2}$).

that provides such an electrical contact. The lack of substantial information regarding the protein architecture of model *Geobacteraceae* biofilms in close vicinity to the electrode (i.e., < 7 nm) means that the nature of the b-RC cannot be identified. However, according to the models describing the ET process within *Geobacteraceae* biofilms, b-RC could be an OMC (as recently proposed by Bonanni et al.),[19] a conducting nanowire, or a periplasmic cytochrome. Regardless of the nature of b-RC, the kinetic description was restricted to the heterogeneous ET ($k_1 = k_2$, vide supra) of the sc-OMC proteins to (and from) the electrode and the ET between the two pools (k_3 and k_4).

We first considered the TR-SERR experiment under turnover conditions using a potential step from −450 mV to 0 mV. At $E_i = -450$ mV the biofilm was catalytically inactive and the pool of sc-OMCs was fully reduced. After the potential was stepped to 0 mV, no oxidized sc-OMC species were detectable even on the millisecond time scale; therefore, we concluded that ET from the b-RC to the sc-OMC pool was much faster than the heterogeneous ET, that is, $k_4 \gg k_1 = k_2$.

It is reasonable to assume that this relationship was also true for non-turnover conditions and thus for the description of the TR-SERR data in Figure 1. According to the model, the ratio between k_3 and k_4 depends upon the difference between the equilibrium potentials of b-RCs and sc-OMCs, which is not known a priori. We therefore carried out kinetic simulations for various k_4/k_3 ratios on the basis of $k_4 \gg k_1 = k_2$. The simulations (Figure 3) only provided a good description of the experimental data in Figure 1 when $k_3 \approx k_4$ (further details are given in Text S1). This finding implies that the equilibrium potentials of the b-RCs and sc-OMCs were very similar (Text S2). Under the assumption that each cytochrome of the sc-OMC pool exchanged electrons with one redox partner of b-RC, the ET process between the pools had to be at least 40 times faster than the heterogenous ET between the sc-OMC and the electrode

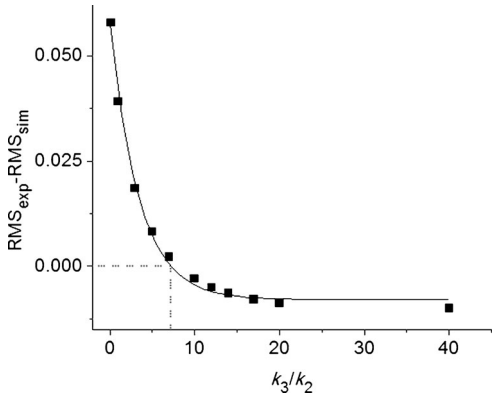

Figure 3. Plot of the difference between the root mean square deviations RMS_{exp} and RMS_{sim} versus the rate constant ratio k_3/k_2 (■). RMS_{sim} refers to the deviation of the kinetic simulation (according to Figure 2) with respect to the experimental data (Figure 1), using $k_1 = k_2 = 0.03\ s^{-1}$ and $k_4 = 1.2\ s^{-1}$ (see text and Text S2 for further details). RMS_{exp} represents the reference value of the mono-exponential fit to the experimental data in Figure 1, determined to be 0.990. The relationship between RMS_{exp}–RMS_{sim} and k_3/k_2 can be approximated by a mono-exponential function (solid line). The k_3/k_2 ratio of 7.2 that corresponds to $RMS_{sim} = RMS_{exp}$ (dashed line) thus affords the lower limit for k_3, that is, $k_3 \geq 0.22\ s^{-1}$.

surface. Therefore, we tentatively estimated the rate constant k_4 to be larger than $1.2\ s^{-1}$.

The slow rate of heterogeneous ET ruled out the direct attachment of the redox-active sc-OMCs to the Ag surface. This conclusion is consistent with the lack of high-spin heme species in the SERR spectra that are usually observed for cytochromes adsorbed on bare Ag electrodes.[20,21] Conversely, the sc-OMCs needed to be separated from the electrode by using poorly conducting biomaterials up to a distance that accounted for the slow ET rate but was sufficient for an appreciable surface enhancement of the RR signals. Considering heterogeneous ET rates and the SERR intensities observed for heme proteins located at well-defined distances from the electrode,[22] the average heme-to-electrode distance of sc-OMCs was in the range of 3–5 nm. At such long distances, direct electron tunneling from the heme to the electrode was less probable and the lack of an overpotential-dependence indicated that the heterogeneous ET must be controlled by a different mechanism. A plausible explanation for these findings could be an electron hopping mechanism as suggested previously for similar slow and overpotential-independent ET over comparably long distances.[23,24] Alternatively, it can be assumed that the heterogeneous ET is limited by another process, tentatively ascribed to proton transfer or biofilm charge/discharge attributable to ion mobility.[4,5]

In conclusion, the lack of an appreciable steady-state or transient concentration of oxidized sc-OMCs in the static and TR-SERR spectra under turnover conditions was because of slow heterogeneous ET, which is likely to be dependent upon the way in which the sc-OMCs are linked to the metal surface. Our conclusions differ substantially from the currently accepted model of the ET within microbial biofilms.[15,19] This model comprises several steps, each one accounting for a different ET process through the entire biofilm and it has been tested with electrochemical techniques on pure *Geobacteraceae* species. Consistently, two groups have estimated very large heterogeneous ET rate constants of 5000 and $10000\ s^{-1}$. Although the sub-millisecond timescale is accessible for TR-SERR spectroscopy, no redox activity associated to the sc-OMCs has been observed on that timescale in our study (see the Supporting Information). Based on this model, Bond et al. predicted a concentration gradient of oxidized cytochromes inside the biofilm under turnover conditions, with cells closer to the anode having the highest concentration of oxidized OMCs.[25] These findings have recently been supported by confocal resonance Raman spectroelectrochemical analysis.[26] Although the presence of such a gradient in the bulk biofilm cannot be directly probed by SERR spectroscopic measurements, the present TR-SERR data under turnover conditions clearly showed that the large majority of sc-OMCs is reduced. These discrepancies may arise from the different electrode material (Ag vs. carbon), the different growth conditions (mixed vs. pure cultures and different applied potentials), or the interplay between these two aspects (e.g. different electrode materials may select different bacterial communities) as well as the presence of further heterogeneous ET mechanisms that could not be detected in our experiments. Accordingly, it would be premature to generalize our conclusions to different biofilm systems.

The present study does not prove nor disprove the conclusions regarding the rate-limiting step of catalytic current production identified in the ET from acetate to internal cytochromes.[15,19] Our results have shown that the slow interfacial ET promoted by the sc-OMCs is followed by a faster, not yet assigned ET process. The present results support the hypothesis that the sc-OMCs act as gates for the electrons exchanged between the electrode and the bulk biofilm, as recently proposed by Inoue et al.[27] Importantly, this model does not exclude the presence of different ET strategies. The b-RCs depicted in Figure 2 could also exchange electrons directly with the electrode through conductive nanowires. However, when the direct ET between these centers occurs (as proven by the presence of a layer of reduced sc-OMCs under turnover conditions), this process is gated by the slow interfacial ET, as shown in the model depicted in Figure 2.

Conclusions

This first TR-SERR spectroscopy study on electroactive microbial biofilms grown on Ag working electrodes has provided unprecedented information regarding the kinetics of the microbial ET. The dynamics of the ET across the biofilm/electrode interface has been directly probed by monitoring the heterogeneous ET of the sc-OMCs. The kinetic simulation of the TR-SERR spectroscopy data obtained under turnover and non-turnover conditions indicates a slow heterogeneous ET of the sc-OMCs, which in turn undergoes rapid electron exchange with a b-RCs. Because of the slow heterogeneous ET, which may reflect an electron hopping mechanism, the sc-OMCs serve as gates for the electrical coupling of the biofilm with the electrode. In this sense, the TR-SERR spectroelectrochemical approach has been shown to be a powerful tool for selectively probing the inter-

facial processes of biofilms close to the electrode surface, both under turnover and non-turnover conditions. Furthermore, these findings may also allow for the elucidation of mechanisms for the recently discovered interspecies ET, for example, in activated sludge granules.[28]

Experimental Section

Microbial inoculum and growth medium

The source of the microbial inoculum was primary waste water, collected from the waste water treatment plant (WWTP) Braunschweig/Steinhof, Germany. The bacterial growth medium contained NH_4Cl (0.31 g L^{-1}), KCl (0.13 g L^{-1}), $NaH_2PO_4{\cdot}H_2O$ (2.69 g L^{-1}), Na_2HPO_4 (4.33 g L^{-1}), trace metal (12.5 mL), and vitamin (12.5 mL) solutions according to Kim et al.[29] Acetate solution (10 mM, pH 6.8) served as the substrate in the growth medium. All solutions were purged with nitrogen before use.

Primary and secondary biofilm formation

As described by Liu et al.[30] for the formation of primary biofilms, 1 mL of waste water per 30 mL of the substrate solution was inoculated into a sealed electrochemical cell incubated at 35 °C. A constant potential of 200 mV versus Ag/AgCl (3.0 M KCl) was applied to the working electrode [graphite rods (CP-Graphite GmbH, Germany)] using a potentiostat (Potentiostat/Galvanostat VMP3, BioLogic Science Instruments, France) to promote and monitor the biofilm formation. The biofilm growth was monitored by measuring the bioelectrocatalytic oxidation current and the substrate (acetate) consumption was analyzed by using HPLC. The exhausted substrate solution was replenished regularly until a steady-state maximum current density was achieved (usually after 3–4 feeding cycles). Afterwards, the primary biofilm was scraped from the carbon electrode in anaerobic and sterile conditions and was used as bacterial inoculum for the secondary biofilm formation following a similar procedure on Ag ring disc electrodes at the applied potential of −50 mV versus Ag/AgCl (3.0 M KCl).[30] After biofilm formation ($j \approx 600\ \mu A\ cm^{-2}$, Figure S 8), these electrodes were used for TR-SERR spectroscopy experiments as described below.

Spectroelectrochemical set-up

Electrochemical measurements on the microbial biofilm were carried out in a homemade spectroelectrochemical cell working in the three-electrode configuration and controlled by a μAutolab potentiostat (Eco Chemie, Utrecht, The Netherlands). The working electrode was a Ag ring with a projected surface area of 0.7 cm^2. All current densities are expressed with respect to the projected electrode area. After mechanical polishing, the electrode was roughened by using the electrochemical procedure described elsewhere,[31] and transferred to the electrochemical cell for biofilm growth (vide supra). A Pt coil and a Ag/AgCl (3.0 M KCl; Dri-Ref, WPI Berlin, Germany) served as the counter and the reference electrode, respectively. All potentials provided in the manuscript are referred to the Ag/AgCl (3.0 M KCl) reference electrode (210 mV versus SHE).

SERR spectroscopy measurements

SERR spectra were measured using a confocal Raman spectrometer (LabRam HR 800, Jobin Yvon) coupled to a liquid-nitrogen-cooled charge-coupled device (CCD) detector. The spectral resolution was 1 cm^{-1} with an increment per data point of 0.75 cm^{-1}. For laser excitation, the 413 nm line of a Krypton laser (Coherent Innova 400) was used. The laser power on the sample was 1.0 mW. The laser beam was focused onto the sample by using a Nikon 20x objective with a working distance of 20.5 mm and a numeric aperture of 0.35. Acquisition times of the SERR spectra ranged between 5 and 60 s. The working electrode was constantly rotated to avoid laser-induced sample degradation. All SERR measurements were carried out in 30 mM phosphate buffer solution at pH 7.

Time-resolved measurements followed the previously described procedure.[31,32] Briefly, potential steps were coupled with short SERR measuring intervals that were defined by gating the continuous-wave laser beam via electrooptical intensity modulators. A home-made multi-channel delay generator was coupled to the potentiostat (EG&G Princeton Applied Research, model 263 A) and the intensity modulators (Linos M 0202) to synchronize potential steps with the measuring intervals.

Acknowledgements

The work was supported by the DFG (Cluster of Excellence "UniCat", PH; SFB 803, CS), the Alexander-von-Humboldt foundation (DM) and the Netherlands Organisation for Scientific Research (NWO) grant 722.011.003 (DM). F.H. acknowledges support by the Fonds der Chemischen Industrie (FCI). U.S. acknowledges the foundation of the professorship Sustainable Chemistry and Energy Research by the Volkswagen AG and the Verband der Deutschen Biokraftstoffindustrie e.V. We would like to thank the reviewers for the thoughtful observations that improved the quality of our work.

Keywords: cytochromes · electron transfer · kinetics · microbial fuel cells · Raman spectroscopy

[1] *Bioelectrochemical Systems: From Extracellular Electron Transfer to Biotechnological Application* (Eds.: K. Rabaey, L. Angenent, U. Schröder, J. Keller), **2010**, IWA Publishing, London, New York.
[2] D. R. Lovley, *Curr. Opin. Biotechnol.* **2008**, *19*, 564 – 571.
[3] U. Schröder, *Phys. Chem. Chem. Phys.* **2007**, *9*, 2619 – 2629.
[4] C. I. Torres, A. K. Marcus, H. S. Lee, P. Parameswaran, R. Krajmalnik-Brown, B. E. Rittmann, *FEMS Microbiol. Rev.* **2010**, *34*, 3 – 17.
[5] A. E. Franks, K. P. Nevin, R. H. Glaven, D. R. Lovley, *ISME J.* **2010**, *4*, 509 – 519.
[6] H. Richter, K. P. Nevin, H. Jia, D. A. Lowy, D. R. Lovley, L. M. Tender, *Energy Environ. Sci.* **2009**, *2*, 506 – 516.
[7] N. S. Malvankar, M. T. Tuominen, D. R. Lovley, *Energy Environ. Sci.* **2012**, *12*, 6247 – 6249.
[8] S. M. Strycharz-Glaven, L. M. Tender, *Energy Environ. Sci.* **2012**, *5*, 6250 – 6255.
[9] F. Harnisch, K. Rabaey, *ChemSusChem* **2012**, *5*, 1027 – 1038.
[10] D. Millo, F. Harnisch, S. A. Patil, K. H. Ly, U. Schröder, P. Hildebrandt, *Angew. Chem.* **2011**, *123*, 2673 – 2675; *Angew. Chem. Int. Ed.* **2011**, *50*, 2625 – 2627.
[11] D. Millo, A. Bonifacio, M. R. Moncelli, V. Sergo, C. Gooijer, G. van der Zwan, *Colloids Surf. B* **2010**, *81*, 212 – 216.
[12] D. Millo, *Biochem. Soc. Trans.* **2012**, *40*, 1284 – 1290.
[13] H. K. Ly, M. Sezer, N. Wisitruangsakul, J. J. Feng, A. Kranich, D. Millo, I. M. Weidinger, I. Zebger, D. H. Murgida, P. Hildebrandt, *FEBS J.* **2011**, *278*, 1382 – 1390.
[14] F. Harnisch, C. Koch, S. A. Patil, T. Hübschmann, S. Müller, U. Schröder, *Energy Environ. Sci.* **2011**, *4*, 1265 – 1267.

[15] S. M. Strycharz, A. P. Malanoski, R. M. Snider, A. Hi, D. R. Lovley, L. M. Tender, *Energy Environ. Sci.* **2011**, *4*, 896 – 913.
[16] K. Fricke, F. Harnisch, U. Schröder, *Energy Environ. Sci.* **2008**, *1*, 144 – 147.
[17] P. Hildebrandt, M. Stockburger, *Biochemistry* **1989**, *28*, 6710 – 6721.
[18] N. S. Malvankar, M. Vargas, K. P. Nevin, A. E. Franks, C. Leang, B. C. Kim, K. Inoue, T. Mester, S. F. Covalla, J. P. Johnson, V. M. Rotello, M. K. Tuominen, D. R. Lovley, *Nat. Nanotechnol.* **2011**, *6*, 573 – 579.
[19] P. S. Bonanni, G. D. Schrott, L. Robuschi, J. P. Busalmen, *Energy Environ. Sci.* **2012**, *5*, 6188 – 6195.
[20] G. Smulevich, T. G. Spiro, *J. Phys. Chem.* **1985**, *89*, 5168 – 5173.
[21] H. Wackerbarth, P. Hildebrandt, *ChemPhysChem* **2003**, *4*, 714 – 724.
[22] D. H. Murgida, P. Hildebrandt, *J. Phys. Chem. B* **2001**, *105*, 1578 – 1586.
[23] T. Morita, S. Kimura, *J. Am. Chem. Soc.* **2003**, *125*, 8732 – 8733.
[24] J. Hrabakova, K. Ataka, J. Heberle, P. Hildebrandt, D. H. Murgida, *Phys. Chem. Chem. Phys.* **2006**, *8*, 759 – 766.
[25] D. R. Bond, S. M. Strycharz-Glaven, L. M. Tender, C. I. Torres, *ChemSusChem* **2012**, *5*, 1099 – 1105.
[26] L. Robuschi, J. P. Tomba, G. D. Schrott, P. S. Bonanni, P. M. Desimone, J. P. Busalmen, *Angew. Chem. Int. Ed.*, **2012**, *52*, 925 – 925; *Angew. Chem.* **2012**, *125*, 959 – 962.
[27] K. Inoue, C. Leang, A. E. Franks, T. L. Woodard, K. P. Nevin, D. R. Lovley, *Environ. Microbiol. Rep.* **2011**, *3*, 211 – 217.
[28] F. Liu, A. E. Rotaru, P. M. Shrestha, N. S. Malvankar, K. P. Nevin, D. R. Lovley, *Energy Environ. Sci.* **2012**, *5*, 8982 – 8989.
[29] J. R. Kim, B. Min, B. E. Logan, *Appl. Microbiol. Biotechnol.* **2005**, *68*, 23 – 30.
[30] Y. Liu, F. Harnisch, K. Fricke, R. Sietmann, U. Schröder, *Biosens. Bioelectron.* **2008**, *24*, 1006 – 1011.
[31] H. Wackerbarth, U. Klar, W. Gunther, P. Hildebrandt, *Appl. Spectrosc.* **1999**, *53*, 283 – 291.
[32] D. H. Murgida, P. Hildebrandt, *J. Am. Chem. Soc.* **2001**, *123*, 4062 – 4068.

Received: August 23, 2012
Revised: November 5, 2012
Published online on ■■ ■■, 0000

Speed dating for electrons: Heterogeneous electron transfer across the biofilm/electrode interface is a slow process promoted by surface-confined cytochromes that are not in direct physical contact with the electrode. Subsequent electron transfer from the surface-confined cytochromes to more remote redox centers within the biofilm is a much faster process. Herein, an approach is identified as a powerful tool for selectively probing interfacial processes of biofilms close to the electrode surface.

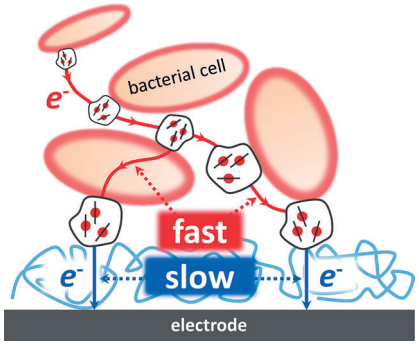

*H. K. Ly, F. Harnisch, S.-F. Hong, U. Schröder, P. Hildebrandt, D. Millo**

■■ – ■■

Unraveling the Interfacial Electron Transfer Dynamics of Electroactive Microbial Biofilms Using Surface-Enhanced Raman Spectroscopy

10

Induced Surface Enhancement in Coral Pt Island Films Attached to Nanostructured Ag Electrodes

Ly, H. K.; Köhler, C.; Fischer, A.; Kabuß, J.; Schlosser, F.; Schoth, M.; Knorr, A.; Weidinger, I. M. *Langmuir* **2012**, 28, 5819–5825.

Langmuir

Article

pubs.acs.org/Langmuir

Induced Surface Enhancement in Coral Pt Island Films Attached to Nanostructured Ag Electrodes

H. Khoa Ly,[†] Christopher Köhler,[‡] Anna Fischer,[†] Julia Kabuss,[‡] Felix Schlosser,[‡] Mario Schoth,[‡] Andreas Knorr,[‡] and Inez M. Weidinger*[,†]

[†]Institut für Chemie, Technische Universität Berlin, Strasse des 17 Juni 135, D-10623 Berlin, Germany

[‡]Institut für Physik, Technische Universität Berlin, Hardenbergstrasse 36, D-10623 Berlin, Germany

Supporting Information

ABSTRACT: Coral Pt islands films are deposited via electrochemical reduction on silica-coated nanostructured Ag electrodes. From these devices surface-enhanced (resonance) Raman [SE(R)R] signals of molecules exclusively attached to Pt are obtained with intensity up to 50% of the value determined for Ag. SE(R)R spectroscopic investigations are carried out with different probe molecules, silica-coating thicknesses, and excitation lines. Additionally, field enhancement calculations on Ag−SiO_2−Pt support geometries are performed to elucidate the influence of the Pt island film nanostructure on the observed Raman intensities. It is concluded that the nonperfect coating of the Pt island film promotes the efficiency of the induced Pt SER activity. Comparison with similar measurements on Ag−SiO_2−Au electrodes further suggests that the chemical nature of the deposited metal island film plays a minor role for the SE(R)R intensity.

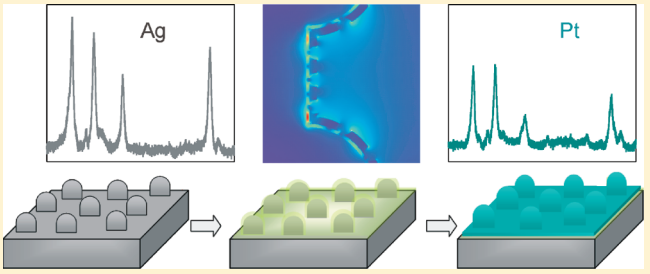

1. INTRODUCTION

Surface chemistry plays a key role in many fields of modern technology such as heterogeneous catalysis, solar energy conversion, or bioelectronics. The efficiency of the surface-confined processes sensitively depends on the interaction of adsorbates with their underlying support. Hence, changing the chemical nature and surface morphology of the support as well as the properties of the surrounding medium can greatly enhance or diminish the performance of the device. Therefore, considerable research efforts have been made to design new types of support materials. However, probing the adsorbates and their processes on such surfaces represents a considerable challenge since there are no generally applicable analytical techniques that provide information about the molecular structure and dynamics of the adsorbates under in situ conditions.

In contrast to most surface-sensitive methods that are only applicable to solid/gas interfaces at very low pressures, surface enhanced Raman (SER) spectroscopy can be employed to surfaces irrespective of the kind of surrounding medium and thus may be the in situ analytical method of choice in surface chemistry.[1−5] The main drawback of SERS that currently prevents a wider applicability is related to the signal enhancement mechanism which requires the resonant coupling of radiation with surface plasmons of the metallic support. Such plasmon resonances strongly depend on the dielectric function and surface morphology of the metal, and so far mainly Ag and Au have been demonstrated to be capable of providing sufficient surface enhancement for reliable SER analysis.[6] In particular, Ag affords a strong surface enhancement in a wide spectral range from the violet to the near-infrared region,[7−9] but unfortunately this metal is only of minor interest for many technological applications. In this respect, other metals such as Pt or Pd are much more relevant; however, their intrinsic SERS activity is lower by several orders of magnitude than in the case of Ag[10] such that they are not considered as suitable supports for in situ SER spectroscopy.

To overcome this drawback several approaches have been developed in the past to induce SER activity for molecules adsorbed on plasmonic inactive surfaces. All these approaches have in common that they are based on hybrid systems consisting of a plasmonic component such as Ag or Au for optical amplification and a nonplasmonic component for surface chemistry: In tip-enhanced Raman (TER) spectroscopy surface enhancement is provided by a nanoscaled Au(Ag) tip that is brought in close vicinity to the adsorbate on a nonplasmonic support.[11−13] Although much insight can be given by this technique it requires a rather demanding setup. In-situ spectroscopy, however, does not necessarily need the high spatial resolution of TER spectroscopy but relies upon a flexible setup that can be easily adapted to specific applications such as heterogeneous catalysis in reactors or electrochemical cells in bioelectronics. Therefore, alternatively a strategy was proposed where the tip is replaced by an ensemble of nanoparticles that are spread onto the probed surface.[14−16] This approach avoids the sophisticated TER setup but at the

Received: December 29, 2011
Revised: February 13, 2012
Published: March 8, 2012

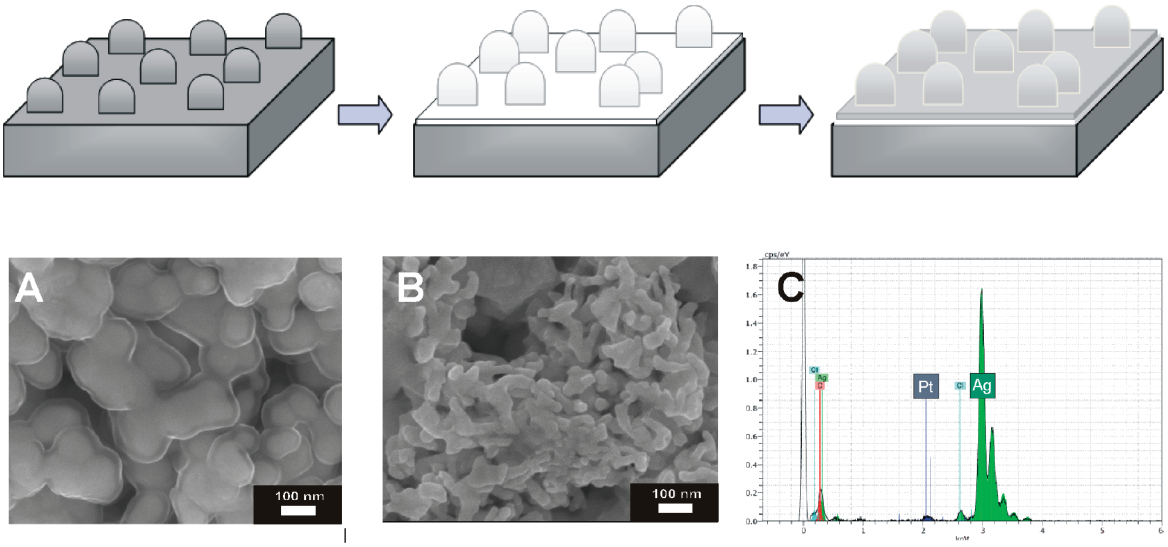

Figure 1. Schematic presentation of the Ag−SiO_2−Pt electrode preparation. First, an Ag electrode was electrochemically roughened, followed by coating with a dielectric SiO_2 spacer layer of defined thickness. Finally, a nanostructured Pt island film was electrochemically deposited on top of the spacer. (Bottom) SEM pictures of Ag−SiO_2 (A) and Ag−SiO_2−Pt (B) electrodes, and an EDX spectra of the Ag−SiO_2−Pt electrode (C).

same time largely decreases the available area for surface chemistry.

Finally, an overlay approach was introduced by Weaver et al. and further developed by us and others where surface enhancement is induced into a nonplasmonic metal film by an underlying nanostructured SERS active support.[17−23] In our previous work, electrochemically roughened Ag electrodes were used as SERS active support and Au as an outer metal layer for surface chemistry. The induced surface enhancement experienced by molecules attached to Au was measured under violet light excitation where Au itself does not show intrinsic plasmonic activity. In contrast to the strategy of Weaver et al., we introduced a defined separation of Au from the rough Ag electrode by coating the latter with a dielectric spacer of defined thickness. Repellent functionalization of the spacer layer guaranteed exclusive adsorption of the adsorbates under investigation on Au even for a nonperfectly closed metal film. With this strategy the enhancement of Raman signals of the probe molecule, i.e., the heme protein cytochrome c (Cyt-c), was found to be similar on the outer Au layer as for direct immobilization on the Ag support. This highly unusual long-range enhancement over a spacer thickness of more than 20 nm was rationalized by field enhancement calculations of Ag−spacer−Au devices.[24]

In this paper we successfully expanded our approach to coral Pt island films. By variation of the excitation line, target molecules, and spacer thickness, it was possible to identify crucial parameters for optimum induced surface enhancement at plasmonic inactive metal films. In addition, field enhancement calculations were performed on different multilayer Ag−spacer−Pt geometries to rationalize the experimental results.

2. MATERIALS AND METHODS

2.1. Chemicals. Tetrachloroplatinate(II) acid ($H_2[PtCl_4]\cdot 6H_2O$, 99.9%), tetraethyl orthosilicate (TEOS, 99.99%), aminopropyl triethoxysilane (APTES), 3-mercaptopropylmethyldimethoxysilane (MPTS), 11-amino-1-undecanethiol (AUT), and 11-mercapto-undecanoic acid (MUA) were purchased from Sigma Aldrich. Ethanol (99.99%), isopropyl alcohol (99%), and ammonium hydroxide (35% aqueous solution) were obtained form Fischer Scientific Co. (Germany). Potassium hydrogen phosphate and potassium dihydrogen phosphate were provided by Merck (Germany). Benzenethiol (BT, 98%) and mercaptopyridine (mPy, > 95%) were purchased from Sigma-Aldrich. All reagents were of analytical grade and used as received. Solutions were prepared using ethanol of analytical grade (99.99%) or Millipore water (Eschborn, Germany) with a resistance > 18 MΩ. Ag ring electrodes of 8 mm diameter and 2.5 mm height were machined from 99.99% Ag rods (Goodfellow, U.K.). Cytochrome c (Cyt c, Sigma-Aldrich) was purified as described previously.[25]

2.2. Spectroscopic and Electrochemical Measurements. Spectroelectrochemistry was performed using cylindrical Ag and Ag−S−Pt rings as working electrode, an Ag/AgCl (3 M KCl) reference electrode (+0.21 V vs SHE), and a platinum counter electrode. SER(R) spectra were measured using a confocal Raman spectrometer (LabRam HR 800, Jobin Yvon) coupled to a liquid-nitrogen-cooled CCD detector. The spectral resolution was 1 cm^{-1} with an increment per data point of 0.28 and 0.15 cm^{-1} using the 413 and 514 nm laser excitation line, respectively. For laser excitation the 413 nm laser line of a Krypton (Coherent Innova 300c) or the 514 nm line of an argon cw laser (Coherent Innova 70c) was used. The laser power on the sample was 1.0 mW. The laser beam was focused onto the sample by a Nikon 20× objective with a working distance of 20.5 mm and a numeric aperture of 0.35. Accumulation times of the SERR spectra were between 1 and 12 s. The working electrode was constantly rotated to average over a high electrode surface and to avoid laser-induced sample degradation. All SER(R)S measurements were done in 30 mM PBS buffer solution. Cyclic voltammetric experiments were performed with a CH instrument 660 C (Austin, USA).

2.3. Electrode Characterization. The surface morphology and elemental composition of the electrodes was characterized with scanning electron microscopy (SEM) and energy-dispersive X-ray spectroscopy (EDX) using a JEOL 7401F operated between 8 and 12 kV equipped with an EDX detector Quantax XFlash Detektor 4010 from Bruker. Specific surface area measurements using multipoint BET were done with Krypton gas adsorption measurements at 77.4 K with an Autosorb-1-C from Quantochrome. Samples were degassed at 80 °C overnight prior to measurement.

2.4. Theoretical Calculations. The field distribution was simulated using the Maxwellsolver JCMsuite, a finite element software for computation of electromagnetic waves, developed by the Zuse Institut Berlin.[26] The experimental structures were modeled by a three-dimensional but rotationally symmetrical geometry. An external

dx.doi.org/10.1021/la205139g | Langmuir 2012, 28, 5819−5825

electromagnetic field was applied with defined polarization, wavelength, and vector amplitude to calculate the field enhancement.

3. RESULTS

3.1. Electrode Preparation. Ag−SiO_2−Pt electrodes were created following the procedure established for Ag−SiO_2−Au in our previous work[19,21] with some modifications. The steps for electrode preparation are illustrated in the top half of Figure 1. First, a nanostructured Ag support was created from a cylindrical Ag bulk electrode via electrochemical roughening using an established protocol.[27,28] The rough Ag electrode was then coated with a silica layer of variable thickness. Thin layers (0.7 nm) were formed by self-assembly of MPTS in ethanolic solution.[21,29] Thicker SiO_2 layers were generated by additional incubation of the electrode in a TEOS solution for 2 h.[30] The thickness of the SiO_2 layer could thereby be tuned by adjusting the concentration of the TEOS precursor.[31] Subsequently, the Ag−SiO_2 electrode was dipped in APTES solution overnight to obtain a positively charged amino-functionalized surface. This step resulted in an additional layer thickness of 1.0 nm.[32,33]

An SEM picture of an Ag−SiO_2 electrode surface is shown in Figure 1A. It can be clearly seen that a closed and dense SiO_2 film covers completely the Ag surface. The average thickness of the SiO_2 layers can be estimated directly from the picture using the included scale. The values were then correlated with the TEOS concentration in the precursor solutions. The thickness of the SiO_2 film in Figure 1A was determined to be 15 nm corresponding to an initial TEOS concentration of 6 μM. In the case of MPTS−APTES-coated electrodes the layer thickness of 1.7 nm was estimated by adding the respective lengths of the individual monolayers. It should be noted that attaching SiO_2 does not affect the surface morphology of the electrode. If the surface pattern of the Ag electrode is approximated by an arrangement of connected coral spheres an average coral diameter of d = 85 ± 20 nm can be estimated. In the last step, the Ag−SiO_2 electrode was dipped into an ethanol solution of 2 wt % of $H_2[PtCl_4]\cdot 6H_2O$ for 30 min to allow for electrostatic binding of $PtCl_4^-$ ions to the positively charged amino groups of the silica surface. After changing the buffer solution, a potential of −0.5 V was applied which resulted in a reduction of $[PtCl_4]^{2-}$ ions and a Pt island film was generated on top of the Ag−SiO_2 electrode. In Figure 1B an SEM picture of the electrode after electrochemical Pt deposition is shown. The electrode surface is now covered by a Pt island film that exhibits also a coral-like structure but with a smaller coral size than the underlying Ag support. The average diameter of the Pt nanocorals is approximated by 30 ± 10 nm. The presence of Pt could be proven by EDX measurements that can be seen in Figure 1C. It has to be noted that with increasing incubation time of the Ag−SiO_2-coated electrode in the $PtCl_4$ solution also islands with a thicker, film-like morphology were formed upon Pt reduction (see Figure S1 Supporting Information). Thicker and thus more closed films, however, led to a decrease in SER intensity of adsorbates (vide infra).

3.2. Determination of REF for Rough Ag Electrodes. Prior to estimation of the surface enhancement of Ag−SiO_2−Pt electrodes the Raman enhancement factor (REF) of the pure electrochemically roughened Ag electrodes had to be determined according to eq 1

$$\mathrm{REF} = \frac{I_{\mathrm{SERS}}}{I_{\mathrm{R}}}\cdot\frac{N_{\mathrm{R}}}{N_{\mathrm{SERS}}} = \frac{I_{\mathrm{SERS}}}{I_{\mathrm{R}}}\cdot\frac{c_{\mathrm{R}}\cdot V}{\Gamma_{\mathrm{SERS}}\cdot A} \quad (1)$$

where I_R and I_{SERS} are the Raman intensities of probe molecules in solution and adsorbed on the Ag surface, respectively. These intensities are normalized to the same accumulation time and laser intensity. N_R and N_{SERS} refer to the number of molecules that are in the focus of the laser beam. These quantities are related to the product of illuminated volume V and bulk concentration c_R in the normal Raman and to the product of the illuminated area A and the surface concentration Γ_{SERS} in the SER experiments. Benzenethiol (BT) was used as a Raman probe to estimate REF following the procedure described by McFarland et al.[34] Raman and SER spectra were measured for BT in solution and adsorbed on the surface using 413 and 514 nm excitation. The intensity ratio of I_{SERS}/I_R was subsequently determined for the 1000 and 1080 cm^{-1} line. The average ratio considering both bands is shown in Table 1. The concentration

Table 1. Ratio between SERS and Normal Raman Intensities of BT and Corresponding Raman Enhancement Factors (REF) of Electrochemically Roughened Ag Electrodes

λ/nm	I_{SERS}/I_R	REF
514	1.1	2×10^3
413	0.2	5×10^2

of the neat BT solution was c_R = 9.54 mol/L. The irradiated volume V was approximated by a cylinder with radius r and height h

$$V = \pi\cdot r^2\cdot h \quad (2)$$

where r is given by the radius of the laser focus which has been estimated by McFarland et al. to be r = 2 μm for a 20× objective independent of the laser wavelength. The height of the cylinder can be approximated by the depth of focus of a Gaussian beam

$$h = 2\cdot r^2\cdot\frac{\pi}{\lambda} \quad (3)$$

Accordingly, the surface area probed in the SERS measurements is given by

$$A = RF\cdot A_{\mathrm{geom}} = RF\cdot\pi\cdot r^2 \quad (4)$$

where A_{geom} stands for the geometrical area of the electrode illuminated by the laser. To obtain the real surface area one has to multiply by a factor that accounts for the surface roughness of the electrode. The surface roughness factor (RF) was determined independently by BET measurements to be 20. The surface concentration of Γ_{SERS} = 1.1 nM/cm^2 of BT on Ag was taken from ref 34.

On the basis of these parameters, we obtain a value for REF = 2×10^3 for 514 nm and 5×10^2 for 413 nm excitation. These values have to be seen as lower limits as we assume that all parts of the surface are accessible by laser light and that a compact BT monolayer is formed on the surface. Nevertheless, the low REF values can be rationalized by the fact that, due to the random coral structure, a large fraction of the surface plasmons is not in resonance with the incoming light. Hence, the averaged signal that is observed in the SERR spectrum might originate only from a small percentage of the surface area. In return this heterogeneity ensures surface enhancement over a broad range of excitation lines.

3.3. SER Spectroscopy of mPy on Pt. Mercaptopyridine (mPy) was used as a Raman probe to test surface enhancement at the Pt surface in Ag−SiO_2−Pt hybrid electrodes. The

dx.doi.org/10.1021/la205139g | Langmuir 2012, 28, 5819−5825

different electrodes were incubated in a 5 mM mPy aequeous solution for 20 min. SER spectra were measured in pure buffer solution after rinsing and incubation in 1 M KCl for 10 min to remove the loosely bound mPy. A typical SER spectrum of mPy adsorbed on bare Ag at 514 nm excitation is shown in Figure 2A. SER measurements under the same conditions using

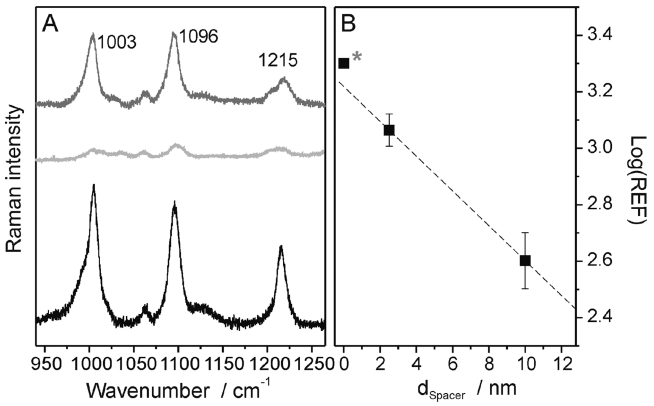

Figure 2. (A) From bottom to top: SER spectra of mPy attached to Ag (black), Ag−MPTS−APTES (light gray), and Ag−MPTS−APTES−Pt (gray) surfaces. (B) Raman enhancement factors (REF) of mPy attached to Pt as a function of the spacer thickness. Value marked with an asterisk corresponds to mPy on bare Ag surfaces system.

an MPTS−APTES-coated Ag electrode yielded a more than 20 times lower signal intensity of mPy. If, however, the electrode was coated additionally with a Pt island film the mPy intensity increased again to roughly 50% of the Raman intensity measured on bare Ag (Figure 2A, top). The intensity of the 1096 cm^{-1} band of mPy adsorbed on Ag was ascribed to the Raman enhancement factor (REF) of 2×10^3 (vide supra). Correspondingly, REF for mPy on Pt was derived by comparison of this band's relative intensity with respect to its value on Ag. The values for log(REF) obtained in this way are plotted in Figure 2B for two different spacer thicknesses, assuming the same mPy surface coverage. The data show that REF decreases with spacer thickness, supporting the view that the surface enhancement generated at the Ag surface is mainly responsible for the observed SER intensity. Nevertheless, even for a 10 nm thick spacer, REF has decreased only by a factor of ca. 5 compared to bare Ag. The decrease in REF as a function of SiO_2 thickness may be considered to be linear with a slope of $\Delta\log(\mathrm{REF})/\Delta d = 0.06\ \mathrm{nm}^{-1}$.

3.4. SERR Spectroscopy of Cyt c at Pt. Intense SERR (surface-enhanced resonance Raman) spectra are obtained for the heme protein cytochrome c (Cyt c) attached to SER-active electrodes under violet light excitation which matches the electronic transition of the heme chromophore. Furthermore, the redox properties of Cyt c are preserved if the metal electrode is coated by biocompatible self-assembled monolayer (SAM). Cyt c is therefore widely used as a reference system to test surface enhancement and electrical communication of novel nanostructured electrodes.[21,35]

Cyt c directly adsorbed on bare Ag surfaces is known to undergo a partial transition to a non-native high-spin state of the heme which can be distinguished from its native state in the SERR spectrum.[36,37] To avoid this adsorption-induced protein denaturation the electrodes are usually coated with a SAM of ω-carboxyl alkanethiols. The increased biocompatibility, however, is achieved at the expense of surface enhancement that drops by a factor of 2 after coating with SAMs of mercaptoundecanoic acid (MUA). For Cyt c directly adsorbed to the Pt surface in Ag−SiO_2−Pt electrodes SERR spectra with high intensity could be obtained. However, the spectra also indicated a strong contribution of the non-native high-spin state (Figure S2 Supporting Information) accompanied by a time-dependent decrease in SERR intensity. The Pt surface was therefore coated with MUA prior to Cyt c adsorption, in analogy to previous experiments on Ag surfaces.[38] The electrodes were incubated in a 0.2 μM Cyt c containing aqueous solution for 30 min, rinsed subsequently with abundant buffer solution, and finally mounted into a spectroelectrochemical cell containing a protein-free buffer solution. Spectra obtained this way were stable over time and could be quantitatively described by a superposition of spectra of the native ferrous and ferric form of Cyt c only. The SERR spectra of Cyt c attached to Ag−MUA and Ag−S−Pt−MUA with S = MPTES−APTES differ only slightly in SERR intensity, which is lowered by roughly a factor of 2 for the Pt hybrid system (Figure 3A). By changing the applied potential of

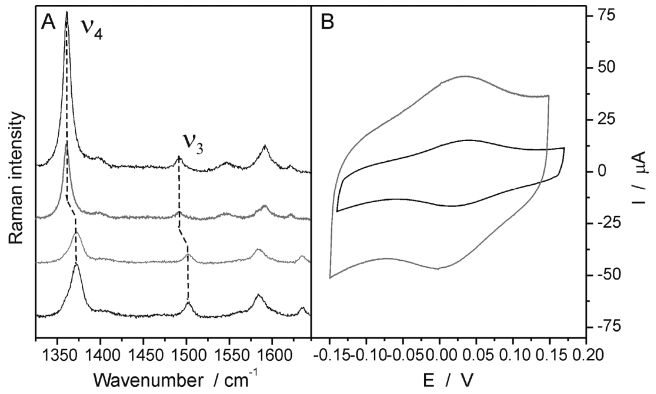

Figure 3. (A) Potential-dependent SERR spectra of Cyt c on (from top to bottom) Ag−MUA (E = +150 mV), Ag−S−Pt−MUA (E = +150 mV), Ag−S−Pt−MUA (E = −400 mV), Ag−MUA (E = −400 mV). (B) CV of Cyt c on Ag−MUA (black) and Ag−S−Pt−MUA (gray). S = MPTES−APTES. Scan rate: 100 mV/s.

the spectroelectrochemical cell the protein could be completely reduced and reoxidized when adsorbed on the Pt surface, which demonstrates that the electrical communication between the working electrode and Cyt c is still intact. The Cyt c midpoint potential was determined to be E_m = 20 mV, which is identical to its value on Ag−MUA.[38]

REF on the Pt surface was obtained by comparison of the relative Cyt c SERR intensities attached to Ag−MUA and Ag−S−Pt−MUA supports. Thus, the REF on Ag−MUA was estimated to be 2.5×10^2 taking into account the effect of the MUA coating on surface enhancement (vide supra). In order to eliminate the effect on signal intensity that arises from variations in the number of probed Cyt c molecules CV measurements were carried out concomitant to the spectroscopic investigations. CV plots of Cyt c attached to either Ag−MUA or Ag−S−Pt−MUA electrodes are shown in Figure 3B. Integration of the voltammetric peaks allowed one to determine the Cyt c surface coverage Γ_{Cyt} for both systems. Γ_{Cyt} was calculated for Ag−MUA to be 6.5×10^{-11} M cm^{-2} with respect to the geometrical area of the electrode. On Ag−S−Pt−MUA a nearly 2 times higher value of 1.2×10^{-10} M cm^{-2} was determined. One has to note that these values represent

dx.doi.org/10.1021/la205139g | Langmuir 2012, 28, 5819−5825

apparent surface concentrations as the respective surface roughness of the different electrodes is not considered. Multiplication of Γ_{Cyt} with the area of the laser spot gives the number of Cyt c molecules that contribute to the observed Raman signal. Thus, REF on Pt was corrected for the higher number of probed Cyt c molecules and is presented in Figure 4A as a function of SiO_2 spacer thickness. In Figure 4A also the

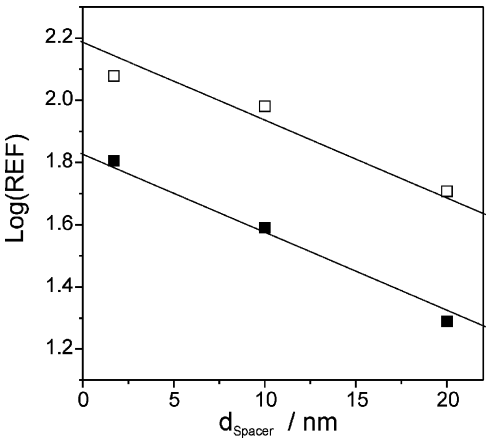

Figure 4. Raman enhancement factors (REF) for Cyt c on Ag−SiO_2−Au−MUA (open squares, taken from ref 32) and Ag−SiO_2−Pt−MUA (solid squares, this work) electrodes as a function of SiO_2 spacer thickness.

REF values previously determined for Ag−SiO_2−Au−MUA electrodes[21,39] are shown. As can be seen, the overall value for REF will be slightly higher if one uses Au as the outer metal. Nevertheless, the slope of a linear fit in Figure 4A, which was determined to be $\Delta\log(\mathrm{REF})/\Delta d = 0.025\ \mathrm{nm}^{-1}$ for Pt coatings, is nearly the same for Au and Pt hybrid electrodes.[39]

3.5. Calculations. The electric field enhancement distribution was calculated using the finite element method for a electrode model geometry. The multilayered electrode depicted in Figure 5A was modeled as follows: Starting with an infinite long bulk Ag electrode (y direction) with a height of 100 nm, 3 half spheres were attached with a radius r_0 = 42.5 nm corresponding to the experimentally determined average Ag coral size. The distance between the half spheres is unevenly distributed with two spheres being in close vicinity (6 nm) and a third one in a wider distance (62.5 nm). This structure is coated with a 2 nm dielectric spacer of SiO_2 and a 5 nm thin Pt film of the same surface morphology. Water was taken as the surrounding medium. The applied external electromagnetic field is taken as a plane wave incoming from the right, propagating along the x direction. The light is assumed to be linearly polarized parallel to the y axis, the wavelength is set to λ = 413 nm, and the vector amplitude is set to $|\vec{E}_0| = 1$. For the chosen geometry it can be clearly seen that surface enhancement of the fields is still present at the Pt−H_2O interface. Due to the choice $|\vec{E}_0| = 1$ the field enhancement is given by the absolute value of the electric field $|\vec{E}|$. Maximum field enhancement is achieved in the interspaces of the two close-by half spheres. The perfect coated uniform Pt film in Figure 5A (2D plot left side), however, does not resemble the Pt film that is present in the experiments. One of the main differences compared to the real samples lies in the fact that the Pt island film, as shown in Figure 1, is not completely covering the underlying electrode, i.e., it exhibits hole-like defects. To approximate the experimental conditions more closely, holes were introduced into the Pt film shown in Figure 5B. Interestingly, these defects enhance the average electric field at the Pt surface. Figure 5 (right side) shows the corresponding 3D plots of the field enhancement for the perfect and disordered system. It can be seen that introducing hole-like defects generates more "hot spots" for surface enhancement in the SiO_2/Pt interface. Most remarkable are the "hot spots" at the top of the half sphere and in the wider gap between the two spheres where no surface enhancement was observed in the absence of defects. It has to be further noted that a particularly large enhancement is observed at the sharp edges of the Pt islands, which are missing in closed films.

To obtain the average SERS enhancement for molecules adsorbed on Pt, $|\vec{E}|$ was read out at equidistant points 1 nm above the Pt surface for the geometries shown in Figure 5A and 5B, respectively. The SERS enhancement of adsorbates placed at these positions is then given by $g = |\vec{E}|^4$.[40] Direct comparison of both types of Pt films shows that the average SERS enhancement per surface area is increased by approximately 80% for the disordered film.

4. DISCUSSION

High-quality SER(R) signals in Ag−SiO_2−Pt constructs could be seen for nonresonant Raman (mPy) and RR probes (Cyt c), suggesting that the optical properties of the adsorbate itself do not play a role in the magnitude of induced surface enhancement at the Pt surface. Depending on the thickness of the spacer layer the surface enhancement at the Pt layer was estimated to reach 15−50% of the enhancement of pure Ag. This is 2 orders of magnitude higher than the intrinsic enhancement of pure Pt, which roughly reaches 0.2% of the Ag value.[10] Furthermore, the comparable SERR enhancement achieved for Pt and Au films in similar hybrid systems indicates that the chemical nature of the outer metal island film is also not highly relevant for the magnitude of induced SER activity. These results suggest that the in situ Raman detection method, proposed in this work, most likely can be applied for a variety of metal films and adsorbates.

The surface enhancement of rough Ag electrodes was determined to be 4 times higher at 514 nm compared to 413 nm laser excitation. The same wavelength-dependent enhancement ratio was observed on Pt if thin spacer layers (1.7 nm) would be used. This finding supports our hypothesis that the optical properties solely of Ag are responsible for the observed enhancement at the outer metal film. However, the distance-dependent decrease of the REF was 3 times stronger for 514 nm excitation than for 413 nm. It might be that different spots or local areas in the coral-like structures of Ag and Pt are responsible for field enhancement at 514 and 413 nm. For thinner coatings the wavelength-dependent field enhancement distribution is not altered, whereas thicker coatings that have a stronger influence on the overall surface morphology shift the enhancement distribution to lower wavelengths.

This raises the question whether geometrical parameters of the multilayer hybrid system in general are the main factor for the magnitude of SER/SERR enhancement at the Pt surface.

The morphology of the Pt island film (Figure 1) shows a coral-like nanostructure with smaller dimensions than the corals of the underlying Ag. Furthermore, the Ag−SiO_2 substrate contains areas with no or nondetectable Pt coverage. Both effects were simulated in the field enhancement calculations shown in Figure 5 by introducing small holes into the Pt film.

dx.doi.org/10.1021/la205139g | Langmuir 2012, 28, 5819−5825

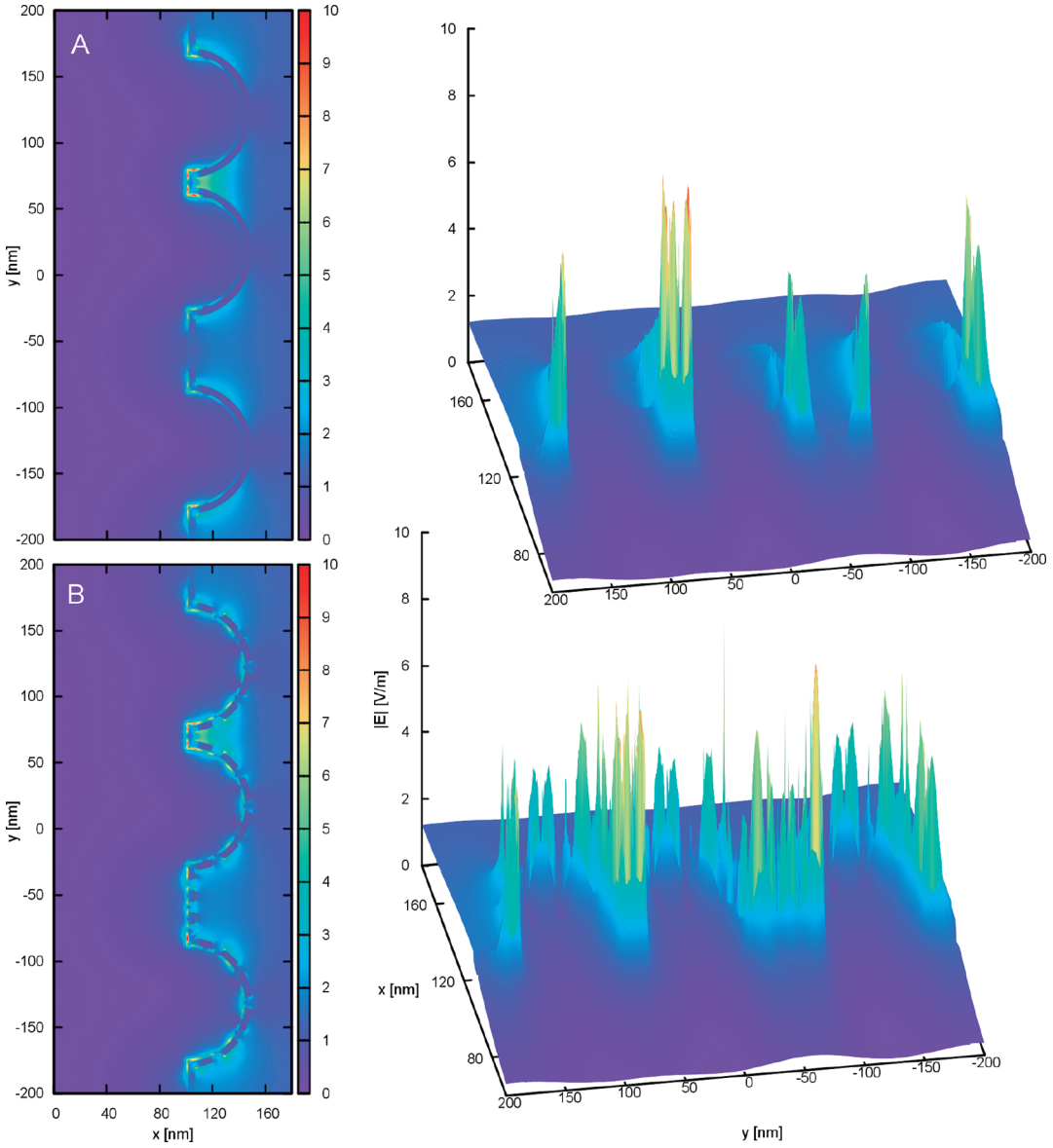

Figure 5. Field enhancement calculations of Ag−SiO_2−Pt geometries using a defect-free (A) and defect-containing (B) Pt film. On the right side the corresponding 3D plots of the field enhancement are displayed.

As a result, the average SERS enhancement is increased by ca. 80%.

This finding can be rationalized on the basis of two factors. First, the presence of holes will increase the number of incident photons on the Ag surface for excitation of surface plasmons and thus for field enhancement, whereas for closed Pt film losses due to reflection are much more severe. Second, the defects also create sharp edges within the Pt nanostructure. According to theoretical predictions, such a geometric anisotropy in nanostructures provides a non-negligible contribution to the overall SER enhancement.[41,42] This so-called lightening rod effect focuses electric fields at the tip of metallic ellipsoids constituting an additional contribution to the field enhancement generated by metal particle plasmons. For Pt, which displays only a poor field enhancement due to particle plasmon resonances, such geometrical aspects are considered as the most important parameter for its marginal intrinsic SER activity.[10]

In view of these considerations, we conclude that the morphology of the Pt film plays the most crucial role for its observed high SER activity. Simple electrochemical deposition, as proposed in this work, creates Pt islands on top of coated Ag nanostructures with a favorable geometry for induced surface enhancement. This hypothesis is further supported by SERR measurements on Ag−SiO_2−Au hybrid electrodes where the outer Au film was formed via sputtering and thus exhibited a largely defect-free surface morphology. For this multilayer system no SERR signals of Cyt c could be detected.

5. CONCLUSION

This work presents a detailed investigation on how SER spectroscopy can be optimized in thin metal films that do not have intrinsic plasmonic activity. In the present Ag−spacer−Pt devices the SER intensity reaches ca. 50% of its value for Ag under otherwise identical conditions. The separation of Pt from Ag by a dielectric spacer has only a small effect on the surface enhancement, but the silica coating efficiently prevents

dx.doi.org/10.1021/la205139g | *Langmuir* 2012, 28, 5819−5825

interaction of Ag with the adsorbates. As the most crucial parameter for the magnitude of SER enhancement the surface morphology of the metal island film could be identified, whereas the chemical nature of the metal seems to play only a minor role. The defect-containing outer Pt layer allows an efficient excitation of the Ag plasmons that are required to enhance the electric field in the vicinity of the Pt surface. The anisotropic shape of the Pt corals additionally promotes surface enhancement via the lightning rod effect. In summary, our results suggest that geometrical parameters of such multilayered electrode dominate the induced SERS efficiency on intrinsically SER-inactive metal films. Hence, the present approach should be applicable for analysis of adsorbates also on other types of metals and thus may contribute to establish SER spectroscopy as a versatile in situ analytical tool for various applications.

■ ASSOCIATED CONTENT

Ⓢ Supporting Information

Further electrode characterization by SEM and SERRS; SERR spectra of Cyt c directly on Pt. This material is available free of charge via the Internet at http://pubs.acs.org.

■ AUTHOR INFORMATION

Corresponding Author

*E-mail: i.weidinger@mailbox.tu-berlin.de.

Notes

The authors declare no competing financial interest.

■ ACKNOWLEDGMENTS

The authors thank Peter Hildebrandt for encouragement and support. Furthermore, we thank Ralph Krähnert and Ulrich Gernert for their support in SEM measurements and the Konrad-Zuse-Zentrum Berlin for providing the Maxwell solver JCMsuite (www.jcmwave.com). Financial support from the Fonds der Chemie and the DFG (Unicat, SPP Nanooptics) is gratefully acknowledged.

■ REFERENCES

(1) Kim, H.; Kosuda, K. M.; Van Duyne, R. P.; Stair, P. C. *Chem. Soc. Rev.* **2010**, *39*, 4820−4844.
(2) In *Surface Enhanced Raman Spectroscopy Analytical, Biophysical and Life Science Applications*; Schlucker, S., Ed.; Wiley-VCH: Weinheim, Germany, 2011.
(3) Smith, W. E.; Faulds, K.; Graham, D. *Surface-Enhanced Raman Scattering: Physics and Applications*; Springer-Verlag: Berlin Heidelberg, 2006; Vol. *103*, pp 381−396.
(4) Siebert, F.; Hildebrandt, P. *Vibrational Spectroscopy in Life Science*; Wiley-VCH: Weinheim, Germany, 2008.
(5) Bantz, K. C.; Meyer, A. F.; Wittenberg, N. J.; Im, H.; Kurtulus, O.; Lee, S. H.; Lindquist, N. C.; Oh, S. H.; Haynes, C. L. *Phys. Chem. Chem. Phys.* **2011**, *13*, 11551−11567.
(6) Le Ru, E. C.; Etchegoin, P. G. *Principles of Surface-Enhanced Raman Spectroscopy*; Elsevier: Oxford, 2009.
(7) GarciaVidal, F. J.; Pendry, J. B. *Phys. Rev. Lett.* **1996**, *77*, 1163−1166.
(8) Sanchez-Gil, J. A.; Garcia-Ramos, J. V. *J. Chem. Phys.* **1998**, *108*, 317−325.
(9) Hildebrandt, P.; Stockburger, M. *J. Phys. Chem.* **1986**, *90*, 6017−6024.
(10) Tian, Z. Q.; Ren, B.; Wu, D. Y. *J. Phys. Chem. B* **2002**, *106*, 9463−9483.
(11) Domke, K. F.; Pettinger, B. *ChemPhysChem* **2010**, *11*, 1365−1373.
(12) Bailo, E.; Deckert, V. *Chem. Soc. Rev.* **2008**, *37*, 921−930.
(13) Hermann, P.; Hermelink, A.; Lausch, V.; Holland, G.; Moller, L.; Bannert, N.; Naumann, D. *Analyst* **2011**, *136*, 1148−1152.
(14) Schmuck, C.; Wich, P.; Kustner, B.; Kiefer, W.; Schlucker, S. *Angew. Chem., Int. Ed.* **2007**, *46*, 4786−4789.
(15) Li, J. F.; Huang, Y. F.; Ding, Y.; Yang, Z. L.; Li, S. B.; Zhou, X. S.; Fan, F. R.; Zhang, W.; Zhou, Z. Y.; Wu, D. Y.; Ren, B.; Wang, Z. L.; Tian, Z. Q. *Nature* **2010**, *464*, 392−395.
(16) Anema, J. R.; Li, J. F.; Yang, Z. L.; Ren, B.; Tian, Z. Q. *Annu. Rev. Anal. Chem.* **2011**, *4*, 129−150.
(17) Leung, L. W. H.; Weaver, M. J. *J. Am. Chem. Soc.* **1987**, *109*, 5113−5119.
(18) Luo, H.; Weaver, M. J. *Langmuir* **1999**, *15*, 8743−8749.
(19) Feng, J. J.; Gernert, U.; Sezer, M.; Kuhlmann, U.; Murgida, D. H.; David, C.; Richter, M.; Knorr, A.; Hildebrandt, P.; Weidinger, I. M. *Nano Lett.* **2009**, *9*, 298−303.
(20) Sezer, M.; Feng, J. J.; Ly, H. K.; Shen, Y. F.; Nakanishi, T.; Kuhlmann, U.; Hildebrandt, P.; Mohwald, H.; Weidinger, I. M. *Phys. Chem. Chem. Phys.* **2010**, *12*, 9822−9829.
(21) Feng, J. J.; Gernert, U.; Hildebrandt, P.; Weidinger, I. M. *Adv. Funct. Mater.* **2010**, *20*, 1954−1961.
(22) Zou, S.; Weaver, M. J.; Li, X. Q.; Ren, B.; Tian, Z. Q. *J. Phys. Chem. B* **1999**, *103*, 4218−4222.
(23) Heck, K. N.; Janesko, B. G.; Scuseria, G. E.; Halas, N. J.; Wong, M. S. *J. Am. Chem. Soc.* **2008**, *130*, 16592−16600.
(24) David, C.; Richter, M.; Knorr, A.; Weidinger, I. M.; Hildebrandt, P. *J. Chem. Phys.* **2010**, *132*, 024712.
(25) Hildebrandt, P.; Stockburger, M. *Biochemistry* **1989**, *28*, 6710−6721.
(26) Pomplun, J.; Zschiedrich, L.; Klose, R.; Schmidt, F.; Burger, S. *Phys. Status Solidi A* **2007**, *204*, 3822−3837.
(27) Hildebrandt, P.; Macor, K. A.; Czernuszewicz, R. S. *J. Raman Spectrosc.* **1988**, *19*, 65−69.
(28) Wackerbarth, H.; Klar, U.; Gunther, W.; Hildebrandt, P. *Appl. Spectrosc.* **1999**, *53*, 283−291.
(29) Bain, C. D.; Troughton, E. B.; Tao, Y. T.; Evall, J.; Whitesides, G. M.; Nuzzo, R. G. *J. Am. Chem. Soc.* **1989**, *111*, 321−335.
(30) Stober, W.; Fink, A.; Bohn, E. *J. Colloid Interface Sci.* **1968**, *26*, 62−&.
(31) Lu, Y.; McLellan, J.; Xia, Y. N. *Langmuir* **2004**, *20*, 3464−3470.
(32) Haller, I. *J. Am. Chem. Soc.* **1978**, *100*, 8050−8055.
(33) Gu, J.; Xiao, X. Y.; Takulapalli, B. R.; Morrison, M. E.; Zhang, P.; Zenhausern, F. *J. Vac. Sci. Technol. B* **2008**, *26*, 1860−1865.
(34) McFarland, A. D.; Young, M. A.; Dieringer, J. A.; Van Duyne, R. P. *J. Phys. Chem. B* **2005**, *109*, 11279−11285.
(35) Frasca, S.; von Graberg, T.; Feng, J. J.; Thomas, A.; Smarsly, B. M.; Weidinger, I. M.; Scheller, F. W.; Hildebrandt, P.; Wollenberger, U. *ChemCatChem* **2010**, *2*, 839−845.
(36) Oellerich, S.; Wackerbarth, H.; Hildebrandt, P. *J. Phys. Chem. B* **2002**, *106*, 6566−6580.
(37) Wackerbarth, H.; Hildebrandt, P. *ChemPhysChem* **2003**, *4*, 714−724.
(38) Ly, H. K.; Marti, M. A.; Martin, D. F.; varez-Paggi, D.; Meister, W.; Kranich, A.; Weidinger, I. M.; Hildebrandt, P.; Murgida, D. H. *ChemPhysChem* **2010**, *11*, 1225−1235.
(39) Sezer, M.; Feng, J. J.; Sivanesan, A.; Weidinger, I. M. In *On Biomimetics*; Pramatarova, L. D., Eds.; InTech: Vienna, Austria, 2011.
(40) Kabuss, J.; Werner, S.; Hoffmann, A.; Hildebrandt, P.; Knorr, A.; Richter, M. *Phys. Rev. B* **2010**, *81*, 075314.
(41) Gersten, J.; Nitzan, A. *J. Chem. Phys.* **1980**, *73*, 3023−3037.
(42) Liao, P. F.; Wokaun, A. *J. Chem. Phys.* **1982**, *76*, 751−752.

Danksagung

Ich möchte mich bei allen bedanken, die mich während dieser Zeit unterstützt haben. Mein besonderer Dank gilt dabei folgenden Personen:

- Prof. Dr. Peter Hildebrandt für die Betreuung während der Doktorarbeit und für seine Unterstützung in jeglicher Hinsicht.
- Dr. Inez Weidinger für die Betreuung und die fruchtbare Zusammenarbeit.
- Dr. Diego Millo für die Zusammenarbeit, die vielen netten Gespräche und die Initiierung der unvergesslichen "Hilde-Band".
- Dr. Anna Fischer für anregende Unterhaltungen und die SEM-Messungen.
- Prof. Dr. Uwe Schröder, Dr. Falk Harnisch und Siang-Fu Hong für die Bereitstellung der Geobacter-Proben.
- Prof. Dr. Miguel A. de la Rosa und Dr. Irene Diaz-Moreno für die nitrierten Cytochrom-Proben.
- Prof. Dr. Andreas Knorr und Diplom Physiker Christoph Köhler für die Feldberechnungen.
- Dr. Uwe Kuhlmann für Seine Hilfe im Umgang mit den Spektrometern.
- Claudia Schulz für Ihre Hilfe im Labor.
- Jürgen Krauss und Dr. Hendrik Naumann für Ihre Hilfe bei technischen Problemen.
- Lars Paasche für Seine stete Hilfsbereitschaft bei allen Fragen.
- Meinen Freunden und Bürokollegen Jacek Kozuch und Francisco Velazquez-Escobar für die nette Arbeitsatmosphäre und die gemeinsame Zeit.
- Meinem alten Weggefährten Murat Sezer mit dem ich so manche Stunden im Labor verbracht habe.
- Marius Horch, Tillmann Utesch und allen weiteren Stammgästen des Mittagstisches. Der schönste Freitag bleibt unvergesslich.
- Marina Böttcher, Sara Bruun, Dörte DiFiore, Dr. Jiu-Ju Feng, Nina Heidary, Julia Hellmich, Anke Keidel, Dr. Friedhelm Lendzian, Wiebke Meister, Nobert Michael, Dr. Maria Andrea Mroginski, Yvonne Rippers, Johannes Salewski, Dr. Eberhard Schlodder, Gal Schkolnik, Elisabeth Siebert, Dr. Arumugam Sivanesan, Dr. Neslihan Tavraz, Dr. Ingo Zebger und allen weiteren Mitgliedern des Max-Volmer Laboratoriums für eine angenehme Arbeitsatmosphäre.
- Nele Bensmann für Ihre Unterstützung.

Meiner lieben Familie!

Selbständigkeitserklärung

Die selbstständige und eigenhändige Anfertigung dieser Arbeit versichere ich an Eides statt.

_____

Hoang Khoa Ly

Berlin, 15.08.2012